DEVELOPMENT AND MODEL FORMULATION OF SCALABLE CARBON NANOTUBE PROCESSES: HiPCO AND CoMoCAT PROCESS MODELS

A Thesis
Submitted to the Graduate Faculty of the
Louisiana State University and
Agricultural and Mechanical College
in partial fulfillment of the
requirements for the degree of
Master of Science in Chemical Engineering

in

The Department of Chemical Engineering

Adedeji Ebenezer Agboola
B.Sc., Obafemi Awolowo University, Nigeria, 1998
M.S., Louisiana State University, 2005
December, 2005

ACKNOWLEDGEMENTS

I wish to express my sincere appreciation to my research advisor, Professor Ralph W. Pike, for his technical guidance and support during the course of this research work. His assistance and suggestions were crucial in the realization of this work.

I would also like to thank Dr Armando Corripio and Dr F. Carl Knopf for being a part of my examination committee, and recognize their efforts in reviewing and evaluating this research. In addition, I would like to acknowledge and thank the Chemical Engineering Department at Louisiana State University for providing the opportunity and the financial wherewithal to accomplish my goals at LSU.

This research work is dedicated to my mother and siblings for their support, prayers, encouragement and love. Thank you for being a part of my life.

Graduate studies in the department have been a rewarding, satisfying and fulfilling experience. However, as much as the graduate school experience was rewarding, it is the people I met and interacted with: family, friends, colleagues, faculty, and others that made the whole journey worthwhile. Thank you for being a part of my experience at LSU.

"It takes the Grace of God.....and a Good Heart to be a Blessing"

TABLE OF CONTENTS

ACKNOWLEGEMENTS……ii

LIST OF TABLES……vi

LIST OF FIGURES……xii

ABSTRACT……xvii

CHAPTER ONE: INTRODUCTION……1
1.1 Overview……3
1.2 Structure……5
1.3 Properties……10
1.3.1 Electronic Properties……11
1.3.2 Mechanical Properties……12
1.3.3 Chemical Reactivity……13
1.4 Applications……14
1.4.1 Energy Storage……14
1.4.1a Hydrogen Storage……15
1.4.1b Lithium Intercalation……15
1.4.1c Electrochemical Supercapacitors and Actuators……17
1.4.2 Carbon Nanotube Based Electronics……18
1.4.2a Molecular Junctions……18
1.4.2b Field Effect Transistors……19
1.4.3 Field Emitting Devices……21
1.4.4 Nanoprobes……22
1.4.5 Nanosensors……23
1.4.6 Nanotube Composites……24
1.4.7 Nanotube Templates……25
1.5 Production Cost and Future Outlook……25
1.6 Summary ……29

CHAPTER TWO: LITERATURE REVIEW……33
2.1 Carbon Nanotube Synthesis ……33
2.1.1 Electric Arc Discharge ……34
2.1.2 Laser Vaporization ……37
2.1.3 Chemical Vapor Deposition ……38
2.1.3a Thermal Chemical Vapor Deposition ……40
2.1.3b Plasma Enhanced Chemical Vapor Deposition ……41
2.1.4 Electrolysis Technique ……42
2.1.5 Solar Production of Carbon Nanotubes ……44
2.2 Growth Mechanism ……45
2.3 Carbon Nanotube Processes ……49
2.4 Evaluation of Synthesis Methods ……73

2.5 Purification of Carbon Nanotubes ……83
2.5.1 Oxidation ……83
2.5.2 Acid Treatment ……88
2.5.3 Ultrasonication ……89
2.5.4 Mechanical Purification …….....90
2.5.5 Functionalization …….....91
2.5.6 Microfiltration …….....92
2.5.7 Chromatography ……..93
2.6 Evaluation of the Purification Methods ……...95
2.7 Summary …….....95

CHAPTER THREE: PROCESS MODEL DEVELOPMENT AND FORMULATION…….....99
3.1 Process Model Development ……..100
3.2 Description of HiPCO Carbon Nanotube Process ……..102
3.2.1 Feed Preparation Section …….....102
3.2.2 Reactor Section ……..106
3.2.3 Separation/Purification Section …….....109
3.2.4 Absorber Section …….....111
3.3 Model for HiPCO Carbon Nanotube Process …….....113
3.3.1 Heat Exchanger Network …….....113
3.3.2 Reactor Section …….....115
3.3.3 Separation/Purification Zone…….....120
3.4 Description of CoMoCAT Carbon Nanotube Process ……...126
3.4.1 Feed Preparation Section ……...126
3.4.2 Reactor Section …….....130
3.4.3 Absorber Section …….....132
3.4.4 Separation/Purification Section ……..…….....133
3.5 Model for CoMoCAT Carbon Nanotube Process ……..……...136
3.5.1 Heat Exchanger Network …….....137
3.5.2 Reaction Section ……...138
3.5.3 Separation/Purification Section ……....141
3.5.4 Absorption Section …….…..146
3.6 Summary …….....148

CHAPTER FOUR: RESULTS FROM ANALYSIS OF HiPCO AND CoMoCAT PROCESS MODELS 150
4.1 Analysis of HiPCO Process Model ……..…..150
4.2 Analysis of CoMoCAT Process Model …….....170
4.3 Summary …….....194

CHAPTER FIVE: ECONOMIC ANALYSIS OF HiPCO AND CoMoCAT PROCESS MODELS 198
5.1 Economic Decision Analysis ……..……....198
5.1.1 Total Plant Costs ……..…….....199

5.1.2 Total Product Costs …….....205
5.2 Profitability Analysis …….....214
5.3 Comparison of Energy Consumption and Emissions from HiPCO and CoMoCAT Processes …….....219
5.4 Summary ……...222

CHAPTER SIX: CONCLUSIONS AND RECOMMENDATIONS FOR FUTURE RESEARCH ……...…….…….. 225
6.1 Conclusions …….……..…226
6.2 Recommendations for Future Research …….……...229

REFERENCES…….....231

APPENDIX A: THERMODYNAMIC DATA OF PROCESS STREAMS.....240

APPENDIX B: MATERIAL AND ENERGY BALANCE EQUATIONS……...246

APPENDIX C: ANALYSIS OF HiPCO AND CoMoCAT PROCESS MODELS …….....289

APPENDIX D: SAMPLE CALCULATION COST ESTIMATES……...……400

VITA…….....……..406

LIST OF TABLES

1.1 Production – Cost Estimates for MWNT as–grown for a High and Low Cost Scenario …….....26

1.2 Companies Producing Carbon Nanotubes and their Product Prices ……...30

2.1 Arc – Discharge Synthesis Processes …….....74

2.2 Laser Vaporization Synthesis Processes ……75

2.3 Chemical Vapor Deposition (CVD) Synthesis Processes …….....76

2.4 Other Synthesis Methods …….....78

2.5 Companies Making Equipments for Carbon Nanotube Synthesis …….....98

3.1 Production Capacity for Carbon Fiber Facilities …….....100

3.2 Process Units for the Carbon Nanotube HiPCO Process Model ……104

3.3 Process Streams in the HiPCO Process Model ……105

3.4 Material and Energy Balance Equations for Reactor Gas Effluent – Feed Recycle Cross Heat Exchanger (E–102) ……....116

3.5 Material and Energy Balance Equations for the Reactor (V–102) ……..119

3.6 Material and Energy Balance Equations for Gas–Solid Filter (Z–101) ……..122

3.7 Material and Energy Balance Equations for Gas Absorption Column (T–101) 125

3.8 Process Units for CoMoCAT Process Model .....….128

3.9 Process Streams in the CoMoCAT Process Model ....……...……...129

3.10 Material and Energy Balance Equations for Waste Heat Boiler (E–202)……...139

3.11 Material and Energy Balance Equations for Fluidized Bed Reactor (V–201)…….....142

3.12 Standard Cyclone Proportions.……..……..143

3.13 Material and Energy Balance Equations for Cyclone Separator (Z – 201)…….....144

3.14 Material and Energy Balance Equations for Froth Flotation Column (T–203)…...145

3.15 Material and Energy Balance Equations for Gas Absorption Column (T–201)…..147

3.16 Material and Energy Balance Equations for Gas Stripping Column (T–202)…….148

4.1. Process Units for the Carbon Nanotube HiPCO Process Model ……..153

4.2. Preliminary Equipment Summary Table for HiPCO Process Model ……...154

4.3. Flow Summary Table for HiPCO Process Model ……162

4.4. Utility Flow Summary Table for HiPCO Process Model …….....167

4.5. Process Units for the CoMoCAT Process Model …….....174

4.6. Preliminary Equipment Summary Table for CoMoCAT Process Model …….....176

4.7. Flow Summary Table for CoMoCAT Process Model ……..185

4.8. Utility Flow Summary Table for CoMoCAT Process Model ……...190

4.9. Reaction Products, Byproducts and Emissions of HiPCO Process …….....195

4.10. Reaction Products, Byproducts and Emissions of CoMoCAT Process…...…….195

5.1. Terms Used in Economic Decision Analysis on an Annual Basis…….200

5.2 Partial List of Elements in a Plant Cost Estimates …….201

5.3 Total Plant Cost Estimates for HiPCO Process …...……...203

5.4 Total Plant Cost Estimates for CoMoCAT Process ……204

5.5 List of Components in Total Product Cost Estimates …….206

5.6 Economic Data Summary for the HiPCO Process …….209

5.7. Economic Data Summary for the CoMoCAT Process …….…..……...209

5.8. Total Product Cost Estimates for HiPCO Process …….212

5.9. Total product Cost Estimates for the CoMoCAT Process……. ……213

5.10 Net Present Value Analysis for the HiPCO Process…….....216

5.11 Net Present Value Analysis for the CoMoCAT Process ……...218

5.12 Comparison of Raw Materials, Energy Consumption, and Emissions from HiPCO and CoMoCAT Processes ……...220

5.13 Economic and Profitability Analysis of HiPCO and CoMoCAT Processes …….223

A.1. Thermodynamic Coefficient Data for Specific Enthalpy and Specific Heat Capacity ……...241

A.2. Mean Specific Heat Capacities and Enthalpy of Formation ……242

A.3. Molecular Weights of Components in HiPCO and CoMoCAT Processes ……...245

B1.1 Material and Energy Balance Equations for Mixer (V–101)……..……..247

B1.2 Material and Energy Balance Equations for Reactor (V–102) ……....248

B1.3 Material and Energy Balance Equations for Reactor Gas Effluent–Feed Recycle Cross Heat Exchanger (E–102) …….249

B1.4 Material and Energy Balance Equations for CO Feed Recycle Gas–Fired Heater (E–101) ……...250

B1.5 Material and Energy Balance Equations for Waste Heat Boiler (E–103) ……..251

B1.6 Material and Energy Balance Equations for Water Cooler 1 (E–104) ……...252

B1.7 Material and Energy Balance Equations for Solute Rich–Lean Solvent Cross Heat Exchanger (E–105) ……...……...253

B1.8 Material and Energy Balance Equations for Gas–Solid Filter (Z–101) …….254

B1.9 Material and Energy Balance Equations for Air Oxidizer (V–103) ……...255

B1.10 Material and Energy Balance Equations for Acid Treatment Tank (V–104) ……256

B1.11 Material and Energy Balance Equations for Liquid–Solid Filter (Z–102) ….....257

B1.12 Material and Energy Balance Equations for Gas Absorption Column (T–101) ……258

B1.13 Material and Energy Balance Equations for Gas Stripping Column (T–102) ……259

B1.14 Material and Energy Balance Equations for Reboiler (E–106) ……260

B1.15 Material and Energy Balance Equations for Flash Drum (V–105) ……..261

B1.16 Material and Energy Balance Equations for Gas Compressor (C–101) ……..262

B1.17 Material and Energy Balance Equations for Vent Valve (Z–105) ……...263

B1.18 Material and Energy Balance Equations for Acid Regenerator (Z–104) …….264

B1.19 Material and Energy Balance Equations for Product Drier (Z–103) ……...265

B1.20 Material and Energy Balance Equations for Centrifuge Separator (Z–106) ...266

B2.1 Material and Energy Balance Equations for CO Feed Gas-Fired Heater (E–201)……..…….....267

B2.2 Material and Energy Balance Equations for Fluidized Bed Reactor (V–201) ……..……...268

B2.3 Material and Energy Balance Equations for Cyclone Separator (Z–201).…….269

B2.4 Material and Energy Balance Equations for Waste Heat Boiler (E–202) …….270

B2.5 Material and Energy Balance Equations for Water Cooler 1 (E–203) ……..271

B2.6 Material and Energy Balance Equations for Solute Rich–Lean Solvent Cross Heat Exchanger (E–204) ……...……..272

B2.7 Material and Energy Balance Equations for Gas–Solid Filter (Z–202) ……273

B2.8 Material and Energy Balance Equations for Silica Leaching Tank (V–202) …….274

B2.9 Material and Energy Balance Equations for Froth Flotation Column (T–203) ……...275

B2.10 Material and Energy Balance Equations for Liquid–Solid Filter (Z–204) ….....276

B2.11 Material and Energy Balance Equations for Centrifuge Separator (Z–203) …….……...277

B2.12 Material and Energy Balance Equations for Acid Dissolution Tank (V–203) ……...278

B2.13 Material and Energy Balance Equations for Liquid–Solid Filter (Z–205) …...279

B2.14 Material and Energy Balance Equations for Gas Absorption Column (T–201) ……..……..280

B2.15 Material and Energy Balance Equations for Gas Stripping Column (T–202) ……..……...281

B2.16 Material and Energy Balance Equations for Reboiler (E–205) ……..……...282

B2.17 Material and Energy Balance Equations for Flash Drum (V–204) ……..….283

B2.18 Material and Energy Balance Equations for Gas Compressor (C–201) ……...284

B2.19 Material and Energy Balance Equations for Vent Valve (Z–209) ……285

B2.20 Material and Energy Balance Equations for Product Drier (Z–206) ……286

B2.21 Material and Energy Balance Equations for Acid Regenerator (Z–208) ……..287

B2.22 Material and Energy Balance Equations for Catalyst Regenerator (Z–207) …288

C1.1 Enthalpy Data for HiPCO Flow Reactor (V–102)…….……..……299

C1.2 Enthalpy Data for Cross Heat Exchanger (E–102) ……..…...306

C1.3 Enthalpy Data for Waste Heat Boiler (E–103) ……..…….309

C1.4 Enthalpy Data for Heat Exchanger Water Cooler (E–104) ……311

C1.5 Enthalpy Data for CO Feed Recycle Heater (E–101) …….…..…..314

C1.6 Enthalpy Data for Gas Stripping Column (T–102) …….324

C1.7 Enthalpy Data for Cross Heat Exchanger (E–105) …….....327

C1.8 Enthalpy Data for Reboiler (E–106)……..……..…329

C1.9 Enthalpy Data for Air Oxidizer (V–103) ……..……..335

C2.1 Enthalpy Data for CoMoCAT Fluidized Bed Reactor (V–201)……..…355

C2.2 Enthalpy Data for CO Feed Gas–Fired Heater (E–201) …….357

C2.3 Enthalpy Data for Waste Heat Boiler (E–202) ……..…….363

C2.4 Enthalpy Data for Heat Exchanger Water Cooler (E–203) ……365

C2.5 Enthalpy Data for Gas Stripping Column (T–202) …….....374

C2.6 Enthalpy Data for Cross Heat Exchanger (E–204) ……376

C2.7 Enthalpy Data for Reboiler (E–205)……..…….378

LIST OF FIGURES

1.1 Tetrahedrally–bonded Structure of Diamond ……2

1.2 Trigonally–bonded Graphite Structure ……2

1.3 sp^3 and sp^2 Hybridization Scheme in C–C Structure ……....3

1.4 Buckminster Fullerene or 'Buckyball' Structure ……..4

1.5 Molecular Model of a Carbon Nanotube Capped by Six Pentagons in Each End ……...4

1.6 Schematic Theoretical Model for a Single Wall Carbon Nanotube …….7

1.7a Chiral Vector ……...8

1.7b Possible Chiral Vectors in terms of (*n, m*) ……..8

1.8 Molecular Models of SWNTs Exhibiting Different Chiralities ……..10

1.9 Electronic band Structure of Carbon Nanotubes ……12

1.10 Simulated Buckling Behavior in Carbon Nanotubes …….13

1.11 Hydrogen Storage Capacities for SWNTs …….16

1.12 Charging–Discharging Mechanism of Li^+ Battery ……....16

1.13 Two–Terminal Semi–conducting (10, 0) / Metallic (6, 6) Nanotube Junction Showing Rectification Behavior …….19

1.14 Carbon Nanotube – Top: T–junction; Bottom: Y–junction ……...20

1.15 Carbon Nanotube Field–Effect Transistor …….21

1.16 Longitudinal Cross–Section of a Fluorescent Display with a Field Emission Cathode Constructed from MWNT ……....22

1.17 Single–Walled Carbon Nanotube Tip at the end of an Atomic Force microscope (AFM) ……..23

1.18 Future Global Production Estimates of SWNTs and MWNTs ……..28

1.19 MWNT Production Capacity by Countries ……28

1.20 SWNT Production Capacity by Countries ……....29

1.21 Chart Displaying the Exponential Growth of the Number of
Nanotube Publications per Year from 1991 – 2001 …….....31

2.1 Schematics of an Electric–Arc Discharge Apparatus …….35

2.2 TEM Pictures of Standard Core Material from the Arc Deposit ……36

2.3 Laser Vaporization Apparatus ……....38

2.4 Schematic Diagram of a Thermal CVD Apparatus ……....40

2.5 Schematic Diagram of the Plasma CVD Apparatus ……...41

2.6 Schematic Diagram of the Electrolysis Apparatus for
Liquid – Phase Production of Carbon Nanotubes ……...43

2.7 Sketch of a Solar Reactor for Carbon Nanotube Production ……..44

2.8 Proposed Open–Ended Growth Mechanism of Carbon Nanotubes
by the Absorption of C_2 (Dimers) and C_3 (Trimers) ……...47

2.9 Schematics Depicting the Various Carbon Nanotube
Growth Probabilities Starting from a Nucleus O by the
addition of Hexagons, H(6), Pentagons, P(5) and Heptagons, S(7) …….48

2.10 Thermo Gravimetric Analyses of MWNT and C_{60} ……...84

2.11 Schematic Diagram of SWNT Magnetic Purification Apparatus …….....91

2.12 Schematic Diagram of a Micro Filtration Cell …….....94

3.1 Process Flow Diagram for the HiPCO Carbon Nanotube
Production Process …….103

3.2 Process Flow Diagram for the CoMoCAT Carbon Nanotube
Production Process …….....127

4.1 Process Flow Diagram for the HiPCO Carbon Nanotube
Production Process …….152

4.2 Process Flow Diagram for the CoMoCAT Carbon Nanotube
Production Process …….173

C1.1 Input – Output Structure for the Overall HiPCO Process ……..290

C1.2 Input – Output Component Structure for HiPCO Flow Reactor (V–102)…....292

C1.3 Input – Output Component Structure for Mixer (V–101) …….....301

C1.4 Input – Output Component Structure for Gas–Solid Filter (Z–101) ……..303

C1.5 Input – Output Component Structure for Cross Heat Exchanger (E–102) ……305

C1.6 Input – Output Component Structure for Waste Heat Boiler (E–103) ……..308

C1.7 Input – Output Component Structure for Water Cooler (E–104) ……..310

C1.8 Input – Output Component Structure for CO Recycle Heater (E–101) …….313

C1.9 Input – Output Component Structure for Gas Compressor (C–101) …….……315

C1.10 Input – Output Component Structure for Gas Absorption Column (T–101).……..317

C1.11 Input – Output Component Structure for Gas Stripping Column (T–102)….....322

C1.12 Input – Output Component Structure for Cross Heat Exchanger (E–105) …….....326

C1.13 Input – Output Component Structure for Reboiler (E–106) ……..……..329

C1.14 Input – Output Component Structure for Flash Drum (V–105) ……..…331

C1.15 Input – Output Component Structure for Vent Valve (Z–105) ……..….332

C1.16 Input – Output Component Structure for Air Oxidizer (V–103) ...…….334

C1.17 Input – Output Component Structure for Acid Treatment Tank (V–104) ……..338

C1.18 Input – Output Component Structure for Liquid – Solid Filter (Z–102) ……..339

C1.19 Input – Output Component Structure for Product Drier (Z–103) ……...340

C1.20 Input – Output Component Structure for Acid Regeneration Column (Z–104) …….343

C1.21 Input – Output Component Structure for Centrifuge Separator (Z–106) ……345

C2.1 Input – Output Structure for the Overall CoMoCAT Process ……..…….348

C2.2 Input – Output Component Structure for CoMoCAT Fluidized Bed Reactor (V–201)…….....350

C2.3 Input – Output Component Structure for CO Feed Heater (E–201) ….…...357

C2.4 Input – Output Component Structure for Cyclone Separator (Z–201) ……..359

C2.5 Input – Output Component Structure for Gas–Solid Filter (Z–202) …….361

C2.6 Input – Output Component Structure for Waste Heat Boiler (E–202) ……..363

C2.7 Input – Output Component Structure for Water Cooler (E–203) ……..365

C2.8 Input – Output Component Structure for Gas Compressor (C–201) …….……367

C2.9 Input – Output Component Structure for Gas Absorption Column (T–201).……..370

C2.10 Input – Output Component Structure for Gas Stripping Column (T–202)….....373

C2.11 Input – Output Component Structure for Cross Heat Exchanger (E–204) …….....375

C2.12 Input – Output Component Structure for Reboiler (E–205) ……..……..377

C2.13 Input – Output Component Structure for Flash Drum (V–204) ……..….379

C2.14 Input – Output Component Structure for Vent Valve (Z–209) ……..…..380

C2.15 Input – Output Component Structure for Silica Leaching Tank (V–202) .....……....381

C2.16 Input – Output Component Structure for Froth Flotation Column (T–203)……...384

C2.17 Input – Output Component Structure for Liquid – Solid Filter (Z–204) ……...386

C2.18 Input – Output Component Structure for Dissolution Tank (V–203) ……388

C2.19 Input – Output Component Structure for Liquid – Solid Filter 2 (Z–205) ……390

C2.20 Input – Output Component Structure for Product Drier (Z–206) ……391

C2.21 Input – Output Component Structure for Catalyst Regeneration Bed (Z–207) ……394

C2.22 Input – Output Component Structure for Acid Regeneration Column (Z–208) ……..……397

C2.23 Input – Output Component Structure for Centrifuge Separator (Z–203) …....399

ABSTRACT

Carbon nanotubes are seamless cylindrical tubes, consisting of carbon atoms arranged in a regular hexagonal structure. It is considered as the ultimate engineering material because of its unique and distinct electronic, mechanical and material characteristics. The discovery of these materials pioneered the nanotechnology revolution, which encompasses a broad and multidisciplinary spectrum, including nanomaterials, nanobiotechnology, and nanoelectronics.

Hundreds of published articles of laboratory scale and pilot plant processes were reviewed that describe potential synthesis and post–synthesis purification methods for large scale production of carbon nanotubes. The main production technologies include electric arc discharge, laser vaporization, and catalytic chemical vapor deposition. These production technologies were evaluated based on criteria such as operating conditions, continuous processes, feedstock source, yield, catalyst and product selectivity.

Based on these criteria, two catalytic chemical vapor deposition production technologies were identified, and used as a basis for the conceptual design and development of two, 5,000 metric tons per year carbon nanotube production plants. The production technologies selected are the high–pressure carbon monoxide (HiPCO) process, and the cobalt–molybdenum catalyst (CoMoCAT) process.

The HiPCO production technology is a gas–phase homogeneous process that employs a floating catalyst approach, whereby the growth catalyst is formed *in situ* during the production process. Carbon nanotubes are produced from the disproportionation of carbon monoxide over catalytic iron nanoparticles at 1,323 K and 450 psia. In the HiPCO process, a multi–step purification approach, involving oxidation, acid treatment and

filtration, was used to remove amorphous carbon and residual iron impurities from the final carbon nanotube product.

The CoMoCAT production technology is a heterogeneous process involving growth on supported catalysts. Carbon nanotubes are produced by the catalytic decomposition of carbon monoxide on silica supported, Co–Mo bimetallic catalyst particles, at 1,223 K and 150 psia. The silica supports, residual cobalt and molybdenum particles, and amorphous carbon are removed from the final carbon nanotube product by silica leaching, froth flotation, acid treatment and filtration purification processes.

Economic and profitability analysis showed a positive net present value (NPV) of $609 million and $753 million for the HiPCO and CoMoCAT processes respectively. The rate of return (ROR) on investment, based on an economic life of ten years, was calculated to be 37.4% and 48.2% for the HiPCO and CoMoCAT processes respectively. These results showed the scalability, economic feasibility and viability of the proposed HiPCO and CoMoCAT technologies with a design capacity of 5,000 metric tons per year of carbon nanotubes. Hence, the route to multi tons production of high purity carbon nanotubes at affordable prices would soon be a reality.

CHAPTER ONE: INTRODUCTION

This chapter serves as an introduction to the emerging and interesting world of carbon nanotubes. It reviews the discovery, structure and properties of these unique and fascinating carbon materials. This chapter also provides information on the latest research advances, production and purification techniques, costs and applications of carbon nanotubes developed over the past decade.

Carbon nanotubes regarded as another form of pure carbon are perfectly straight tubules with diameter in nanometers, length in microns and properties close to those of an ideal graphite fiber (Ajayan, 2000). Carbon, a highly versatile element, due to its ability to bond in diverse ways to form materials with different properties, has four valence electrons and a ground state electronic configuration of $2s^2\ 2p^2$. The two natural crystalline forms of pure carbon known are diamond and graphite.

Carbon forms diamond, which is composed of tetrahedrally bonded carbon atoms, under conditions of extreme temperature and/or pressure. Graphite, a soft, grey solid, is composed of sheets of trigonally bonded carbon atoms arranged in hexagonal sheets called graphene sheets with high electrical conductivity along the direction of its graphene layers. The tetrahedrally–bonded diamond and trigonally–bonded graphite structures are shown in Figure 1.1 and Figure 1.2 respectively.

Carbon atoms exhibit sp^3 hybridization (sp^3 C–C bond length ~1.56A) in diamond, whereby four bonds are directed towards the corners of a regular tetrahedron to form an extremely rigid three–dimensional structure, and hence, its hardness. In graphite, sp^2 hybridization occurs, such that each atom is connected evenly to three carbon atoms in the x–y plane and a weak π bond (a van der Waals bond) due to the p_z orbital is present in the

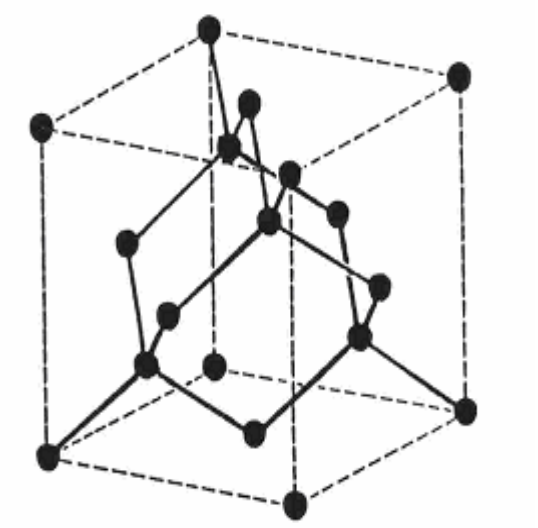

Figure 1.1. Tetrahedrally–bonded Structure of Diamond, from Dresselhaus et al, 1996

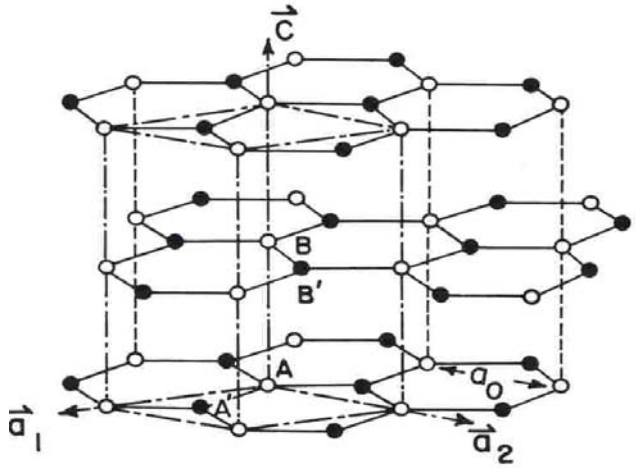

Figure1.2. Trigonally–bonded Graphite Structure, from Dresselhaus et al, 1996

x–y plane and a weak π bond (a van der Waals bond) due to the p_z orbital is present in the z-axis (Terrones, 2003).

Unlike the sp^3 hybridized diamond structure, in which all electrons are localized in the sp^3 framework, the free electrons in the p_z orbital of the graphite lattice are delocalized and move within the lattice framework. Consequently, graphite is able to conduct electricity

while diamond behaves as an insulator. The sp^3 and sp^2 hybridization scheme in the C–C structure is depicted by Figure 1.3.

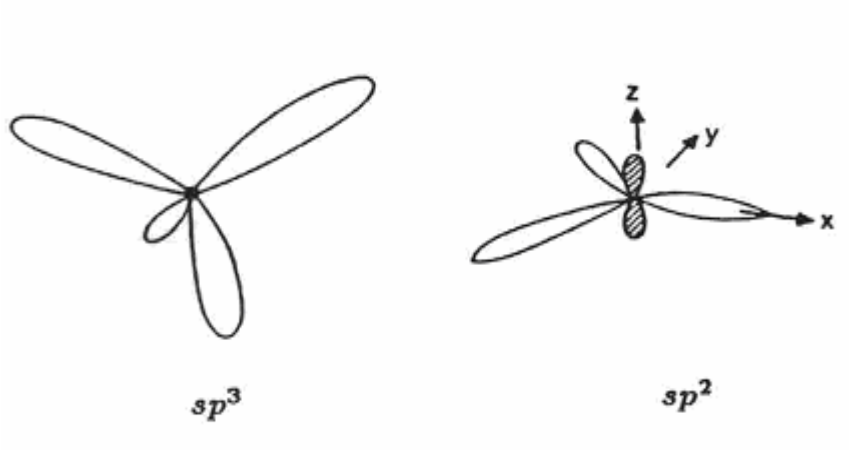

Figure 1.3 sp^3 and sp^2 Hybridization Scheme in C–C Structure, from Dresselhaus et al, 1996

1.1 OVERVIEW

In the mid–1980s, Kroto, Smalley, and co–workers in a collaborative research effort involving the synthesis of cyanopolyynes from laser vaporization of a graphite target discovered a family of large 60–carbon atom, closed–cage clusters with high gas–phase stability from the mass spectra of evaporated carbon samples (Dresselhaus et al, 1996). These molecules resembled the geodesic domes designed and built by R. Buckminster Fuller, and thus, were referred to as 'Fullerenes'. The most famous fullerene, which is the C_{60} molecule, is referred to as the 'Buckminster fullerene' or 'buckyball', and its structure is shown in Figure 1.4.

In 1991, while studying carbonaceous deposit from an arc discharge between graphite electrodes, Iijima and co–workers, using a high–resolution electron transmission microscope (HRTEM), observed highly crystallized, helical carbon filaments. These carbon filaments have a small diameter (a few nanometers) and a large length (several microns),

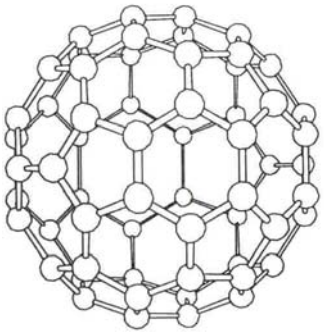

Figure 1.4 Buckminster Fullerene or ‘Buckyball’ Structure, from Dresselhaus et al, 1996

resulting in a large aspect ratio and were referred to as carbon nanotubes. Carbon nanotubes, a new form of pure carbon, contain a hexagonal network of carbon atoms rolled up to form seamless cylindrical tubes that are capped by pentagonal carbon rings (Terrones, 2003). A molecular model of carbon nanotubes closed on both ends by six hemispherical pentagons is shown in Figure 1.5.

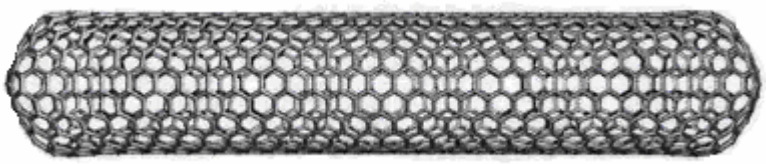

Figure 1.5 Molecular Model of a Carbon Nanotube Capped by Six Pentagons in Each End, from Terrones, 2003.

The two main categories of carbon nanotubes are the single–walled carbon nanotubes (SWNTs) and multi–walled carbon nanotubes (MWNTs). The 1991 discovery by Iijima and co–workers consists of mainly the graphitic multi–walled nanotubes while the single–walled nanotubes were not discovered until a couple of years later. Single–walled carbon nanotubes contain long wrapped graphene sheets and are regarded as the

fundamental cylindrical structures. Single–walled carbon nanotubes form the building blocks of both multi–walled carbon nanotubes, and the ordered arrays of single–walled nanotubes called ‘ropes’, held together by van der Waals forces (Dresselhaus et al, 1998).

Several methods exist today to synthesize carbon nanotubes, including electric–arc discharge pioneered by Iijima, laser ablation technique developed at Rice University, and catalytic chemical vapor deposition methods. In all of these synthesis methods, carbon vapor is made to condense into tubular structures, with or without the presence of catalysts, which are mostly nanoparticles of transition metals.

The as–produced reaction product typically contains a mixture of carbon nanotubes, amorphous carbon and catalyst metal particles. However, the ratio of the constituents varies from process to process and depends on growth conditions for a given process. Consequently, various purification techniques have been developed to separate the carbon nanotubes from all the undesired impurities.

Some of these purification techniques include oxidation, acid treatment, annealing, ultrasonication, micro–filtration, and chromatography techniques. The synthesis techniques and post–synthesis purification methods for carbon nanotubes are discussed further in Chapter Two.

1.2 STRUCTURE

The discovery of carbon nanotubes by Iijima in 1991 pioneered a new direction in carbon research that complemented the activities on the fullerene research front. Unlike the fullerene structure, where carbon atoms form a sphere, carbon nanotubes are cylindrical structures, either infinite in length or with caps at each end; such that the two end caps can be joined to form a fullerene (Dresselhaus et al, 1996).

Carbon nanotubes are composed wholly of sp^2 bonds, which provide them with their unique strength. Under extreme conditions of pressure, carbon nanotubes can merge together, exchanging some sp^2 bonds for sp^3 bonds, with the possibility of forming strong, unlimited length wires through high–pressure nanotube linking (en.wikkipedia.org).

Single–walled carbon nanotubes are cylindrical in shape and composed of singular graphene cylindrical walls with diameters ranging between 1nm and 2nm, whereas, multi–walled carbon nanotubes refer to a collection of concentric single walled carbon nanotubes with different diameters consisting of several co–axial graphene cylinders separated by a spacing ~ 0.34nm (Ajayan, 2000).

Due to the differences in the length and diameter of single and multi walled carbon nanotubes, their physical and chemical properties differ, also. Single–walled carbon nanotubes consist of two separate regions; the two hemispherical end caps and the sidewall tube, with distinct physical and chemical properties.

Three types of carbon nanotubes are possible: armchair nanotubes, zig–zag nanotubes, and chiral nanotubes, depending on how the two–dimensional (2–D) grapheme (a single layer from a 3D graphite crystal) sheet is rolled up. By rolling a graphene sheet into a cylinder and capping each end of the cylinder with half of a fullerene molecule, a fullerene derived tubule; one atomic layer is formed as shown in Figure 1.6. This direction in a graphite sheet and the nanotube diameter are derived from a pair of integers (n, m) (Dresselhaus et al, 1996).

Two atoms in the graphene sheet plane are chosen; the vector pointing from the first atom towards the other atom is called the chiral vector, C_h, which connects the two crystallographically equivalent sites, ‘O’ and ‘A’, on a two–dimensional graphene sheet

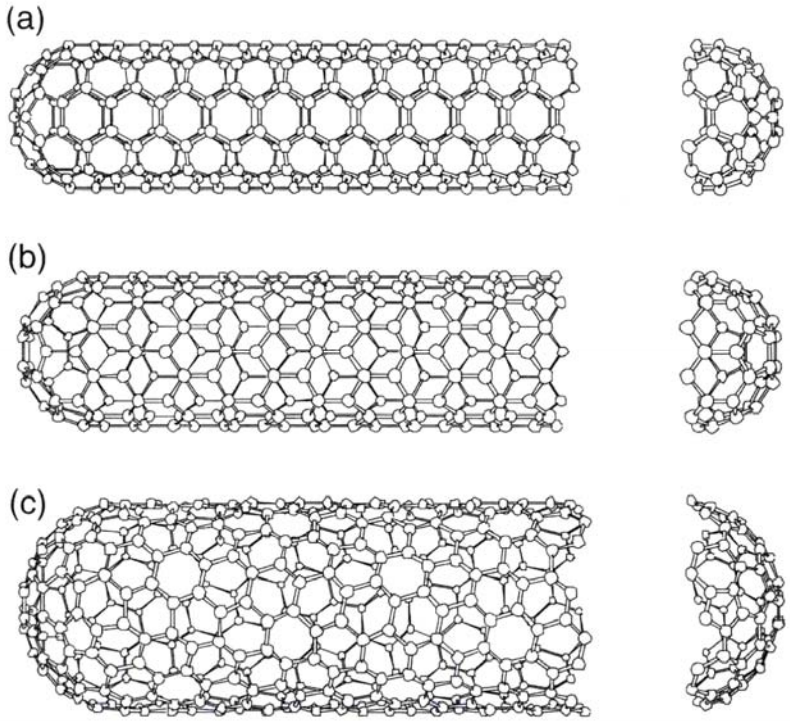

Figure 1.6 Schematic Theoretical Model for a Single Wall Carbon Nanotube, with the tube axis normal to (a) $\theta = 30^0$ direction (an armchair nanotube):(n, m) = (5,5), (b) $\theta = 0^0$ direction (a zig– zag nanotube):(n, m) = (9, 0) and (c) $0 < \theta < 30^0$ (a chiral nanotube): (n, m) = (10, 5), from Terrones, 2003

plane, where a carbon atom is located at each vertex of the honeycomb structure, as shown in Figure 1.7a (Dresselhaus et al, 1996). The chiral vector can be represented mathematically by:

$$C_h = na_1 + ma_2 \qquad (1\text{-}1)$$

where a_1, a_2 are unit lattice vectors in the 2–D hexagonal lattice, and n, m are integers. Equation (1-1) can be used to specify a collection of possible chiral vectors in terms of pairs of the integers (n, m), which is shown in Figure1.7b. Each pair of integers (n, m) specifies a different way of rolling the graphene sheet to form a carbon nanotube.

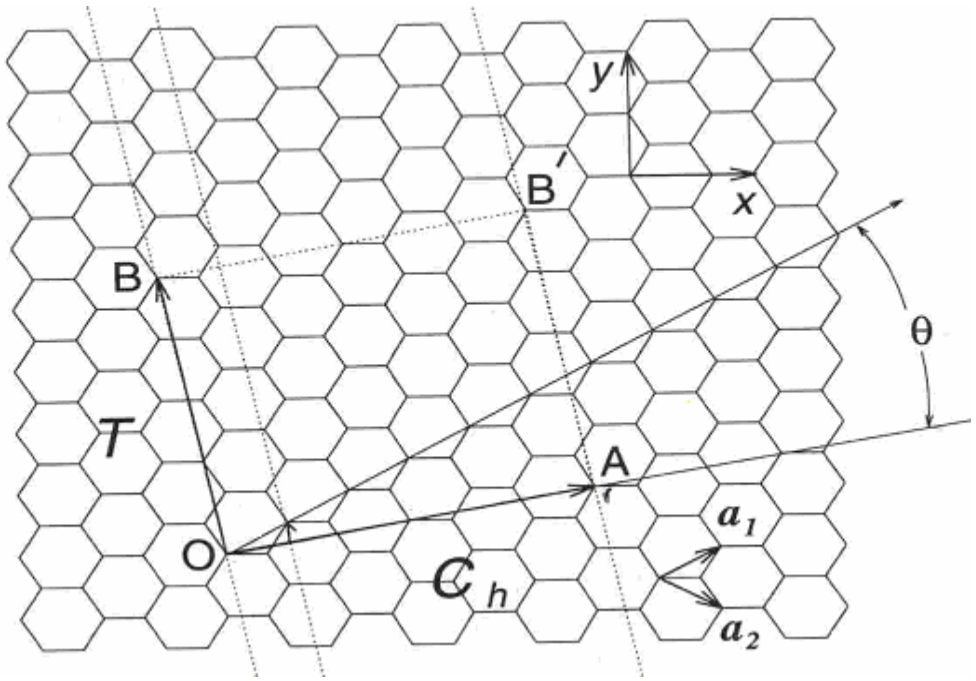

Figure 1.7a Chiral Vector, from Dresselhaus et al, 1996

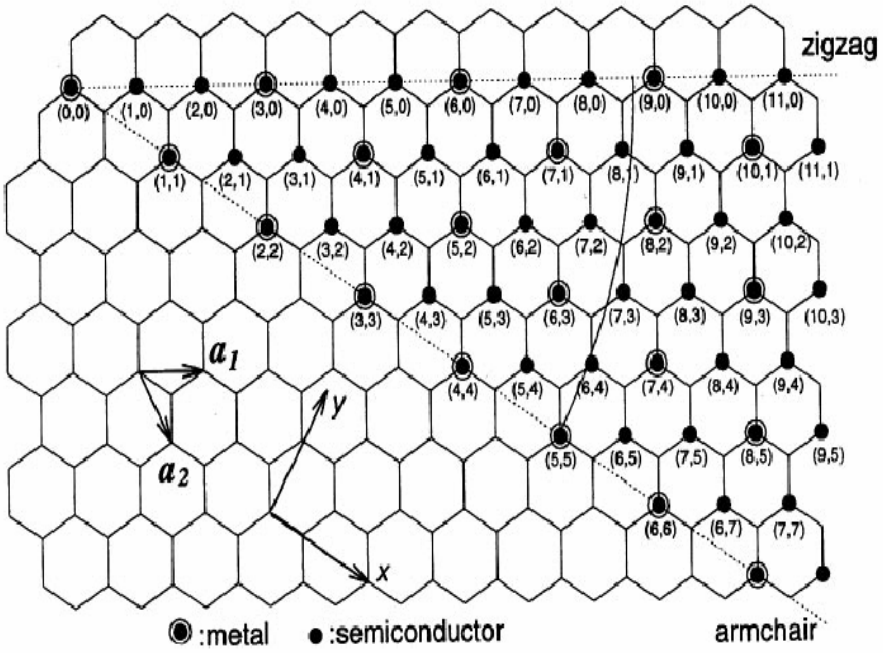

Figure 1.7b. Possible Chiral Vectors in terms of (*n*, *m*), from Dresselhaus et al, 1996.

In terms of the integers (*n*, *m*), the diameter of a carbon tubule, d_t is given by Equation (1.2), (Dresselhaus et al, 1996):

$$d_t = \frac{C_h}{\pi} = \frac{\sqrt{3} * a_{C-C} * (m^2 + mn + n^2)^{1/2}}{\pi} \qquad (1\text{-}2)$$

where $a_{c\text{-}c}$ = 1.42A, and corresponds to the C–C distance for sp^2–hybridized carbon.

Another important parameter, the chiral angle, θ is the angle between the chiral vector, C_h and the unit lattice vector, a_1, given by:

$$\theta = \tan^{-1}\left(\frac{\sqrt{3}m}{m + 2n}\right) \qquad (1\text{-}3)$$

The graphene sheet is rolled until the two atoms, 'O' and 'A' coincide by superimposing the two ends OA of the chiral vector, C_h. The cylinder joint is made by joining the line AB' to the parallel line OB in Figure1.7a, where the direction of the nanotube axis; lines OB and AB', are perpendicular to the chiral vector, C_h, at each end.

In the non–chiral configurations, also known as armchair and zig–zag arrangements, the honeycomb lattice at the top and bottom is always parallel to the tube axis, as shown in Figure 1.8. The armchair geometry occurs when the two C–C bonds on opposite sides of each hexagon are perpendicular to the tube axis, as shown in Figure 1.8a, whereas the zig–zag structure results when the two C–C bonds are parallel to the tube axis, as shown in Figure 1.8b (Terrones, 2003).

In terms of the pairs of integers (*n*, *m*) and the chiral angle (θ); the armchair tube is denoted by (*n*, *n*), and $\theta = 30^0$, whereas the zig–zag tube is specified by (*n*, 0) and $\theta = 0^0$. All other configurations in which the C–C bonds lie at an angle to the tube axis ($0^0 < \theta < 30^0$), and represented by (*n*, *m*) are referred to as chiral carbon nanotubes as shown in Figure 1.8c.

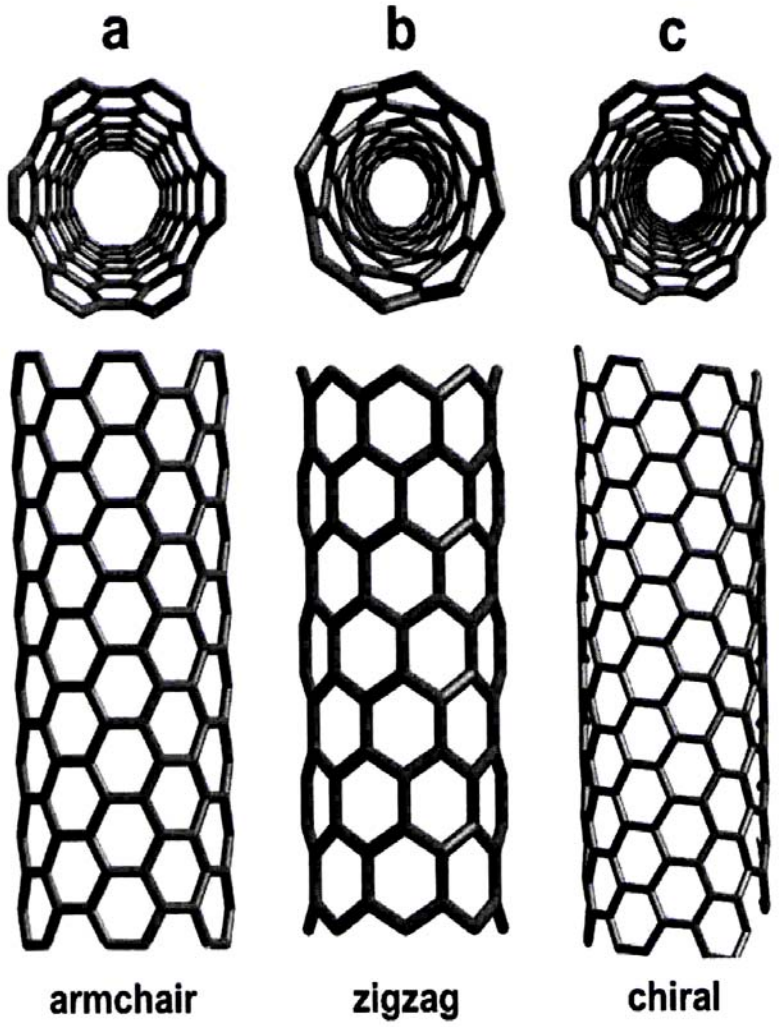

Figure 1.8 Molecular Models of SWNTs Exhibiting Different Chiralities: (a) armchair structure (b) zig–zag structure and (c) chiral or helical structure, from Terrones, 2003

1.3 PROPERTIES

Carbon nanotubes are tubular carbon molecules with exciting and fascinating properties compared to the parent planar graphite due to the unique structure, topology and dimensions of the nanotubes. The topology or the closed geometry of individual carbon nanotube layers also impact significantly on the nanotube physical properties. The combination of size, structure and topology endows carbon nanotubes with their unique electrical, mechanical, optical, chemical, and surface properties (Ajayan, 2000).

1.3.1 Electronic Properties

Despite structural similarity to a single sheet of graphite, which is a semiconductor with zero band gap, early theoretical studies predicted a strong dependence of the electrical conducting properties of carbon nanotubes on its structure, such that nanotubes could be metallic or semi conducting depending on their helicity and diameter. These studies showed that all armchair tubes are metallic, whereas the zig–zag and chiral carbon nanotubes can be either metallic or semi conducting (Ajayan, 2000).

Single–walled nanotubes can be either metallic or semi conducting, depending on the pair of integers (n, m), even though the C–C chemical bonds within the tubes are similar and no impurities or doping are present in the nanotube. This unique characteristic in carbon nanotube properties is related to its electronic band structure as shown in Figure 1.9.

The unique electronic properties of carbon nanotubes are due to the quantum confinement of electrons normal to the carbon nanotube axis, resulting in electron propagation occurring only along the carbon nanotube axis. The number of 1–D conduction and valence bands resulting from the electron propagation depends on the standing waves set up around the carbon nanotube circumference. The sharp intensities observed in Figure 1.9 are known as van Hove singularities and result from 1–D quantum conduction in carbon nanotubes (Terrones, 2003).

Electronic transport in metallic carbon nanotubes occurs ballistically (i.e., without scattering), over long nanotube lengths because of the nearly 1–D electronic structure in carbon nanotubes. Thus, carbon nanotubes are able to transport high currents with essentially little or no heating. In addition, phonons are able to propagate easily along the carbon nanotube length (Baughman, et al, 2002).

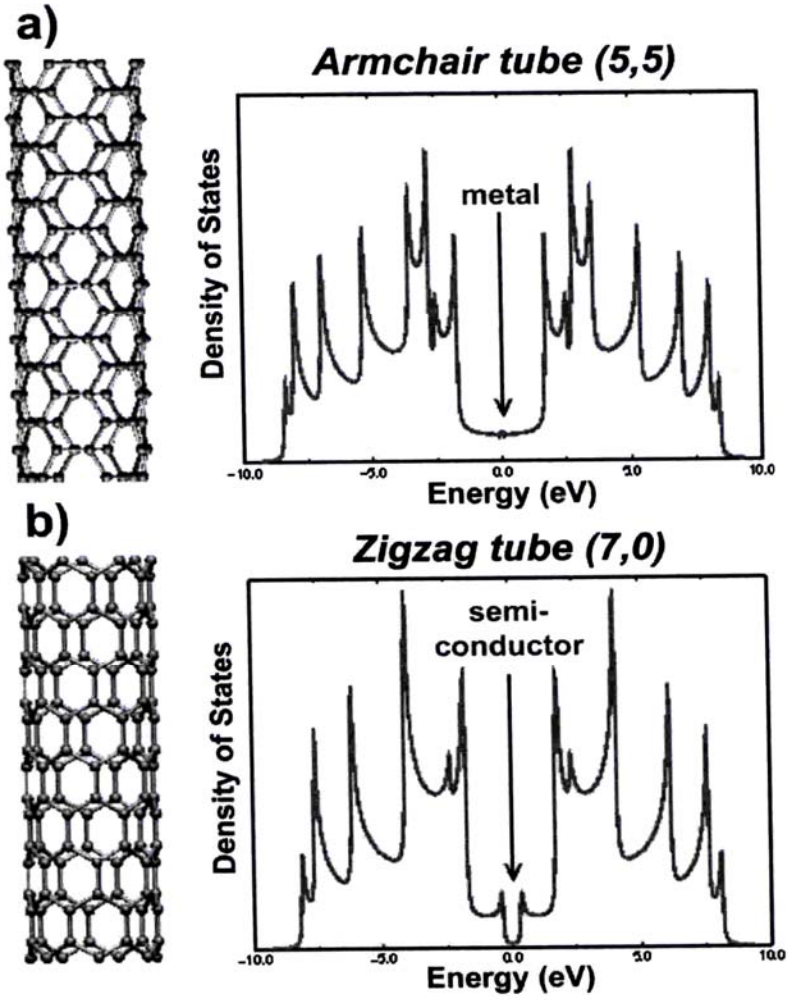

Figure 1.9 Electronic Band Structure of Carbon Nanotubes: (a) metallic armchair tube and (b) zig–zag tube showing semi conducting attributes, from Terrones, 2003

1.3.2 Mechanical Properties

Carbon nanotubes are composed entirely of sp^2–hybridized C–C covalent bonds, which are stronger than the sp^3 bonds found in diamond. This bonding structure is one of the strongest in nature and endows carbon nanotubes with their unique strength, and thus, carbon nanotubes are one of the stiffest and most robust synthesized structures, with high Young's modulus and high tensile strength. Early theoretical calculations predicted a Young modulus as high as 1–5 TPa, while other researcher scientists predicted that the carbon

nanotubes would soften with decreasing radius, and by varying the carbon nanotube chirality (Ajayan, 2000).

In comparison to graphite and carbon fibers, carbon nanotubes are considered the ultimate carbon fiber that can be made from graphite structure. Unlike carbon fibers which fracture easily under compression, carbon nanotubes are highly flexible and do not break upon bending or under severe distortion (Dresselhaus et al, 1998). They form kink–like ridges that can relax elastically when the stress is released and can be twisted, flattened, bent into small circles or around small bends without breaking as shown in Figure 1.10.

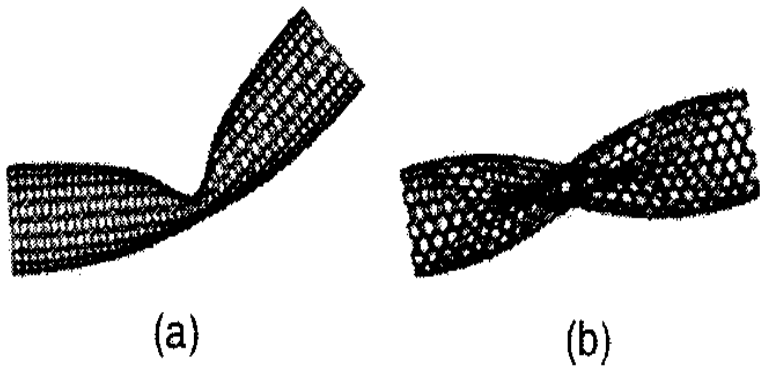

Figure 1.10 Simulated Buckling Behavior in Carbon Nanotubes (a) under bending load (b) under torsional load, from Qian et al, 2003

1.3.3 Chemical Reactivity

In comparison to a graphene sheet, the chemical reactivity of carbon nanotubes is greatly enhanced by the nanotube surface curvature and is directly related to the pi–orbital mismatch caused by an increased curvature. The sidewall and end caps of the carbon nanotube structure have different chemical reactivity with reactivity increasing as the nanotube diameter decreases, such that the end caps are more reactive than the sidewalls and a smaller nanotube results in increased reactivity. For example, the solubility of carbon

nanotubes in different solvents can be controlled by the covalent chemical modification of either the sidewalls or the hemispherical end caps (Daenen et al, 2003).

Since carbon nanotubes are composed of graphitic carbon, they are highly resistant to chemical attack and exhibit high thermal stability. Oxidation studies have shown that, since the end caps are more reactive than the sidewalls, the carbon nanotubes are usually oxidized from their tips, thus, leading to the possibility of opening carbon nanotubes by oxidation techniques (Ajayan, 2000).

Studies of the catalytic nature of carbon nanotube surfaces have also shown that carbon nanotubes are catalytically active. The catalytic activity have been demonstrated by the higher selectivity shown by multi–walled carbon nanotubes embedded with metals in heterogeneous catalysis (e.g. liquid phase hydrogenation reaction using Ru on nanotubes) compared to same metals attached on other carbon substrates (Ajayan, 2000).

1.4 APPLICATIONS

Since the discovery of carbon nanotubes in 1991, several studies carried out have demonstrated the potential applications of carbon nanotubes in existing and/or new technologies, based on their unique electronic properties, size, mechanical strength and flexibility. These applications include energy storage, molecular electronics, nanoprobes/nanosensors, nanotube composites and nanotube templates.

1.4.1 Energy Storage

The most commonly used electrodes for energy storage in fuel cells, batteries and other electrochemical devices are graphite, carbon fibers and carbonaceous materials. Thus, carbon nanotubes with their small dimensions, smooth surface topology and perfect surface specifity can be used as electrodes for energy storage in most of these devices.

In fuel cell applications, studies have shown that the electron transfer rate at the carbon electrodes, which determines its efficiency, is fastest on carbon nanotubes (Daenen et al, 2003). The applications of carbon nanotubes for energy storage in electrochemical devices include the potential use of carbon nanotube as hydrogen storage media, and the intercalation of lithium ions in carbon nanotube materials (Baughman, et al, 2002).

1.4.1a Hydrogen Storage

Carbon nanotubes behave as efficient gas, liquid or metal containers due to their hollow, cylindrical and nanometer–scale dimensions. Consequently, hydrogen, which has water as its combustion product, can be stored as an energy source inside the well-defined carbon nanotube pores (Daenen et al, 2003).

Apart from gas–phase storage, hydrogen can also be stored by electrochemical adsorption, whereby a hydrogen atom rather than a hydrogen molecule is adsorbed via chemisorption. Hydrogen storage in carbon nanotubes would readily find application in the fabrication of fuel cells for powering electric vehicles (Terrones, 2003). The hydrogen storage capacities by weight percent for three single–walled carbon nanotube samples are shown in Figure 1.11.

1.4.1b Lithium Intercalation

Lithium is one of the best elements used in the fabrication of light–weight and efficient batteries because it has the lowest electronegativity and electrons are readily donated from Li^+. Due to the high reactivity of lithium, the negative lithium electrode reacts easily and the efficiency of the metal electrode decreases very rapidly (Terrones, 2003).

However, by intercalating lithium ions, Li^+ within graphite–like structures, the Li^+ migrate from a graphitic anode to the cathode (e.g. $LiCoO_2$, $LiNiO_2$, $LiMn_2O_4$). The charge

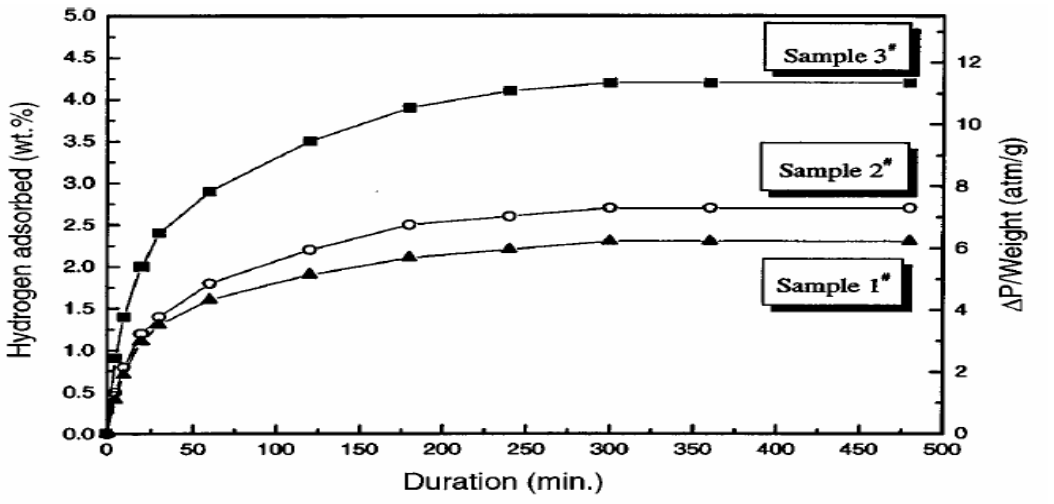

Figure 1.11 Hydrogen Storage Capacities for SWNTs, from Terrones, 2003.

and discharge phenomena in lithium batteries, based on the electrochemical intercalation and de–intercalation of Li^+ in both electrodes is shown in Figure 1.12 (Terrones, 2003).

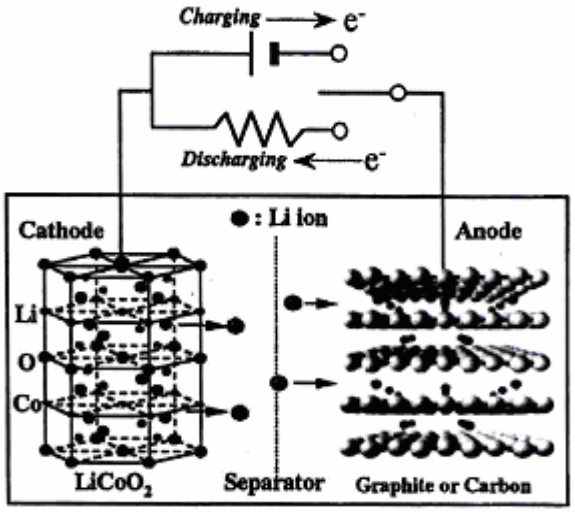

Figure 1.12 Charging–Discharging Mechanism of Li^+ Battery, from Terrones, 2003.

The capacity, determined by the lithium saturation concentration of the electrode materials, is highest in carbon nanotubes if all the interstitial spaces are accessible for lithium intercalation. Lithium ion batteries have found application as energy storage media in portable electronic devices such as mobile phones, digital cameras, and computers.

1.4.1c Electrochemical Supercapacitors and Actuators

The high electrical conductivity and large electrochemically accessible surface area of porous multi–wall carbon nanotubes are excellent properties for energy storage in the fabrication of devices that use electrochemical double–layer charge injection, such as supercapacitors, and electromechanical actuators. Supercapacitors typically have huge capacitances in comparison with that of ordinary dielectric–based capacitors, whereas electromechanical actuators could be used in robots or as artificial muscles (Baughman, et al, 2002).

Like typical supercapacitors, carbon nanotube supercapacitors and electromechanical actuators are comprised of two electrodes, separated by an insulating material that is ionically conducting in the electrochemical devices. Unlike the capacitance of an ordinary capacitor, which depends on the interelectrode distance, the capacitance of an electromechanical device is dependent on the separation between the charge on the electrode and the countercharge in the electrolyte. Consequently, since this separation is about a nanometer for carbon nanotube electrodes, as against the larger separation in ordinary dielectric capacitors, very large capacitances result from the high carbon nanotube surface area accessible to the electrolyte (Baughman, et al, 2002).

Supercapacitors with carbon nanotube electrodes can be used for applications that require higher power and storage capabilities, such as provision of fast acceleration and electrical storage of braking energy in hybrid electric vehicles. Carbon nanotube electromechanical actuators can function at low voltages and temperatures up to 350 ^{o}C, while operation at higher temperatures appear feasible, considering the thermal stability of carbon nanotubes and industrial application of carbon electrodes (Terrones, 2003)

1.4.2. Carbon Nanotube–Based Nanoelectronics

The possibility of using carbon nanotubes in place of silicon for downsizing circuit dimensions, based on the metallic and semiconducting behavior, as well as the electronic transport properties of carbon nanotubes is of considerable interest in the nanotechnology field. Consequently, the integration of multiple nanotube devices into circuits may be feasible in the future if molecular self–assembly techniques can be controlled to produce carbon nanotubes with desired dimensions, properties and lower contact resistances (Terrones, 2003).

1.4.2a Molecular Junctions

Molecular junctions, created by introducing pairs of heptagon and pentagon in an otherwise perfect hexagonal lattice carbon nanotube structure raises the possibility of connecting nanotubes of different diameter and chirality in nanotube heterojunctions as molecular electronic devices or switching components. The molecular junction could be metal–metal, metal–semiconductor, or semiconductor–semiconductor and behaves like a rectifying diode, as shown in Figure 1.13 (Meyyappan et al, 2003).

There are two ways to create heterojunctions with more than two terminals with the difference in the two approaches being the nature and characteristics of the junctions forming the device. The first approach involves connecting different nanotubes through topological–defect–mediated junctions such that the nanotubes are chemically connected through bonding networks to form a stable junction in switching, logic and transistor applications (Meyyappan et al, 2003).

The second approach involves laying down crossed nanotubes over each other to form physically contacted junctions amenable to changes in electromechanical applications,

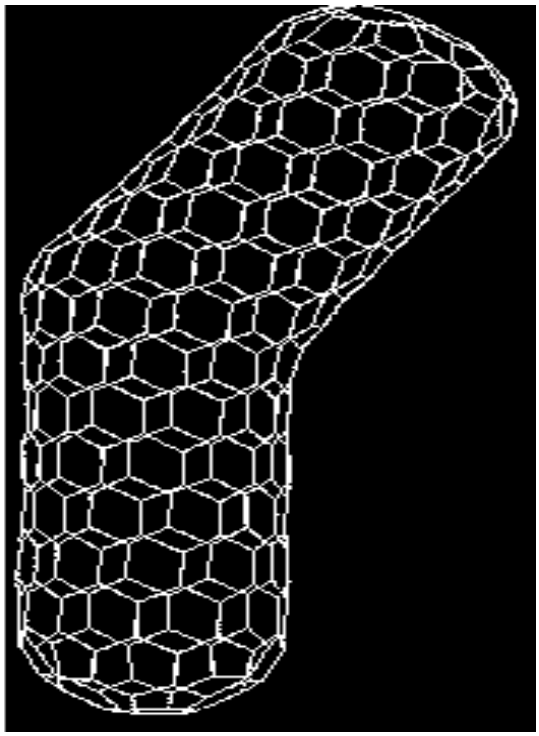

Figure 1.13 Two–Terminal Semi–conducting (10,0) / Metallic (6,6) Nanotube Junction, Showing Rectification Behavior, from Meyyappan et al, 2003.

such as bi–stable switches and sensors. Novel structures of carbon nanotube T– and Y–junctions have been proposed as models of three–terminal nanoscale monomolecular electronic devices. The T–junctions can be considered as a specific case of Y junctions in which two connecting nanotubes are perpendicular to each other, as shown in Figure 1.14.

1.4.2b Field Effect Transistors

The fabrication of nanotube–based three–terminal devices involves horizontally placing nanotubes between two metal nanoelectrodes, while the room temperature demonstration of a three–terminal switch device based upon a nanotube molecule such as in field–effect transistors first appeared in 1998 (Meyyappan et al, 2003).

This field transistor consists of single–walled carbon nanotube placed to bridge a pair of metal electrodes serving as a source and a drain. The electrodes were lithographically

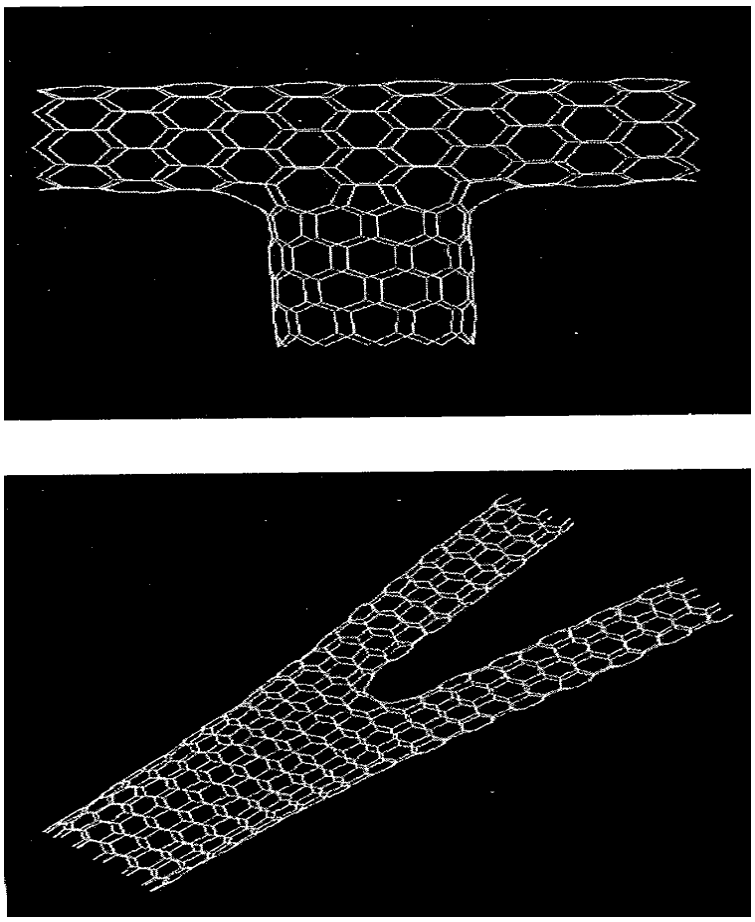

Figure 1.14.Carbon Nanotube – Top: T–junction and Y, Bottom: Y–junctions, from Meyyappan et al, 2003.

defined by applying a layer of SiO_2 on a silicon wafer, which acts as the back gate (Meyyappan, et al., 2003). A carbon nanotube field–effect transistor assembly is shown in Figure 1.15.

It should be noted that a transistor assembled this way may or may not work, depending on whether the selected carbon nanotube is semiconducting or metallic. However, recent developments have shown that the patterned growth of carbon nanotubes on a silicon wafer may be an important step in the evolution of integrated carbon nanotube devices in the future (Baughman, et al., 2002).

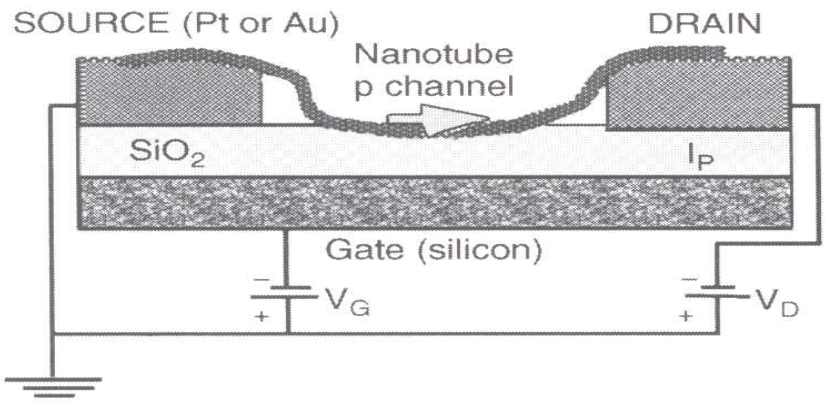

Figure 1.15 Carbon Nanotube Field–Effect Transistor, from Meyyappan et al, 2003

1.4.3 Field Emitting Devices

At sufficiently high electric field, electrons can be extracted from a solid by tunneling through the surface potential barrier generating an emission current that depends on the strength of the local electric field the emission surface and its work function. Since the applied electric field must be high to extract an electron, the elongated shape of carbon nanotubes ensures a very large field amplification to meet this requirement, such that when a potential is applied between a nanotube surface and an anode, electrons are readily emitted from their tips (Terrones, 2003).

Using this principle and due to their nanometer–size diameter, high electrical conductivity, small energy spread, high chemical stability and structural integrity, carbon nanotubes can be used as efficient field emission sources for the fabrication of multiple electronic devices. These devices include flat panel displays, electron guns for electron microscopes, gas–discharge tubes in telecoms networks, intense light sources, microwave amplifiers and x–ray sources (Terrones, 2003). A schematic representation of a fluorescent display unit with MWNT as field emission source is shown in Figure 1.16.

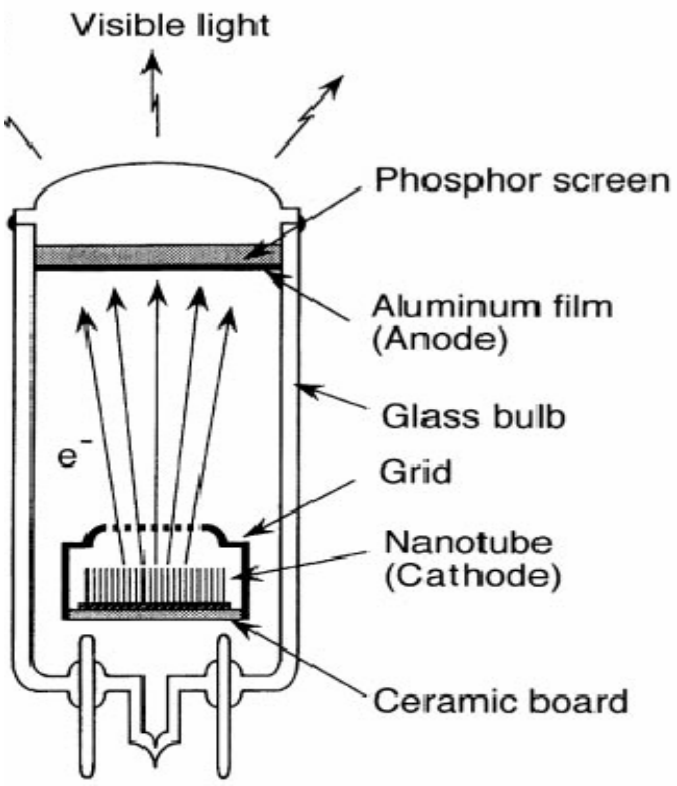

Figure 1.16 Longitudinal Cross–Section of a Fluorescent Display with a Field Emission Cathode Constructed from MWNT, from Terrones, 2003

1.4.4 Nanoprobes

Carbon nanotubes, due to its high–aspect ratio, robust mechanical strength and elasticity characteristics, are excellent materials for the production of scanning probe tips for atomic probe microscopes. The mechanical robustness and low buckling force of carbon nanotubes result in a remarkable increase in the probe life, as well as minimizing sample damage during hard crashes into substrates. In addition, the nanotubes tips are typically immune to crashes with hard surfaces due to their flexibility.

The cylindrical shape and nanometer scale dimensions of carbon nanotube probe tips allow imaging in narrow, deep crevices, while offering improved image resolution in comparison with the image observed using other conventional probe tips such as silicon or

metal tips. Other applications include the use of a pair of carbon nanotubes on a probe tip as tweezers to move nanoscale structures on surfaces, and the use of carbon nanotube tips in imaging thin films in semiconductor metrology. An atomic force microscope (AFM) probe with single walled carbon nanotube tip is shown in Figure 1.17.

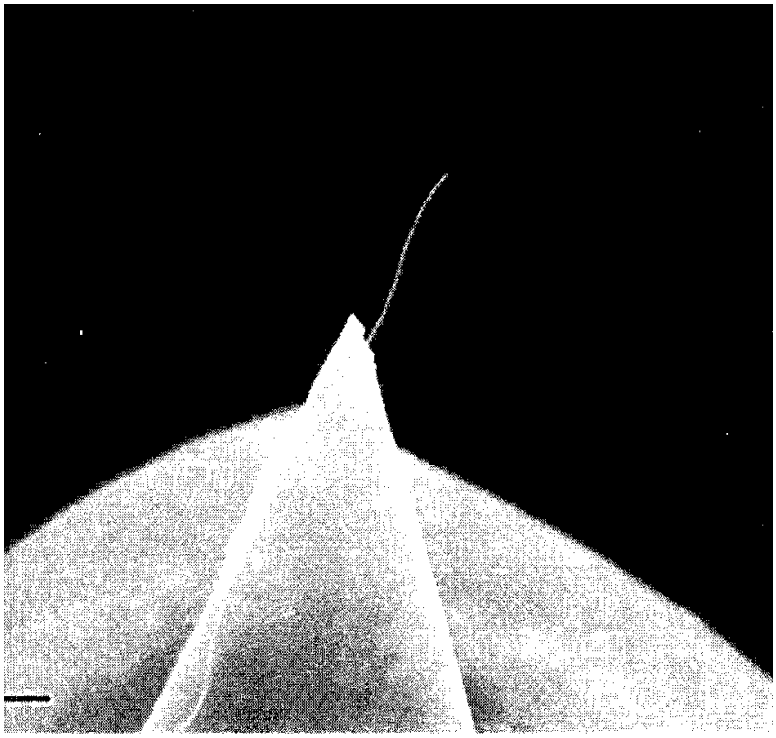

Figure 1.17 Single–Walled Carbon Nanotube Tip at the end of an Atomic Force Microscope (AFM), from Meyyappan et al, 2003

1.4.5. Nanosensors

Significant research is in progress to develop carbon nanotube–based chemical, biological and physical sensors. These efforts can be broadly classified into two categories: one that utilizes certain properties of the nanotube, such as a change in conductivity with gas adsorption, and the second, that depends on the ability to modify the carbon nanotube tip and/or side–wall with functional groups that serve as sensing elements.

However, the major benefits of nanosensor applications include the nanometer dimension of the nanotube sensing element and the corresponding minute amount of material required for a response. The applications of nanosensors using carbon nanotubes include gas sensors used to monitor leaks in chemical plants, biosensors for cancer diagnostics and sensitive environmental pressure sensors.

1.4.6 Nanotube Composites

One of the first commercial applications of multi–walled carbon nanotubes is in its use as electrically conducting materials in polymer composites. The combination of high–aspect ratio, stiffness, mechanical strength, low density, small size and high conductivity makes carbon nanotubes ideal substitutes to carbon fibers as reinforcements in high strength, low–weight and high performance polymer composites. In addition, incorporation of carbon nanotubes in plastics can potentially result in remarkable increase in the modulus and strength of structural materials.

However, the success of the carbon nanotube–reinforced composites depends on the strength of the interface between the nanotubes and the polymer matrix, uniform dispersion of the carbon nanotubes in the polymer matrix, and the prevention of intra–tube sliding between carbon nanotubes (Baughman, et al., 2002). The weak carbon nanotube–polymer matrix adhesion could be as a result of the atomically smooth surface, and small diameter of the carbon nanotubes, which is nearly the same as that of a polymer chain (Daenen et al, 2003).

Since carbon nanotube aggregates behave differently to loads than individual nanotubes, sliding of cylinders in multi walled carbon nanotubes and shearing of tubes in single–walled carbon nanotube ropes, could be limiting factors for load transfer in polymer

composites. In order to overcome this constraint, the carbon nanotube aggregates are usually broken up and dispersed or cross–linked to prevent slippage (Daenen, et al, 2003). In addition to improved electrical conduction and better performance during compressive load, carbon nanotubes reinforcement also increase the toughness of the structural polymer composite by absorbing energy during its elastic behavior (Daenen et al, 2003).

1.4.7 Nanotube Templates

The very small channels found in carbon nanotubes results in strong capillary forces within the nanotube structure, such that the forces are strong enough to hold gases and fluids in its hollow cavities, and hence, the possibility of filling the cavities of the nanotubes to create nanowires.

The critical factor in this application is the wetting characteristics of the carbon nanotubes; while filling MWNTs is relatively easier than filling SWNTs because of their larger pore sizes (Daenen et al, 2003). A novel application of this technology is the nanoreactor, which raises the prospect of chemical reactions being carried out inside these filled cavities.

1.5 PRODUCTION, COST AND FUTURE OUTLOOK

Carbon nanotubes, long touted as the ultimate engineering material because of its remarkable physical properties and potential applications, can be considered as one of the building blocks for nanoscale science and nanotechnology. Since the discovery of carbon nanotubes in 1991, rapid progress has taken place in the theoretical understanding of the fundamental properties required to characterize its structure.

However, the advances in the scalability of the production processes have not moved at a comparable pace and thus, the large–scale synthesis of carbon nanotubes is

current limitation for commercial application (Corrias et al, 2003). The lack of a reliable, large–volume production capacity, the high price and the fact that there is little selectivity in controlling the properties of the product are the three factors that have principally inhibited the commercialization of carbon nanotube technologies (Andrews et al, 2002).

Consequently, the scalability of the production processes is essential for any commercial consideration. For example, some of the technologies use equipment that simply cannot be made bigger, and the only way to increase production is to make more pieces of equipment, which will not produce the economies of scale required to lower costs significantly (Roman et al, 2004).

The price of carbon nanotubes is presently too high (around US$200/g for multi–walled carbon nanotubes to ten times this value for purified single–walled carbon nanotubes) for any realistic industrialization and commercial application of these unique materials (Corrias et al, 2003). However, by using high– and low–cost scenarios, shown in Table 1.1, De Jong and Geus proposed a production–cost estimate of US$10–50/kg for multi–walled carbon nanotubes for the low cost scenario.

Table 1.1 Production–Cost Estimates for MWNT As–grown for a High– and Low–Cost Scenario, from De Jong and Geus, 2000

Case	**High Cost**	**Low Cost**
Scale of Production	Low	High
Reactor Type	Fixed bed	Fluidized Bed
Type of Operation	Batch	Continuous
Yield (m/m)	~ 50	~ 200
Growth Time (h)	2	0.5
Cost Estimate ($/kg)	> 50	< 10

This low cost scenario is dependent on the following economic factors (De Jong et al, 2000):

(a) the scale of production

(b) the feedstock used (e.g., ethene or natural gas)

(c) the reactor type and related type of operation

(d) the yield of MWNTs and (e) the reaction time and temperature

A recent survey of forty–four global producers of carbon nanotubes projected that nanotube production has reached a tipping point where the combination of decreasing prices and increased availability will enable more widespread applications. The survey estimates total global production capacity for multi–walled carbon nanotubes to be about 99 tons a year and is expected to increase to at least 268 tons annually by 2007 (Roman et al, 2004).

Current global production of single–walled carbon nanotubes can be estimated to be about 9000 kg/year and the production is expected to increase up to more than 27 tons by 2005 and is expected to reach 100 tons by 2008 (Roman et al, 2004). The projected global production estimates for multi–walled and single–walled carbon nanotubes are shown in Figure 1.18.

Presently, almost one half of the MWNT production takes place in the United States, followed by Japan with ~ 40% of total production. Likewise, the United States leads production of SWNTs with more than 70% holding of total production capacity, while China ranks second with 22%, and the European Union with nearly 4% of total production (Roman et al, 2004). Multi–walled and single–walled carbon nanotube production capacity estimates by countries are shown in Figure 1.19 and Figure 1.20 respectively. Some of the companies producing carbon nanotubes, carbon nanotube type and purity, and the corresponding product prices are listed in Table 1.2.

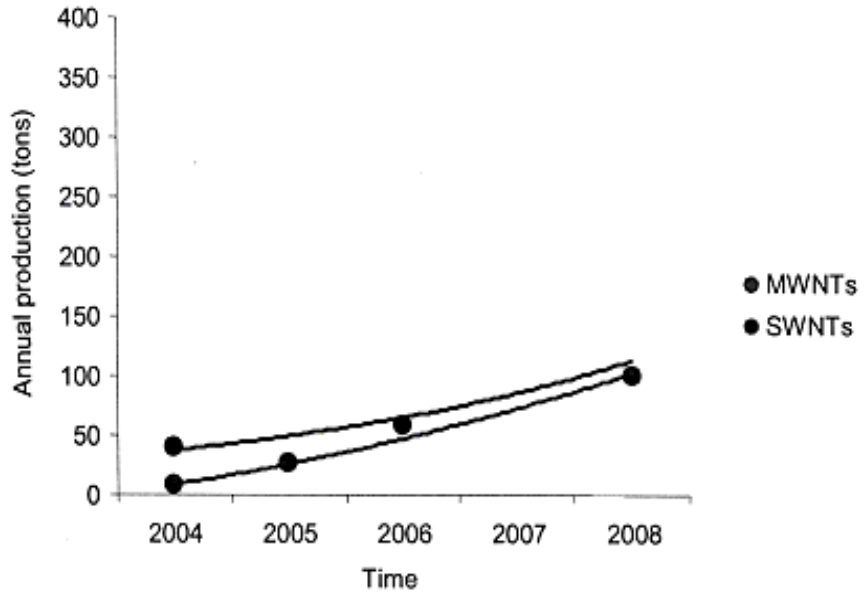

Figure 1.18 Future Global Production Estimates of SWNTs and MWNTs, from Roman et al, 2004.

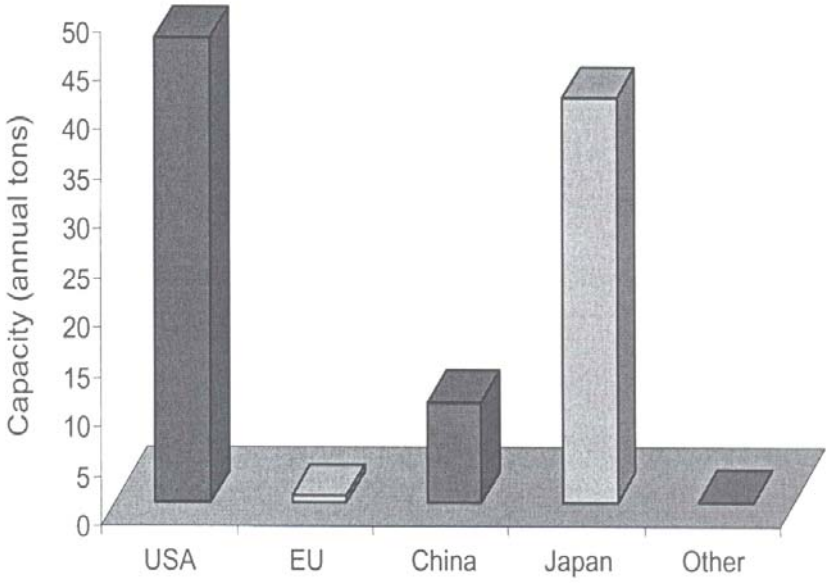

Figure 1.19 MWNT Production Capacity by Countries, from Roman et al, 2004

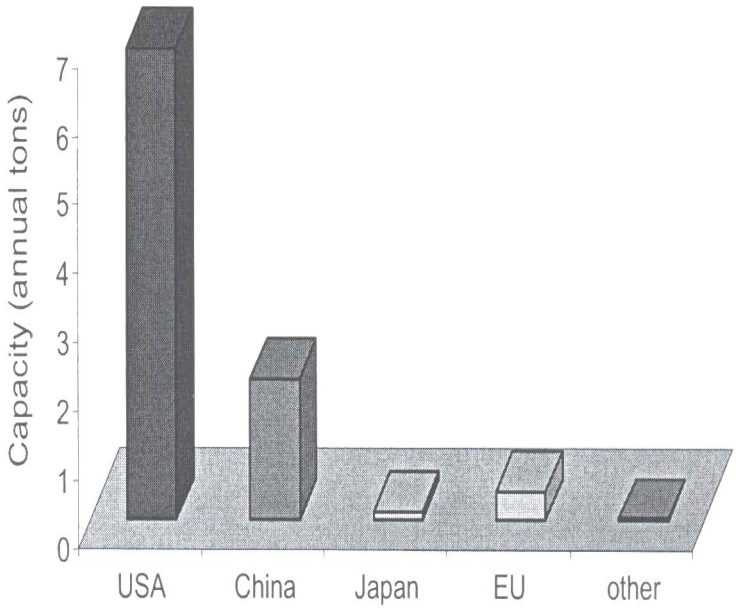

Figure 1.20 SWNT Production Capacity by Countries, from Roman et al, 2004

1.6 SUMMARY

In a short period of time, from its discovery in 1991 to present day, carbon nanotubes have caught the attention of chemists, physicists, material scientists as well as investors. Due to their remarkable mechanical and electronic properties: one hundred times the tensile strength of steel, thermal conductivity better than all but the purest diamond, and electrical conductivity similar to copper, this fascinating material seems destined to change our world as we know it.

However, the biggest challenge in developing potential applications for carbon nanotubes is the production and availability of purified carbon nanotubes in commercial quantities, and at affordable prices. Presently, the known synthesis methods have limited production capacity with no economies of scale, such that the market price of carbon nanotubes is prohibitive. Consequently, the development of scalable production technologies

Table 1.2 Companies Producing Carbon Nanotubes and their Product Prices.

Production Company	Product Description	Purity	Order Size	Price (US$)
Nanolab	MWNT (Hollow)	> 95%	N/A	125.00/g
	MWNT (Bamboo)			150.00/g
	DWNT			500.00/g
Carbon Nanotechnology Inc.	SWNT	N/A	N/A	500.00/g
	BuckyPlus			900.00/g
Nanocs Nanotubes	MWNT–COOH	N/A	N/A	80.00/100mg
	SWNT–COOH			80.00/50mg
	MWNT–SH			249.00/100mg
	SWNT–SH			349.00/100mg
Apex Nanomaterials	CNT 1020–0010	~ 50–80% Chemically Purified	N/A	380.00/10g
	CNT 1020–0100			2800.00/100g
	CNT 1050–001			250.00/g
	CNT 1050–010			1850.00/10g
Carbon Solutions Inc.	AP–SWNT	40–60%	N/A	50.00/g
	RFP–SWNT	60–80%		250.00/g
	P2–SWNT	70–90%		400.00/g
	P3–SWNT	80–90%		400.00/g
Carbolex	AP – Grade	N/A	< 50g	100.00/g
	SWNT		> 100g	60.00/g
Rosseter Holdings	Ros 1	N/A	5g minimum	20.00/g
	Ros 2			25.00/g
	Ros 3			20.00/g
Hyperion Catalysis	FIBRIL	N/A	N/A	N/A
Bucky USA	BU–601	C60	N/A	35.00/g
	CNT–1020-0100	> 98%		25.00/g
	BU–602	C60		45.00/g
		> 99%		30.00/g
	BU–603	C60		80.00/g
		> 99.5%		65.00/g
	BU–604	C60		150.00/g
		> 99.9%		100.00/g
Nanocyl	Thin MWNT	95%	10g	45 Euros/g
	Very Thin MWNT	95%		70 Euros/g
	SWNT	70%		100 Euros/g
Guangzhou	N/A	N/A	N/A	N/A

based on a continuous growth process, for large–scale commercial production of carbon nanotubes at accessible costs, is essential to the economic viability of the emerging and potential carbon nanotube technologies.

In recent years, the interest in carbon nanotube has overshadowed that of fullerenes, although carbon nanotubes are still not as readily available as fullerenes, such that the number of researchers and groups working in the nanotube field has shot up significantly. This has led to an exponential growth on nanotube research and technologies, as observed in the number of nanotube publications (Terrones, 2000). The exponential growth in nanotube publications over the decade spanning from 1991 to 2001 is shown in Figure 1.21.

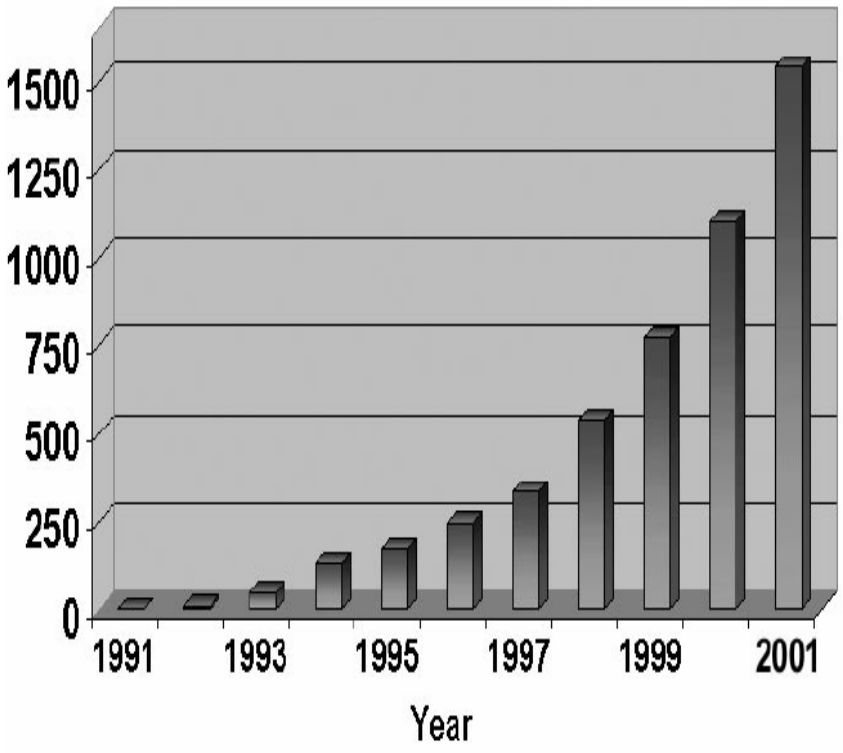

Figure 1.21.Chart Depicting the Exponential Growth of the Number of Nanotube Publications per Year from 1991–2001, from Terrones, 2003.

In the next chapter, the synthesis techniques, growth mechanism, and the post–synthesis, purification methods for carbon nanotubes will be discussed. Furthermore, the various production technologies would be evaluated and scalable carbon nanotube production processes identified, selected and used as a basis for the conceptual design of industrial–scale carbon nanotube production processes.

CHAPTER TWO: LITERATURE REVIEW

The structure, properties and applications of carbon nanotubes were presented in the last chapter. In this chapter, the synthesis, growth processes and purification of carbon nanotubes will be reviewed. The literature review of various laboratory scale processes and the influence of design parameters on the yield and quality of nanotubes produced will be discussed, also.

2.1 CARBON NANOTUBE SYNTHESIS

Carbon nanotubes can be synthesized using different techniques involving gas–phase processes. These gas–phase processes provide access to the high synthetic temperatures required for carbon nanotube production. The three main methods of producing carbon nanotubes are: electric arc discharge, laser vaporization, and chemical vapor deposition. Other techniques include electrolytic synthesis, solar production method, etc. Presently, active research is being aggressively pursued on these methods, and other alternative strategies are being developed to find more economical ways of producing these unique and novel materials.

In the arc discharge method, carbon nanotubes are produced from the carbon vapor generated by an arc discharge between two graphite electrodes (with or without catalysts), under an inert gas atmosphere.

The laser vaporization technique involves the evaporation of a graphite (with or without catalyst) target by a high–power, pulsed or continuous laser beam under an inert gas atmosphere, to yield carbon nanotubes.

The chemical vapor deposition (CVD) technique involves the application of an energy source, such as a plasma source or a heat source, to a carbon feedstock in the gas phase to produce carbon nanotubes on a heated (catalytic or non–catalytic) substrate.

Generally, carbon nanotubes produced by the arc discharge or laser ablation techniques have fewer structural defects than those synthesized by other production methods. This is due to the higher synthesis temperatures of the arc discharge and laser ablation techniques. The higher synthesis temperature ensures a perfect annealing of structural defects in the as–produced carbon nanotubes from the arc discharge and laser vaporization processes.

The chemical vapor deposition (CVD) grown multi–walled carbon nanotubes exhibit high densities of structural defects compared to the as–grown, multi–walled carbon nanotubes by the arc discharge and laser ablation methods. This is due to the relatively low growth process temperature of the metal–catalyzed CVD process, which does not provide sufficient thermal energy to anneal nanotubes into perfectly crystalline structures.

In this section, the production techniques mentioned earlier would be described, while a detailed review of the literature of carbon nanotube processes and post–synthesis purification methods would be discussed later in this chapter.

2.1.1 Electric Arc Discharge

The electric arc discharge technique was originally employed in fullerene synthesis. However, the discovery of carbon nanotubes at the ends of graphite electrodes during fullerene synthesis prompted the use of the arc process in carbon nanotube synthesis. The carbon nanotubes were first observed as needlelike structures dispersed in graphitic soot on the cathode surface of an electric arc discharge chamber.

Typical synthesis conditions for the carbon arc discharge method employ a direct current of 50–100 A and a voltage of 20–25 V operating in an inert atmosphere. The magnitude of the current required is proportional to the diameter of the electrode, as higher

currents are needed to vaporize larger electrodes (Dresselhaus et al, 1996). A typical electric arc discharge apparatus is shown in Figure 2.1.

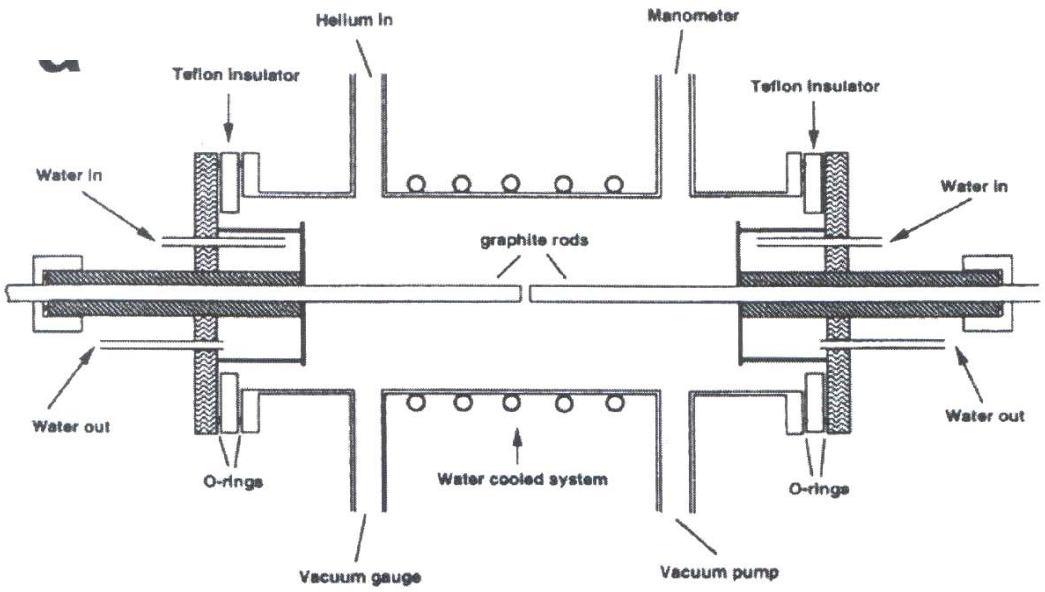

Figure 2.1.Schematics of an Electric–Arc Discharge Apparatus, from Terrones, 2003

The passage of the direct current creates a high temperature discharge between the two electrodes, which results in the vaporization of one of the carbon electrodes (anode) to form a rod–shaped deposit at the rate of ~1mm per minute on the cathode. The carbon nanotubes form mainly where the current flows, and the inner region of the electrodes, where the most copious tubule harvest is obtained has an estimated temperature of 2500–3000^0C (Dresselhaus et al, 1996).

The electric arc deposit typically consists of a hard, gray outer shell made of pyrolitic graphite, and a soft, fibrous dark core containing about two–thirds columnar growth of carbon nanotubes, dispersed in bundle like structures and one–thirds closed graphite nanoparticles (Dresselhaus et al, 1996). Transmission electron microscope (TEM)

pictures of the core material of the carbon arc deposit containing both nanotubes and nanoparticles and purified nanotubes are shown in Figure 2.2a and 2.2b respectively.

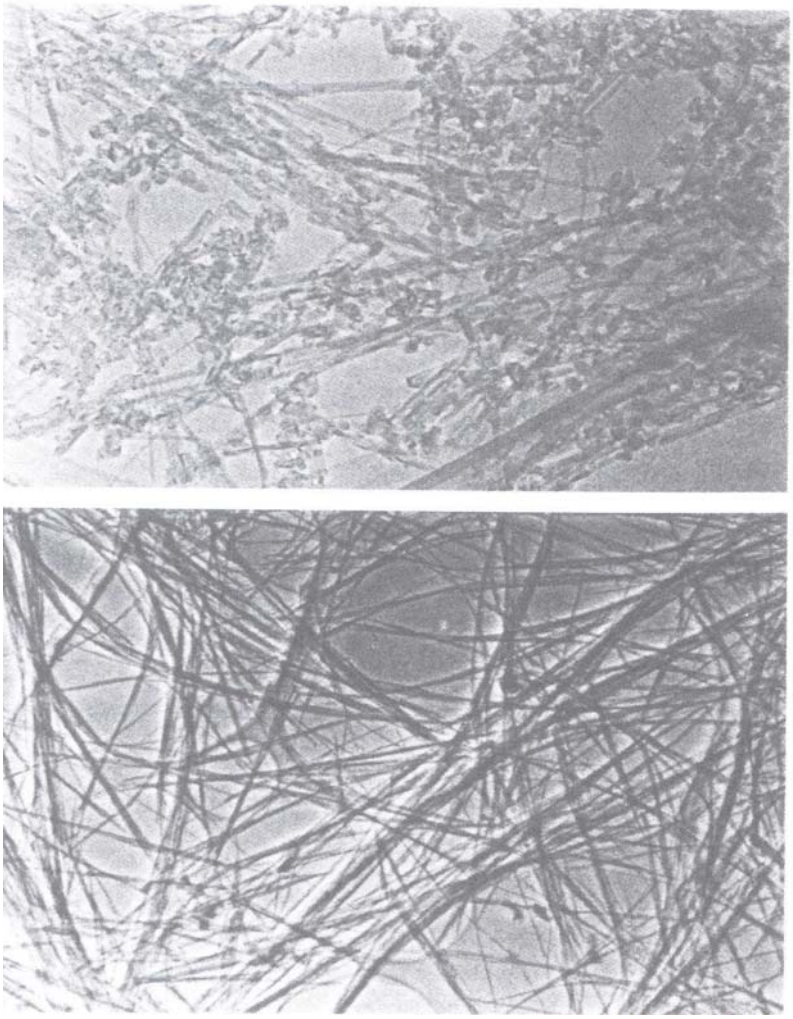

Figure 2.2 TEM Pictures of Standard Core Material from the Arc Deposit (a) Top– containing both nanotubes and nanoparticles and (b) Bottom– purified nanotubes, from Dresselhaus et al, 1996.

Multi–walled carbon nanotubes are the main products generated by the electric arc–discharge technique if both electrodes are graphite, while single–walled carbon nanotubes are synthesized by co–vaporization of a hollow graphite anode mixed with transition metals such as iron, Fe, cobalt, Co, nickel, Ni, molybdenum, Mo, and yttrium, Y,

etc. The electric arc discharge synthesis technique results in a mixture of components, and requires the separation/purification of the carbon nanotubes from the soot and other impurities present in the crude reaction products.

The yield of the carbon nanotubes produced depends on the uniformity and stability of the arc and the temperature of the deposit formed on the negative electrode. Adequate cooling of the reaction chamber is necessary to maximize the yield and ordering of the carbon nanotubes produced (Ebbesen et al, 1992). The cost of producing carbon nanotubes through the arc discharge method is quite expensive because of the high–purity graphite electrodes, metal powders and high–purity inert (Helium/Argon) gases employed in the production process.

2.1.2 Laser Vaporization

In 1996, Smalley and coworkers, at Rice University found a relatively efficient method, using laser vaporization of a carbon target to synthesize single walled carbon nanotubes. The laser vaporization technique involves the use of a pulsed or continuous laser to vaporize a graphite target, containing a small amount of transition metal particle catalysts, inside a tube furnace heated to 1200^0C in an inert gas atmosphere. An oven laser vaporization apparatus is shown in Figure 2.3.

The laser vaporizes the metal–graphite target and nucleates carbon nanotubes in the shockwave just in front of the target, while flowing argon gas sweeps the vapor and nucleated nanotubes, which continue to grow, from the furnace to a water-cooled copper collector (Meyyappan et al, 2003). Multi–walled carbon nanotubes are generated by this method when the vaporized carbon target is pure graphite whereas the addition of transition metals (Co, Ni, Fe or Y) as catalysts to the graphite target results in the production of single

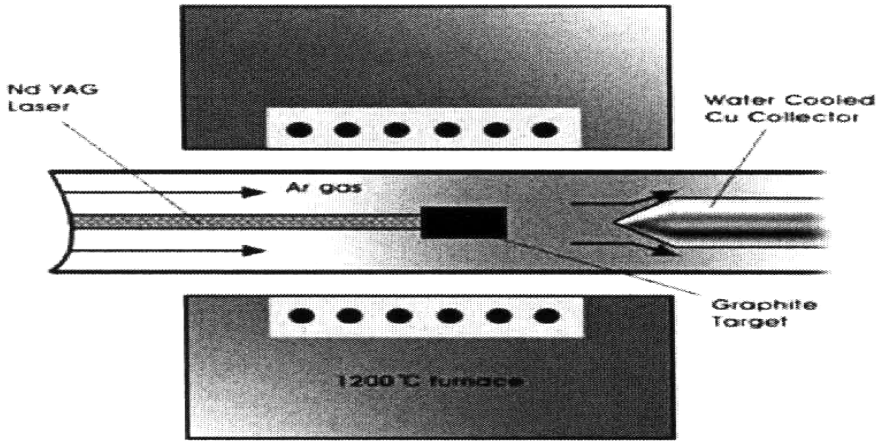

Figure 2.3 Laser Vaporization Apparatus, from Daenen et al, 2003

walled carbon nanotubes. The single–walled carbon nanotubes formed, exist as 'ropes' and are bundled together by van der Waals forces (Dresselhaus et al, 1998).

By using two laser pulses 50 ns apart, (the first to ablate the carbon–metal mixture and the second to break up the larger ablated particles, which are fed into the growing nanotube structures), the growth conditions can be maintained over a larger volume and for a longer period. This results in more uniform vaporization and better control of the growth parameters, such that 70–90% of the carbon target can be converted to carbon nanotubes (Dresselhaus et al, 1998, Ajayan, 2000).

2.1.3 Chemical Vapor Deposition (CVD)

Chemical vapor deposition (CVD) technique involve the use of an energy source, such as a plasma, a resistive or inductive heater, or furnace to transfer energy to a gas–phase carbon molecule over metal catalysts deposited on substrates to produce fullerenes, carbon nanotubes and other sp^2–like nanostructures (Meyyappan, 2004). Commonly used gaseous carbon sources include carbon monoxide and hydrocarbon feedstock such as methane, acetylene, ethylene, and n– hexane.

The chemical vapor deposition technique can be applied both in the absence and presence of a substrate; the former being a gas–phase homogeneous process where the catalyst is in the gas–phase, the latter being a heterogeneous process using a supported catalyst (Corrias et al, 2003). The CVD technique can be used to preferentially synthesize single or multi–walled nanotubes depending on the choice of appropriate metal catalyst.

Carbon nanotubes generated by the template–based chemical vapor deposition technique exhibit excellent alignment and positional control on a nanometer scale. The size of the particles and pores, which determine the size of the nanotubes, can be controlled prior to carbon deposition. Furthermore, by regulating the amount of carbon feedstock supplied and the thickness of the membranes, the length of the carbon nanotubes formed can be controlled (Ajayan, 2000).

The chemical vapor deposition method is regarded as a two–step process, consisting of a catalyst preparation step, accompanied by the actual synthesis of the carbon nanotube. Catalysts are usually prepared by sputtering a transition metal catalyst onto a substrate from solutions containing the metal ions or by direct physical deposition techniques. The solution–based approach includes steps such as dissolution, stirring, precipitation, refluxing, separation, cooling, gel formation, drying, annealing, etc (Meyyappan, 2004).

The chemical vapor deposition synthesis techniques can be categorized according to the energy source: thermal chemical vapor deposition and plasma enhanced chemical vapor deposition (PECVD). Thermal chemical vapor deposition uses conventional heat source as its energy source, while a plasma source is used to create a glow discharge in the plasma enhanced chemical vapor deposition (PECVD).

2.1.3a. Thermal Chemical Vapor Deposition

The thermal CVD synthesis of carbon nanotubes by the supported catalyst approach involves the initial deposition of transition metal catalyst or their alloys on a substrate. The substrate, after being etched in a diluted HF solution with distilled water, is placed in a quartz boat inserted in a tubular furnace. Subsequent etching of the catalytic substrate using ammonia gas at growth temperatures of 500 ^{0}C to 1000 ^{0}C leads to the formation of fine catalytic metal particles, which induces carbon nanotube growth.

A typical thermal CVD growth run involves purging the reactor with argon or some other inert gas in order to prevent the oxidation of the nano–size fine catalytic particles while increasing the reactor temperature to the desired growth temperature (Han et al, 2002). A schematic diagram of the thermal CVD apparatus is shown in Figure 2.4.

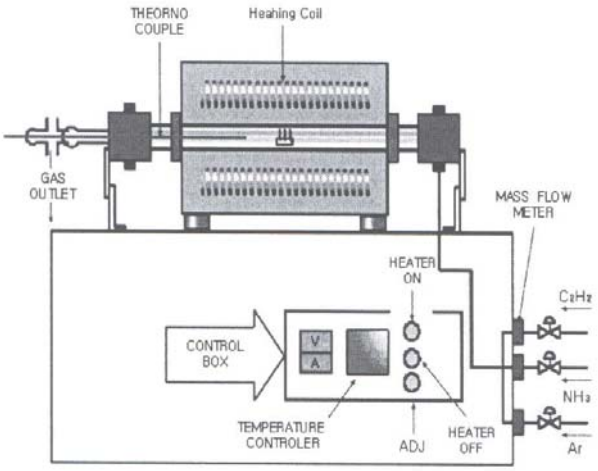

Figure 2.4.Schematic Diagram of a Thermal CVD Apparatus, from Daenen, et. al., 2003

The undiluted reaction gas, which is either carbon monoxide or some hydrocarbon, and metered through a mass flow controller, is fed through one end of the apparatus while the gas outlet is at the other end. At the end of the reaction period, the flow is switched back to the

inert gas while the reactor cools down to prevent damage to the carbon nanotube produced due to exposure to air at elevated temperatures (Meyyappan, 2004).

2.1.3b. Plasma Enhanced Chemical Vapor Deposition (PECVD)

The plasma enhanced CVD (PECVD) synthesis technique combines non–equilibrium plasma reaction, such as hot filament plasma, microwave plasma, radio frequency plasma and D.C. glow plasma, with template–controlled growth technology to synthesize carbon nanotubes at low process temperature (Li et al, 2004). A typical plasma CVD apparatus with a parallel electrode configuration is shown in Figure 2.5.

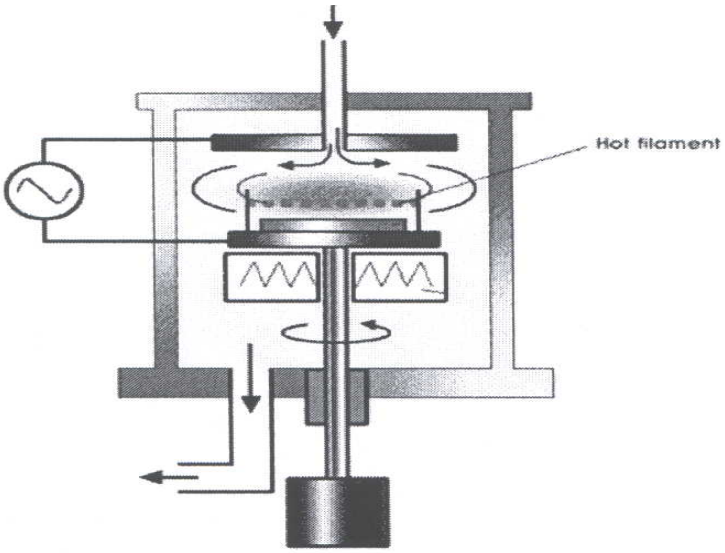

Figure 2.5 Schematic Diagram of the Plasma CVD Apparatus, from Daenen et al, 2003.

The plasma reactor consists of a pair of electrodes in a chamber or reaction furnace, with one electrode grounded and the second connected to a high frequency power supply. The hot filament directly heats the catalytic substrate, placed on the grounded electrode, while the carbon rich feedstock such as ethylene, methane, ethane, and carbon monoxide is supplied from the opposite plate to the reaction chamber during the discharge.

Carbon nanotubes grow on the nano–size fine metal particles, formed on the catalytic substrate, by the glow discharge generated from the high frequency discharge. However, the PECVD technique requires relatively low gas pressure and complex vacuum equipments (Li et al, 2003). Due to its low process temperature, the PECVD is useful in semiconductor device fabrication, as some processes cannot tolerate the elevated temperatures of the thermal chemical vapor deposition (Meyyappan, 2004).

2.1.4 Electrolysis Technique

The formation of carbon nanostructures by electrochemical methods represents a novel development in the production of fullerene related materials. The electrolysis technique showed that carbon nanotube synthesis is not confined, as hitherto assumed, to condensation from the vapor phase only. A schematic diagram of the electrolysis apparatus used to produce nanotubes in the liquid phase is shown in Figure 2.6.

The electrolysis apparatus consists of a quartz glass tube with a gas inlet /outlet and electrical connectors on the end flanges. The anode crucible, made by drilling a hole in a cylindrical block of high purity graphite, contains the electrolyte (typically alkali halides salts, e.g. lithium chloride).

The electrolyte is heated by an external surface (20 ^{0}C/minute) until it melted, while the cathode (graphite) rod is immersed at various depths in the electrolyte, under an inert (argon) atmosphere (Hsu et al, 1996). Carbon nanomaterials, which consist of carbon nanotubes, encapsulated particles, amorphous carbon and carbon filaments, are synthesized by the application of dc voltage (3–20 A; 0–20 V) between the graphite electrodes at temperatures above 600 ^{0}C (Hsu et al, 1996).

However, the quality and yield of carbon nanotubes produced by electrochemical

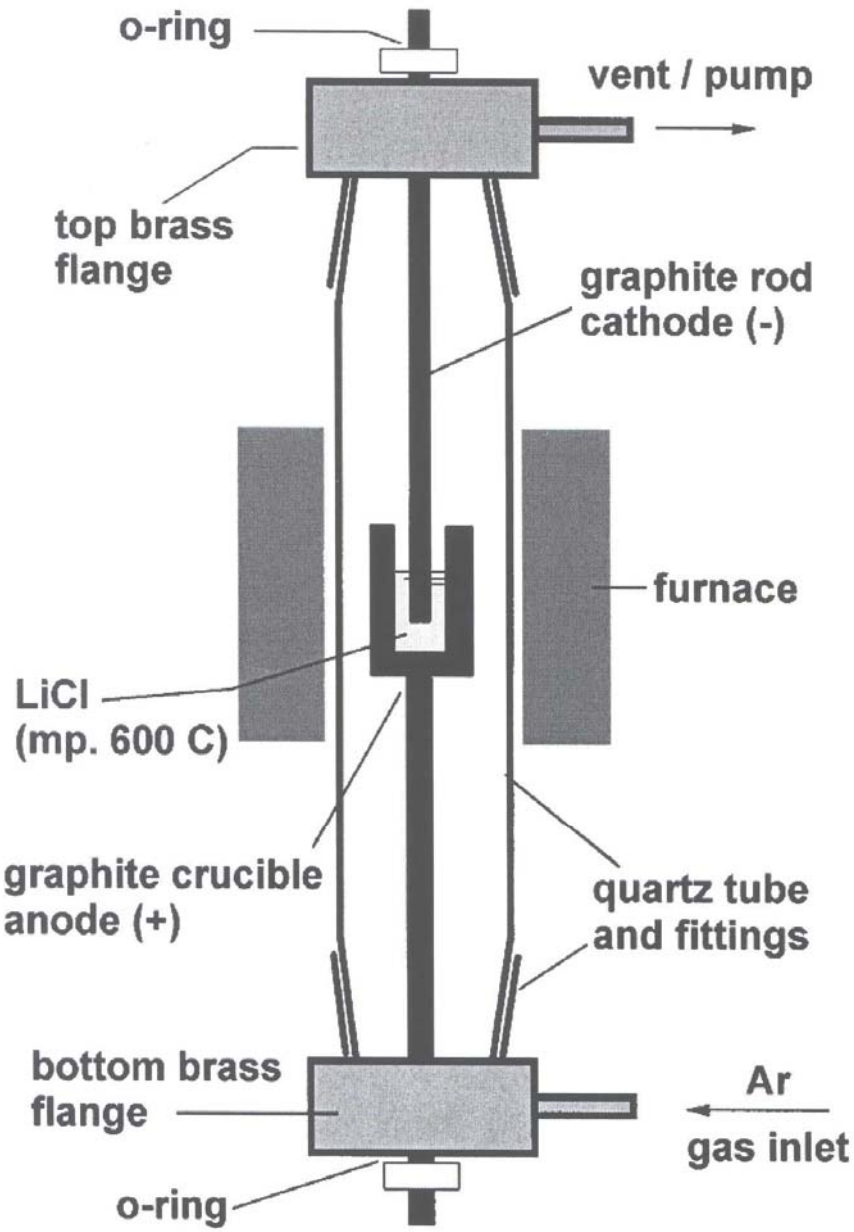

Figure 2.6 Schematic Diagram of the Electrolysis Apparatus for Liquid–Phase Production of Carbon Nanotubes, from Hsu et al, 1996.

method is difficult to control, and depends on factors such as the electrolysis voltage and current, depth of cathode immersion in the electrolyte, reaction time and the electrolyte. Other salts, which have been successfully used in the production of nanotubes by the electrolysis approach, include lithium chloride, potassium chloride, lithium bromide, etc.

2.1.5 Solar Production of Carbon Nanotubes

Solar energy generation of carbon nanotubes offers another alternative to high lasers, arc discharge, and other techniques of synthesizing both single walled and multi walled carbon nanotubes. Guillard et al, 2000, reported the production of carbon nanotubes by direct vaporization of graphite targets, containing different catalyst combinations, using a 2 kW solar furnace. A solar reactor for producing fullerenes and carbon nanotubes is shown schematically in Figure 2.7.

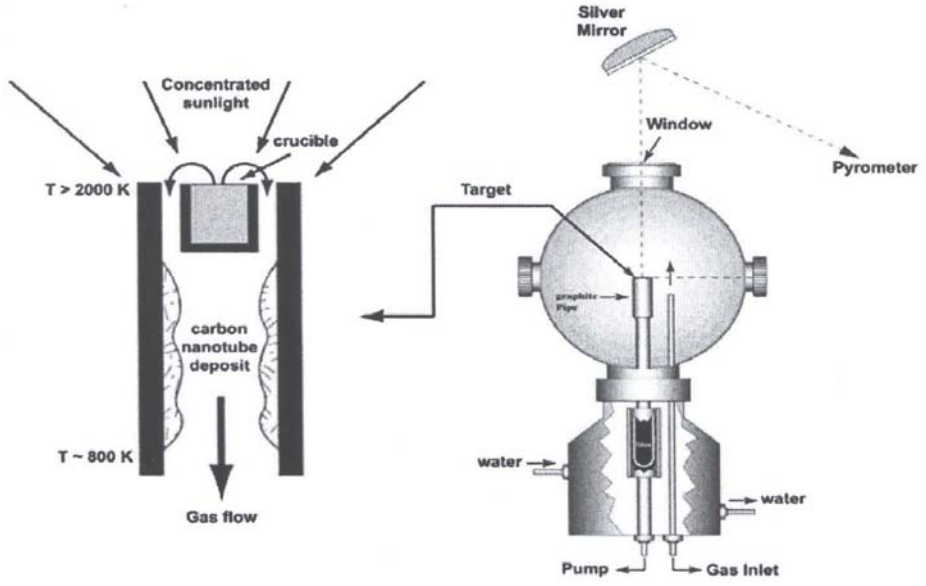

Figure 2.7 Sketch of a Solar Reactor for Carbon Nanotube Production, from Terrones, 2003.

The solar furnace, formed by a flat tracking mirror, reflects vertically the sunlight towards a parabolic mirror. The target, a graphite crucible, is filled with a mixture of powdered graphite and transition metal catalysts and connected to a cellulose filter, which collects the reaction products. The reactor, which is swept by argon during vaporization, can be adjusted such that the top of the crucible is at the focus of the parabolic mirror (Guillard et al, 2000).

Guillard et al, demonstrated that solar energy with an average incident solar flux close to 950 W/cm^2 corresponding to a peak power of ~ 1330 W/cm^2 at the focus of the solar furnace can be used to vaporize graphite metal targets to produce single walled carbon nanotubes. The measured temperature of the crucible is ~3000 K (Guillard et al, 2000).

The yield and quality of the single walled carbon nanotubes produced by this technique depends on the target temperature and composition, the reactor pressure and cooling rate of the carbon vapor (Guillard et al, 2000).

2.2. GROWTH MECHANISM

The growth mechanism of carbon nanotubes is quite fascinating, since carbon is the only elemental material that forms hollow tubes, perhaps as a result of the strong surface energy anisotropy of graphite basal planes compared to other lattice planes (Iijima, Ajayan, and Ichihashi, 1992). Carbon nanotubes consist of concentric cylinders of hollow carbon hexagonal networks arranged around one another, often with a helical twist with the tips of the tubes almost always closed, with the presence of pentagons in the hexagonal lattice (Iijima et al, 1992).

The actual mechanisms by which carbon nanotubes are formed are not exactly known, although, various growth models based on experimental and quantitative studies have been proposed. However, it seems more likely that two entirely different mechanisms operate during the growth of MWNTs and SWNTs, because the presence of a catalyst is absolutely necessary for the growth of the latter (Ajayan et al, 1996).

One school of thought assumes that the tubes are always capped and that the growth process involves a C_2 absorption process that is aided by the pentagonal defects on the cap. The second school of thought assumes the tubes are open during the growth process

and that carbon atoms are added at the open ends of the tubes (Dresselhaus et al, 1996).

Carbon nanotubes synthesized by the arc–discharge technique are thought to grow by the open–ended growth mechanism (Figure 2.8). For chiral structures (Figure 2.8a), the absorption of a single C_2 dimer at the active dangling bond edge site will add one hexagon to the open end, such that the sequential addition of C_2 dimers will lead to continuous growth of the chiral nanotubes. However, if carbon atoms are added out of sequence, then addition of a C_2 dimer would result in the addition of a pentagon, which could induce the closure of the tubes, while the addition of a C_3 trimer out of sequence as shown in Figure 2.8a merely adds a hexagon (Dresselhaus et al, 1996).

In the case of the armchair edge, a single C_2 dimer will add a hexagon, while multiple additions of C_2 dimers lead to multiple additions of hexagons as shown in Figure 2.8b. In the zig–zag geometry (Figure 2.8c), growth is initiated by one C_3 trimer, which then provides the requisite edge site to complete one row of growth through the addition of C_2 dimers, except for the last hexagon in the row, which requires only a C_1 monomers.

However, a C_2 dimer initially attached at a zig–zag edge will form a pentagon, which introduces a curvature to the open end of the tube, inducing the formation of a cap and thus the growth of the tube by the open–ended process will be terminated (Dresselhaus et al, 1996).

The roles of pentagon and heptagon are very important in the growth process of carbon nanotubes. The pentagons provide positive surface disinclinations ($+60^0$), whereas heptagons (-60^0) provide negative curvature for the transformation of conical shapes into tubes (Iijima et al, 1992). Consequently, the formation of pentagons, which induces tube closure, is detrimental to the growth of long parallel tubes, whereas heptagons can annul the

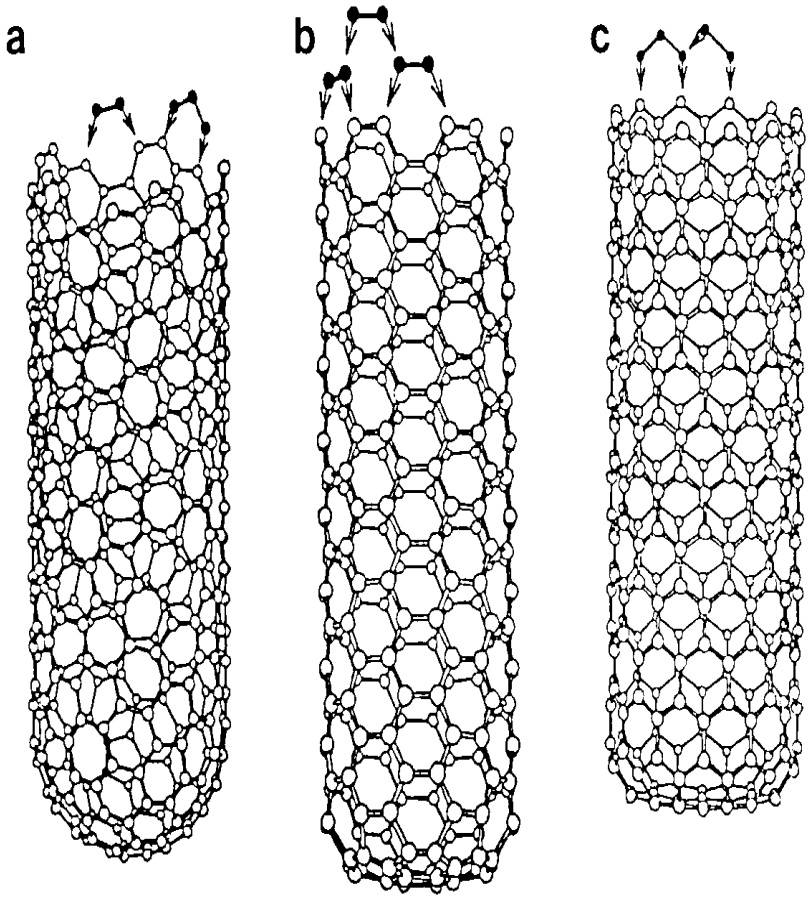

Figure 2.8 Proposed Open–Ended Growth Mechanism of Carbon Nanotubes by the Absorption of C_2 (dimers) and C_3 (trimers). (a) Absorption of C_2 dimers at the most active edge site of a chiral nanotube resulting in the addition of one hexagon, also shown is an out of sequence absorption of a C_3 trimer. (b) Absorption of C_2 dimers at the open end of an armchair nanotube. (c) Absorption of a C_3 trimer at the open end of a zigzag nanotube and subsequent C_2 dimer absorption. (Dresselhaus et al, 1996).

effect of pentagons and aid in the growth process by opening up the growing carbon nanotube ends (Iijima et al, 1992).

Figure 2.9 shows the various growth morphologies that might result by adding hexagons, H (6), pentagons, P (5), and heptagons, S (7) on the periphery of open tube ends based on a growth model proposed by Iijima et al, 1992, for carbon nanotubes. Addition of only hexagons to the periphery of an open tube causes growth into longer nanotubes with no defects. Successive addition of pentagons induces a closure of the carbon nanotube ends

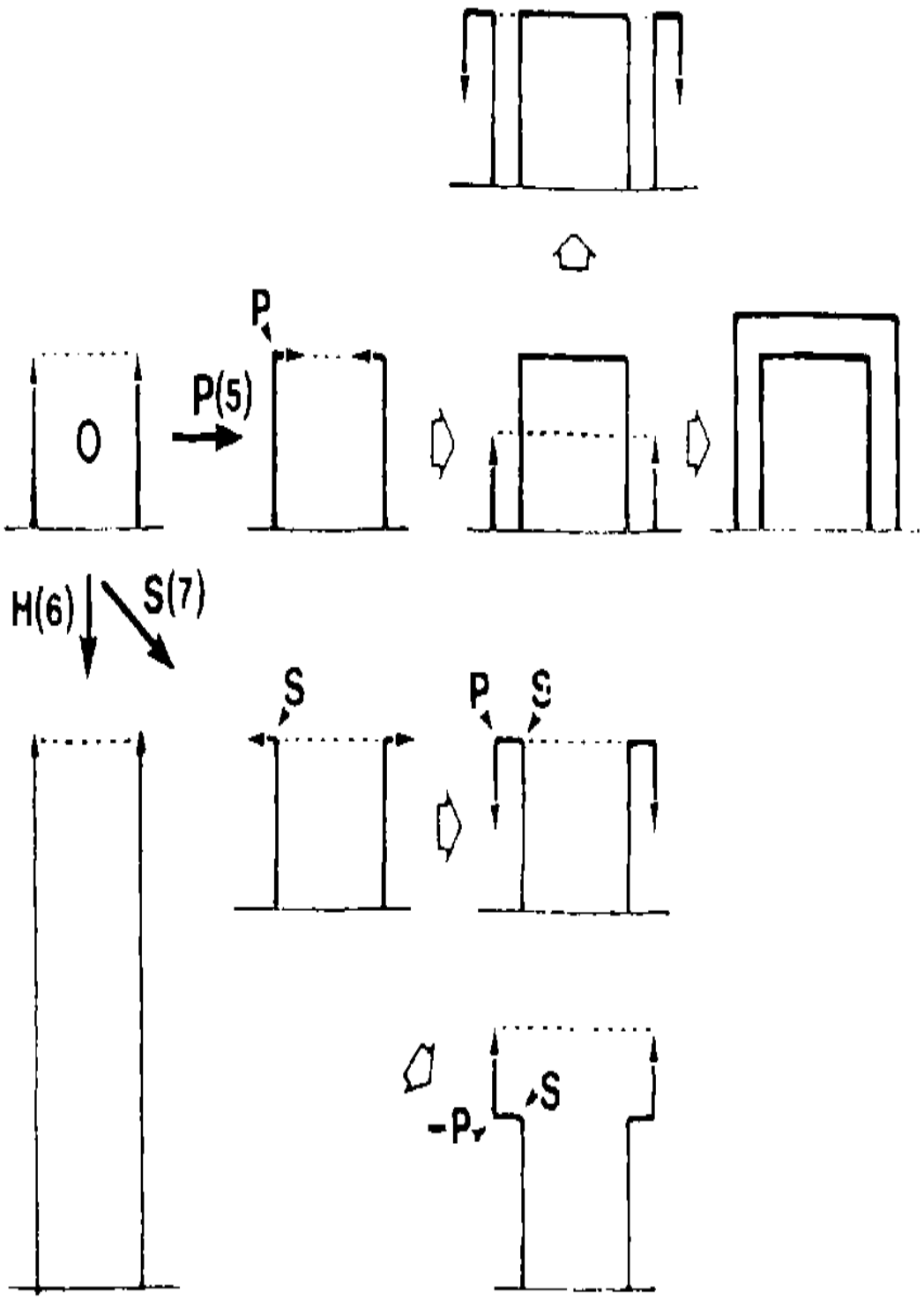

Figure 2.9.Schematic Depicting the Various Carbon Nanotube Growth Probabilities Starting from a Nucleus O by the Addition of Hexagons, H(6), Pentagons, P(5), and Heptagons, S(7), successive addition of heptagons causes an opening up (Iijima et al, 1992).

while successive addition of heptagons causes an opening up (Iijima, et al, 1992)

Since the chemical vapor deposition process occurs at about 1,100 ^{0}C, the growth of the carbon nanotube core, and the thickening process occurs separately in the lower temperature regime. Thus, any dangling bonds that might be involved in the open tube growth mechanism would be unstable, and the closed tube mechanism would be favored at such lower temperature regime (Dresselhaus et al, 1996).

In contrast, the electric arc–discharge synthesis technique's growth region occurs at about 3,400 ^{0}C and the carbon nanotube is close to the melting point. At these high temperatures, carbon nanotube growth and the graphitization of the thickening deposits occur simultaneously. Consequently, all the coaxial carbon nanotubes tubes grow at once at these elevated temperatures and the open–ended growth mechanism is favored (Dresselhaus et al, 1996).

2.3 CARBON NANOTUBE PROCESSES

An extensive literature review of the laboratory–scale processes for carbon nanotube production by the various synthesis techniques earlier mentioned in this chapter is discussed. The design parameters such as reactor type, length, diameter, heat requirements, and operational parameters like temperature, pressure, voltage, current, coolant flow rate, graphite evaporation rate, electrode diameter, etc. are specified.

Furthermore, the reaction products, reactants, catalysts, carrier gas, conversion, carbon nanotube yield and selectivity as well as the purification techniques employed in these experimental studies are stated. These laboratory–scale carbon nanotube production and post–synthesis purification processes for carbon nanotube are discussed in more detail below.

A. Electric Arc Discharge

- **Lee, S.J., Baik, H.K., Yoo, J., Han, J.H., 2002, "Large scale synthesis of carbon nanotubes by plasma rotating arc discharge technique", Diamond and Related Materials, 11, 914–917.**

The large–scale synthesis of carbon nanotubes by plasma rotating arc discharge is investigated.

The carbon nanotube is formed by the condensation of high–density carbon vapor transferred out of the plasma region by the centrifugal force generated by the rotation of the electrodes.

The rotating electrode prevents the local concentration of the electric field, and spreads the microdischarge uniformly over the whole electrodes, thus ensuring a higher discharge volume and more stable plasma.

As the rotating speed of the electrode increases, the plasma volume increases and the collector temperature rises. Since the supply of the carbon vapor and the temperature of the collector determine the nanotube growth, the nanotube yield increases as the rotation speed of the anode increases.

Consequently, the plasma rotating arc process is very efficient method for potential mass production of carbon nanotubes.

Reactor:	Plasma rotating electrode process (PREP) reactor
Discharge Current:	80–120 A with voltage ~ 20–30 V
Electrodes:	Pure graphite – anode (12 mm OD);
	– cathode (15mm OD)
Anode Rotation Speed:	0–10000 rev/min
Reactor Pressure:	500 torr
Reactor Temperature:	Not specified
Carrier Gas:	Helium
Flow rate:	5 liter/min
Yield:	~ 80%
Selectivity:	Not stated
Purification:	Heating at 700 ^{0}C in the atmosphere

- **Jung, S.H., Kim, M. R., Jeong, S.H., Kim, S.U., Lee, O.J., Lee, K.H., Suh, J.H., Park, C.K., 2003, "High-yield synthesis of multi-walled carbon nanotubes by arc discharge in liquid nitrogen", Applied Physics A 76, 285-286.**

The synthesis of multi–walled carbon nanotubes using the arc discharge technique, in which the conventional vacuum arc discharge chamber replaced by a liquid nitrogen filled chamber is reported.

The distance between the two electrodes was adjusted until arc discharge occurred and direct current was supplied using a power supply.

The carbon materials evaporated from the anode and deposited to the cathode, after removal from liquid nitrogen were characterized by field emission scanning electron microscope (FE–SEM), transmission electron microscope (TEM) and Raman spectroscopy.

The as synthesized MWNTs have a diameter range of 20–50 nm and can be high as 70% of the reaction product.

Reactor:	Dewar flask
Atmosphere:	Liquid nitrogen
Anode:	Pure carbon rod–anode (8 mm OD); cathode (10mm OD)
DC Current:	~ 80 A at 20–27.5 V
Reactor Temperature:	Not stated
Reactor Pressure:	Not stated
Yield:	~70%
Purification Technique:	Desiccation, Dissolution in ethanol.

• Alexandrou, I., Wang, H., Sano, N., Amaratunga, G.A.J., 2003, "Structure of carbon onions and nanotubes formed by arc in liquids", Journal of Chemical Physics, 120(2), 1055-1058.

The use and comparison of a cathodic arc in two liquids: liquid nitrogen and de–ionized water, as a non–vacuum method of producing carbon nanotubes is carried out. During the carbon arc discharge, the two electrodes and liquid in the vicinity of the arc spot vaporize due to the intense heat.

Liquid nitrogen and water environments essentially satisfy the same principle: the confinement and condensation of the vapor produced during the arc discharge. However, due to the marked difference in the volatility of the two liquids and the consequent influence on the stability and uniformity of the gaseous bubble around the arc spot, the arc in water was more controllable.

The reaction products contain multi–walled carbon nanotubes, carbon onions and amorphous carbon. However, the full structural characterization of the nanotube produced is not reported.

Reactor:	Not specified
Atmosphere:	(a) Liquid nitrogen (b) De–ionized water
Electrodes:	Pure carbon electrodes
DC Current:	30 A (constant)
Reactor Temperature:	Not stated
Reactor Pressure:	Not stated
Yield:	Not stated
Purification:	Drying, Dispersion in ultrasonic bath of toluene

• Li, M., Hu, Z, Wang, X., Wu, Q., Chen, Y., Tian, Y., 2004, "Low temperature synthesis of carbon nanotubes using corona discharge plasma at atmospheric pressure", Diamond and Related Materials, 13, 111–115.

The synthesis of aligned carbon nanotubes at atmospheric pressure and low temperature by a new method, which combines non–equilibrium corona discharge plasma reaction with template–controlled growth technology, is reported.

Multi–walled carbon nanotubes with diameters of approximately 40 nm were restrainedly formed in the channels of the anodic aluminum oxide (AAO) template from a methane/hydrogen reactant gas mixture at a temperature below 200 ^{0}C.

Unlike the conventional arc discharge method, in which nanotubes are formed by the vaporization of graphite precursor at high temperature (3000 ^{0}C), the corona discharge method synthesizes carbon nanotubes from hydrocarbon radicals like CH_3 or CH_2 from methane decomposition at low temperature (200 ^{0}C).

Reactor:	Quartz tube reactor
Catalyst:	Cobalt
Reactants (ratio):	Methane: Hydrogen (1: 10)
Feed Rate/Reaction time:	22 sccm/10 min
Reactor Temperature:	25–200 ^{0}C
Reactor Pressure:	Atmospheric pressure
AC Generator:	8000 V, 25 kHz, 40 W
Purification:	Dissolution in NaOH and HCl; Dispersion by ultrasonic treatment

- **Yu, J., Lucas, J., Strezov, V., Wall, T., 2003, "Coal and carbon nanotube production", Fuel, 82, 2025–2032.**

An overview on synthesis of carbon nanotubes, using coal or coke as source materials, by plasma arcing technique is presented.

The use of coal for carbon nanotube production over other materials may be more advantageous because coal is cheap and abundant; weak bonds in coal macromolecular structure may lead to more effective synthesis of nanotubes.

In addition, the coal itself can be used as a purification medium, in particular, coal with high proportions of mesopores, while catalyst agent can be easily added into coal during production processes. However, the yield level and purity of the carbon nanotubes produced constitute the major constraints in this production technique

Reactor:	Not stated
Carbon Source:	Coal or Coke
Catalysts:	Not stated
Reactor Temperature:	Not stated
Reactor Pressure:	Not stated
Yield:	~ 10 %
Purification:	Not stated

- **Journet, C., Maser, W.K., Bernier, P., Loiseau, A., Lamy de la Chapelle, M., Lefrant, S., Denlard, P., Lee, R., Fischer, J.E., 1997, "Large–scale production of single–walled carbon nanotubes by the electric–arc technique", Nature, 388, 756– 758.**

Large quantities of single–walled carbon nanotubes with similar characteristics to those obtained by laser ablation were synthesized by the electric–arc technique.

The carbon nanotubes were produced by an arc discharge between two electrodes: a graphite cathode and a graphite anode, in which a hole had been drilled and filled with a mixture of metallic catalyst (Ni–Co, Co–Y, or Ni–Y) and graphite powders.

The reaction products consist of large amount of entangled carbon filaments, homogeneously distributed over large areas with diameters ranging from 10 to 20 nm.

Each carbon filament consists of smaller aligned SWNTs; self organized into bundle–like crystallites with diameters ranging from 5–20 nm.

The carbon nanotube yield (with respect to the total volume of the solid material) is estimated to be of the order of 80%.

The products were characterized by SEM, HRTEM, XRD and Raman spectroscopy analysis.

Reactor:	Electric–arc discharge apparatus (vague)
Catalysts:	Ni–Co, Co–Y, Ni–Y
Carbon Source:	Graphite
Reactor Temperature:	Not stated
Reactor Pressure:	660 mbar
Discharge Current:	100 A at a voltage of 30 V
Atmosphere:	Helium
Yield:	~ 70–90%
Selectivity:	Not stated
Purification:	Not stated

• Ebbesen, T.W., Ajayan, P.M., 1992, "Large scale synthesis of carbon nanotubes", Nature, 358, 220-222.

The synthesis of graphitic carbon nanotubes in gram quantities, using a variant of the standard arc–discharge technique for fullerene synthesis under a helium atmosphere is reported.

Under certain conditions, carbonaceous materials, consisting of pure carbon nanotubes and nanoscale particles are deposited on one of the graphite electrodes. The purity and yield depend on the gas pressure in the reaction vessel.

The nanotube yield was optimized by varying conditions such as type of inert gas, nature of the current (a.c. or d.c.), the voltage and the relative graphite electrode size.

It was found that at ~500 torr, the total yield of carbon nanotubes as a proportion of graphitic starting material is optimal.

Reactor:	Fullerene reactor (vague)
Electrodes:	Pure graphite rods – anode (6 mm OD); Cathode (9 mm OD)
Reactor Pressure:	~500 Torr (Optimal)
Reactor Temperature:	Not specified
Current (a.c./d.c.):	~100 A at ~18 V
Atmosphere:	Helium gas
Yield:	Not stated
Purification:	Not stated

B. Laser Vaporization

- **Guo, T., Nikolaev, P., Thess, A., Colbert, D.T., Smalley, R.E., 1995, "Catalytic growth of single–walled nanotubes by laser vaporization", Chemical Physics Letters, 243, 49–54.**

A new method for synthesizing single–walled carbon nanotubes (SWNTs) is presented, in which a mixture of carbon and transition metals are vaporized by a laser impinging on a metal–graphite composite target.

In this technique, single–walled carbon nanotubes are produced in condensing vapor in a heated flow tube by evaporating from the anode, simultaneously a small percentage of transition metal.

In contrast to the arc technique, direct vaporization allows far greater control over growth conditions, permits continuous operation, and produces better quality nanotubes in higher yield.

A series of mono– and bi–metal catalysts were evaluated for yield and quality of single walled carbon nanotubes: Ni, Co, Cu, Nb, Pt, Co/Ni, Co/Pt, Co/Cu, Ni/Pt. For mono–catalysts, Ni produced the highest yield, while Co/Ni and Co/Pt bi–metal catalysts yielded SWNTs in high abundance with yields 10–100 times the single metals alone.

The carbon nanotube yields were observed to increase with temperature up to the furnace limit of 1200 ^{0}C.

Reactor:	Quartz tube mounted in high temperature furnace.
Catalysts:	Ni, Co, Cu, Nb, Pt, Co/Ni, Co/Pt, Co/Cu, Ni/Pt,
Reactor Temperature:	1200 ^{0}C
Reactor Pressure:	500 Torr
Laser Source:	Continuum DCR–16S, 300 mJ/pulse at 0.532 μm
Atmosphere:	Argon, Ar
Flow Rates:	Ar – 50sccm
Yield:	15–50%
Purification:	Sonication in methanol

- **Maser, K.W., Benito, A.M., Munoz, E., Marta de Val, G., Martinez, M.T., Larrea, A., Fuente, G.F., 2001, "Production of carbon nanotubes by CO_2–laser evaporation of various carbonaceous feedstock materials", Nanotechnology, 12, 147–151**.

The production of single–wall carbon nanotubes (SWNT) by the continuous wave CO_2 laser evaporation method using graphite, pitch and coke as carbonaceous feedstock materials is reported.

This synthesis technique is very simple in contrast to other laser methods, as it requires only one laser and no external furnace around the evaporation chamber.

It was also shown that non–graphitic, cheap carbonaceous residue materials, such as coke and pitch, can be used as feedstock for carbon nanotube formation.

However, the SWNT yield obtained is less then in the case when graphite is used as the precursor material.

The effects of the target composition, type of gas, pressure and laser–operating mode on SWNT synthesis were also investigated.

Qualitative analysis showed that the formation of SWNT is closely related to the choice of an appropriate feedstock material as well as to favorable local temperature conditions experienced by the evaporated species.

Reactor:	Stainless steel chamber
Laser Source:	250 W CO_2 laser: cw–mode at a wavelength of 10.6 μm
Carbon Source:	Graphite, Pitch, Coke
Catalysts:	Ni, Co, Y, Fe, Ni/Y, Ni/Co, Co/Y, Ni/La
Evaporation Rate:	200 mg/h (optimal at power densities of 12 kW cm^{-2})
Reactor Pressure:	200–500 Torr
Reactor Temperature:	~ 1200–3000 ^{0}C
Buffer Gases:	Argon, Nitrogen, Helium
Yield:	Not stated
Purification:	Not stated

- **Munoz, E., Maser, W.K., Benito, A.M., Fuente, G.F., Righi, A., Sauvajol, J.L., Anglaret, E., Maniette, Y., 2000, "Single–walled carbon nanotubes produced by cw CO_2–laser ablation: study of parameters important for their formation", Applied Physics A 70, 145–151.**

The synthesis of single–walled carbon nanotubes using a CO_2–laser system operating in continuous wave (cw) mode is presented.

Experimental studies were carried out at 400 Torr under both dynamic (gas flow ~1 l/min) and static (without any gas flow) conditions.

The influences of parameters such as the composition of the graphite/metal targets, the buffer gas, its flow rate, and its pressure on the formation of SWNTs were studied.

The results showed that the conditions near the evaporation zone; especially the local temperature environment is strongly influenced by most of the parameters studied.

Thus, the local temperature conditions as well as the used metal catalysts play a key role in the synthesis of SWNTs.

Reactor:	Stainless steel evaporation chamber (~7 liters) with quartz tube.
Laser Source:	CO_2 laser; cw mode at 10.6 μm (power density: ~12kW/cm^2)
Catalysts:	Co, Y, Fe, Ni/Co, Ni/Y, Ni/Fe, Co/Y, Co/La
Buffer Gases:	Argon, Nitrogen, Helium
Reactor Pressure:	Dynamic: ~400 Torr Static: ~50–500 Torr
Reactor Temperature:	Not stated
Yield:	~80 vol% (graphite/bi–metal (Ni/Y, Ni/Co) targets
Selectivity:	Not stated
Purification:	Not stated

C. Chemical Vapor Deposition

• Mauron, Ph., Emmenegger, Ch., Sudan, P., Wenger, P., Rentsch, S., Zuttel, A., 2003, "Fluidized–bed CVD synthesis of carbon nanotubes on Fe_2O_3/MgO", Diamond and Related Materials, 12, 780–785.

Carbon nanotubes were synthesized by the fluidized–bed chemical vapor deposition of iso–pentane (C_5H_{12}) on a magnesium oxide (MgO) powder impregnated with an iron nitrate ($Fe(NO_3)_3.9H_2O$) solution. The Fe_2O_3/MgO combination has the substrate is easily removed with hydrochloric acid.

In the fluidized–bed synthesis, a large quantity of a precursor powder, with high specific surface area (100 m^2g^{-1}) is in good contact with the gas due to fluidization of the powder. Consequently, large quantities of carbon nanotubes can be produced.

The effects of different synthesis parameters such as the iron ratio in the precursor (2.5–15%), the synthesis temperature (450–800 ^{0}C), the synthesis time (0.5–40 min) and the type of carbon feedstock on the yield were examined.

Depending on the synthesis temperature, both MWNT (500–650 ^{0}C) and SWNT (700–800 ^{0}C) are synthesized with acetylene as the carbon source. However, with iso–pentane, MWNT were produced at 700 ^{0}C.

Reactor:	Fluidized–bed reactor consisting of a vertical furnace and a quartz glass tube
Catalysts:	Magnesium oxide/Iron nitrate
Carbon Source:	Acetylene, Iso–pentane
Carrier Gas:	Argon
Reactor Temperature:	450–800 ^{0}C
Reactor Pressure:	Not stated
Gas Flow:	410 sccm
Purification:	– Dissolution in HCl at a temperature of 75 ^{0}C to remove MgO – Filtration.

• Liu, X., Huang, B., Coville, N.J., 2002, "The Influence of synthesis parameters on the production of multi-walled carbon nanotubes by the ferrocene catalyzed pyrolysis of toluene", Fullerenes, Nanotubes and Nanostructures, 10(4), 339–352.

The use of an improved synthetic method to generate high yields of carbon nanotubes, using optimized parameters (pyrolysis temperature, injection speed, carrier gas flow rate, and ferrocene content) is presented.

Multi–walled carbon nanotubes were synthesized in an iron–catalyzed reaction by an improved solution injection method using toluene as hydrocarbon feedstock and ferrocene as catalyst precursor. The pyrolysis temperature, ferrocene concentration, solution feeding rate and carrier gas flow rate all influenced the yield of carbon nanotubes

A high carbon nanotube yield of 32 wt% with high purity was observed at a flow rate of 0.1 mL/min, using 10 wt% ferrocene/toluene solution and a carrier gas flow rate of 150 mL/min at a pyrolysis temperature of 900 ^{0}C.

Reactor: Tubular quartz reactor placed in a furnace
Catalyst: Ferrocene
Carbon Source: Toluene
Carrier Gas: Hydrogen/Argon
Reactor Temperature: 800–1000 ^{0}C
Reactor Pressure: Atmospheric Pressure
Yield: ~ 32 wt%
Selectivity: Not stated
Purification: Not stated

- **Lyu, S.C., Liu, B.C., Lee, S.H., Park, C.Y., Kang, H.K., Yang, C.W., Lee, C.J., 2004, "Large–scale synthesis of high–quality single–walled carbon nanotubes by catalytic decomposition of ethylene", Journal Physical Chemistry B, 108, 1613–1616.**

The synthesis of high–quality single walled carbon nanotubes (SWNTs) with high yield over Fe–Mo/MgO catalyst by catalytic decomposition of ethylene at 800 ^{0}C is reported.

The synthesized reaction product consists mainly of a SWNT bundle and a very small amount of amorphous carbon. The diameter of a single SWNT is in the range 0.7–2.8 nm, showing a wider diameter distribution compared with SWNTs by the arc discharge technique.

A weight gain measurement for the reaction product indicated a high yield of over 55% relative to the weight of Fe–Mo metal in the MgO supported bimetallic catalyst. The as–synthesized carbon nanotubes were characterized by SEM, HRTEM, and XRD.

Reactor: Quartz tube reactor
Catalyst: Fe–Mo supported on MgO
Carbon Source: Ethylene
Reaction Temperature: 800–900 ^{0}C
Reaction Pressure: Not stated
Atmosphere: Argon
Flow Rates: 40 sccm (ethylene), 2000 sccm (argon)
Yield: 55%
Selectivity: Not stated
Purification: Sonication in alcohol (ethanol).

- **Andrews, R., Jacques, D., Qian, D., Rantell, T., 2002, "Multi-wall carbon nanotubes: Synthesis and Application", Account of Chemical. Research, 35, 1008–1017.**

The development of a low–cost chemical vapor deposition process for the continuous production of aligned multi–walled carbon nanotubes (MWNTs) is reported. The effects of reactor temperature, reaction time, and carbon partial pressure on the yield, purity, and size of the MWNTs were investigated.

During the decomposition of xylene and ferrocene at temperatures in the range 625–775 ^{0}C, iron nanoparticles are nucleated and begin to deposit carbon as aligned pure multi walled carbon nanotube arrays.

As the MWNT growth is initiated after the deposition of a Fe catalyst, the production rate is directly proportional to the decomposing to the amount of surface area available to the decomposing hydrocarbons.

Reactor:	Quartz tube in a multi–zone furnace
Catalyst:	Iron nanoparticles
Carbon Source:	Xylene–Ferrocene mixture
Reactor Temperature:	625–775 ^{0}C
Reactor Pressure:	Atmospheric pressure
Production Rate:	~ 1.5 g m^{-2} min^{-1}
Yield:	~ 70%
Purification:	Graphitization: Heat treatment in an inert atmosphere (1800–2600 ^{0}C)

• **Corrias, M., Caussat, B., Ayral, A., Durand, J., Kihn, Y., Kalck, Ph., Serp, Ph., 2003, "Carbon nanotubes produced by fluidized bed catalytic CVD: first approach of the process", Chemical Engineering Science, 58, 4475–4482.**

The first feasibility experiments for the synthesis of carbon nanotubes on an iron-supported catalyst by fluidized bed catalytic chemical vapor deposition are presented. The carbon nanotubes formed are multi–walled type, with mean outer diameter of 17 nm and the inner diameter around 8 nm.

The process selectivity to form carbon nanotubes is close to 100%, as neither soot nor encapsulated catalytic particles were detected by either TEM studies or thermo gravimetric analysis (TGA) of the as–synthesized product. The observed carbon yield often exceeds 95%.

Reactor:	Stainless steel fluidized bed reactor
Catalysts:	Fe/Al_2O_3
Carbon Source:	Ethylene
Reaction Gas:	Hydrogen/Nitrogen
Reactor Temperature:	650 ^{0}C
Reactor Pressure:	Not stated
Fluidization Velocity:	0.14 cm/s
Mean Deposition Rate:	~ 0.22g/min
Yield:	~ 95%
Selectivity:	~ 100%
Purification:	Chemical treatment in acid bath to completely dissolve Fe/alumina catalyst.

• **Emmenegger, C., Bonard, J.M., Mauron, P., Sudan, P., Lepora, A., Groberty, B., Zuttel, A., Schlapbach, L., 2003, "Synthesis of carbon nanotubes over Fe catalyst on aluminum and suggested growth mechanism", Carbon, 41, 539–547.**

The growth of carbon nanotubes by the decomposition of acetylene over a thin catalyst film by chemical vapor deposition is reported. The catalyst was prepared from an iron nitrate precursor solution that was spin–coated on an aluminum substrate.

The iron nitrate film formed an amorphous iron oxide layer that transformed to crystalline Fe_2O_3, which was reduced to Fe_3O_4 and FeO in contact with the acetylene/nitrogen atmosphere.

Carbon nanotube synthesis occurred on small iron carbide (Fe_3C) particles that were formed from the FeO. The catalyst concentration, temperature, growth time, gas composition and flow rate greatly influenced the yield of carbon nanotube produced.

Consequently, the largest carbon nanotube density can be obtained only by controlling precisely parameters such as deposition time, temperature and iron nitrate concentration.

Reactor: Quartz tube furnace
Catalysts: Iron nitrate coated on aluminum substrate
Carbon Source: Acetylene (2–6 sccm)
Carrier Gas: Nitrogen (500 sccm)
Reactor Temperature: 650 ^{0}C
Reactor Pressure: 1 bar
Yield: 0.28 mg cm^{-2}
Purification: Not stated

• Perez–Cabero, M., Rodriguez–Ramos, I.,Guerrero–Ruiz, A., 2003, "Characterization of carbon nanotubes and carbon nanofibers prepared by catalytic decomposition of acetylene in a fluidized bed reactor", Journal of catalysis, 215, 305–316.

The synthesis of carbon nanotubes by catalytic decomposition of acetylene, over several iron/silica catalysts in a fluidized bed reactor at 973 K is reported. The catalysts were prepared by the sol–gel method, which ensures a highly homogeneous distribution of transition metal ions in the silica matrix.

The selectivity for carbon nanotube formation varies with the metallic iron content and dispersion during acetylene decomposition over the catalysts, prepared by the sol–gel method. The catalysts become more active at higher iron contents, however, this activity results in lower selectivity to homogeneous and well –defined carbon nanotubes.

Generally, multi–walled carbon nanotubes were produced, while the reaction products and catalysts were characterized by TEM, XRD, N_2 adsorption isotherms (BET surface area), temperature–programmed reduction (TPR), temperature–programmed oxidation (TPO), and CO volumetric chemisorption.

Reactor: Vertical quartz reactor
Catalysts: Iron/silica (prepared by sol–gel method)
Carbon Source: Acetylene
Reactor Temperature: 973 K
Reactor Pressure: Not stated
Carrier Gas: Nitrogen/Hydrogen
Purification: – Elimination of the silica support in excess HF at 303 K.
– After filtration, oxidant treatment in excess HNO_3 at 343 K in a reflux system to solubilize all the iron present.
– The solid is then filtered, washed with distilled water and drying.

- **Cheung, C.L., Kurtz, A., Park, H., Lieber, C.M., 2002, "Diameter–controlled synthesis of carbon nanotubes", Journal Physical Chemistry B, 106, 2429–2433.**

The concept of using different size nanocluster catalysts to control the diameters and structures of CVD–grown carbon nanotubes is demonstrated. Chemical vapor deposition growth of carbon nanotubes catalyzed by the iron nanoclusters was carried out using ethylene or methane as the carbon source.

Nearly monodisperse iron nanoparticles having three distinct average diameters (3, 9, 13 nm) were used to grow carbon nanotubes with similar average diameters (3, 7, 12 nm) respectively.

TEM images of the reaction product revealed that nanotubes produced from the 3 nm iron nanoclusters consist mainly of single–walled carbon nanotubes, whereas the 9 nm catalyst nanoclusters produced a mixture of single–walled and thin multi–walled carbon nanotubes. The large (13nm) nanoclusters catalyze the growth of thin, multi–walled carbon nanotubes with typical wall thickness of 2–4 graphene sheets.

Reactor: Not specified
Catalyst: Iron nanoclusters
Carbon Source: Ethylene, Methane
Flow Rate: 2–200 sccm (ethylene), 1000 sccm (methane)
Reactor Temperature: 800–1000 ^{0}C
Reactor Pressure: Not stated
Purification: Not stated

- **Nerushev, O.A., Dittmar, S., Morjan, R.E., Rohmund, F., Campbell, E.E.B., 2003, "Particle size dependence and model for iron–catalyzed growth of carbon nanotubes by thermal chemical vapor deposition", Journal of Applied Physics, 93(7), 4185–4190.**

Multi–walled carbon nanotubes were synthesized by iron–catalyzed thermal chemical vapor deposition of two different molecules, ethylene (C_2H_2) and fullerene (C_{60}), as carbon feedstock gases. The dependence of the growth product on the size of catalytic iron particles was also investigated. In the particle size range between 25 and 500 nm, the use of ethylene leads exclusively to the synthesis of carbon nanotubes.

The nanotube diameters increase with increasing catalytic particle sizes. However, carbon nanotube production from fullerene occurs only if the particle sizes are sufficiently small with an optimum between 20 and 30 nm.

The as–prepared carbon nanotubes were characterized by SEM and TEM, while the iron particle distributions were determined by atomic force microscopy.

Reactor: Horizontal tube furnace
Catalysts: Iron deposited on SiO_2 substrate
Carbon Source: Ethylene, Fullerene
Reactor Temperature: 750 ^{0}C
Reactor Pressure: Atmospheric pressure
Carrier Gas: Argon (600 sccm)/Hydrogen (100 sccm)
Yield: Not stated

- **Maruyama, S., Marukami, Y., Miyauchi, Y., Chashi, S., 2003, "Catalytic CVD generation and optical characterization of single–walled carbon nanotubes from alcohol", Presentation at AIChE Annual Meeting.**

High quality single–walled carbon nanotubes (SWNTs) were synthesized by the alcohol catalytic chemical vapor deposition (ACCVD), using ethanol vapor as carbon feedstock over iron/cobalt alloy supported on zeolite powder.

Single–walled carbon nanotube bundles with typical thickness of 10–20 nm were produced as a dense covering on the surface of the zeolite powders.

The yield of SWNTs grown on zeolite support as estimated by thermo gravimetric analysis (TGA) was more than 40% over the weight of the zeolite support powder. This estimate corresponds to more than 80% yield over the weight of the catalytic metal alloy (Fe/Co).

Since the optical properties of the as–produced SWNT material are readily measured, this method is considered to open up new application of SWNT in novel optical devices.

Reactor: Not stated
Catalysts: Iron/Cobalt alloy supported on zeolite
Carbon Feedstock: Ethanol vapor
Reactor Temperature: 850 ^{0}C
Reactor Pressure: Not stated
Atmosphere: Argon/Hydrogen
Yield: ~ 80% relative to Fe/Co catalyst weight
Purification: Not stated

- **Lee, D.C., Mikulev, F.V., Korgel, B.A., 2004, "Carbon nanotube synthesis in supercritical toluene", Journal American Chemical Society, 126, 4951–4957.**

Multi–walled carbon nanotubes were synthesized in supercritical toluene at 600 ^{0}C and ~12.4 MPa using ferrocene, iron, FePt nanocrystals as growth catalysts. In this process, toluene serves as both the carbon source for nanotube growth and the reaction solvent.

Ferrocene thermally decomposes to form Fe particles, which catalyze toluene degradation and promote nanotube and nanofilament formation.

Multi–walled carbon nanotubes ranging from 10 to 50 nm in outer diameter with wall thickness ranging from 5 to 40 nm were produced. The nanotubes were characterized by HRTEM, HRSEM and electron energy loss spectroscopy (EELS).

Reactor: High–pressure stainless steel reactor.
Catalysts: Ferrocene/FePt nanocrystals
Carbon Source: Toluene
Reactor Temperature: 600 ^{0}C
Reactor Pressure: ~12.4 MPa
Yield: 2 wt%
Selectivity: Not stated
Purification: – Dispersion in hexane
– Centrifugation at 8000 rpm

• **Lyu, S.C., Liu, B.C., Lee, S.H., Park, C.Y., Kang, H.K., Yang, C.W., Lee, C.J., 2003, "Large–scale synthesis of high–quality double–walled carbon nanotubes by catalytic decomposition of n–hexane", Journal Physical Chemistry B, 108, 2192–2194.**

The large–scale production of high quality double–walled carbon nanotubes (DWNT) over a Fe–Mo/MgO catalyst by catalytic decomposition of n–hexane is reported.

The synthesis of highly selective DWNTs with high yield can be mostly attributed to the large quantities of highly dispersed catalytic metal particles with a uniform size, catalyst composition and carbon feed gas.

The outer tubes of the as–synthesized DWNTs mostly range from 1.5–2.6 nm, with inner tube diameters ranging from 0.75–1.8 nm. The products were characterized by HRTEM, SEM and Raman spectroscopy analysis.

Reactor:	Quartz tube reactor/Tube furnace
Catalysts:	Fe–Mo/ MgO (Fe: Mo: MgO = 1: 0.1: 12)
Carbon Source:	n–hexane
Reactor Temperature:	900 ^{0}C
Reactor Pressure:	Not stated
Reaction Gas:	Ar (2000 sccm) /H_2 (100 sccm)
Atmosphere:	Argon
Yield:	Not stated
Purification:	Not stated

• **Resasco, D.E., Alvarez, W.E., Pompeo, F., Balzano, L., Herrera, J.E., Kitiyanan, B., Borgna, A., 2001, "A scalable process for production of single–walled carbon nanotubes by catalytic disproportionation of CO on a solid catalyst'', Journal of Nanoparticle Research**, **00, 1–6.**

The development of a catalytic method (CoMoCAT process) that synthesizes high quality single–walled carbon nanotubes (SWNTs) at very high selectivity and with a remarkably narrow distribution of tube diameter is reported.

In this technique, SWNTs are produced by CO disproportionation (decomposition into C and CO_2) at 700–950 ^{0}C in a flow of pure CO. The synergistic effect between Co and Mo catalysts is essential in its performance, such that the catalyst is only effective when both metals are simultaneously present on a silica support with low Co: Mo. Separated, they are either inactive (Mo alone) or unselective (Co alone).

The SWNT produced were characterized by TEM, SEM, AFM, Raman spectroscopy and temperature programmed oxidation (TPO).

Reactor:	Not Specified
Catalysts:	Cobalt (Co), Molybdenum (Mo)
Carbon Source:	Carbon monoxide
Reactor Temperature:	700–950 ^{0}C
Reactor Pressure:	1 – 10 atm
Production Rate:	~0.25 g SWNT/g catalyst
Selectivity:	≥ 80%

Purification: –Base treatment with 2 M NaOH solution to remove SiO_2, Mo and Co
–Oxidation in air at 200–250 ^{0}C and acid (HCl/HNO_3) treatment.

This CoMoCAT process is one of the two processes selected for the process model developed in Chapter 3.

• Nikolaev, P., Bronikowski, M. J., Bradley, R. K., Rohmund, F., Colbert, D. T., Smith, K. A., Smalley, R. E., 1999, "Gas–phase catalytic growth of single–walled carbon nanotubes from carbon monoxide", Chemical Physics Letters, 313, 91–97.

The gas–phase catalytic synthesis of single walled carbon nanotubes in a continuous flow of carbon monoxide as carbon feedstock and iron pentacarbonyl as the iron–containing precursor, is reported.

The growth catalyst is formed in situ by thermal decomposition of iron pentacarbonyl in a heated flow of CO at pressures of 1–10 atm and at temperatures ranging from 800 ^{0}C to 1200 ^{0}C.

The flow cell apparatus consists of a 1″ outer diameter quartz flow tube placed in a tube furnace, through which reactant gases are flowed. The tube section inside the furnace is heated to between 800 ^{0}C and 1200 ^{0}C, while maintaining the tube inlet and exit at room temperature.

The flow of carbon monoxide and iron pentacarbonyl mixtures through the heated reactor leads to formation of single wall carbon nanotubes and iron particles apparently overcoated with carbon.

The yield and quality of the carbon nanotubes produced depends on the rate at which the reactants are heated, other reaction conditions and the flow–cell geometry. The size and diameter of the carbon nanotubes produced can be roughly selected by controlling the pressure of CO in the reaction chamber.

The process, being a continuous flow process can be scaled up for mass production of carbon nanotubes.

Reactor: 1″ OD Quartz flow tube in a tube furnace
Catalysts: Iron pentacarbonyl
Carbon Source: Carbon monoxide (1–2 standard liters per minute)
Coolant: Water
Reactor Temperature: 800 ^{0}C–1,200 ^{0}C
Reactor Pressure: 1–10 atm
Yield: 61–79 mole %
Purification: Not stated

• Bronikowski, M. J., Willis, P. A., Colbert, T. D., Smith, K. A. Smalley, R. E., 2001 "Gas–phase Production of Carbon Single–walled nanotubes from carbon monoxide via the HiPCO Process: A parametric study", Journal Vacuum Science Technology A, 19(4), 1800–1805.

The large–scale production of single–walled carbon nanotubes, using a gas–phase chemical vapor deposition process, is reported. This process, referred to as the HiPCO

process, involves the production of carbon nanotubes from carbon monoxide disproportionation over iron catalysts at high–pressure (30–50 atm), and high–temperature (900 – 1100 ^{0}C).

The iron catalytic clusters, formed *in situ* from the decomposition of the catalyst precursor, iron pentacarbonyl, acts as nuclei upon which the carbon nanotubes nucleate and grow. The effect of process parameters such as temperature, carbon monoxide pressure, and catalyst concentration on the growth rate of carbon nanotubes were investigated.

Carbon nanotubes of up to 97 % purity, at production rates of up to 450 mg/h have been reported for the HiPCO process.

The process employs a closed loop through which unconverted carbon monoxide is continuously recycled. Consequently, the feasibility of continuous production of carbon nanotubes is demonstrated by the HiPCO process.

Reactor: High–pressure quartz tube reactor in a tube furnace
Catalysts: Iron pentacarbonyl
Carbon Source: Carbon monoxide (9.8L/min)
Coolant: Water
Reactor Temperature: 900^{0}C–1100^{0}C
Reactor Pressure: 30–50 atm
Yield: ~ 450 mg/h or ~11 g/day
Selectivity: Not stated
Purification: Filtration

This HiPCO process is one of the two processes selected for the process models developed in Chapter Three.

• Komatsu, T., Inoue, H., 2002, "Synthesis of thin wall multi–walled carbon nanotubes by catalytic decomposition of hydrocarbon using metallophtalocyanine as catalyst", Molecular Crystal Liquid Crystal, 387, (337)/113–(340)/116.

The synthesis of multi–walled carbon nanotubes by thermal catalytic decomposition of hydrocarbons using metallophtalocyanine as catalyst is reported.

The diameter of the carbon nanotube produced, which depends on the diameter of the catalytic particle, ranges between 10–20 nm. The carbon nanotubes were characterized by SEM and TEM analysis.

Reactor: Flow reactor
Catalysts: Iron (III) phtalocyanine (FePc)
Hydrocarbon Feedstock: Benzene/Thiopene
Carrier Gas: Hydrogen
Reactor Temperature: 1100 ^{0}C
Reactor Pressure: Not stated
Yield: Not stated
Selectivity: Not stated
Purification: Not stated

- **Coquay, P., Vandenberghe, R.E., De Grave, E., Fonseca, A., Piedigrosso, P., Nagy, J.B., 2002, "X–ray diffraction and Mossbauer characterization of a Fe/SiO_2 catalyst for the synthesis of carbon nanotubes", Journal of Applied Physics, 92(3), 1286–1291.**

The selective reduction of a catalyst powder, prepared by adsorption, and precipitation of iron acetate on a silica support, at a controlled pH, in a nitrogen/ethylene atmosphere at 700 ^{0}C, generated multi–walled carbon nanotubes.

The study by x–ray diffraction and Mossbauer spectroscopy of the catalyst and reduced powders revealed that hematite particles were involved in the formation of multi–walled carbon nanotubes with a diameter distribution close to the particle–size distribution (8–20 nm).

The particles involved in the formation of carbon nanotubes end up as Fe_3C after the catalysis process.

Reactor: Fixed bed flow quartz reactor
Catalysts: Iron acetate/silica
Carbon Source: Ethylene
Reactor Temperature: 700 ^{0}C
Reactor Pressure: Atmospheric pressure
Atmosphere: Nitrogen
Yield: Not stated
Selectivity: Not stated
Purification: Not stated

- **Jeong, S.H., Lee, O.J., Lee, K.H., 2003, "Synthesis of carbon nanotubes with prescribed dimensions", Presentation at 2003 AIChE Annual Meeting.**

Carbon nanotubes with prescribed dimensions were produced using anodic aluminum oxide (AAO) template in the presence of hydrogen. The effect of a reaction gas (H_2) and catalyst (Cobalt) on the growth of carbon nanotubes in the anodic aluminum oxide (AAO) template was investigated.

The main advantage of AAO templates is the precise control of template dimensions, such as pore diameter, length and density. Thus, precise and reproducible control of dimensions of a carbon nanotube can be achieved by synthesizing in the pores of the template.

The nanotube growth process involves the competitive catalytic carbon deposition between Co particles deposited at the bottom of the pores and on the AAO template itself. However, carbon nanotubes can be synthesized without catalysts by the catalytic action of an AAO template.

Carbon nanotube synthesis by CO disproportionation showed a lower growth rate and a higher degree of ordering than those grown by ethylene pyrolysis.

Reactor: Not stated
Catalyst: Cobalt deposited on anodic aluminum oxide (AAO) templates
Carbon Source: Ethylene, Carbon monoxide
Reaction Gas: Hydrogen

Reactor Temperature: 650–700 ^{0}C
Reactor Pressure: Not stated
Atmosphere: Argon
Flow Rate: 200 sccm (C_2H_2, CO)
Yield: Not stated
Purification: Not stated

• Weizhong, Q., Fei, W., Zhanwen, W., Tang, L., Hao, Y., Guohua, L., Lan, X., Xiangyi, D., 2003, "Production of carbon nanotubes in a packed bed and a fluidized bed", AIChE Journal, 49(3), 619–625.

The preparation of carbon nanotubes from ethylene decomposition over iron/alumina catalyst in a packed bed reactor (PB) and a nanoagglomerate fluidized bed reactor (NABR) is presented. The Fe/Al_2O_3 catalyst is prepared by co–precipitation method.

The conversion of ethylene is above 95% in the packed bed reactor during the entire reaction period while ethylene conversion in the NABR, which is initially 100%, is finally reduced to about 50% after 307 minutes.

However, the space velocity of ethylene in the NABR is 10 times higher than that in the packed bed reactor. Consequently, the total yield of carbon nanotubes in the NABR is 6–7 times that in the packed bed reactor at the end of the reaction, although carbon nanotube yield increases steadily with reaction time in both reactors.

The diameter distribution of carbon nanotubes from the NABR is very narrow with an average diameter of 8 nm, while the average diameter of the nanotubes from the packed bed reactor is 16 nm. The synthesized carbon nanotubes were characterized by TEM, Raman spectroscopy and particle size analysis.

Reactor: Packed–bed reactor; Nanoagglomerate fluidized bed reactor
Catalysts: Fe/Al_2O_3
Carbon Source: Ethylene/Hydrogen
Reactor Temperature: 823 K
Reactor Pressure: Not stated
Carrier Gas: Nitrogen
Yield: 30–150 g carbon nanotube/10g catalyst
Purification: Not stated

C. Other Methods

• Hong, E.H., Lee, K., Oh, S.O., Park, C., 2003, "Synthesis of carbon nanotubes using microwave radiation", Advanced Functional Materials, 13(12), 961–966.

A novel method for carbon nanotube synthesis using microwave irradiation is reported. Microwaves are electromagnetic waves with a frequency range from 300 MHz to 300 GHz.

Microwave heating, where the microwave energy is delivered to the materials through molecular interactions with the electromagnetic field, has the advantage of uniform, rapid and volumetric heating. However, it is limited in applications, as some materials cannot be easily heated by microwave.

Carbon nanotubes were successfully synthesized by microwave heating of catalysts (3d transition metals and metal sulfides) on low–melting substrates under flowing acetylene gas used as a hydrocarbon source.

Different carbon yields and morphologies (filamentous and particulate) were observed depending on the reaction conditions. HRTEM showed that that the filamentous carbons (linear or Y–branches) are either carbon nanotubes or graphitic carbon nanofibers.

Reactor:	Quartz reactor placed in microwave oven (2.45 GHz, 800 W)
Catalysts:	Co, Fe, Ni, Cobalt sulfide
Reactants:	Acetylene
Substrates:	Teflon, Polycarbonate, Carbon black,
Co–reactant Gas:	$H_2S/H_2/NH_3$
Reactor Temperature:	500 ^{0}C
Reactor Pressure:	Atmospheric pressure
Yield:	7.5–31.5 wt%
Purification:	Not stated

- **Height, M.J., Howard, J.B., Tester, J.W., 2003, "Flame synthesis of carbon nanotubes", Materials Research Society Symposia Proceedings, 772, 55–61.**

Combustion systems offer a potential means of producing bulk quantities of carbon nanotubes in a continuous, economically favorable process. The synthesis of carbon nanotubes in premixed flames and their primary formation mechanisms in the combustion environment is examined.

Carbon nanotubes were synthesized in the post flame region of a premixed acetylene/oxygen/argon flame operated at 50 Torr (6.7 kPa) with iron pentacarbonyl vapor used as a source of metallic catalyst. HRTEM resolution revealed the nanotubes are primarily single–walled carbon nanotubes (SWNTs).

The flame synthesis technique preferentially forms SWNTs rather than MWNTs, which indicates a high degree of selectivity despite the array of competing processes occurring in the flame system.

Reactor:	Stainless steel vacuum chamber – burner
Reactants:	Acetylene/oxygen/argon flame
Burner Pressure:	50 Torr
Burner Plate Temperature:	70–80 ^{0}C
Carrier Gas:	Argon
Yield:	Not stated
Purification:	Not stated

- **Guillard, T., Cetout, S., Flamant, G., Laplaze, D., 2000, "Solar production of carbon nanotubes; structure evolution with experimental conditions", Journal of Materials Science, 35, 419–425.**

The production of carbon nanotubes by direct vaporization of graphite targets containing different metallic catalysts using a 2 kW solar furnace is presented.

The structural evolution of the synthesized carbon nanotube as a function of pressure, flow rate of inert gas and target composition with changes in experimental conditions is also studied.

The dilution of the carbon vapor, which increases with the pressure of the inert gas, favors the production of SWNTs. However, the purity of the reaction product depends on the target temperature and the cooling rate of the vapor.

Reactor:	Solar furnace (2 kW)
Carbon Source:	Powdered graphite
Catalysts:	Cobalt, Nickel, Lanthanum
Carrier Gas:	Argon
Reactor Temperature:	~3000 K
Reactor Pressure:	120, 250, 400 and 600 mbar
Yield:	Not stated
Purification:	Not stated

• Liu, J., Shao, M., Xie, Q., Kong, L., Yu, W., Qian, Y., 2003, "Single–source precursor route to carbon nanotubes at mild temperature", Carbon, 41, 2101–2104.

The preparation of carbon nanotubes under solvothermal conditions through a single–source precursor method at 500 ^{0}C, using iron carbonyl both as carbon source and catalyst, is reported. As iron carbonyl acted as catalyst, carbon source and solvent, this technique avoids the separation of raw material from solvent and simplifies the operation process.

The fact that the iron carbonyl acted as a solvent helps to accelerate diffusion, adsorption, reaction rate and crystallization in the formation of carbon nanotubes. Consequently, a lower reaction temperature is observed compared to other methods using carbon monoxide as the carbon source.

TEM images of the reaction product revealed nanotubes with an average inner (outer) diameter of 30 nm (60 nm) with the yield of the as–produced products as high as 85%.

Reactor:	Stainless steel autoclave
Catalysts:	Iron carbonyl
Reactants:	Iron carbonyl, $Fe(CO)_5$
Reaction Time:	12 h
Reactor Temperature:	500 ^{0}C
Reactor Pressure:	ca. 4 MPa
Yield:	~ 85%
Purification:	Treatment with dilute hydrochloric acid

• Shao, M., Wang, D., Yu, G., Hu, B., Yu, W., Qian, Y., 2004, "The synthesis of carbon nanotubes at low temperature via carbon suboxide disproportionation", Carbon, 42, 183–185.

The development of a novel route, involving a carbon suboxide disproportionation reaction to synthesize multi–walled carbon nanotubes in the presence of an iron catalyst at 180 ^{0}C is reported.

In this process, carbon suboxide disproportionates to form carbon and carbon dioxide. The freshly formed carbon atoms assemble into hexagonal carbon clusters, which may grow into nanotubes at the surface of the catalyst particles.

The products were characterized with XRD, TEM, HRTEM and Raman spectroscopy. The carbon nanotubes are open–ended, with an average inner (outer) diameter of 5–20 nm (15–40 nm).

Reactor:	Teflon reactor
Catalysts:	Iron, Fe
Reactants:	Malonic acid, phosphorus pentoxide
Reactor Temperature:	180 ^{0}C
Reactor Pressure:	Not stated
Reaction Time:	5 days
Yield:	~ 15%
Selectivity:	Not atated
Purification:	– Treatment with 0.5 M HCl at 80 ^{0}C; – Vacuum drying at 50 ^{0}C

- **Shah, N., Wang, Y., Panjala, D., Huffman, G.P., 2004, "Production of hydrogen and carbon nanostructures by non–oxidative catalytic dehydrogenation of ethane and propane", Energy and Fuels, A–I.**

Nanoscale binary M–Fe (M = Mo, Ni or Pd) catalysts supported on alumina were shown to be very effective for the non–oxidative catalytic dehydrogenation of undiluted ethane and propane to yield hydrogen and multi–walled carbon nanotubes.

Depending on the reaction temperature, two distinct forms of carbon structures were produced.

At higher reaction temperatures (> 650 ^{0}C), multi–walled carbon nanotubes with a high degree of parallelism between the graphene wall layers were synthesized.

At lower reaction temperatures, the carbon produced were in form of nanofibers consisting of stacked truncated cones.

One of the major constraints with non–oxidative dehydrogenation is coking of the catalyst and reactor due to carbon buildup.

However, these binary catalysts, under proper reaction conditions, promote the growth of carbon nanotubes that transport carbon away from the catalyst surfaces, thus preventing catalyst deactivation by coking as well as producing a valuable byproduct.

Reactor:	Fixed–bed, plug–flow quartz reactor
Catalysts:	0.5%M –4.5% Fe /Al_2O_3, (M = Mo, Ni or Pd)
Feedstock:	Ethane, Propane
Reactor Temperature:	650–800 ^{0}C
Reactor Pressure:	Not stated
Reaction Time:	Not stated
Yield:	Not stated
Selectivity:	Not stated
Purification:	Not stated

- **Choi, H.C., Kim, W., Wang, D., Dai, H., 2002, "Delivery of catalytic metal species onto surfaces with dendrimer carriers for the synthesis of carbon nanotube with narrow diameter distribution", The Journal of Physical Chemistry B, 106(48), 12361–12365.**

Carbon nanotube synthesis by chemical vapor deposition on catalytic nanoparticle derived from polyamidoamine (PAMAM) dendrimers is reported.

Polyamidoamine dendrimers were used as carriers to deliver complexed Fe(III) ions uniformly on silicon oxide substrates for the formation of iron oxide nanoparticles with a narrow diameter distribution in the range 1–2 nm.

These nanoparticles were subsequently used for chemical vapor deposition to produce single–walled carbon nanotubes with diameters in the 1–2 nm range.

Dendrimers are hyper–branched macromolecules used in various applications, such as drug delivery systems, adhesion materials for high quality metal film formation and nanoparticle template formation.

Reactor: Not stated
Catalysts: Iron oxide nanoparticles (derived from Fe(III)/G6OH dendrimers)
Reactants: Methane (1000 sccm)/Hydrogen (500 sccm)/Ethane (20 sccm)
Reactor Temperature: 900 ^{0}C
Reactor Pressure: Not stated
Yield: Not stated
Purification: Not stated

- **Motiei, M., Hacohen, Y.R., Calderon–Moreno, J., Gedanken, A., 2001, "Preparing carbon nanotubes and nested fullerenes from supercritical CO_2 by a chemical reaction", Journal American Chemical Society, 123, 8624–8625.**

Carbon nanotubes were synthesized from the chemical reaction between supercritical carbon dioxide and magnesium. The reaction products contain MgO, which is removed by treatment with aqueous HCl, and carbon, containing carbon nanotubes and nested fullerenes.

The total yield of carbonaceous materials (relative to the CO_2 starting material) is about 16%, of which carbon nanotubes account for 10% of this material. The carbon nanotubes produced as revealed by HRTEM images have a length of 500–60 nm and a width of 30–40 nm.

The complexities of using a flowing gas at controlled pressure and high temperatures were avoided in this simple chemical method of growing well–crystallized carbon nanotubes from supercritical carbon dioxide in the presence of magnesium.

Reactor: Stainless steel closed cell.
Reactants: CO_2 and Magnesium
Reactor Temperature: Not stated
Reactor Pressure: Not stated
Yield: ~ 10%
Selectivity: Not stated
Purification: Dissolution in 8 M aqueous HCl at 70 ^{0}C; Microflitration

• **O'Loughlin, J.L., Kiang, C.H., Wallace, C.H., Reynolds, T.K., Rao, L., Kaner, R.B., 2001, "Rapid synthesis of carbon nanotubes by solid–state metathesis reactions", J. Phys. Chem. B, 105, 1921–1924.**

The rapid synthesis of carbon nanotubes by solid–state metathesis (exchange) reactions between carbon halides and lithium acetylide catalyzed by cobalt dichloride is reported.

The reaction product contains single–walled and multi–walled carbon nanotubes along with graphite encapsulated cobalt nanoparticles, with the catalyst added. Without the catalyst, only graphite and amorphous carbon are produced. The effects of catalyst concentration and reaction scale on the product distribution were also investigated.

Solid–state metathesis reactions serve as a simple and effective route to materials that are difficult to synthesize by conventional methods.

These reactions, which are self–propagating, can be initiated with a heated filament and can be controlled by regulating the reaction temperature. Thus, a potential route to optimization is to lower the reaction temperature.

Reactor:	Not stated
Catalyst:	Cobalt dichloride
Reactants:	Hexachloroethane and Lithium acetylide
Reaction Temperature:	2,302 K (theoretical)
Reactor Pressure:	Not stated
Yield:	Not stated
Selectivity:	Not stated
Purification:	Concentrated nitric acid treatment to remove free (amorphous/graphitic) carbon and unencapsulated cobalt metal

• **Hu, G., Cheng, M., Ma, D., Bao, X., 2003, "Synthesis of carbon nanotube bundles with mesoporous structure by a self–assembly solvothermal route", Chemical Materials, 15, 1470–1473.**

The synthesis of carbon nanotubes by a simple one–step solvothermal reaction between sodium and hexachlorobenzene (HCB), using nickel chloride as catalyst precursor is presented.

Prior to the reaction, the catalyst precursor was initially dispersed ultrasonically in cyclohexane, and then pre–reduced by sodium at 230 ^{0}C to small nickel particles in reduced state. Thus, the catalytic function of nickel could be fully realized in the subsequent reaction with hexachlorobenzene.

Highly ordered carbon nanotube bundles with mesoporous structure (the pore size is about 5 nm) were produced. The carbon nanotube (outer diameter of ~ 25 nm) yield is over 70% in the as synthesized product.

Reactor:	Stainless steel autoclave
Catalyst:	Nickel chloride
Reactants:	Hexachlorobenzene, Sodium
Reactor temperature:	230 ^{0}C

Reactor Pressure: Not stated
Yield: ~ 70%
Selectivity: Not Stated
Purification: – Sequential treatment with ethanol, hot cyclohexane, and diluted H_2SO_4
– Drying at 80 ^{0}C.

• Liu, J., Shao, M., Chen, X., Yu, W., Liu, X., Qian, Y., 2003, "Large–scale synthesis of carbon nanotubes by ethanol thermal reduction process", Journal American Chemical Society", 125, 8088–8089.

The large–scale synthesis of carbon nanotubes from the reaction between ethanol with magnesium, by ethanol thermal reduction process, in which ethanol is used as the carbon source and magnesium used as the reducing agent. Thus, this synthesis method completely avoids the use of toxic or corrosive reagents as a reducing agent.

The reaction product as characterized by SEM, TEM, HRTEM and Raman spectroscopy consists of bamboo–shaped multi–walled carbon nanotubes (30–100 nm outer diameters), with an estimated yield of 80% and Y–junction carbon nanotubes. The thermal reduction process can be formulated as:

$$CH_3CH_2OH + Mg \rightarrow 2C + MgO + 3H_2$$

Reactor: Stainless Autoclave
Carbon Source: Ethanol
Reducing Agent: Magnesium
Reactor Temperature: 600 ^{0}C
Reactor Pressure: Not stated
Yield: ~ 80%
Purification: –Washing with absolute ethanol, dilute HCl, and distilled water
–Vacuum drying at 65 ^{0}C.

• Hlavaty, J., Kavan, L., Kasahara, N., Oya, A., 2001, "Polymerization of 1–iodohexa–1, 3, 5–triyne and hexa–1, 3, 5–triyne: a new synthesis of carbon nanotubes at low temperatures", Chemical Communication, 737–738.

The synthesis of a solid carbonaceous material, which contains polyyne–like structures and multi–walled carbon nanotubes with outer diameter 10–20 nm and length 100–200 nm from spontaneous polymerization of 1–iodohexa–1, 3, 5–triyne and hexa–1, 3, 5–triyne in aprotic solution, is reported.

The carbon nanotubes formed agglomerates and were embedded in a material with an amorphous shape. The yield of carbon nanotubes is estimated to be ~ 1%.

Reactor: Not stated
Carbon Source: 1–iodohexa–1, 3, 5–triyne and hexa–1, 3, 5–triyne
Catalyst: Not stated
Reactor Temperature: Not stated
Reactor Pressure: Not stated

Yield: ~ 1 %
Purification: Not stated

2.4. EVALUATION OF SYNTHESIS METHODS

A summary of the various carbon nanotube production processes reviewed in the last section is presented in Table 2.1, Table 2.2, and Table 3.3. The electric arc production processes are listed in Table 2.1, while laser vaporization processes are given in Table 2.2. The chemical vapor deposition production processes are listed in Table 2.3, while other carbon nanotube production processes are given in Table 2.4.

The applications for carbon nanotubes, which range from field emitters, nanoprobes and nanosensors, to nanoelectronics and composites, require the development of growth processes, capable of producing high purity materials in tons/day quantities in order to realize the potential of this unique and novel material.

However, the commercialization of carbon nanotube technologies has essentially been inhibited by three factors: (a) lack of a reliable, large–volume production capacity, (b) high selling price of the final carbon nanotube product, and (c) little selectivity in controlling the properties of the carbon nanotube produced (Andrews, et al., 2002). Consequently, the commercial use of carbon nanotubes in potential applications is highly dependent on the development of low cost, continuous, high throughput, and commercially scalable carbon nanotube production processes.

The criteria for selecting a scalable production process include capital and operating cost, raw materials selection, operation mode (semi–batch, batch or continuous), bulk production and post–synthesis purification requirements. The process operating conditions, such as pressure, temperature, catalyst performance, reactant conversion and selectivity, are also considered for selecting processes for model development.

Table 2.1 Arc–Discharge Synthesis Processes

Reactor	Carbon Source	Catalysts	Electrodes	Discharge Current	Temperature	Inert Gas	Yield	Literature
Plasma Rotating Electrode Process System (PREP)	Pure Graphite Anode	Not stated	12–mm φ pure graphite anode; 15–mm φ pure graphite cathode; at ~ 3 mm apart.	120 A ~20–30 V	Above ^{0}C 1200	Helium 5L/min 500 Torr	Not Stated	Lee et al, 2002
Dewar Flask	Pure Carbon Anode	None	8–mm φ pure carbon anode; 10–mm φ pure carbon cathode; at ~ 1 mm apart	~ 80 A ~ 20–28 V	Not stated	Liquid Nitrogen	~70%	Jung et al, 2003
Not stated	Pure Carbon Anode	None	Pure Carbon electrodes; kept ~10 cm below the liquid surface	~30 A d.c.	Not stated	Liquid N_2; Deionized water	Not stated	Alexandrou et al, 2004
Quartz Tube Reactor; 12–mm inner diameter	CH_4 : H_2 (1:10); Total feed rate 22 sccm	Cobalt	Axially centered upper tungsten wire and lower stainless steel circular plate; ~5mm apart	8000 V 25 KHz 40 W 82 W/cm^2	Below ^{0}C 200	None Atm. Pressure	Not stated	Li et al, 2004
Electric–Arc Discharge Apparatus	Graphite powder and anode.	Ni–Co; Ni–Y; Co–Y.	6–mm φ graphite anode;16–mm φ graphite cathode; at ~3mm apart	100 A	Not stated	Helium 660 mbar	~80%	Journet et al, 1997
Reaction Vessel	Graphite anode	None	6–mm φ anode; 9–mm φ cathode; at ~1mm apart	30 V a.c./ d.c. ~ 100 A ~ 18 V	Not stated	Helium ~500 Torr	~75%	Ebbesen et al, 1992

Table 2.2 Laser Vaporization Synthesis Processes

Reactor	Target Rods	Catalysts	Laser	Buffer Gases	Temperature	Power Density	Yield	Literature
Oven–Laser Vaporization Apparatus	Metal-Graphite Target: 6–7 mm φ spot	Co, Cu, Ni, Pt, Co–Ni, Co–Pt, Co–Cu, Ni–Pt,	Scanning Laser (300 mJ/pulse, 0.532μm); 200 cm focal length,75cm focal distance	Argon 50sccm 500 Torr	1200 ^{0}C	Not stated	~15% to ~50%	Gou et. al., 1995
Stainless Steel Evaporation Chamber: with quartz tube and no external furnace	Graphite-Metal Powders; 6–mm φ, 5 mm length Coke / Pitch as Precursors	Ni, Co, Y, Fe, Ni–Y, Ni–Co, Ni–La, Co–Y	250 W CO_2–laser operating in cw mode: at ~10.6 μm wavelength; ~ 1–mm spot size; 0.8 mm^2 focal area	Argon Nitrogen Helium 50–500 Torr	1200–3000 ^{0}C	12KW/cm^2 (200 mg/h) 9 KW/cm^2 (90 mg/h)	Not stated	Maser et. al., 2001
Stainless Steel Evaporation Chamber: with (dynamic) and without (static) quartz tube	Cylindrical Graphite-Metal Targets: 5.5–6 mm diameter, φ	Ni, Co, Y, Fe, Ni–Co, Ni–Y, Ni–Fe, Ni–La, Co–Y	CO_2 Laser operating in continuous wave (cw) mode at ~ 10.6 μm	Argon Helium Nitrogen 50–500 Torr	1200 ^{0}C (Hot zone of ~1 cm around the focal spot)	12 KW/cm^2 (200 mg/h)	~80%	Munoz et al, 2000

Table 2.3 Chemical Vapor Deposition (CVD) Synthesis Processes

Reactor	Reactants	Catalysts	Carrier Gas	Temperature	Pressure	Yield	Literature
Quartz Glass Tube and Vertical furnace	Acetylene (C_2H_2) or iso–pentane	Fe$_2O_3$/MgO (3–15% Fe ratio)	Argon	400–850 ^oC	Not stated	0.5 g	Mauron et al, 2003
Tubular Reactor (800 x 28 mm ID)		Ferrocene (0–15 wt.%)	5% H_2 in Ar (v/v)	800–1000 ^oC	Atm. Pressure	32 wt.%	Liu et al, 2002
Quartz Tube Reactor within a Furnace	Toluene Xylene	nanoparticles	Inert gas	625–775 ^oC	Atm. Pressure	70%	Andrews et al, 2002
Quartz Tube Furnace	Ferrocene Ethylene (2–6 sccm)	Iron Iron Carbide (Fe_3C)	Nitrogen (500sccm)	^oC	1 bar	Not stated	Emmeneger et al, 2003
Quartz Tube Reactor (70mm ID) mounted in a Tube Furnace		(Fe	Argon Ar/H_2	650 ^oC	Not stated	90%	Lyu et al, 2004
Stainless Steel Fluidized Bed (5.3cm ID, 1 m height)	n–hexane	Fe–Mo/MgO 2.5% Fe/Al_2O_3 (w/w)	N_2/H_2	900 ^oC	Not stated	95%	Corrias et al, 2003
Quartz Reactor (2.2 cm ID, 120 cm long)	Ethylene		N_2/H_2	650	Not stated	10%	Perez-Cabero et al, 2001
Horizontal Tube	Acetylene C_2H_2 (8 scccm)	Iron/Silica $_2$	N Ar/H_2 (600/100 sccm)	973 K ^oC	Not stated	Not stated	Nerushev et al, 2003
Furnace Not stated	Fullerene C_2H_2 (200 sccm) CH_4 (1000sccm)	Fe/SiO Fe/Silica	Ar/H_2 (600/400 sccm)	750 800–1000 ^oC	Not stated	Not stated	Cheung et al, 2004

Table 2.3 (continued)

Reactor	Reactants	Catalysts	Carrier Gas	Temperature	Pressure	Yield	Literature
Not Specified	Carbon Monoxide	Co/Mo on Silica support	Not stated	700–950 °C	1–10 atm	0.25gCNT /g catalyst	Resasco et al, 2002
Quartz Flow Tube	Carbon Monoxide	Iron pentacarbonyl	Not stated	800–1200 °C	1–12 atm	37–44 wt.%	Nikolaev et al, 1999
Quartz Tube in Electric Furnace	Benzene (5 mL) Thiopene (1 g)	Phtallocyanine Iron (III)	Hydrogen Argon	°C	Not stated	Not stated	Komatsu et al, 2002
Quartz Tube Flow Reactor – Fixed Bed	Ethylene (1.2 L/h)	Fe/SiO_2	Nitrogen (18 L/h)	1200 °C	Atm. Pressure	32 wt.%	Coquay et al, 2002
Anodic Aluminum Oxide Template	Ethylene (20%) Hydrogen (10%)		Argon	700 650–700 °C	Not stated	Not stated	Jeong et al, 2003
Fluidized Bed and Packed Bed Reactors		Cobalt Fe/Al_2O_3 (10 g)	Nitrogen		Not stated	30–150 g	Weizhong et al, 2003
High Pressure Quartz Tube Reactor	Ethylene Carbon Monoxide	Iron pentacarbonyl	Not stated	823 K 900–1100 °C	30–50 atm	450 mg/h	Bronikowski et al, 2001
Quartz Tube Furnace	Fullerene (C_{60}-C_{70})	Fe/Co on Zeolite	Argon (200sccm)	°C	0.05 Torr	Not stated	Maruyana et al, 2003
Stainless Steel Reactor	Supercritical Toluene (40 sccm) Ethylene (1 sccm)	support Ferrocene, Fe, or FePt (1 g)	Nitrogen	825 °C	12.4 MPa	2%	Lee et al, 2004
Quartz Tube Reactor		Fe-Mo/MgO	Argon	600 800–900 °C	Not stated	55%	Lyu et al, 2004

Table 2.4 Other Synthesis Methods

Reactor	Carbon Source	Catalysts	Carrier Gas	Temperature	Pressure	Yield	Literature
Quartz Reactor	Acetylene	Co, Ni, Fe	H_2S/NH_3 /H_2	500 °C	1 atm	8–32%	Hong et al, 2003
Vacuum Chamber				700–800 °C		Not stated	Height et al, 2003
Burner	Acetylene	None	Argon		50 Torr		
Stainless Steel	Iron carbonyl	Iron carbonyl	None	500 °C	4 MPa	85%	Liu et al, 2003
Autoclave	Malonic acid/ Phosphorus pentoxide		None	180 °C	Not stated	15%	Shao, et al, 2004
Teflon Reactor		Iron					
Fixed Bed Quartz	Ethane, Propane	Fe_2O_3	None	650–800 °C	Not stated	Not stated	Shah, et al, 2004
Reactor	Supercritical CO_2, Magnesium	Fe/Al	None	Not stated	Not stated		Motiei et al, 1992
Stainless Steel							
Closed Cell	Chloroethane, Lithium acetylide	None	None	Not stated	Not stated	10% Not stated	O'Loughlin et al, 2001
Not stated	Chlorobenzene,	Cobalt dichloride	None	2,302 K °C	Not stated		Hu, et al, 2003
Stainless Steel		Nickel Chloride				70%	
Autoclave	Sodium	Iron oxide	None	230 °C	Not stated	Not stated	Choi, et al, 2002
Not stated	$CH_4/H_2/C_2H_6$		None	900			

The process conditions, such as operating temperature and pressure are important criteria for selecting an economically scalable production process, because a lower operating temperature and pressure have the potential to reduce both operating costs and energy requirements of such a process.

The catalyst performance, which includes its activity, deactivation time, and regeneration method, determines the extent of reaction, as well as the process selectivity to the desired product. Thus, any process that exhibits better catalyst performance has the potential to operate at lower energy requirement and higher product yield.

Generally, the carbon nanotubes synthesized by the high–temperature electric arc or laser vaporization processes have fewer structural defects, in addition to superior mechanical and electrical properties, than the low–temperature chemical vapor deposition processes. However, the electric arc and laser ablation processes allow production of carbon nanotubes in grams quantities only, which contrast markedly with the multi–ton production requirements of most carbon nanotube applications.

The commercial scalability of the arc and laser processes have been limited so far in terms of production capacity, ease and cost of production, and scale–up constraints, due to their elaborate configuration. It appears the economical reasonable limit for scaling up the arc process has been reached, with a production rate of ~ 100 g/h of raw carbon nanotube product achieved per industrial apparatus (Moravsky, et. al., 2004).

The catalytic chemical vapor deposition process, being a low temperature process and technically simpler than the arc or laser ablation processes, is considered an economical route for the tons/day production of carbon nanotubes. The production process also show a higher selectivity to form carbon nanotubes than the arc and laser vaporization processes,

since the electric–arc discharge and laser vaporization methods result in mixtures of carbon materials (Perez–Cabero, et al., 2003).

An analysis of the chemical vapor deposition production processes reviewed based on criteria such as process operating conditions, selectivity, continuous growth, and yield showed that the high–pressure carbon monoxide (HiPCO) disproportionation and the CoMoCAT fluidized bed catalytic processes provide a commercial basis for the conceptual design of scalable carbon nanotube processes.

The high–pressure carbon monoxide (HiPCO) process is a gas–phase process that uses the floating catalyst approach, whereby the catalytic particles are formed *in situ* by thermal decomposition of the catalyst precursor. The process can be operated as a continuous process rather than a batch process by using continuous filtration to separate the carbon nanotubes containing the iron catalyst from the unreacted carbon monoxide.

Carbon nanotube formation by the HiPCO process occurs via carbon monoxide disproportionation over iron particles according to the Boudouard mechanism:

$$CO_{(g)} + CO_{(g)} \rightarrow CO_{2(g)} + C_{(CNT)}$$

Although, the detailed reaction mechanism and rate data for the catalyzed Boudouard reaction is not available, it can be inferred that the rate of the gas–phase reaction scales as a square of the carbon monoxide reactant gas partial pressure. Consequently, the use of high pressure carbon monoxide is essential for efficient carbon nanotube production, and hence, the use of a high–pressure flow reactor in the HiPCO process.

Carbon nanotubes produced by the HiPCO process contain a significant amount of iron particles (~ 5–6 atom %), formed from the decomposition of the catalyst precursor and acting as growth nucleation site. However, the iron nanoparticles are not enclosed in heavy

graphitic shells as in the arc or laser vaporization processes, and consequently, are relatively easier to remove.

A major drawback of the HiPCO process is the low rate of carbon monoxide conversion (~ 15–20 % per cycle), even at high pressure, in the Boudouard reaction. The unconverted carbon monoxide feedstock is recirculated through the reactor on a continuous basis. This feed–reaction–recycle closed configuration makes the HiPCO process amenable for easy scale–up and continuous production of carbon nanotubes in tons/day quantities. The commercialization of the HiPCO carbon nanotube production technology is presently being explored and developed at Carbon Nanotechnologies Incorporation, Houston, Texas.

Another attractive alternative to the chemical vapor deposition production processes is the catalytic decomposition of a carbon–containing molecule on a substrate supported catalyst particles. The CoMoCAT (cobalt–molybdenum catalyst) process employs this substrate–supported catalytic approach in the bulk production of carbon nanotubes. The process involves the detailed characterization of the different phases in the catalyst preparation stage to ensure selective production of carbon nanotubes.

Catalyst preparation in the CoMoCAT process involves the combination of cobalt and molybdenum metal particles on a silica support, such that the catalyst is only effective when both metals are simultaneously present with low cobalt : molybdenum ratio. When the catalytic metal particles are separated on the silica support, the catalysts are either inactive (Molybdenum alone) or unselective (Cobalt alone).

The synergistic effect between the cobalt and molybdenum results in high selectivity (better than 80 %) of the Co–Mo catalysts towards carbon nanotube production by CO disproportionation at 700–950 ^{0}C and a total pressure ranging from 1 to 10 atm:

$$2CO_{(g)} \rightarrow C_{(CNT)} + CO_{2(g)}$$

Carbon monoxide disproportionation reaction is exothermic and can be limited by equilibrium at the high temperatures required to activate CO on the catalyst. Thus, high carbon monoxide pressures are used in order to mitigate the temperature effect and enhance the formation of carbon nanotubes.

Resasco, et. al., 2002, reported that the extent of Co–Mo interaction is a function of the Co : Mo ratio in the catalyst, such that at low Co : Mo ratios, Co interacts with Mo in a superficial cobalt molybdate–like structure, whereas at high ratios, it forms a non interacting Co_3O_4 state. The formation of carbon nanotubes is enhanced at low Co : Mo ratios because the Co : Mo interaction inhibits the cobalt sintering that usually results at the high temperatures required for the growth process.

The CoMoCAT process is amenable to the development of continuous operations and large–scale production involving fluidized bed reactors. In the fluidization regime, a large quantity of silica supported Co–Mo catalyst powder, with high specific surface area, would be in good contact with the carbon monoxide reactant gas. Consequently, large quantities of carbon nanotubes can be produced.

Furthermore, the residence times of the carbon nanotube can be controlled more accurately in a fluidized bed reactor, and the activity of the catalyst utilized sufficiently to ensure high conversion. The optimum utilization of the catalyst particles is essential for large–scale production, since the catalysts are usually costly.

Due to the fluidized state of the carbon monoxide feed gas and the solid catalyst particles in the reactor, there is efficient heat and mass transfer between the carbon nanotube agglomerates and the bulk gas phase in a fluidized bed reactor, to get temperature control as

needed to more–closely approach equilibrium. The carbon nanotubes formed in the CoMoCAT process remain mixed with the silica–supported catalyst particles, and hence, it requires an effective sequence of purification processes to remove these impurities.

In the next section, the relevant literatures for carbon nanotube purification are reviewed, and various post–synthesis purification processes for carbon nanotubes are discussed.

2.5 PURIFICATION OF CARBON NANOTUBES

The carbon nanotubes, as produced by the various synthesis techniques, contain impurities such as graphite nanoparticles, amorphous carbon, smaller fullerenes, and metal catalyst particles. These impurities have to be separated from the carbon nanotubes material before it can be used for applications such as composites, nanoelectronics, etc.

Consequently, various purification techniques have been devised in other to improve the quality and yield of carbon nanotubes obtained. These purification methods employed in the post–syntheses processing of carbon nanotubes include oxidation, acid treatment, annealing, micro filtration, ultrasonication, ferromagnetic separation, functionalization and chromatography techniques.

A detailed literature review of these purification processes is carried out in this section. The purification procedures and process operating conditions such as pressure, temperature, and the procedures used are stated also.

2.5.1. Oxidation

The first technique devised to purify carbon nanotubes relied on the oxidation behavior of carbon nanotubes at temperatures greater than 700 ^{0}C in air or in pure oxygen. However, the main shortcoming of the oxidative treatment is the high likelihood of the

carbon nanotubes being oxidized during impurities oxidation. Thus, the carbon nanotube yield from the oxidative treatment in air/oxygen is usually poor.

In terms of carbon nanotube reactivity, using thermo gravimetric analysis, the onset of carbon nanotube weight loss begins at about 700 ^{0}C, with significant decrease in mass thereafter. The carbon nanotubes are oxidized completely to carbon monoxide and carbon dioxide at about 860 ^{0}C (Terrones, 2003). Figure 2.10 compares the weight loss versus temperature for inner core deposits (containing carbon nanotubes and polyhedral particles) and fullerenes.

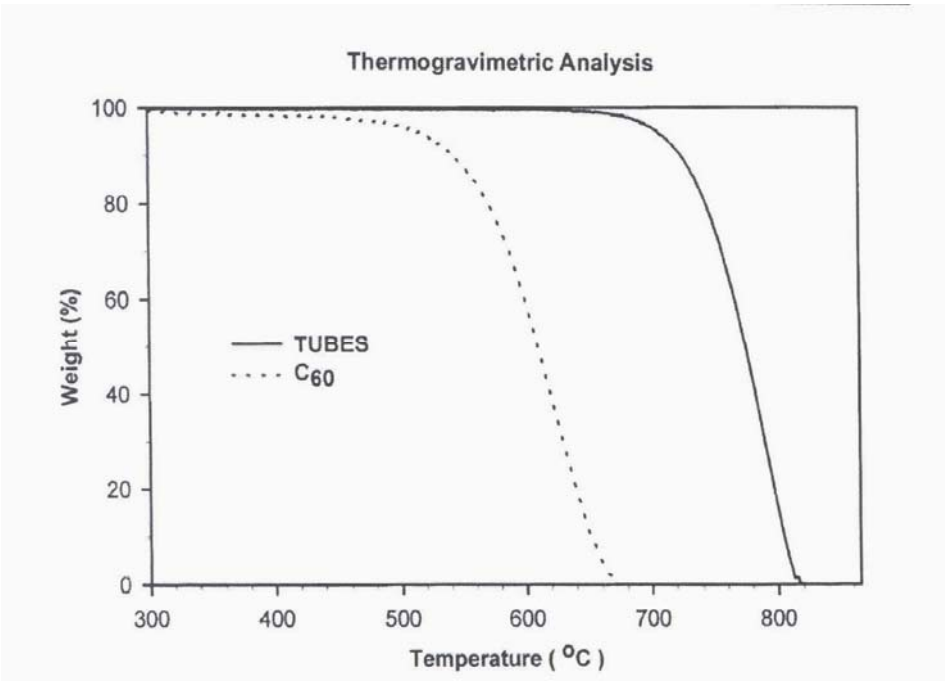

Figure 2.10 Thermo Gravimetric Analyses of MWNT and C_{60}, from Terrones, 2003

The oxidative treatment of carbon nanotubes in air/oxygen removes carbonaceous impurities, such as amorphous carbon, and helps to expose the catalytic metal surface enclosed in the carbon nanotube for further purification techniques. A summary of the literature for the oxidative purification treatment of carbon nanotubes is presented below.

• Park, Y. S., Choi, Y. C., Kim, K. S., Chung, D. C., Bae, D. J., An, K.H., Lim, S. C., Zhu, X., Y., Lee, Y. H., 2001, "High yield purification of multi-walled carbon nanotubes by selective oxidation during thermal annealing", Carbon 39, 655–661.

The purification of multi–walled carbon nanotubes, synthesized by the electric arc discharge, through thermal annealing in air is reported. The annealing apparatus consists of two quartz tubes, whereby the inner tube, which contains the MWNTs, is simply rotated by the outer tube at the rate of 30 rpm during the procedure.

The inner tube rotation allows for the as–produced MWNT samples to be evenly exposed to the surface in order to obtain uniform selective etching by different oxidation rates controlled exclusively by the annealing time.

The as–produced MWNT samples were annealed as a function of time at 760 ^{0}C under ambient air. The supply of sufficient amount of oxygen is pre–requisite in obtaining high yield during this process. Thus, with sufficient supply of air, the quality and yield of the carbon nanotubes obtained is determined by the annealing time. Yield as high as 40% has been reported.

• Chiang, I. W., Brinson, B. E., Smalley, R. E., Margrave, J. L., Hauge, R. H., 2001, "Purification and Characterization of Single–Wall Carbon Nanotubes", Journal Physical Chemistry B, 105, 1157–1161.

A procedure for the purification of laser–ablation grown single–walled carbon nanotubes, initially cleaned with nitric acid, through additional removal of catalytic metals and amorphous carbon by gas–phase oxidation is reported. The method combines acid reflux treatment with water reflux and a two–stage gas phase oxidation process.

1. Filter the starting SWNT samples, obtained as a suspension in toluene and wash with methanol to remove additional soluble residue from the nitric acid treatment.
2. The washed, filtered black residue is refluxed in water for 2–5 hours to remove any aromatic carboxylic acids.
3. Successive two–stage gas phase oxidation in 5% O_2/Ar, 1 atm mixture at 300 ^{0}C and 500 ^{0}C, followed by extraction with concentrated HCl solution, is carried to remove catalytic metals (Co and Ni) with minimal weight loss of nanotubes.
4. The sample is dried in a vacuum at 150 ^{0}C and the weight loss after each procedure determined.

The final metal content after the second gas–phase oxidation at 500 ^{0}C is about 0.1 atomic percent relative to carbon and carbon nanotube purity 99.9% has been reported.

• Chiang, I. W., Brinson, B. E., Huang, A. Y., Willis, P. A., Bronikowski, M. J., Smalley, R. E., Margrave, J. L., Hauge, R. H., 2001, "Purification and Characterization of Single–Wall Carbon Nanotubes Obtained from the Gas–Phase Decomposition of CO (HiPCO) ", Journal Physical Chemistry B, 105, 8297–8301.

A method for extracting iron metal catalyst and amorphous carbon from single–walled carbon nanotubes produced by the HiPCO process is given.

The method involves low temperature, metal catalyzed, wet air oxidation of HiPCO nanotubes to selectively remove amorphous carbon and enable extraction of iron with concentrated HCl.

The procedure is described below:

1. Low density raw HiPCO nanotubes, physically compressed onto a dry filter paper, is placed in a ceramic boat and inserted into a quartz tube furnace.
2. Gas mixture of 20% O_2 in Ar is passed through a water bubbler and over the sample at a total flow rate of 100 sccm.
3. The sample is heated to 225 ^{0}C for 18 hours followed by sonication for ~15 minutes or prolonged (overnight) stirring in concentrated HCl solution. Typically, yellowish solution results due to dissolved Fe^{3+}.
4. Single wall carbon nanotubes in the acid solution is then filtered onto a 47mm, 1μm pore Teflon membrane and washed several times with deionized water/methanol.
5. The nanotubes are dried in a vacuum oven dry at 100 ^{0}C for a minimum of 2 hours and weighed.
6. The wet air oxidation and acid extraction cycle is repeated at 325 ^{0}C for 1.5 hours and 425 ^{0}C for 1 hour.
7. After drying in the vacuum oven, the carbon nanotube sample is annealed at 800 ^{0}C in Ar for 1 hour.

The purity of the final carbon nanotubes obtained has a catalytic metal content of less than 1.0% (wt.)

• Hou, P. X., Bai, S., Yang, Q. H., Liu, C., Cheng, H. M., 2002, "Multi–step purification of carbon nanotubes", Carbon, 40, 81–85.

An efficient purification procedure for multi–walled carbon nanotubes synthesized by the floating catalyst method is presented.

The process, which involves ultrasonication, heat treatment in hot water, bromination, oxidation and acid treatment, effectively removes most of amorphous carbon, multishell carbon nanocapsules as well as metal particles from the reaction product.

The multi–step procedure is stated below:

1. The raw multi walled carbon nanotubes are first ultra–sonicated and heat treated to disperse the MWNT sample.
2. The heat treatment is followed by sample immersion in bromine water at 90 ^{0}C for 3 h.
3. The residual substance is then heated in air at 520 ^{0}C for 45 minutes.
4. The black product is soaked in 5 mol/l hydrochloric acid to remove iron particles at room temperature.
5. Finally, the sample is washed with de–ionized water and dried in an oven at 150 ^{0}C for 12 hours.

Carbon nanotubes with purity greater than 94% were obtained, while the yields of the purified material vary from 30% to 50%, depending on the oxidation time and temperature.

• **Harutyunyan, A. R., Pradhan, B. K., Chang, J., Chen, G., Eklund, P. C., 2002, "Purification of Single–Wall Carbon Nanotubes by Selective Microwave Heating of Catalyst Particles", Journal of Physical Chemistry B, 106, 8671–8675.**

A scalable method for the purification of single walled carbon nanotubes, produced by electric arc discharge, using microwave heating in air is reported.

The local microwave heating in air, coupled to the residual metal catalyst, increases significantly the local temperature, and thus, induces the combustion of the amorphous carbon shell layer to form CO/CO_2.

This microwave–processing step is then followed by a mild acid treatment to remove most of the catalytic metals in the sample.

The two–stage purification procedure is summarized below:

1. The carbon nanotube sample, placed in a quartz tube, is subjected to microwave heating at 2.5 GHz, 150 W, and 500 ^{0}C in flowing air (100 sccm) for 20 minutes.
2. The sample is subsequently refluxed in 4 M HCl for 6 hours to dissolve and remove the residual catalysts (nickel and yttrium).

The purified single–walled carbon nanotubes reportedly contained a residual metal level lower than 0.2 wt%.

• **Vasquez, E., Georgakilas, V., Prato, M., 2002, "Microwave–assisted purification of HiPCO carbon nanotubes", Chemical Communications, 20, 2308–2309.**

Microwave heating of raw HiPCO produced single walled carbon nanotubes under ambient air conditions followed by treatment with concentrated hydrochloric acid is reported.

The procedure is stated below:

1. Compact HiPCO nanotube sample, obtained after soaking raw nanotubes in diethyl ether and evaporating the solvent, is placed in a Erlenmeyer flask.
2. The flask is then subjected to microwave heating using a power of 80 W.
3. The flask is removed from the oven after 5 seconds: the mass shaken gently with a spatula and subjected to microwave heating. This process is repeated for a total of 5 min of microwave irradiation.
4. The sample is then washed with concentrated HCl (35%): a typical yellow color develops due to dissolved Fe^{3+}. The mixture is centrifuged and the solution removed.
5. The solid residue, washed with water, methanol, and ethyl ether, is then dried.
6. The entire procedure (microwave treatment and acid treatment) is repeated twice to ensure the maximum removal of iron catalytic particles.

This purification method led to a decrease from about 26%w/w iron (Fe) content in the raw carbon nanotubes product to ~7% w/w iron (Fe) content in the purified carbon nanotubes.

2.5.2. Acid Treatment

Acid treatment of single walled carbon nanotubes is used to remove metal catalyst from the reaction products. The process is usually preceded by a mild oxidation or sonication step, to clear and expose the metal surface, followed by the solvation of the metal catalyst on exposure to an acid, while the carbon nanotubes remain in suspended form. A review of the literature on the acid treatment purification method is given below.

• Rinzler, A. G., Liu, J., Dai, H., Huffman, C.B., Rodriguez–Macias, F. J., Boul, P. J., Lu, A. H., Heymann, D., Colbert, D. T., Lee, R. S., Fischer, J. E., Rao, A. M., Eklund, P. C., Smalley, R. E., 1998, "Large–scale purification of single – wall carbon nanotubes: process, product, and characterization", Applied Physics A, 67, 29–37.

A readily scalable purification process capable of handling single wall carbon nanotubes, produced by dual pulsed laser vaporization technique in large quantities, is reported.

The procedure followed in the purification process is stated below:

1. The SWNT sample is refluxed in 2–3 M nitric acid (typically 1 liter of acid per 10 g of raw carbon nanotube) for 45 hours.
2. The resultant black solution following the reflux is centrifuged, leaving a black sediment at the bottom of the centrifuge bottle and a clear, brownish–yellow supernatant acid, which is decanted off.
3. The sediment is re–suspended in de–ionized water to remove any trapped acid, centrifuged and the supernatant liquid decanted. The washing/centrifugation cycle is repeated until the nearly neutral solution (black) is obtained.
4. After the acid treatment, the sediment, dispersed in NaOH solution (pH 10) containing 0.5 vol. % Triton–X 100 by ultrasonic agitation (in a bath sonicator) for ~1 hour, is filtered by hollow–fiber, cross–flow filtration (CFF).
5. The single wall carbon nanotube collected after CFF is subjected further to successive oxidizing acid treatments. The first being treatment with a 3:1 mixture of sulfuric (98%) and nitric (30%) acids, stirred and maintained at 70 ^{0}C in an oil bath for 20–30 minutes.
6. This acid treatment is followed by another cross flow filtration cycle.
7. The final acid treatment is done with a 4:1 mixture of sulfuric acid (98%) and hydrogen peroxide (30%), following the same procedure as with the sulfuric/nitric acid mixture.
8. The carbon nanotube sample obtained from the final CFF is then dried in a vacuum at 1,200 ^{0}C.

This acid treatment purification procedure resulted in a 10–20 wt.% carbon nanotube yield, while the purity of the material obtained was not stated.

2.5.3. Ultrasonication

This purification technique involves the separation of particles due to ultrasonic vibrations whereby agglomerates of different nanoparticles undergo forced vibration and become more dispersed. The separation efficiency is dependent on the surfactant, solvent and reagent used. Some of the literature reviews of processes using the ultrasonication purification method are presented below.

• Shelimov, K. B., Esenaliev, R. O., Rinzler, A. G., Huffman, C. B., Smalley, R.E., 1998, "Purification of single–wall carbon nanotubes by ultrasonically assisted filtration", Chemical Physics Letters, 282, 429–434.

The development of an ultrasonically–assisted filtration method for the purification of single wall carbon nanotubes, produced by the laser–vaporization process is reported. Ultrasonication applied to the sample during filtration maintains the material in suspension and prevents cake formation on the surface of the filter.

The purification procedure is as stated below:

1. The as–produced SWNT soot, suspended in toluene, is filtered to extract soluble fullerenes. The toluene–insoluble fraction is then re–suspended in methanol.
2. The suspension is then transferred into a 47 mm filtration funnel. A 25.4 mm ultrasonic horn is inserted to the funnel and placed ~ 1 cm above the surface of a polycarbonate track–etched filter membrane (0.8 μm pore size).
3. The horn, driven by 600 W, 20 kHz ultrasonic processor, has a tip amplitude vibration in air of 33 μm, while the filtration funnel is cooled to ~0 ^{0}C to increase cavitation efficiency.
4. Methanol is added continuously to the filtration funnel to maintain a constant filtration volume
5. After filtration, the residue is washed with 6 M sulfuric acid to remove traces of any metal (mostly titanium) introduced into the sample from the ultrasonic horn.

The ultrasonically assisted filtration purification method produced carbon nanotube materials with purity greater than 90%, with yields ranging between 30–70%.

• Hernadi, K., Fonseca, A., Nagy, J. B., Bernaerts, D., Riga, J., Lucas, A., 1996, "Catalytic synthesis and purification of carbon nanotubes", Synthetic Metals, 77, 31–34.

Carbon nanotube synthesis by catalytic decomposition of acetylene over supported Co/silica and Fe/silica, and the purification of the as produced carbon nanotubes by a combination of ultrasound and various chemical treatments is reported. The combined

physical and chemical purification procedures employed in separating carbon nanotubes from the other impurities are presented below:

1. The sample is treated with dilute nitric acid (30%) for 4 hours to dissolve any metallic particle (Co/Fe), through which the nanotubes are bonded to the catalyst support. The sample is then filtered, washed with distilled water and acetone.
2. The nanotube sample is sonicated in a mixture of organic solvents: n–hexane, acetone and iso–propanol (ratio 1:1:1) for 10 minutes at 40% output power.
3. The mixture is allowed to settle for 20 minutes, followed by decantation. The sedimentation period allows for the separation of the carbon nanotubes and the catalyst support particles.
4. This treatment is repeated five times and the liquid phases collected together.
5. The carbon nanotube suspension obtained after sonication is evaporated to dryness and the black product collected.
6. Sample hydrogenation is then carried out at 900 ^{0}C for 4.5 hours to remove any amorphous carbon contamination in the final product.

The purity and yield of carbon nanotubes generated from this purification technique were not specified.

2.5.4. Mechanical Purification

In this purification technique, the catalytic metal particles enclosed in the carbon nanotube graphitic shells are mechanically removed. The mechanical separation process, based on the ferromagnetic properties of the metal particles, is reviewed below.

• Thien–Nga, L., Hernadi, K., Ljubovic, E., Garaj, S., Forro, L., 2002, "Mechanical Purification of Single–walled Carbon Nanotube Bundles from Catalytic Particles", Nano Letters, 2(12), 1349–1352.

A purification method, based on mixing the as produced SWNT suspension, containing metal particles, with inorganic nanoparticles in an ultrasonic bath, which mechanically separates the ferromagnetic particles from their graphitic shells, is reported.

The separated ferromagnetic particles can then be trapped by permanent magnetic poles, followed by a chemical treatment to obtain high purity SWNTs. The purification process is summarized below:

1. The SWNT sample is initially suspended in either in soap solution or toluene, and subsequently dispersed in various solvents such as N, N–dimethyl formamide or 30% nitric acid.
2. Nanoparticles powder (zirconium oxide or calcium carbonate), insoluble in the given medium, is then added to the suspension to form a slurry.
3. The resultant slurry is sonicated with a horn tip and adjustable power for 24 hours. The ultrasonic bath mechanically removes the ferromagnetic particles from their

graphitic shells and the magnetic particles are trapped with permanent magnets

4. The sample is subjected to an additional acid treatment in order to dissolve the nanoparticles powder, $ZrO_2/CaCO_3$.
5. The purified SWNT is filtered and subjected to high–temperature heat treatment to remove any defect.

A schematic diagram of the magnetic purification apparatus is shown in Figure 2.11.

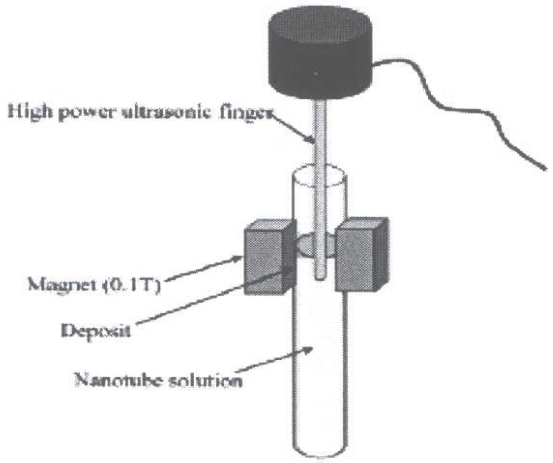

Figure 2.11.Schematic Diagram of SWNT Magnetic Purification Apparatus, from Thien–Nga et al, 2002.

2.5.5. Functionalization

This purification technique is based on making single walled carbon nanotubes more soluble than the impurities by attaching functional groups to the tubes, and thus, it becomes easier to separate the carbon nanotubes from such insoluble catalytic impurities.

The functionalization technique consists of the following steps (Georgakillas et al, 2002):

(a) Organic functionalization of the as produced nanotubes,

(b) Purification of the soluble functionalized nanotubes, and

(c) Removal of the functional groups and recovery of purified carbon nanotubes

A literature review of the purification technique is summarized below:

• **Georgakilas, V., Voulgaris, D., Vasquez, E., Prato, M., Guldi, D. M., Kukovecz, A., Kuzmany, H., 2002, "Purification of HiPCO Carbon Nanotubes via Organic Functionalization", Journal American Chemical Society, 124, 14318–14319**.

The purification of HiPCO carbon nanotubes via organic functionalization is presented. The procedure is as follows:

1. The as produced SWNT is modified based on 1, 3 dipolar cycloaddition of azomethineylides in dimethylformamide (DMF) suspension. This enhances the solubility of the functionalized SWNT while the catalytic metal particles remain insoluble. However, amorphous carbon impurities also dissolve in the DMF suspension.
2. The modified carbon nanotubes are further separated from the amorphous carbon through a slow precipitation process that takes place by adding diethyl ether to a chloroform solution of functionalized SWNT.
3. This process is repeated about three times with the recovered soluble material whereas, the solid residue, containing the amorphous carbon impurities, is discarded.
4. The purified SWNTs are recovered by thermal treatment at 350 ^{0}C, which eliminates the functional group attachments, followed by annealing to 900 ^{0}C.

The iron content in the as produced SWNT and functionalized SWNT as measured by atomic absorption analysis was ~26% Fe (w/w) and ~0.4% Fe (w/w) respectively

2.5.6. Microfiltration

This purification technique, based on size or particle separation, separates coexisting carbon nanospheres (CNS), metal nanoparticles, polyaromatic carbons and fullerenes from single walled carbon nanotubes, grown by pulsed laser vaporization. It involves the suspension of CNS, metal nanoparticles and SWNTs in an aqueous solution using a cationic surfactant. The carbon nanotubes are subsequently trapped using a membrane filter, while other nanoparticles (metal nanoparticles and carbon nanospheres) pass through the filter (Bandow et al., 1997).

• **Bandow, S., Rao, A. M., Williams, K.A., Thess, A., Smalley, R. E., Eklund, P. C., 1997, "Purification of Single–Wall Carbon Nanotubes by Microfiltration", Journal Physical Chemistry B, 101, 8839–8842.**

The details of a microfiltration technique used to separate SWNTs from other impurities present in the soot synthesized by the laser vaporization method are reported.

The procedure, which is described below, separates the as produced SWNTs into three separate fractions without the use of acid, heat, or oxidative treatment.

1. The as prepared sample is soaked in organic solvents, such as CS_2, to dissolve and extract polyaromatic carbons and fullerenes.
2. The CS_2 insoluble fractions are then trapped in a filter, while the CS_2 soluble fractions that passed through the filter are collected for further analysis.
3. The insoluble solids trapped by the filter paper are removed, and dispersed in aqueous solution of 0.1% cationic surfactant (benzalkonium chloride), using ultrasonic agitation, to separate the CNS and metal particles from the SWNTs.
4. Microfiltration: After sonication for 2 hours, the suspension is forced through a micro filtration cell using an overpressure (~2 atm) of N_2 gas.
5. A stirring unit is used to prevent surface contamination of the membrane filter by the unfiltered components.
6. Most of the CNS and metal nanoparticles pass through the filter while the SWNTs and a small amount of residual CNS and metal particles are caught on the filter.
7. The micro filtration process is repeated for three cycles to minimize the amount of residual CNS and metal nanoparticles trapped between the SWNT ropes.
8. Both the CNS and SWNT fractions are soaked in ethanol to wash out the surfactant. The suspension (CNS fraction) that passed through the membrane filter is then dried in a rotary evaporator at 60 ^{0}C.

The individual weight percentages of the separated fractions are 6, 10, and 84 wt. % for the CS_2 extracts, CNS and SWNTs respectively. The purity of the SWNTs in the final purified fraction is in excess of 90 wt. %.

However, it should be emphasized that the carbon soot containing low SWNT yield should be pre–treated by centrifugation for effective purification by the microfiltration process.

A schematic diagram of a micro filtration cell is shown in Figure 2.12.

2.5.7. Chromatography

This technique is mainly employed in separating small amounts of single walled carbon nanotubes into fractions with small size (length and diameter) distribution. The process involves running single walled carbon nanotubes over a column with porous material, through which the carbon nanotubes will flow.

The columns used are High Performance Liquid Chromatography–Size Exclusion Chromatography (HPLC–SEC) and Gel Permeation Chromatography (GPC). A review of the chromatography purification technique is outlined below:

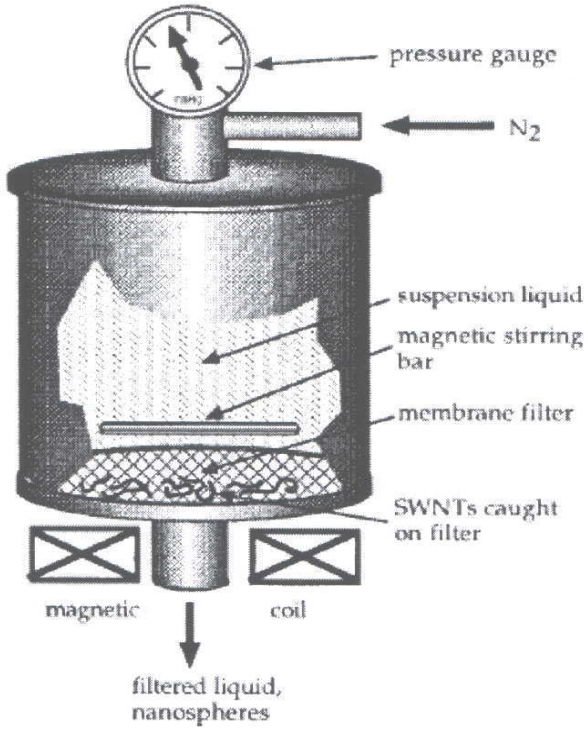

Figure 2.12. Schematic Diagram of a Micro Filtration Cell: SWNTs and small amount of nanoparticles are caught on the filter, from Bandow et al, 1997.

• Niyogi, S., Hu, H., Hamon, M. A., Bhowmik, P., Zhao, B., Rozenzhak, S. M., Chen, J., Itkis, M. E., Meier, M. S., Haddon, R. C., 2001, "Chromatographic Purification of Soluble Single–Walled Carbon Nanotubes (s–SWNTs)", Journal American Chemical Society, 123, 733–734.

The separation of soluble SWNTs (s–SWNTs) from particulate matter, which is solubilized in a nanotube dissolution process, in a gel permeation chromatographic (GPC) column, is reported.

The SWNT sample, prepared by a modified electric arc technique is initially purified, shortened and polished prior to being run over GPC column.

The procedure involved is summarized below:

1. Shortened SWNTs are covalently functionalized with octadecylamine to give soluble carbon nanotubes and are dissolved in tetrahydrofuran (THF)
2. The solution is run over a gel permeation chromatographic column, (Styragel HMW7) with THF as the mobile phase.
3. The chromatogram, obtained using a photodiode array detector (PDA), shows the elution of two bands.
4. Two main fractions are obtained: the first fraction contains semi–conducting SWNT material, whereas the second fraction contains nanoparticles and amorphous carbon.

It is estimated that 50% of the s–SWNTs in the soot is recovered from the first fraction eluted from the column. In addition, this technique offers the promise of sorting single walled carbon nanotubes by length, diameter and chirality.

2.6 EVALUATION OF PURIFICATION METHODS:

The review of the various purification processes carried out above showed a multi–step approach to the post–synthesis treatment of carbon nanotubes. The processes reviewed usually combine two or more purification techniques.

Typically, an initial mild oxidation step is used to remove amorphous carbon and expose catalyst metal particles to the surface. This mild oxidation step is usually followed by treatment in strong acids to dissolve the catalyst particles or treatment in organic solvents to dissolve fullerenes. The carbon nanotube product is subsequently filtered off and washed with alcohol or deionized water to any remove residual acid. The carbon nanotube products are then dried at elevated temperatures (800–1,200 ^{o}C).

However, since each of the purification techniques alter the structural surface of the carbon nanotube, extreme caution should be exercised when any of these purification processes is being considered (Ajayan, 2000). The focus of any purification process adopted should be one that removes the carbonaceous impurities and the catalyst metal particles, with nil or minimal impact on the carbon nanotubes.

2.7. SUMMARY

The various laboratory–scale carbon nanotube synthesis techniques and post–synthesis purification processes have been reviewed in this chapter. The most frequently used methods for producing carbon nanotubes rely on the condensation of a carbon vapor or on the catalytic action of transition metal particles on carbon vapor. Typical catalytic transition metals, reported with high carbon nanotube yield are iron, nickel, and cobalt.

For most of the production processes reviewed, the large–scale synthesis of carbon nanotubes are reported in grams/day quantity. However, the use of carbon nanotubes in both present and future applications requires tons/day production capacity. Consequently, the development of low cost, large–volume and commercially scalable carbon nanotube processes is essential in order to maximize the potential and benefits of these novel materials.

In addition to the tons/day production requirement, most applications require high purity carbon nanotube materials. The carbon nanotubes as produced usually contain impurities, such as amorphous carbon and catalyst particles, which have to be removed. The basis of any post–synthesis purification processes adopted should be to remove the amorphous carbon, catalyst metal and other impurities, with minimal or no impact on the carbon nanotube structure.

The criteria for selecting a scalable production process include low cost and high purity product. The process operating conditions, such as temperature, pressure, catalyst performance, process selectivity, reactant conversion, and availability of raw materials and catalysts, are considered in selecting a process to be used for commercial design.

Among the different production processes reviewed, the catalytic chemical vapor deposition processes appear to be the most promising to be used as a basis for industrial scale–up. Furthermore, the catalytic chemical vapor deposition processes, which operate at moderate temperatures, have been reported to be the most selective in carbon nanotube formation (Perez–Cabero, et al., 2003).

Two catalytic chemical vapor deposition processes were selected as a basis for the conceptual design of scalable carbon nanotube processes based on the selection criteria

discussed previously. The selected processes are the high–pressure carbon monoxide disproportionation reaction over iron catalytic particle clusters (HiPCO process), and the catalytic disproportionation of carbon monoxide or hydrocarbon over a silica supported cobalt–molybdenum catalyst (CoMoCAT process).

These two processes will be used as the basis for the development of continuous large–scale production processes in the next chapter. A detailed conceptual design of these production processes, involving the feed/raw material preparation section, the synthesis/reaction section and post–synthesis purification section, will be discussed in the next chapter. The material, energy, reaction rate and equilibrium models for the process units and streams will be formulated there also.

Companies that manufacture equipment for carbon nanotube synthesis, as well as other nanotechnology companies are listed in Table 2.5. Seocal and Atomate specialize in the fabrication of chemical vapor deposition reactors for nanotube, nanowire and diamond synthesis, whereas Simagis Nanotubes produces software for automated analysis of nanotube images. The other companies listed apply nanotechnology to the chemicals and advanced materials market.

Table 2.5 Companies Making Equipment for Carbon Nanotube Synthesis and Other Nanotechnology Companies

Company	Activity
Seocal	CVD Reactors for carbon nanotube and diamond synthesis
Atomate	CVD Reactors for carbon nanotube and nanowire synthesis
Simagis Nanotubes	Software for automated analysis of nanotube images
Adelan	Develops nanoparticle catalysts for fuel cells
Admatechs	Produces nanopowders with applications as fillers in resins
Akzo Nobel	Produces and market products containing nanoparticles
Altair Nanotechnologies	Produces nanoparticles applied in coatings, paints and fillers
Apyron Nanotechnologies	Makes nanoscale catalysts for methanol production
Argonide Nanomaterials	Produces nanopowder based bio– and non–adhesive ceramic nanowires, artificial bone and nanofibers for filtration
Atofina	Produces nanocomposites using carbon nanotubes
Honeywell	Produces a nylon–based nanocomposites using nanoclays
Engelhard	Uses nanoscale particles as catalysts for oxidation reactions
Hybrid Plastics	Produces nanocomposites from silsesquioxanes (POSS)
BASF	Developing nanocubes for hydrogen storage in fuel cells
DuPont	Use of nanoparticles for thick films and nanocomposites
General Electric	Produce nanotubes, nanowires, nanocomposites, etc
Johnson Matthey	Engages in R & D on nanopowders for catalyst and coatings
Samsung	Catalytic nanoparticles for fuel cells, and coatings

CHAPTER THREE: PROCESS MODEL DEVELOPMENT AND FORMULATION

The various processes for the production and purification of carbon nanotubes were discussed in Chapter Two. For these processes, there are hundreds of published articles of laboratory–scale experiments describing the synthesis and purification of carbon nanotubes in grams/day quantities. However, most potential carbon nanotube applications require tons/day of high purity production volume.

The objective of this research is to identify scalable carbon nanotube production processes and develop conceptual designs for low cost, bulk production (tons/year) of high purity carbon nanotubes from these processes. The selected processes are designed as industrial scale processes, and the process models for these processes are formulated.

From an analysis of the various laboratory–scale production processes reviewed in Chapter Two, two catalytic chemical vapor deposition processes: HiPCO and CoMoCAT processes, were identified as potentially scalable processes. These processes were selected based on criteria such as: low cost, high product yield and selectivity, catalyst performance, continuous processes, and moderate growth temperatures.

The design capacity for the proposed carbon nanotube production processes is 5,000 metric tons/year. This capacity is based on the projected size of a carbon nanofiber production plant operated by Grafil, a California–based Mitsubishi Rayon subsidiary (C & EN, 2005). The plant capacity estimates also compares reasonably with the production capacities of other carbon fiber production facilities. Table 3.1 shows the production capacities of some carbon fiber manufacturing facilities.

The conceptual design of these production technologies begins with the development of a process flow diagram (PFD) and the formulation of a process model based

Table 3.1 Production Capacity for Carbon Fiber Facilities (Traceski, F.T., 1999)

Manufacturer	Facility	Capacity (lb/year)
Amoco	Greenville, SC	2,200,000
Zoltek	St Louis, MO	3,500,000
Akzo Fortafil	Rockwood, TN	5,000,000
Mitsubishi Grafil	Sacramento, CA	2,000,000
Aldila	Evanston, WY	2,500,000

on the process flow diagram (PFD). The process model is a set of balance equations, rate equations and equilibrium relationships that describe the material and energy transport, as well as the chemical reactions of the process. In the process models, each process unit and process stream included in the process flow diagram has a name and a description.

This chapter describes the conceptual design of two, 5,000 metric tons/year carbon nanotube production processes, and the formulation of process models for the selected production processes. In developing these conceptual designs and formulating the process models, the processes would first be described. Subsequently, the material and energy balances, the rate equations, and the equilibrium relationships in the process models will be established.

3.1 PROCESS MODEL DEVELOPMENT

A process model of a chemical engineering process is defined by a set of material and energy balance equations, rate equations and equilibrium relationships. These equations are used to formulate a mathematical relationship between the different plant units and process streams involved in the production process.

The material and energy balance equations for each process unit are given in a table. The material balance equations typically include the overall material balance and the component material balance equations. The mass balance for each component is formulated based on conservation laws. The steady state material balance for a component is written as:

$$F_{inlet}^{(i)} - F_{outlet}^{(i)} + F_{gen}^{(i)} = 0 \qquad (3.1)$$

where *i* represents the name of component, and *F* stands for mass flow rate in kg/hr. The overall mass balance is the summation of all component material balances.

The steady state overall energy balance is formulated based on the first law of thermodynamics. Assuming that the changes in kinetic and potential energy are neglected, the energy balance equation is, (Felder and Rousseau, 1986):

$$\Delta H = Q - W \qquad (3.2)$$

where Q is the net heat added to the system; W is the work done by the system on the surroundings; and ΔH is the change in enthalpy between input and output streams. Thus,

$$\Delta H = \sum_{output} n^{(i)} h^{(i)} - \sum_{input} n^{(i)} h^{(i)} \qquad (3.3)$$

The reference condition for enthalpy is the elements that constitute the reactants and products at 298 K and the non–reactive molecular species at any convenient temperature. The specific enthalpy, $h_k^{(i)}$ of component, *i*, in stream *k*, can be expressed as a function of temperature (McBride et al, 2002):

$$h_k^{(i)}(T) = R * (a_1^{(i)} T + \frac{a_2^{(i)}}{2} T^2 + \frac{a_3^{(i)}}{3} T^3 + \frac{a_4^{(i)}}{4} T^4 + \frac{a_5^{(i)}}{5} T^5 + \frac{b_1^{(i)}}{T}) \text{ kJ/kgmol} \qquad (3.4)$$

where a_1, a_2, a_3, a_4, a_5 and b_1 are thermodynamic coefficients; T is temperature (K); and R is gas constant (kJ/kgmol K). The detailed enthalpy function for the component species in the

HiPCO and CoMoCAT carbon nanotube production processes are given in Appendix A.

3.2 DESCRIPTION OF HiPCO CARBON NANOTUBE PROCESS

The carbon nanotube production process used in this design is based on the high–pressure carbon monoxide (HiPCO) process developed by a team of research scientists at Rice University. The HiPCO process converts carbon monoxide into single walled carbon nanotubes and carbon dioxide, at high pressures (30–50 bar), and at temperatures between 1,273 K and 1,473 K on iron catalyst particles.

The design capacity for the HiPCO process is 5,000 metric tons/year (595 kg/hr) of 97 mol% carbon nanotubes. The overall conversion of gaseous carbon monoxide to carbon nanotubes in the HiPCO process is 20 mol%. The production system uses a four–step process that produces carbon nanotubes and carbon dioxide from carbon monoxide and iron pentacarbonyl catalyst precursor.

The process flow diagram is shown in Figure 3.1, while the process units and process streams description are listed in Table 3.2 and Table 3.3 respectively. The process consists of four sections, which are the feed preparation section, the reactor section, the separation/purification section and the absorber section.

3.2.1 Feed Preparation Section

The process equipment used in this section include a mixer (V–101), a gas–fired heater (E–101) and a gas compressor (C–101). The gas streams entering the mixer (V–101) consist of 2,637 kg/hr fresh CO (SR01) and 627 kg/hr iron pentacarbonyl vapor (SR02). Iron pentacarbonyl is vaporized into the CO stream by passing pure CO stream through a liquid $Fe(CO)_5$–filled bubbler (Nikolaev, 2004). The mixer blends the fresh CO feed (SR01) and iron pentacarbonyl vapor (SR02) streams together at 303 K.

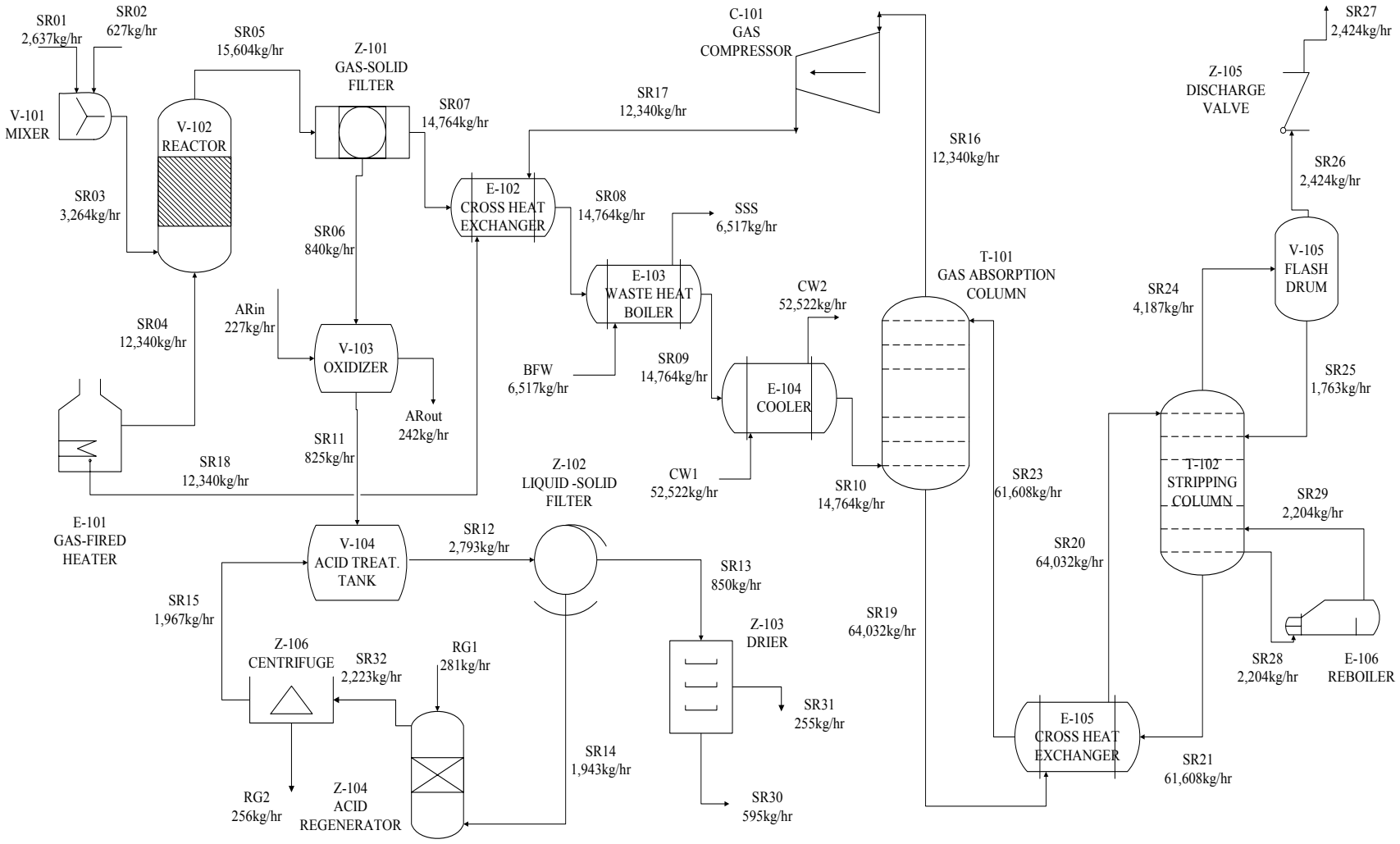

Figure 3.1 Process Flow Diagram for the HiPCO Carbon Nanotube Production Process

Table 3.2 Process Units for the Carbon Nanotube HiPCO Process Model (Refer to Figure 3.1, the Process Flow diagram)

Name of Unit	Description
Heat Exchangers	
E–101	CO Feed Recycle Gas–Fired Heater
E–102	Reactor Gas Effluent–Feed Recycle Cross Heat Exchanger
E–103	Waste Heat Boiler
E–104	Heat Exchanger Water Cooler 1
E–105	Solute Rich-Lean Solvent Cross Heat Exchanger
E–106	Kettle Reboiler
Process Vessels	
V–101	Mixer
V–102	High Pressure Flow Reactor
V–103	Air Oxidizer
V–104	Acid Treatment Tank
V–105	Flash Drum
T–101	Gas Absorption Column
T–102	Gas Stripping Column
C–101	Gas Compressor
Z–101	Gas–Solid Filter
Z–102	Liquid–Solid Filter
Z–103	Product Drier
Z–104	Acid Regeneration Column
Z–105	Vent/Discharge Valve
Z–106	Centrifuge Separator

Table 3.3 Process Streams in the HiPCO Process Model (Refer to Figure 3.1)

Name of Stream	Description of Process Streams
SR01	Fresh CO Feed to Mixer (V–101)
SR02	Iron Pentacarbonyl Vapor to Mixer (V–101)
SR03	Mixed CO and $Fe(CO)_5$ Feed to Reactor (V–102)
SR04	CO Feed Recycle from Heater (E–100) to Reactor (V–102)
SR05	Effluent Stream from Reactor (V–102) to Filter 1 (Z–101)
SR06	Carbon Nanotube from Filter 1 (Z–101) to Oxidizer (V–103)
SR07	Gas Stream from Filter 1 (Z–101) to Heat Exchanger (E–102)
SR08	Mixed Gas Stream from E–102 to Waste Heat Boiler (E–103)
SR09	Mixed Gas Stream from E–103 to Cooler 1 (E–104)
SR10	Gas Stream from Cooler 1 (E–104) to Gas Absorber (T–101)
SR11	Carbon Nanotube from V–103 to Acid Treatment Tank (V–104)
SR12	Carbon Nanotube Slurry from V–104 to Filter 2 (Z–102)
SR13	Carbon Nanotube from Filter 2 (Z–102) to Drier (Z–103)
SR14	Acid Stream from Filter 2 (Z–102) to Regenerator (Z–104)
SR15	Acid Stream from Centrifuge (Z–106) to Acid Tank (V–104)
SR16	CO Gas Stream from Absorber (T–101) to Compressor (C–101)
SR17	CO Recycle from Compressor (C–101) to Exchanger (E–102)
SR18	CO Recycle from Exchanger (E–102) to Heater (E–101)
SR19	CO_2–Rich MEA Solution from T–101 to Exchanger (E–105)
SR20	CO_2–Rich Solution from E–105 to Stripping Column (T–102)
SR21	Lean MEA Solution from T–102 to Exchanger (E–105)
SR23	Lean MEA Solution from E–105 to Gas Absorber (T–101)
SR24	CO_2 Vapor from T–102 to Flash Drum (V–105)
SR25	Recovered MEA Solution from V–105 to Stripper (T–102)
SR26	CO_2 Gas from Flash Drum (V–105) to Vent Valve (Z–105)
SR27	CO_2 Gas from Z–105 to Other Processes
SR28	Lean MEA Solution from Stripper (T–102) to Reboiler (E–106)
SR29	MEA Vapor from E–105 to Stripping Column (T–102)
SR30	Carbon Nanotube from Product Drier (Z–103) to Storage or Sales
SR31	Water Evaporated from Carbon Nanotube Product from Z–103
SR32	Mixed Product Stream from Z–104 to Centrifuge (Z–106)
Utility Streams	
CW1	Cooling Water Inlet Stream of Heat Exchanger Cooler 1 (E–104)
CW2	Cooling Water Outlet Stream of Heat Exchanger Cooler 1 (E–104)
BFW	Boiler Feed Water to Waste Heat Boiler (E–103)
SSS	Saturated Steam from Boiler (E–103) to Reboiler (E–106)
ARin	Air Inlet Stream to Oxidizer (V–103)
ARout	Air Outlet Stream from Oxidizer (V – 103)
RG1	Fresh Feed to the Acid Regeneration Column(Z–104)
RG2	Waste Stream from Centrifuge Separator (Z–106)

The gas stream (SR03) leaving the mixer, which consists of carbon monoxide saturated with iron pentacarbonyl vapor, is sent to the flow reactor (V–102) at 303 K and atmospheric pressure. The unconverted CO reactant is completely recovered and recycled to the reactor from the compressor. The gas compressor (C–101) supplies 12,340 kg/hr CO feed recycle (SR04) at 1,323 K and 450 psia.

The CO recycle is passed through two heat exchanger units (E–102 and E–101) successively to increase its temperature. The cross heat exchanger (E–102) increases the temperature of the CO recycle stream from 551 K (SR17) to 707 K (SR18); while the gas–fired heater (E–101) increases the temperature from 707 K (SR18) to 1,323 K (SR04). The sample calculations for the mass flow rates of the iron pentacarbonyl feed, CO feed and CO feed recycle streams are given in Appendix C.

3.2.2 Reactor Section

The process units used in this section include a high–pressure reactor (V–102), a gas–solid filter (Z–101), the reactor effluent–feed recycle cross heat exchanger (E–102), the waste heat boiler (E–103), and the heat exchanger water cooler 1 (E–104). The mixed gas stream (SR03) containing CO saturated with iron pentacarbonyl vapor, and the CO feed recycle (SR04), from the heater, are passed through the flow reactor (V–102).

In the reactor, the mixed stream (SR03), containing CO and $Fe(CO)_5$, is rapidly mixed and heated with the hot CO feed recycle stream (SR04). The flow reactor is modeled as an isothermal flow reactor at an operating pressure of 450 psia, and operating temperature of 1,323 K, based on laboratory experiments (Nikolaev, 2004). Upon heating, the iron pentacarbonyl vapor decomposes to iron atoms and CO according to Equation (3.5):

$$Fe(CO)_5 \xrightarrow{Heat} Fe_{(s)} + 5CO_{(g)} \qquad (3.5)$$

The iron formed from the decomposition of the iron pentacarbonyl, nucleates and form iron clusters that initiate the growth of carbon nanotubes in the gas phase, through carbon monoxide disproportionation reaction (Boudouard reaction):

$$xCO_{(g)} \xrightarrow{Fe} CNT_{(s)} + \frac{x}{2} CO_{2(g)} \qquad (3.6)$$

The stoichiometrically balanced form of Equation (3.6) based on a carbon nanotube molecule containing 3,000 carbon atoms is given by Equation (3.7), (Scott, et al, 2003):

$$6000CO_{(g)} \xrightarrow{Fe} C_{3000(s)} + 3000CO_{2(g)} \qquad (3.7)$$

Carbon nanotubes nucleate and grow in the gas phase on catalytic iron nanoparticle clusters. Growth starts when the catalyst particles are sufficiently large enough for carbon nanotube nucleation; and growth ceases when the catalyst cluster grows too large and prevents the diffusion of additional CO to the particle's surface. The growth of carbon nanotube occurs throughout the length of the reactor. The carbon monoxide disproportionation reaction over iron catalyst is slightly exothermic: $\Delta H = -172.5$ kJ/kgmol (Dateo, et al, 2002).

In this design, the conversion of CO in the flow reactor to form carbon nanotube, based on Equation (3.7), is 20 mol%, i.e., 0.20 kgmol CO reacted to form CNT per kgmol CO fed to the reactor. The conversion used is based on the optimal conversion obtained in the laboratory–scale HiPCO production process (Davis, 2005). The selectivity of the CO reactant to form carbon nanotubes, based on Equation (3.7), is 90%, i.e., 0.9 kgmol CO reacted to form carbon nanotube per kgmol CO reacted.

Amorphous carbon is formed in the reactor according to Equation (3.8):

$$2CO_{(g)} \rightarrow C_{(s)} + CO_{2(g)} \qquad (3.8)$$

The selectivity of the CO reactant to form amorphous carbon, based on Equation (3.8) is 10%, i.e., 0.1 kgmol CO reacted to form amorphous carbon per kgmol CO reacted. The selectivity values used in the HiPCO analysis are based on high TEM studies, which revealed that carbon nanotubes produced by the HiPCO process contain lower amorphous carbon overcoating in contrast to carbon nanotubes produced by the laser vaporization or arc discharge processes (Bronikowski, et. al., 2001).

The effluents stream (SR05) from the reactor contains carbon nanotube (CNT), amorphous carbon, iron particles, CO_2 and unconverted CO. The carbon nanotube formed contains residual iron particles from the thermal decomposition of iron pentacarbonyl. The carbon nanotube produced is transported out of the flow reactor by the continuous gas flow and sent to a gas–solid filter (Z–101). The gas–solid filter separates the solid products (SR06) containing carbon nanotube, residual iron and amorphous carbon from the hot, mixed carbon monoxide and carbon dioxide gas stream (SR07).

In addition to amorphous carbon impurities in the reactor product, the carbon nanotube produced in the reactor contains significant amount of residual iron nanoparticles. The residual iron content in the reactor product is up to 30% by weight of the final carbon nanotube product (Meyyappan, 2005).

Typically, these residual iron nanoparticles are encased in the carbon outer layers of the carbon nanotube produced. It is essential to remove 99.999% solids upstream of the compressor, in order to minimize erosion of turbine.

The hot, mixed–gas stream (SR07) from the gas–solid filter (Z–101) is initially cooled in the reactor–effluent/feed–recycle cross heat exchanger (E–102). The cross heat exchanger cools the gas stream from 1,323 K (SR07) to 1,223 K (SR08), and preheats the

CO feed recycle stream from 551 K (SR17) to 707 K (SR18). The mixed gas stream (SR08) from the cross heat exchanger is then passed to the waste heat boiler (E–103).

The waste heat boiler (E–103) cools the mixed gas stream from 1,223 K (SR08) to 573 K (SR09) by removing heat from the mixed gas stream to produce saturated steam. Boiler feed water (BFW) is supplied to the waste heat boiler (E–103) at 303 K, while saturated steam (SSS) is produced at 533 K and 675 psia. The saturated steam produced is used for process heating in other process units such as the reboiler and heater.

The gas stream exiting the waste heat boiler is further cooled from 573 K (SR09) to 330 K (SR10) in the heat exchanger water cooler 1 (E–104). Cooling water is supplied to the heat exchanger cooler at 303 K (CW1) and exits at 323 K (CW2). The gas stream leaving the water cooler (SR10) is then fed into the gas absorption column (T–101) as bottoms at 330 K.

3.2.3 Separation/Purification Section

The process units used in the separation/purification section include a gas–solid filter (Z–101), an air oxidizer (V–103), an acid treatment tank (V–104), a liquid–solid filter (Z–102), a product drier (Z–103), an acid regeneration column (Z–104) and a centrifuge separator (Z–106). These process units are used to separate and purify the carbon nanotube product from impurities such as amorphous carbon and iron nanoparticles.

The gas–solid filter (Z–101) separates the carbon nanotubes product from the hot gas effluent stream from the reactor. The carbon nanotubes are collected as solid residues on the surfaces of the gas–solid filter as the reactor effluent stream (SR05) flows through the filter. The solid product (SR06) collected on the filter surface contains carbon nanotubes, amorphous carbon and residual iron particles. Consequently, additional purification steps are

required to remove the amorphous carbon and residual iron particle impurities from the carbon nanotube product.

The purification of the carbon nanotube product in the HiPCO process involves a multi–step approach: oxidation, acid treatment, filtration and drying. The purification section consists of an oxidizer (V–103), in which a heated air gas stream is passed over the carbon nanotube product (SR06) collected from the filter (Z–101). The oxidation treatment is used to selectively remove amorphous carbon impurities without affecting the structural integrity of the carbon nanotube product.

In addition to the removal of amorphous carbon, the oxidation step exposes the iron nanoparticles embedded in the outer carbon layers to the nanotube surface and oxidizes the iron particles to iron oxide (Chiang, et al, 2001). Consequently, the encased iron particles, hitherto impervious to dissolution in acid solution, are easily extracted as soluble iron oxides by treatment in concentrated hydrochloric acid.

In the acid treatment tank (V–104), the oxidized carbon nanotube product (SR11) containing iron oxides, is treated with 12% hydrochloric acid (HCl) solution (Meyyappan, 2004). The iron oxide dissolves in the acid solution to form iron chloride ($FeCl_2$) and water. The ratio of the amount of iron oxide removed to the amount of HCl used is based on the reaction between iron oxide and HCl solution. However, since organometallics [$Fe(CO)_5$] are used to nucleate the carbon nanotubes produced, there will always be some iron particles in the HiPCO carbon nanotube final product. Consequently, the final carbon nanotube product contains 97 mol% carbon nanotubes and 3 mol% iron (Bronikowski, et al., 2001).

The nanotube slurry (SR12), containing the dissolved iron chloride, and carbon nanotubes is sent to the liquid–solid filter (Z–102), which separates the purified carbon

nanotube product (SR13) from the iron chloride solution (SR14). The carbon nanotube collected on the filter surface is washed several times with deionized water to remove any trace of hydrochloric acid from the carbon nanotube product. The washed, filtered and purified carbon nanotube product (SR13) is then dried at 800 K in the product drier (Z–103). The final carbon nanotube product (SR30), from the drier, is then sent to storage for packaging and sales.

The iron chloride solution (SR14) from the liquid–solid product filter is sent to an acid regeneration column (Z–104), where the hydrochloric acid solution is regenerated. The iron chloride solution is oxidized in the column to produce hydrochloric acid and iron oxide residue. The iron oxide residue produced is saturated with hydrochloric acid and is removed from the acid solution in the centrifuge separator (Z–106) (www.acidrecovery.com). The recovered hydrochloric acid (SR15) from the centrifuge is recirculated back to the acid treatment tank (V–104) for another reaction cycle.

3.2.4. Absorber Section

The process units in the absorber section include: a gas absorber (T–101), a gas stripping column (T–102), and a cross heat exchanger (E–105). Other process units include a kettle reboiler (E–106), a flash drum (V–105) and a discharge/vent valve (Z–105). The carbon dioxide produced during the CO disproportionation reaction over catalytic iron nanoparticles is absorbed in the counter–current flow of monoethanol amine (MEA) solution in the gas (CO_2) absorption column.

The mixed gas stream (SR10) from the heat exchanger water cooler (E–104), containing CO_2 and unconverted CO, enters the gas absorption column as bottoms feed at 330 K and 75 psia. The carbon dioxide is absorbed in the counter–current flow of

monoethanol amine solution (SR23) fed into the absorption column at the top. The gas stream exiting the gas absorber at the top (SR16) contains unconverted CO from the reactor.

However, since the CO feed recycle stream (SR16) recovered from the gas absorption column is not at the same pressure as the reaction pressure (450 psia), due to pressure losses at the filter, reactor, and flow losses, the CO feed recycle stream is passed through a gas compressor (C–101). The gas compressor increases the pressure of the CO feed recycle stream by adiabatic compression from 75 psia (SR16) to 450 psia (SR17).

The CO_2–rich monoethanol amine (MEA) solution (SR19) leaves the gas absorption column at the bottom at 330 K and enters the solute rich–lean solvent cross heat exchanger (E–105). The cross heat exchanger preheats the CO_2–rich MEA solution from 330 K (SR19) to 393 K (SR20). The cross heat exchange occurs between the solute–rich MEA solution (SR19) and the lean MEA bottoms stream (SR21) from the stripping column.

The preheated solute–rich monoethanol amine liquid stream (SR20) enters the gas stripping column (T–102) at the top. Carbon dioxide gas is stripped from the solute–rich monoethanol amine solution in the column by steam stripping. Saturated steam is supplied to the reboiler (E–106) for gas stripping from the waste heat boiler (E–103).

The gas stripped (SR24) from the stripping column containing CO_2 and water vapor is sent to the flash drum (V–105), where the aqueous fraction liquid carryover (SR25) is recovered and returned to the stripping column. The carbon dioxide gas stream (SR26) separated in the flash drum is either transferred from the plant to other carbon dioxide consuming processes, or discharged from the plant in form of flue gas (SR27), as long as emission standards are met. The back pressure control valve (Z–105) controls the CO_2 emission and discharge from the production plant.

The lean monoethanol amine solution (SR21) recovered in the stripping column leaves the gas stripper at the bottom, and exchanges heat with the CO_2–rich monoethanol amine solution (SR19) from the gas absorption column in the cross heat exchanger (E–105). The lean MEA solution from the stripping column enters the cross heat exchanger (E–105) at 393 K (SR21) and leaves at 330 K (SR23).

This concludes the description of the HiPCO carbon nanotube production process. The next section explains the development and formulation of the process models: material and energy balance equations, rate equations and equilibrium relationships, for the HiPCO carbon nanotube production process.

3.3 PROCESS MODEL FOR HiPCO CARBON NANOTUBE PROCESS

In order to formulate the set of material and energy balance equations that represents the process model accurately, it is essential to identify and include the main process units and components in the process model. The process units and streams to be included in the HiPCO process model are as shown in the process flow diagram (Figure 3.1), while the complete list of the process units and streams to be included in the model is given in Table 3.2 and Table 3.3 respectively.

The process units in the HiPCO process flow diagram of the can be categorized according to their functions as Heat Exchanger Network, Reactor section, and Separation section. Each of these categories will be used to explain how material and energy balance equations are developed and applied to specific process equipment in these categories.

3.3.1 Heat Exchanger Network

The heat exchanger network of the HiPCO production process, as shown in the HiPCO process flow diagram (Figure 3.1), includes: the gas–fired heater (E–101), the cross

heat exchangers (E–102 and E–105), the waste heat boiler (E–103), the gas–to–cooling water heat exchanger (E–104), and the reboiler (E–106). In these process units, there is no chemical reaction or mass transfer, and the inlet component mass flow rates equal the outlet component mass flow rates for both sides.

The energy balance requires that the enthalpy decrease in the hot side be equal to the enthalpy increase on the cold side plus any heat loss in the heat exchanger, Q_{loss}:

$$\left(H^{inlet} - H^{outlet}\right)_{hot} = \left(H^{outlet} - H^{inlet}\right)_{cold} + Q_{loss} \qquad (3.9)$$

Typically, the heat loss in a heat exchanger unit is 3–5% of the heat energy transferred in the heat exchangers (Ulrich, 1984). However, in this design, any heat loss in the heat exchangers is not considered in the energy balance calculations (i.e. $Q_{loss} = 0$). Thus, the energy balance for the heat exchanger units is given by Equation (3.10):

$$\left(H^{inlet} - H^{outlet}\right)_{hot} = \left(H^{outlet} - H^{inlet}\right)_{cold} \qquad (3.10)$$

The heat transferred in a heat exchanger, Q is directly proportional to the heat transfer area *A*, the overall heat transfer coefficient *U*, and the logarithmic mean temperature difference between the two sides, ΔT_{lm}, i.e.,

$$Q = U * A * \Delta T_{lm} \qquad (3.11)$$

where *Q* is the enthalpy change on the cold side, and given by ($Q_{loss} = 0$):

$$Q = \left(H^{outlet} - H^{inlet}\right)_{cold} \qquad (3.12)$$

In a heat exchanger network, the material and energy balance equations are quite similar for all the process units in the network. The reactor–effluent/feed–recycle cross heat exchanger (E–102) is used as an example to develop the material and energy balance equations for all the process units in the HiPCO heat exchanger network.

The process flow diagram (Figure 3.1) shows that heat is exchanged between the hot effluent gas stream (SR07) from the gas–solid filter (Z–101) and the CO feed recycle stream (SR17) from the gas compressor (C–101) in the cross heat exchanger (E–102). The material and energy balance equations for the reactor–effluent/feed–recycle cross heat exchanger (E–102) are given in Table 3.4.

In Table 3.4, F represents the mass flow rate (kg/hr), ΔH is the difference in enthalpy between out– and in–flowing streams, MW is the molecular weight, Q is the heat transferred in the cross heat exchanger, $h_k^{(i)}$ is the specific enthalpy of component 'i' in stream k respectively The stream enthalpies are calculated from the individual component specific enthalpies. The reference state for the enthalpy function is 298 K and 1 bar.

The material and energy balance equations for all the process units in the heat exchanger network of the HiPCO process flow diagram are given in Appendix B.

3.3.2 Reactor Section

The reactor system in the HiPCO process model, as shown in the process flow diagram (Figure 3.1), consists of an isothermal, high–pressure flow reactor (V–102). The process involves the disproportionation of carbon monoxide reactant over iron catalysts to form carbon nanotubes and carbon dioxide according to Boudouard reaction mechanism (Equation 3.6)

$$xCO_{(g)} \xrightarrow{Fe} CNT_{(s)} + \frac{x}{2} CO_{2(g)} \qquad (3.6)$$

The stoichiometrically balanced form of Equation (3.6) based on a carbon nanotube molecule containing 3,000 carbon atoms (Scott, et. al., 2003) is expressed as Equation (3.7):

$$6000CO_{(g)} \xrightarrow{Fe} C_{3000} + 3000CO_{2(g)} \qquad (3.7)$$

Table 3.4 Material and Energy Balance Equations for Reactor Gas Effluent–Feed Recycle Cross Heat Exchanger (E–102).

Description	Input Streams SR07: CO, CO_2, SR17: CO	Output Streams SR08: CO, CO_2, SR18: CO
Material Balances		
Overall	$F_{07} - F_{08} = 0$ $F_{17} - F_{18} = 0$	
Species	CO: $F_{08}^{(CO)} - F_{07}^{(CO)} = 0$ $F_{18}^{(CO)} - F_{17}^{(CO)} = 0$ CO_2: $F_{08}^{(CO_2)} - F_{07}^{(CO_2)} = 0$	
Energy Balances	$i = CO, CO_2; k = 07,08,17,18$	
Overall	$\Delta H = \sum_{output} F_k^{(i)} H_k^{(i)} - \sum_{input} F_k^{(i)} H_k^{(i)}$ $(\sum_i F_{18}^{(i)} H_{18}^{(i)} - \sum_i F_{17}^{(i)} H_{17}^{(i)}) - (\sum_i F_{08}^{(i)} H_{08}^{(i)} - \sum_i F_{07}^{(i)} H_{07}^{(i)}) = 0$ $H_k^{(i)}(kJ/kg) = \frac{h_k^{(i)}(kJ/kgmol)}{MW^{(i)}(kg/kgmol)}$ $h_k^{(i)}(T) = R*(a_1^{(i)}T + \frac{a_2^{(i)}}{2}T^2 + \frac{a_3^{(i)}}{3}T^3 + \frac{a_4^{(i)}}{4}T^4 + \frac{a_5^{(i)}}{5}T^5 + \frac{b_1^{(i)}}{T})\frac{kJ}{kgmol}$ $Q_{E-102} = \sum_i F_{18}^{(i)} H_{18}^{(i)} - \sum_i F_{17}^{(i)} H_{17}^{(i)}$ $Q_{E-102} - U_{E-102} A_{E-102} \Delta T_{lm} = 0$ $\Delta T_{lm} = \frac{(T_{07} - T_{18}) - (T_{08} - T_{17})}{\ln\left((T_{07} - T_{18})/(T_{08} - T_{17})\right)}$	

The operating temperature and pressure in the HiPCO flow reactor (V–102), based on the HiPCO laboratory production process, is 1,323 K and 450 psia respectively (Bronikowski, et. al., 2001).

The carbon monoxide conversion to carbon nanotubes in the flow reactor used in this design is 20 mol%, i.e., 0.20 kgmol CO converted to carbon nanotubes per kgmol CO supplied to the reactor. This conversion is based on the optimal CO conversion obtained in the HiPCO laboratory–scale experiments (Davis, 2005). The CO conversion in the reactor is based on Equation (3.7), and given by Equation (3.13):

Conversion = Moles of CO Converted / Moles of CO Fed (3.13)

Selectivity is defined as the fraction of the reactant converted that ends up as the desired product. The selectivity of the CO reactant to form carbon nanotubes and amorphous carbon, based on Equations (3.7 and 3.8), is 90% and 10% respectively. The selectivity of CO to form carbon nanotubes in the HiPCO process is high, because the carbon nanotube products contain low amounts of amorphous carbon overcoatings (Bronikowski, et al., 2001). The selectivity of the HiPCO process to form carbon nanotubes (CNT), based on Equation (3.7) is given by Equation (3.14):

Selectivity = Moles of CO reacted to form CNT/ Moles of CO reacted (3.14)

The conversion (20 mol%) and selectivity (90%) values are incorporated and used in the material and energy balances for this process unit in Appendix C.

Carbon monoxide is supplied to the reactor from the fresh CO feed stream (SR01), the CO feed recycle stream (SR04) and the CO formed as decomposition products of the iron pentacarbonyl catalyst precursor (SR02) in the reactor. The catalyst precursor decomposes upon heating to iron nanoparticle clusters and CO according to Equation (3.5):

$$Fe(CO)_{5(g)} \xrightarrow{Heat} Fe_{(s)} + 5CO_{(g)} \qquad (3.5)$$

The material and energy balance equations for the flow reactor are developed using the mass balance to describe the relationship between input and output flow rates of a process unit for each component. In the reactor, reaction rate and stoichiometric coefficients are used to formulate the material and energy balance equations. The formulation of each component mass balance is based on the law of conservation of matter.

The material and energy balances equations for the reactor are given in Table 3.5. The first two rows of Table 3.5, under material balance give the overall material balance and component material balances, whereas the row under energy balance give the overall energy balance. The component material balance equations in Table 3.5 are formulated based on the conversion, product selectivity and stoichiometric ratios of reactants and products in Equation (3.7) and Equation (3.8). Carbon monoxide is supplied to the flow reactor from three sources: the make–up CO from the mixer, $F_{03}^{(CO)}$ (2,637 kg CO/hr), CO feed recycle, $F_{04}^{(CO)}$ (12,340 kg CO/hr) and CO from the thermal decomposition of iron pentacarbonyl (448 kg CO/hr). The sample calculations are given in Appendix C.

In Table 3.5, F represents the mass flow rate (kg/hr), *conv*l is the CO conversion (20 mol%, i.e., 0.20 kgmol CO reacted to form CNT per kgmol CO fed), and *selc*l is the CO selectivity (90%, i.e., 0.90 kgmol CO reacted to form CNT per kgmol CO reacted) to form carbon nanotubes, based on Equation (3.7). The stream enthalpies, H (kJ/kg) are based on the enthalpies of the elemental species that constitute the reactants and products at their reference states: 298 K and 1 bar. The superscript 'i' and subscript 'k' refer to the component species and stream numbers respectively.

Table 3.5. Material and Energy Balance Equations for Reactor (V–102)

Description	Inlet Streams SR03: CO, $Fe(CO)_5$ SR04: CO	Outlet Stream SR05: CO, CO_2, CNT, Fe, C
Material Balances	$conv1 = 0.20$ kgmol CO Converted/kgmol CO Fed $selc1 = 0.90$ kgmol CO Reacted to CNT/kgmol CO Reacted	
Overall	$F_{05} - (F_{03} + F_{04}) = 0$	
Species	Total CO from Thermal Decomposition of $Fe(CO)_5$: $= \frac{5 kgmol CO}{1 kgmol Fe(CO)_5} * \frac{MW^{(CO)}}{MW^{(Fe(CO)_5)}} * F_{03}^{(Fe(CO)_5)}$	
CO:	$F_{05}^{(CO)} - (1 - conv1) * (F_{03}^{(CO)} + F_{04}^{(CO)}) = 0$	
CO_2:	$F_{05}^{(CO_2)} - [F_{30}^{(CNT)} * \frac{MW^{(CO_2)}}{MW^{(CNT)}} * \frac{3000 kgmol CO_2}{1 kgmol CNT}]$ $- [F_{05}^{(C)} * \frac{MW^{(CO_2)}}{MW^{(C)}} * \frac{1 kgmol CO_2}{1 kgmol C}] = 0$	
CNT:	$F_{05}^{(CNT)} - \frac{1 kgmol CNT}{6000 kgmol CO} * \frac{MW^{(CNT)}}{MW^{(CO)}} * (conv1) * (selc1) * (F_{03}^{(CO)} + F_{04}^{(CO)}) = 0$	
Fe:	$F_{05}^{(Fe)} = \frac{1 kgmol Fe}{1 kgmol Fe(CO)_5} * \frac{MW^{(Fe)}}{MW^{(Fe(CO)_5)}} * F_{03}^{(Fe(CO)_5)}$	
C:	$F_{05}^{(C)} - \frac{1 kgmol C}{2 kgmol CO} * \frac{MW^{(C)}}{MW^{(CO)}} * (conv1) * (1 - selc1) * (F_{03}^{(CO)} + F_{04}^{(CO)}) = 0$	
Energy Balance	$T_{ref} = 298K$; 1 bar; $i = CO, CO_2, CNT, Fe, C$; $k = 03,04,05$	
Overall	$\sum_i F_{03}^{(i)} H_{03}^{(i)} + \sum_i F_{04}^{(i)} H_{04}^{(i)} - \sum_i F_{05}^{(i)} H_{05}^{(i)} + Q_{V-102} = 0$ Q_{V-102} = Heat Added to Reactor $H_k^{(i)}$ (kJ/kg) is the enthalpy of component 'i' in stream, k $F_k^{(i)}$ is the mass flow rate (kg/hr) respectively	

The overall energy balance is formulated according to the first law of thermodynamics: the reactor being non–adiabatic ($Q \neq 0$), and assuming no work is done on or by the reactor (i.e. W = 0), then the steady state overall energy balance equation for multiple reactions is, (Felder, et al, 2000):

$$\sum_i F_{inlet}^{(i)} H_{inlet}^{(i)} - \sum_i F_{outlet}^{(i)} H_{outlet}^{(i)} + Q_{V-102} = 0 \qquad (3.15)$$

In Equation (3.15), the first and second term represents the total energy for components entering and leaving the reactor respectively. The third term denotes the heat added to the flow reactor. The heats of reaction terms are not required in Equation (3.15), since the elements that constitute the reactants and products are chosen as references. Consequently, the heats of reaction are implicitly included when the heats of formation of the reactants are subtracted from those of the products (Felder, et al, 2000).

At present, the reaction kinetics for carbon nanotube formation is not well understood and not available in the literature. However, CO conversion in the reactor is used to determine the generation rate of individual reaction species. The generation rate for each component is related to the total flow rate of carbon monoxide in the reactor, and the stoichiometric ratios of the components in the reaction. Furthermore, the reaction rate of a product component has a positive value and the reaction rate of a reactant component has a negative value.

3.3.3 Separation/Purification Zone

This section consists of a gas–solid filter (Z–101), a liquid–solid filter (Z–102), a gas absorption column (T–101), and a gas stripping column (T–102). Other process units include an air oxidizer (V–103), an acid treatment tank (V–104), an acid regeneration

column (Z–104), a vent valve (Z–105), and a centrifuge separator (Z–106). These process units are employed in the separation/purification of the carbon nanotube product from other reactor products, unconverted CO, amorphous carbon and residual iron particles.

The amorphous carbon impurities in the carbon nanotube produced in the reactor is removed in the air oxidizer (V–103) by selective oxidation of the carbon nanotube product in air. The residual iron particles embedded in the carbon outer layers gets oxidized to iron oxide, which is extracted by dissolution in 12% hydrochloric acid solution.

The unconverted CO is recovered and recycled back to the flow reactor, while other process streams, such as HCl, used for metal extraction, and MEA solution, used for CO_2 absorption are continuously recovered and recycled back for re–use in the production process.

a). Gas–Solid Filter (Z–101)

There are two product filters used for the separation and purification of the carbon nanotube product. The first one is a continuous gas–solid filtration unit (Z–101), which removes the solid particles (SR06) entrained in the gaseous effluent stream (SR05) from the reactor. The solid product, thus separated, contains carbon nanotube, amorphous carbon and residual iron particles.

The material and energy balance equations for the gas–solid filter (Z–101) are given in Table 3.6. The first two rows give the overall and component material balances, while the last row gives the overall energy balance for the streams associated with the gas–solid filter. The material and energy balance equations for the liquid–solid filter (Z–102), which are similar to the balance equations for the gas–solid filter (Z–101), are given in Appendix B.

Table 3.6 Material and Energy Balance Equations for Gas–Solid Filter (Z–101)

Description	Inlet Stream SR05: CO, CO_2, CNT, Fe, C	Outlet Stream SR07: CO, CO_2 SR06: CNT, Fe, C
Material Balances		
Overall	$F_{05} - (F_{06} + F_{07}) = 0$	
Species	CO: $F_{07}^{(CO)} - F_{05}^{(CO)} = 0$ CO_2: $F_{07}^{(CO_2)} - F_{05}^{(CO_2)} = 0$ CNT: $F_{06}^{(CNT)} - F_{05}^{(CNT)} = 0$ Fe: $F_{06}^{(Fe)} - F_{05}^{(Fe)} = 0$ C: $F_{06}^{(C)} - F_{05}^{(C)} = 0$	
Energy Balances	$i = CO, CO_2, CNT, Fe$; $k = 05,06,07$	
Overall	$T_{05} = T_{06} = T_{07}$	

b) Air Oxidizer (V–103)

The carbon nanotube product formed in the reactor contains impurities such as amorphous carbon and residual iron nanoparticles. Typically, the residual iron particles are embedded in the outer carbon layers that make the metal particles impervious to dissolution in acid solutions (Chiang, et al, 2001). Subsequently, the carbon nanotubes collected from the gas–solid filter (Z–101) is sent to an air oxidizer (V–103) for the oxidation of the amorphous carbon and residual iron particles.

The carbon nanotube product (SR06) is selectively oxidized in an air/argon mixture to remove amorphous carbon and expose the residual metal particles, without damaging the structural integrity of the carbon nanotubes produced. The selective gas–phase oxidation in air converts the iron particles to iron oxide, and the amorphous carbon to carbon dioxide. The oxidation of the iron particle to iron oxide is given by Equation (3.16):

$$Fe_{(s)} + O_{2(g)} \rightarrow FeO_{(s)} \qquad (3.16)$$

The expansion of the metal particles due to the lower density of the oxide breaks the outer carbon shells open and exposes the metal (Chiang, et. al., 2001). The exposed iron particles are subsequently removed as iron oxides by dissolution in 12% hydrochloric acid solution (Meyyappan, 2004). The ratio of the amount of iron oxide removed to the amount of hydrochloric acid used is based on the reaction between iron oxide and hydrochloric acid. The carbon nanotube slurry (SR12) leaving the acid treatment tank (V–104) is then passed through the liquid–solid filter (Z–102), which separates the purified carbon nanotube product (SR13) from the liquid stream (SR14) leaving the acid treatment tank.

However, the purified carbon nanotube product (SR13) still contains residual iron particles from the organometallics catalyst used to nucleate the carbon nanotubes produced. Typically, the final product of the HiPCO process consists of 97 mol% carbon nanotubes and 3 mol% iron particles (Bronikowski, et. al., 2001). The purified carbon nanotube product is subsequently annealed in a product drier (Z–103) at 800 K and the final product (SR30) sent to storage for packaging and sales.

c) Gas Absorption Column (T–101)

This process unit is used to separate the carbon dioxide byproduct formed during CO disproportionation over iron catalysts from the unconverted CO feed recycle. In this

design, the carbon dioxide contained in the mixed gas stream (SR10) is completely absorbed by the counter–current flow of monoethanol amine (MEA) solution (SR23). The carbon monoxide in the mixed stream (SR10) is considered as an inert gas, and thus, flows upwards in the column without any loss.

The total mass flow rate of the solute–rich monoethanol solution leaving the absorber (SR19) is counted as the sum of mass flow rates of carbon dioxide and monoethanol amine in the solution. The gas absorption column is operated isothermally at 330 K and 75 psia pressure. The material and energy balance equations for the gas absorption column (T–101) are given in Table 3.7, where MEA solution (SR23) absorbs the carbon dioxide from the mixed gas stream (SR10). In Table 3.7, *F* is the component mass flow rates (kg/hr) and *T* is the process stream temperature (K).

The CO_2 absorbed in the absorption column is steam–stripped from the MEA solution in the gas stripping column (T–102). The gas stream (SR25) leaving the stripping column, contains CO_2 and water vapor. The stripped gas stream (SR24) is sent to an isothermal flash drum (V–105), where it is flashed and separated into a vapor phase (SR26) and a liquid phase (SR25). The flashing occurs as a result of the sudden reduction in pressure from the stripping column (45 psia) to the flash drum (15 psia).

In this design, the feed stream (SR24) from the stripper undergoes perfect separation in the flash drum (V–105), such that the entire lighter component fraction (CO_2) goes to the vapor phase (SR26), while the aqueous fraction, (i.e., H_2O) goes to the liquid phase (SR25), (Douglas, 1988). The liquid condensate (SR25) recovered from the flash drum is returned to the gas stripping column, while the carbon dioxide (SR26) is sent to other carbon dioxide consuming processes.

Table 3.7 Material and Energy Balance Equations for the Gas Absorption Column (T–101)

Description	Input Streams SR10: CO, CO_2 SR23: MEA	Output Streams SR16: CO SR19: MEA, CO_2
Material balances		
Overall	$F_{16} + F_{19} - F_{10} - F_{23} = 0$	
Species	CO: $F_{16}^{(CO)} - F_{10}^{(CO)} = 0$ CO_2: $F_{19}^{(CO_2)} - F_{10}^{(CO_2)} = 0$ MEA: $F_{19}^{(MEA)} - F_{23}^{(MEA)} = 0$ H_2O: $F_{19}^{(H_2O)} - F_{23}^{(H_2O)} = 0$	
Energy Balances	$i = CO, CO_2, MEA, H_2O$; $k = 08,14,17,21$	
Overall	Isothermal Absorption Column: $T_{10} = T_{16} = T_{19} = T_{23}$ T_k is the temperature of stream, k	

The material and energy balance equations for all the process equipments in the separation/purification section of the HiPCO process model are given in Appendix B. The complete listing of the material and energy balance equations for all the process units and streams in the HiPCO process model are given in Appendix B.

This concludes the development and formulation of material and energy balance equations for the HiPCO production process. The sample calculations included in

description of the HiPCO process model are given in Appendix C. The analysis of the material and energy balance equations formulated for the HiPCO process model in this section will be given in the next chapter.

3.4 DESCRIPTION OF CoMoCAT CARBON NANOTUBE PROCESS

The CoMoCAT carbon nanotube production process, used in this study is based on a catalytic production method developed by a team of researcher scientists at University of Oklahoma. The process involves carbon monoxide decomposition over mixed cobalt–molybdenum catalyst on silica support. The reaction forms carbon nanotubes and carbon dioxide at temperatures between 973 K and 1,223 K, and total pressure ranging from 15 psia to 150 psia (Resasco et al., 2001)

The production process proposed has four steps that produce carbon nanotubes and CO_2 from the reaction of gaseous CO on silica–supported Co–Mo bimetallic catalysts. The process consists of the feed preparation section, the reactor section, the absorber section and the separation/purification section. The process flow diagram for the CoMoCAT process is shown in Figure 3.2. The description of the process units and streams, in the process flow diagram, are given in Table 3.8 and Table 3.9 respectively.

3.4.1 Feed Preparation Section

The process units in the feed preparation section include the heater (E–201) and the gas compressor (C–201). Fresh CO feed stream (SR01) at 303 K is combined with the CO feed recycle stream (SR17) at 490 K in the gas–fired heater (E–201). The temperature of the combined CO feed stream (SR02) leaving the heater is at 1,223 K, and the stream is sent to the reactor (V–201). The operating conditions in the reactor is maintained at 1,223 K and 150 psia, based on the experimental conditions in the laboratory–scale CoMoCAT process.

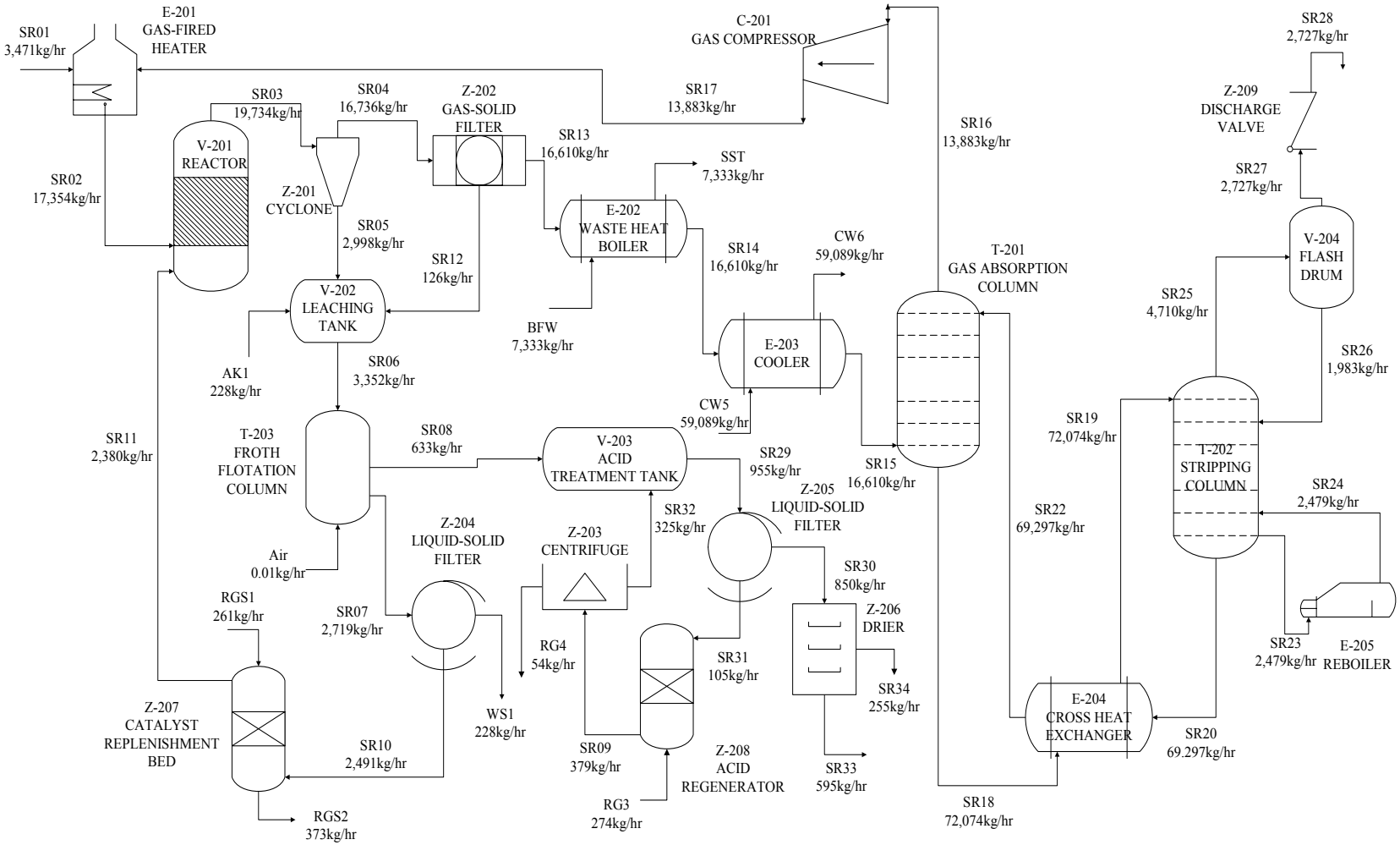

Figure 3.2 Process Flow Diagram for the CoMoCAT Carbon Nanotube Production Process

Table 3.8 Process Units for the CoMoCAT Process Model (Refer to Figure 3.2)

Name of Unit	Process Unit Description
Heat Exchangers	
E–201	CO Feed and Recycle Gas–Fired Heater
E–202	Waste Heat Boiler
E–203	Heat Exchanger Water Cooler 1
E–204	Solute Rich–Lean Solvent Cross Heat Exchanger
E–205	Kettle Reboiler
Process Vessels	
V–201	Fluidized Bed Reactor
V–202	Alkali Leaching Tank
V–203	Acid Treatment Tank
V–204	Flash Drum
T–201	Gas Absorption Column
T–202	Gas Stripping Column
T–203	Froth Flotation Column
C–201	Gas Compressor
Z–201	Cyclone Separator 1
Z–202	Gas–Solid Filter
Z–203	Centrifuge Separator
Z–204	Liquid–Solid Filter 1
Z–205	Liquid–Solid Filter 2
Z–206	Product Drier
Z–207	Catalyst Replenishment Bed
Z–208	Acid Regeneration Column
Z–209	Discharge Valve

Table 3.9. Process Streams in the CoMoCAT Process Model (Refer to Figure 3.2).

Stream	Process Stream Description
SR01	Fresh CO Feed Stream to Mixer/Heater (E–201)
SR02	Combined CO Feed Stream from Heater (E–201) to Reactor (V–201)
SR03	Effluent Stream from Reactor (V–201) to Cyclone (Z–201)
SR04	Mixed Gas Stream from Cyclone (Z–201) to Filter 1(Z–202)
SR05	Solids from Cyclone (Z–201) to Alkali Leaching Tank (V–202)
SR06	Nanotube Slurry from Tank (V–202) to Flotation Column (T–203)
SR07	Effluent Stream containing Catalysts from T–203 to Filter 2 (Z–204)
SR08	Carbon Nanotube Froth from T–203 to Acid Dissolution Tank (V–203)
SR09	Mixed Stream from Acid Regenerator (Z–208) to Centrifuge (Z–203)
SR10	Spent Catalysts from Filter 2 (Z–204) to Regeneration Bed (Z–207)
SR11	Fresh Co–Mo Catalysts from Bed (Z–207) to Reactor (V–201)
SR12	Entrained Solids from Filter 1 (Z–202) to Leaching Tank (V–202)
SR13	Mixed Gas Stream from Filter 1 (Z–202) to Waste Heat Boiler (E–202)
SR14	Mixed Gas Stream from E–202 to Water Cooler 1 (E–203)
SR15	Gas Stream from Cooler 1 (E–203) to Gas Absorber (T–201)
SR16	CO Recycle Stream from Absorber (T–201) to Gas Compressor (C–201)
SR17	CO Feed Recycle from Compressor (C–201) to Heater (E–201)
SR18	CO_2–Rich Amine (MEA) Solution from T–201 to Exchanger (E–204)
SR19	CO_2–Rich MEA Solution from E–204 to Stripping Column (T–202)
SR20	Lean MEA Solvent from Stripper (T–202) to Exchanger (E–204)
SR22	Lean MEA Solvent from Exchanger (E–204) to Absorber (T–201)
SR23	Lean MEA Solvent from Stripper (T–202) to Reboiler (E–205)
SR24	MEA Vapor from Reboiler (E–205) to Gas Stripper (T–202)
SR25	Stripped CO_2 Vapor from Stripper (T–202) to Flash Drum (V–204)
SR26	Recovered MEA Solvent from Flash Drum (V–204) to Stripper (T–202)
SR27	CO_2 Gas Stream from Flash Drum (V–204) to Vent Valve (Z–209)
SR28	CO_2 Gas Discharge from Valve (Z–209) to Other Processes
SR29	Carbon Nanotube Slurry from Acid Tank (V–203) to Filter 3 (Z–205)
SR30	Carbon Nanotube Product from Z–205 to Product Drier (Z–206)
SR31	Mixed Stream from Filter (Z–205) to Acid Regenerator (Z–208)
SR32	Recovered Acid from Centrifuge (Z–203) to Acid Tank (V–203)
SR33	Carbon Nanotube from Product Drier (Z–206) to Storage/Packaging/Sales
SR34	Water Evaporated from Nanotube Product in Drier (Z–206)
Utility Streams	
AK1	Sodium Hydroxide Feed into Alkali Leaching Tank (V–202)
RGS1	High Pressure Steam to Catalyst Regeneration Bed (Z–207)
RG4	Co and Mo Oxide Residues from Centrifuge Separator (Z–203)
BFW & SST	Feed Water and Saturated Steam to and from Waste Heat Boiler (E–202)
CW5 & CW6	Cooling Water Inlet and Outlet Streams for the Water Cooler 1 (E–203)
WS1	Waste Stream from Liquid–Solid Filter 2 (Z–204)
Air	Air Feed to Froth Flotation Column (T–203)

The make–up CO feed stream (SR01) consists of 3,471 kg/hr of CO at 490 K, while the gas compressor (C–201) supplies 13,883 kg/hr of CO feed recycle (SR17) to the heater at 490 K and 150 psia. The combined CO feed stream (SR02) is fed into the fluidized bed reactor (V–201) at 1,223 K and 150 psia. The sample calculations for the make–up CO feed stream (SR01) and the CO recycle feed stream (SR17) are given in Appendix C.

3.4.2. Reactor Section

The reactor section consists of a fluidized bed reactor (V–201), the cyclone separator (Z–201), the gas–solid filter (Z–202), the waste heat boiler (E–202) and the heat exchanger water cooler (E–203). In the fluidized bed reactor, the combined CO feed stream (SR02) from the heater is reacted on silica–supported bimetallic cobalt–molybdenum catalysts (SR11), at operating temperature and pressure of 1,223 K and 150 psia. Carbon nanotubes are formed by the CO decomposition over Co–Mo catalysts, according to the Boudouard reaction:

$$xCO_{(g)} \longrightarrow C_{(CNT)} + \frac{x}{2} CO_{2(g)} \qquad (3.6)$$

The stoichiometrically balanced form of Equation (3.6) based on a carbon nanotube molecule containing 3,000 carbon atoms is given by Equation (3.17), (Scott, et al, 2003):

$$6000CO_{(g)} \xrightarrow{SiO_2 / Co / Mo} C_{3000(s)} + 3000CO_{2(g)} \qquad (3.17)$$

In this design, the conversion of CO in the fluidized bed reactor to form carbon nanotube, based on Equation (3.17), is 20 mol%, i.e., 0.20 kgmol CO reacted to form CNT per kgmol CO fed to the reactor. The carbon monoxide selectivity in the CoMoCAT process to form carbon nanotubes, based on Equation (3.17), is 80%, i.e., 0.8 kgmol CO reacted to form CNT per kgmol CO reacted (Resasco, et al, 2001).

Amorphous carbon is formed in the fluidized bed reactor (V–201) according to Equation (3.18):

$$2CO_{(g)} \rightarrow C_{(s)} + CO_{2(g)} \qquad (3.18)$$

The selectivity of the CO reactant to form amorphous carbon, based on Equation (3.18) is 20%, i.e., 0.2 kgmol CO is converted to CNT per kgmol CO reacted.

The effluent stream (SR03) from the reactor contains carbon nanotubes and amorphous carbon, grown and attached to the silica–supported bimetallic catalysts, carbon dioxide and unconverted carbon monoxide. The effluent stream is initially passed through a cyclone separator (Z–201). The cyclone separates the solid catalyst particles (SR05) from the hot mixed–gas stream (SR04).

The gas stream from the cyclone, containing CO, CO_2, and solid catalyst particle carryover, is passed through a gas–solid filter (Z–202) to remove any solid catalyst entrainments from the gas stream. The entrained solids (SR12) collected by the filter are sent to the alkali leaching tank (V–202).

The hot, gas stream (SR13), from the gas–solid filter (Z–202), is sent through a waste heat boiler (E–202). The waste heat boiler cools the mixed–gas stream from 1,223 K (SR13) to 573 K (SR14). In the process, boiler feed water supplied at 303 K (BFW) is converted to saturated steam at 533 K (SST). The saturated steam produced in the waste heat boiler is used for steam stripping in the stripping column and/or for other heating requirements.

The mixed–gas stream (SR14) leaving the waste heat boiler is passed into the water cooler (E–203), where water cools the mixed–gas stream from 573 K (SR14) to 330 K (SR15), the required inlet temperature of the gas absorber. Cooling water is supplied to the

cooler at 303 K (CW5), and leaves the water cooler at 323 K (CW6). The mixed gas stream from the water cooler, (SR15) is fed to the gas absorber (T–201) bottom at 330 K.

3.4.3. Absorber Section

In the absorber section, the carbon dioxide in the bottoms feed (SR15), from the water cooler, is absorbed in the counter–current flow of monoethanol amine solution (SR22) fed in at the top of the absorption column. The unconverted CO gas stream (SR16) which is not absorbed, leaves the gas absorber at the top and is sent to the gas compressor (C–201). The gas compressor increases the CO recycle gas pressure from 75 psia (SR16) to 150 psia (SR17). The CO feed recycle is subsequently recirculated to the gas–fired heater (E–201), where it is combined with fresh CO feed (SR01) and heated to 1,223 K.

The solute–rich MEA solution (SR18) leaving the gas absorber at the bottom is passed to the solute–rich – lean solvent cross heat exchanger (E–204), where it is preheated by the lean MEA solution (SR20) recovered from the stripping column. The cross heat exchange occurs between the solute–rich MEA solution (SR18) and the lean monoethanol amine solution (SR20) from the stripping column. The solute–rich MEA solution (SR19) enters the top of gas stripping column (T–202) at 393 K. Carbon dioxide gas is steam stripped from the solute–rich solution in the gas stripper. Saturated steam is supplied to the reboiler (E–205) for gas stripping from the waste heat boiler (E–202).

The carbon dioxide (SR25) thus stripped, leaves the stripping column at the top and is sent to the flash drum (V–204) where any liquid entrainment in the vapor stream is recovered and returned to the gas stripping column. The CO_2 gas stream (SR27) which is flashed and separated in the flash drum, is either transferred from the carbon nanotube process to other carbon dioxide consuming processes, or discharged from the plant in form

of flue gas (SR28), as long as emission standards are met. The backpressure control valve (Z–209) discharges the carbon dioxide from the plant.

The lean monoethanol amine solution (SR20) recovered in the gas stripping column leaves the stripping column at the bottom and exchanges heat with the solute–rich monoethanol amine solution (SR18), from the gas absorption column, in the cross heat exchanger (E–204). The lean monoethanol amine solution enters the cross heat exchanger at 393 K (SR20) and leaves at 330 K (SR22).

3.4.4. Separation/Purification Section

The carbon nanotubes produced in the fluidized bed reactor are grown on and remain attached to the silica–supported bimetallic catalysts. In order to separate and purify the carbon nanotube product from the silica–supported, cobalt–molybdenum bimetallic catalysts, the froth flotation purification process is employed.

The process involves the use of inorganic surfactant, and air as a medium of separating the carbon nanotube from the silica–supported bimetallic catalysts. However, the purity of carbon nanotubes produced by the froth flotation process is 80% (Pisan, et al, 2004). Since the carbon nanotubes still contain residual metal particles after the flotation process, additional purification steps are required to increase the purity of the final product closer to 100%.

The carbon nanotube product, containing residual Co and Mo particles, is dissolved in 12% hydrochloric acid (HCl) solution. The ratio of the amount of residual Co and Mo metals removed to the amount of HCl used is based on the reaction between the residual Co/Mo metals and HCl. The treatment of the nanotubes product in 12% HCl improves the purity of the final nanotube product to 97 mol% CNT (Resasco, et. al, 2001).

The silica–supported solid catalyst (SR05) from the cyclone separator (Z–201) is sent to the alkali leaching tank (V–202), where it is washed with 2M sodium hydroxide solution (Resasco, et al, 2001). The sodium hydroxide solution (AK1) is used to break the carbon nanotubes–supported catalysts interaction by silica leaching. The treatment with sodium hydroxide breaks the carbon nanotube–silica attachments, without removing the cobalt–molybdenum metals present on the silica substrate.

The carbon nanotube slurry (SR06) from the alkali leaching tank, which contains the detached carbon nanotubes, silica supports, residual cobalt and molybdenum metals, is passed into the froth flotation column (T–203), filled with an organic surfactant. Typical organic surfactants used in the froth flotation purification process include non–ionic surfonic–24-7 (Pisan, et al., 2004).

Air is used as a medium of separation in the froth floatation column, such that air bubbled through the column at rates high enough, traps the carbon nanotubes at the air–water interface as a result of the reduced surface tension at the surfactant surface. Carbon nanotubes (SR08), trapped at the air–water interface, and washed with deionized water, is separated from the surfactant and sent to an acid treatment tank (V–203).

The residual metal catalytic particles in the carbon nanotube product from the froth flotation column is dissolved and extracted with 12% hydrochloric acid solution (SR32). In the acid treatment tank, the residual cobalt and molybdenum catalysts react with hydrochloric acid solution to form soluble cobalt chloride and molybdenum chloride respectively. The carbon nanotube slurry (SR29) is then passed through a liquid–solid filter (Z–205). The liquid–solid filter separates the purified carbon nanotube product (SR30) from the liquid stream (SR31).

The carbon nanotube product (SR30) is then sent to the product drier (Z–206), where it is annealed at 800 K. The purity of the final carbon nanotubes product, obtained after acid dissolution and filtration, is 97 mol% carbon nanotubes, 1.5 mol% cobalt metal and 1.5 mol% molybdenum metal particles (Resasco, et al, 2001). The final carbon nanotube product (SR33), from the drier, is then sent to storage for packaging and/or sales.

The liquid stream (SR31) from the filter (Z–205) is sent to an acid regeneration column (Z–208), where hydrochloric acid is recovered from the metal chloride solution. Hydrochloric acid is regenerated from the oxidation of the metal chlorides solution in the acid regenerator column. The cobalt and molybdenum oxides produced in the acid regenerator are removed from the hydrochloric acid in the centrifuge separator (Z–203). The recovered acid solution is subsequently recycled to the acid treatment tank (V–203) for another reaction cycle.

The silica–supported catalysts slurry (SR07) from the froth flotation column is passed through another liquid–solid filter (Z–204), where the spent, supported catalyst particles are collected. The spent, supported catalyst particles (SR10) collected on the filter, are sent to a catalyst regeneration bed (Z–207) for catalyst regeneration.

The catalysts are replenished by adding cobalt and molybdenum particles to make up for the cobalt and molybdenum losses in the final product and during the acid purification step. The regenerated catalysts (SR11) are then recirculated back into the fluidized bed reactor for another reaction cycle.

The waste stream (WS1) from the liquid–solid filter (Z–204), which contains process fluids, such as the organic surfactant, and sodium hydroxide, is sent to a solvent recovery unit, where the organic surfactant is recovered and recirculated for re–use.

This concludes the description of the CoMoCAT carbon nanotube production process. The development and formulation of the CoMoCAT process model: the material and energy balance equations, the rate equations and equilibrium relationships, for the process equipments and process streams will be discussed in the next section.

3.5 PROCESS MODEL FOR CoMoCAT CARBON NANOTUBE PROCESS

The model formulation for the CoMoCAT carbon nanotube process involves the development of material and energy balance equations, chemical rate equations and transport equations to establish the mathematical relationship between the various plant units and process streams. These material and energy balance equations are derived from conservation and chemical equilibrium laws.

The process model for the CoMoCAT process includes the material and energy balance equations for process units such as the mixer/heater, fluidized bed reactor, cyclone separator, gas–solid filter, liquid–solid filters, waste heat boiler, heat exchanger water cooler, kettle reboiler and a cross heat exchanger. Other process units in the CoMoCAT process include: gas absorption column, stripping column, a froth flotation column, a flash drum, a gas compressor, silica leaching tank, acid treatment tank, an acid regeneration column, and a product drier.

The process flow diagram for the CoMoCAT process is shown in Figure 3.3, containing the process units and process streams included in the process model. The complete listing and description of these process units and process streams in the CoMoCAT process model are given in Table 3.8 and Table 3.9 respectively. The process units can be classified according to their functions as: Heat Exchanger Network, Reaction Section, Absorber Section, and Separation/Purification Section.

3.5.1 Heat Exchanger Network

The heat exchanger network in the CoMoCAT production process, as shown in the process flow diagram (Figure 3.2), consists of a process heater (E–201), a waste heat boiler (E–202), a cross heat exchanger (E–204), heat exchanger water cooler (E–203) and a kettle reboiler (E–205). There is neither chemical reaction nor mass transfer in these process units. The inlet component mass flow rates are equal to the corresponding outlet component mass flow rates on either side.

The energy balance constraint for these process equipment, without accounting for any heat loss in the heat exchanger equipments (i.e. $Q_{loss} = 0$) require that the decrease of the enthalpy on the hot side be equal to the increase of enthalpy on the cold side:

$$(H^{inlet} - H^{outlet})_{hot} = (H^{outlet} - H^{inlet})_{cold}$$

i.e., Energy Liberated = Energy Absorbed

The heat transferred in a heat exchanger, Q, is related to the overall heat transfer coefficient, U, the total heat transfer area, A, and the log–mean temperature difference between the two sides, ΔT_{lm}, by: $Q = U * A * \Delta T_{lm}$.

All the process units in the heat exchanger network have similar material and energy balance equations. Consequently, the material and energy balance equations, and the heat transfer equations for the waste heat boiler (E–202), are used to illustrate the formulation of material and energy balance equations for all the process units in the heat exchanger network.

The heat exchange in the waste heat boiler (E–202) occurs between the mixed gas stream (SR13) from the gas–solid filter (Z–202), and the cooling water (BFW) supplied to the waste heat boiler. The mixed gas stream flowing through the waste heat boiler is cooled

from 1,223 K (SR13) to 573 K (SR14), while the boiler feed water (BFW) supplied at 303 K is converted to saturated steam at 533 K (SST).

The material and energy balance equations for the waste heat boiler (E–202) are given in Table 3.10. The two upper rows of Table 3.10, under material balance give the overall and individual component mass balances; while the row under energy balances gives the overall energy balance and other heat transfer equations. The inlet component mass flow rates are equal to the corresponding outlet component mass flow rates in the waste heat boiler.

In Table 3.10, F represents the mass flow rate (kg/hr), H is the stream enthalpy (kJ/kg). The stream enthalpies are calculated from the individual specific enthalpies, $h_k^{(i)}$ and the corresponding molecular weight $(MW^{(i)})$. The superscript 'i' and subscript 'k' refer to the component species and stream numbers respectively. The material and energy balance equations for all the process units in the CoMoCAT heat exchanger network are given in Appendix B.

3.5.2 Reaction Section

The reactor unit in this model consists of a fluidized bed reactor (V–201). In the reactor, the CO reactant gas disproportionates over mixed cobalt–molybdenum catalysts on silica–support, to form carbon nanotubes and carbon dioxide according to Boudouard's reaction mechanism. The stoichiometrically balanced form of the Boudouard reaction, based on 3,000 carbon atoms in a carbon nanotube molecule is given by Equation (3.17), (Scott, et al., 2003):

$$6000CO_{(g)} \xrightarrow{Co/Mo/SiO_2} C_{3000} + 3000CO_{2(g)} \qquad (3.17)$$

The growth conditions in the fluidized bed reactor are: temperature 1,223K and 150 psia.

Table 3.10 Material and Energy Balance Equations for Waste Heat Boiler (E–202)

Description	Input Streams SR13: CO, CO_2 BFW: H_2O	Output Streams SR14: CO, CO_2 SST: H_2O
Material Balances		
Overall	$F_{14} - F_{13} = 0$ $F_{SST} - F_{BFW} = 0$ BFW – Boiler Feed Water SST – Saturated Steam from Waste Heat Boiler	
Species	CO: $F_{14}^{(CO)} - F_{13}^{(CO)} = 0$ CO_2: $F_{14}^{(CO_2)} - F_{13}^{(CO_2)} = 0$ H_2O: $F_{SST} - F_{BFW} = 0$	
Energy Balances	$i = CO, CO_2$; $k = 13,14$;	
Overall	Energy Liberated = Energy Absorbed $(\sum_i F_{14}^{(i)} H_{14}^{(i)} - \sum_i F_{13}^{(i)} H_{13}^{(i)}) - (F_{SST} H_{SST} - F_{BFW} H_{BFW}) = 0$ $Q_{E-202} = \sum_i F_{14}^{(i)} H_{14}^{(i)} - \sum_i F_{13}^{(i)} H_{13}^{(i)}$ $Q_{E-202} = F_{SSW} * (C_p^{(H_2O)} \Delta T + \lambda_s)$ $H_k^{(i)}(kJ/kg) = \frac{h_k^{(i)} kJ/kgmol}{MW^{(i)} kg/kgmol}$ λ_s is the latent heat of steam =2,260 kJ/kg (Luyben, et al, 1988) $Q_{E-202} - U_{E-202} A_{E-202} \Delta T_{lm} = 0$ $\Delta T_{lm} = \frac{(T_{13} - T_{SST}) - (T_{14} - T_{BFW})}{\ln\left((T_{13} - T_{SST}) / (T_{14} - T_{BFW})\right)}$	

The CO conversion to carbon nanotubes used in the fluidized bed reactor (V–201) is 20 mol%, based on the experimental studies on carbon nanotube growth by Boudouard reaction mechanism (Davis, 2005). The selectivity of the CO reactant gas to form carbon nanotubes and amorphous carbon in the CoMoCAT process, based on Equation (3.17) and Equation (3.18), is 80% (i.e., 0.8 kgmol CO converted to form CNT per kgmol CO reacted) and 20% (i.e., 0.20 kgmol CO reacted to form amorphous carbon per kgmol CO reacted) respectively. Amorphous carbon is formed in the fluidized bed reactor (V–201) according to Equation (3.18):

$$2CO_{(g)} \rightarrow C_{(s)} + CO_{2(g)} \qquad (3.18)$$

These conversion and selectivity values are incorporated and used in the material and energy balance equation for this process unit in Appendix C.

The overall energy balance is formulated according to the first law of thermodynamics. The fluidized bed reactor being non–adiabatic ($Q \neq 0$), and assuming that no work is done on or by the reactor (W = 0), then the steady state overall energy balance is given by Equation (3.19), (Felder, et al, 2000):

$$\sum_i F_{inlet}^{(i)} H_{inlet}^{(i)} - \sum_i F_{outlet}^{(i)} H_{outlet}^{(i)} + Q_{V-201} = 0 \qquad (3.19)$$

The first and second terms represent the total energy for components entering and leaving the reactor respectively. The third term denotes the generated rates of heat added to the reactor. The heats of reaction terms are not required in Equation (3.19), since the elements that constitute the reactants and products are chosen as references. Consequently, the heats of reaction are implicitly included when the heats of formation of the reactants are subtracted from those of the products (Felder, et al, 2000).

The material and energy balance equations for the fluidized bed reactor (V–201) are given in Table 3.11. The first two rows of Table 3.11, under material balance give the overall mass balance and component material balances respectively. The row under energy balance gives the overall energy balance.

In Table 3.11, F represents the mass flow rate (kg/hr), $conv2$ is the carbon monoxide conversion (20 mol%), and $selc2$ is the carbon monoxide selectivity (80%, i.e., 0.80 kgmol CO reacted to form carbon nanotubes per kgmol CO converted) to form carbon nanotubes. The stream enthalpies, H (kJ/kg) are referenced to the enthalpies of the elemental species that constitute the reactants and products at their reference states: 298 K and 1 bar. The superscript 'i' and subscript 'k' refer to the component species and stream numbers respectively.

3.5.3 Separation/Purification Section

The separation/purification section consists of a cyclone separator (Z–201), a gas–solid filter (Z–202), two gas–liquid filters (Z–204 and Z–205), and an alkali leaching tank (V–202). Other process equipments in this section include a froth flotation column (T–203), a centrifuge separator (Z–203), an acid dissolution tank (V–203), a catalyst regeneration bed (Z–207), an acid regeneration column (Z–208) and a product drier (Z–206). This process equipment is used to separate and purify the carbon nanotube product from other impurities such as amorphous carbon, residual metal particles, silica catalyst support and residual metal catalysts.

a) Cyclone Separator (Z–201): This process unit separates the bulk of the solid catalyst particles (SR05), containing the carbon nanotube product, from the effluent stream (SR03) from the reactor. The cyclone separator uses a centrifugal force generated by a spinning gas

Table 3.11. Material and Energy Balance Equations for Fluidized Bed Reactor (V–201)

Description	Inlet Streams SR02: CO SR11: Catalyst (SiO_2, *Co, Mo.*)	Outlet Stream SR03: CO, CO_2, CNT, C, *Cat.*
Material Balances	$conv2 = 20mol\%;\quad selc2 = 80\%$	
Overall	$F_{03} - (F_{02} + F_{11}) = 0$	
Species CO:	$F_{03}^{(CO)} - (1 - conv2) * F_{02}^{(CO)} = 0$	
CO_2:	$F_{03}^{(CO_2)} - \frac{3000 kgmolCO_2}{6000 kgmolCO} * \frac{MW^{(CO_2)}}{MW^{(CO)}} * (conv2) * F_{02}^{(CO)} = 0$	
CNT:	$F_{03}^{(CNT)} - \frac{1 kgmolCNT}{6000 kgmolCO} * \frac{MW^{(CNT)}}{MW^{(CO)}} * (conv2) * (selc2) * F_{02}^{(CO)} = 0$	
C:	$F_{03}^{(C)} - \frac{1 kgmolC}{2 kgmolCO} * \frac{MW^{(C)}}{MW^{(CO)}} * (conv2) * (1 - selc2) * F_{02}^{(CO)} = 0$	
Catalyst: (SiO_2, Co, Mo)	$F_{03}^{(SiO_2)} = F_{11}^{(SiO_2)};\quad F_{03}^{(Co)} = F_{11}^{(Co)};\quad F_{03}^{(Mo)} = F_{11}^{(Mo)}$	
Energy Balances	$i = CO, Cat, CO_2, CNT, C;\qquad k = 02,03,11$	
Overall	Energy In – Energy Out + Energy Generated = 0 $(F_{02}^{(CO)} H_{02}^{(CO)} + F_{11}^{(Cat)} H_{11}^{(Cat)}) - \sum_i F_{03}^{(i)} H_{03}^{(i)} + Q_{V-201} = 0$ Enthalpy, $H_k^{(i)}(kJ/kg) = \frac{h_k^{(i)}(kJ/kgmol)}{MW^{(i)}(kg/kgmol)}$ Q_{V-201} = Heat Added to Reactor $F_k^{(i)}$ is the mass flow rate of component '*i*' in stream, *k* $h_k^{(i)}$ is the specific enthalpy of component '*i*' in stream *k*	

stream to separate the solid catalyst particles from the mixed gas stream.

However, the mixed gas stream (SR04) exiting the cyclone contains CO_2, unconverted CO and solid catalyst–nanotube particle entrainment. The solid particles carryover in the gas stream depends on the cyclone efficiency. Standard cyclone proportions are given in Table 3.12.

Table 3.12 Standard Cyclone Proportions (Wark, et al., 1998)

Cyclone Diameter, D_o	
Length of Cylinder, L_1	$L_1=2D_o$
Length of Cone, L_2	$L_2=2D_o$
Height of Entrance, H	$H=D_o/2$
Width of Entrance, W	$W=D_o/4$
Diameter of Exit Diameter, D_e	$D_e=D_o/2$
Diameter of Particulate Exit, D_d	$D_d=D_o/4$

The material and energy balance equations for the cyclone separator (Z–201) are given in Table 3.13. The two rows under material balances give the overall and component species material balances around the cyclone separator. The component inlet mass flow rates equal the component outlet flow rates. The row under energy balances gives the overall energy balance for the process equipment.

b) Froth Flotation Column (T–203): This process unit employs a surfactant–based separation process using air as the key separation medium. The advantages of this separation technique include: rapid and continuous operation, low space requirement, high removal efficiency and low operation cost**.** The material and energy balance equations for the froth floatation column are given in Table 3.14.

In Table 3.14, the first two rows under material balance give the overall and component material balances whereas the row under energy balance gives the overall energy

Table 3.13. Material and Energy Balance Equations for Cyclone Separator (Z–201)

Description	Inlet Streams SR03: CO, CO_2, CNT, C, *Cat*.	Outlet Stream SR04: CO, CO_2, CNT, C, *Cat*. SR05: CNT, *Cat*.
Material Balances	Collection Efficiency, $\eta_{Z-201} = 0.96$; *Cat.*: (SiO_2, Co, Mo)	
Overall	$F_{05} + F_{04} - F_{03} = 0$	
Species	CO: $F_{04}^{(CO)} - F_{03}^{(CO)} = 0$ CO_2: $F_{04}^{(CO_2)} - F_{03}^{(CO_2)} = 0$ CNT: $F_{05}^{(CNT)} + F_{04}^{(CNT)} - F_{03}^{(CNT)} = 0$ $F_{05}^{(CNT)} = \eta_{Z-201} * F_{03}^{(CNT)}$ $F_{04}^{(CNT)} = (1-\eta_{Z-201}) * F_{03}^{(CNT)}$ Cat: $F_{05}^{(Cat)} + F_{04}^{(Cat)} - F_{03}^{(Cat)} = 0$ $F_{05}^{(Cat.)} = \eta_{Z-201} * F_{03}^{(Cat.)}$; $F_{04}^{(Cat.)} = (1-\eta_{Z-201}) * F_{03}^{(Cat.)}$ C: $F_{05}^{(C)} + F_{04}^{(C)} - F_{03}^{(C)} = 0$ $F_{05}^{(C)} = \eta_{Z-201} * F_{03}^{(C)}$; $F_{04}^{(C)} = (1-\eta_{Z-201}) * F_{03}^{(C)}$	
Energy Balances		
Overall	$T_{03} = T_{04} = T_{05}$	

Table 3.14. Material and Energy Balance Equations for Froth Flotation Column (T–203)

Description	Input Streams SR06: CNT, C, SiO_2, Co, Mo NaOH	Output Streams SR07: C, SiO_2, Co, Mo, NaOH SR08: CNT, Co, Mo
Material Balances		
Overall	$F_{07} + F_{08} - F_{06} = 0$	
Species	CNT: $F_{08}^{(CNT)} - F_{06}^{(CNT)} = 0$ C: $F_{07}^{(C)} - F_{06}^{(C)} = 0$ SiO_2: $F_{07}^{(SiO_2)} - F_{06}^{(SiO_2)} = 0$ Co: $F_{06}^{(Co)} - (F_{07}^{(Co)} + F_{08}^{(Co)}) = 0$ Mo: $F_{06}^{(Mo)} - (F_{07}^{(Co)} + F_{08}^{(Co)}) = 0$ NaOH: $F_{07}^{(NaOH)} - F_{06}^{(NaOH)} = 0$	
Energy Balances		
Overall	$T_{06} = T_{07} = T_{08}$ T_k is the temperature of stream k	

balance for the process unit. The balance equations for the other process units in the separation/purification section of the CoMoCAT model are given in Appendix B.

3.5.4 Absorption Section

This section includes the gas absorption column (T–201), gas stripping column (T–202), a flash drum (V–204) and two heat exchangers (E–204, and E–205). In the gas absorption column, the mixed gas stream (SR15) from the cooler (E–203) is contacted with the counter–current flow of monoethanol amine solution (SR22), from the top of the absorption column.

The carbon dioxide in the mixed gas stream (SR15) is completely absorbed by the monoethanol amine solution, while the unconverted CO is considered as an inert gas as it flows upwards through the absorption column. The unconverted CO (SR16) leaves the gas absorber at the top, and is sent to the gas compressor (C–201). The gas absorption column operates at an isothermal temperature of 330 K and a pressure of 75 psia.

The material and energy balance equations for the gas absorber (T–201) are given in Table 3.15. In Table 3.15, the two rows under material balances give the overall and component material balances respectively. The row under energy balance gives the overall energy balance for the isothermal gas absorption unit

The material and energy balance equations for the gas stripping column (T–202) are given in Table 3.16. The absorbed carbon dioxide in the solute–rich monoethanol amine solution is removed by steam stripping in the gas stripper. The gas stripping temperature and pressure is 393 K and 45 psia respectively. The first two rows under material balances give the overall and components material balances respectively. The overall energy balance equation for the gas stripping column is given in the last row under energy balances.

The material and energy balance equations for the process equipments in the absorber section of the CoMoCAT production process are given in Appendix B. In addition,

Table 3.15. Material and Energy Balance Equations for Gas Absorption Column (T–201)

Description	Input Streams SR15: CO, CO_2 SR22: MEA, H_2O	Output Streams SR16: CO SR18: MEA,H_2O CO_2
Material balances		
Overall	$F_{16} + F_{18} - F_{15} - F_{22} = 0$	
Species	CO: $F_{16}^{(CO)} - F_{15}^{(CO)} = 0$ CO_2: $F_{18}^{(CO_2)} - F_{15}^{(CO_2)} = 0$ MEA: $F_{18}^{(MEA)} - F_{22}^{(MEA)} = 0$ H_2O: $F_{18}^{(H_2O)} - F_{22}^{(H_2O)} = 0$	
Energy Balances	$i = CO, CO_2, MEA, H_2O$; $k = 15,16,18,22$	
Overall	$T_{15} = T_{16} = T_{18} = T_{22}$ T_k is the temperature of stream, k	

the material and energy balance equations for all the process equipments in the CoMoCAT process model are included in Appendix B.

This concludes the development and formulation of material and energy balance equations for the CoMoCAT process model. The sample calculations included in the CoMoCAT process model are given in Appendix C. The analysis of the material and energy balance equations for the CoMoCAT process model will be given in the next chapter.

Table 3.16. Material and Energy Balance Equations for Gas Stripping Column (T–202)

Description	Input Streams SR19: CO_2, MEA, H_2O SR24: MEA, H_2O SR26: H_2O	Output Streams SR25: CO_2, H_2O SR20: MEA, H_2O SR23: MEA, H_2O
Material balances	$i = CO, CO_2, MEA, H_2O$;	$k = 19,20,23,24,25,26$
Overall	$F_{19} + F_{24} + F_{26} - F_{20} - F_{23} - F_{25} = 0$	
Species	CO_2: $F_{25}^{(CO_2)} - F_{19}^{(CO_2)} = 0$ MEA: $(F_{19}^{(MEA)} + F_{24}^{(MEA)}) - (F_{20}^{(MEA)} + F_{23}^{(MEA)}) = 0$ H_2O: $(F_{19}^{(H_2O)} + F_{24}^{(H_2O)} + F_{26}^{(H_2O)}) - (F_{20}^{(H_2O)} + F_{23}^{(H_2O)} + F_{25}^{(H_2O)}) = 0$	
Energy Balances		
Overall	$Q_{T-202} = \sum_i F_{outlet}^{(i)} H_{outlet}^{(i)} - \sum_i F_{inlet}^{(i)} H_{inlet}^{(i)}$	

3.6 SUMMARY

In this chapter, the conceptual designs and development of material and energy balance equations for the HiPCO and CoMoCAT process models were discussed. The design capacity for the selected production processes is 5,000 metric tons of carbon nanotubes/year, based on plant capacities of similar carbon fiber production facilities. In the next chapter, the analysis of the material and energy balance equations will be discussed.

In addition, the mass flow rate, temperature, pressure and composition of process streams in the HiPCO and CoMoCAT process models will be evaluated. The utility requirements, energy and power requirements, preliminary design data and criteria, for the specification of process equipment in the HiPCO and CoMoCAT process models will be determined and specified, also.

CHAPTER FOUR: RESULTS FROM ANALYSIS OF HiPCO AND CoMoCAT PROCESS MODELS

The conceptual design and development of two potentially scalable carbon nanotube production technologies: HiPCO and CoMoCAT, with a proposed production capacity of 5,000 metric tons of carbon nanotubes/year were discussed in the last chapter. Furthermore, the material and energy balance equations for the selected production technologies were developed and formulated.

In this chapter, the analysis of the material and energy balance equations developed in the last chapter will be presented. The overall and component mass flow rates into and out of the process equipments in the process models will be determined and specified. In addition, preliminary design data such as temperature, pressure, material of construction (MOC), power requirements and size of the major process equipments in the process models will be specified.

4.1 ANALYSIS OF HiPCO PROCESS MODEL

Carbon nanotubes are formed from the disproportionation of carbon monoxide over catalytic iron particles. The carbon nanotube Boudouard reaction is represented by Equation (4.1):

$$xCO_{(g)} \xrightarrow{Fe} CNT_{(s)} + \frac{x}{2} CO_{2(g)} \qquad (4.1)$$

The average–sized carbon nanotube (CNT) formed in the Boudouard reaction contains 3,000 carbon atoms (Scott, et al, 2003). Hence, the stoichiometrically balanced form of Equation (4.1) is expressed by Equation (4.2):

$$6000CO_{(g)} \xrightarrow{Fe} C_{3000} + 3000CO_{2(g)} \qquad (4.2)$$

The catalytic iron particles are formed from the decomposition of iron pentacarbonyl, $Fe(CO)_5$, according to Equation (4.3):

$$Fe(CO)_{5(g)} \xrightarrow{Heat} Fe + 5CO_{(g)} \qquad (4.3)$$

The carbon nanotube product formed contains amorphous carbon and residual iron particles. The amorphous carbon reaction, with product selectivity of 10% is given by Equation (4.4):

$$2CO_{(g)} \longrightarrow C_{(s)} + CO_{2(g)} \qquad (4.4)$$

Consequently, post–nanotube synthesis purification processes, such as low–temperature oxidation in air to remove amorphous carbon, and dissolution in 12% hydrochloric acid solution to extract soluble iron oxides, are used to improve the quality of the final carbon nanotube product.

The plant capacity used in this design is 5,000 metric tons per year of 97 mol% carbon nanotubes (595 kg/hr). The proposed design is based on the production capacity of a carbon nanofiber production facility operated by Grafil, a California–based Mitsubishi Rayon subsidiary (C & EN, 2005). The stream factor, which is the fraction of time that the plant operates in a year, used in this design is 0.96 (8,400 hr/yr). This is based on the production plant being shut down for two weeks in a year for scheduled maintenance.

The process flow diagram (PFD) for the HiPCO production process is shown in Figure 4.1. The conversion of CO to carbon nanotube in the HiPCO process is 20 mol%, and the CO selectivity to form carbon nanotube used is 90%. The unconverted CO is recovered and recycled for continuous production, as shown in Figure 4.1. The description of the process units in the HiPCO process flow diagram is given in Table 4.1, while a summary of the preliminary process equipments used in the HiPCO process is given in Table 4.2.

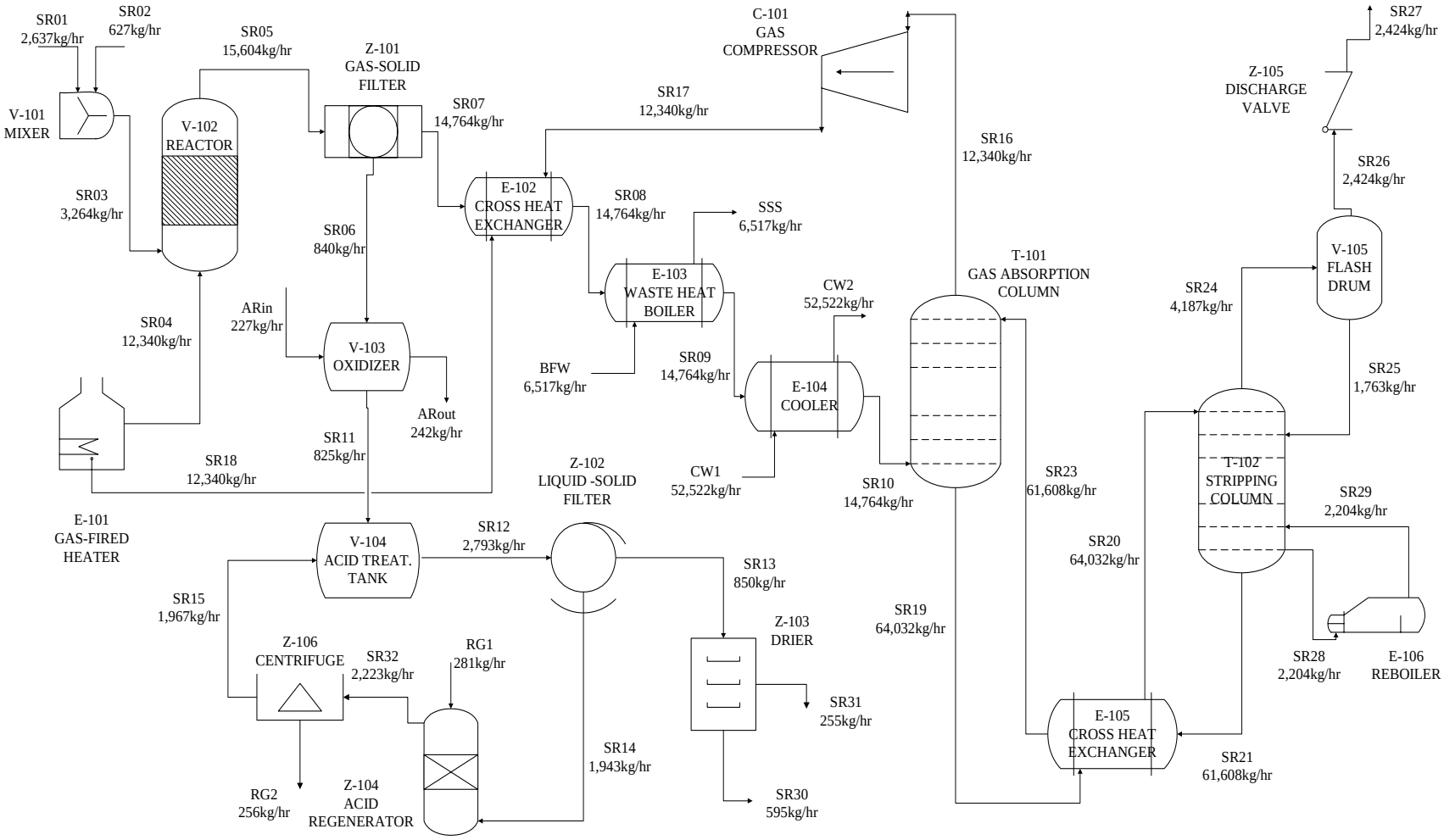

Figure 4.1 Process Flow Diagram for the HiPCO Carbon Nanotube Production Process

Table 4.1 Process Units for the Carbon Nanotube HiPCO Process Model (Refer to Figure 4.1, the Process Flow diagram)

Name of Unit	Description
Heat Exchangers	
E–101	CO Feed Recycle Gas–Fired Heater
E–102	Reactor Gas Effluent–Feed Recycle Cross Heat Exchanger
E–103	Waste Heat Boiler
E–104	Heat Exchanger Water Cooler 1
E–105	Solute Rich-Lean Solvent Cross Heat Exchanger
E–106	Kettle Reboiler
Process Vessels	
V–101	Mixer
V–102	High Pressure Flow Reactor
V–103	Air Oxidizer
V–104	Acid Treatment Tank
V–105	Flash Drum
T–101	Gas Absorption Column
T–102	Gas Stripping Column
C–101	Gas Compressor
Z–101	Gas–Solid Filter
Z–102	Liquid–Solid Filter
Z–103	Product Drier
Z–104	Acid Regeneration Column
Z–105	Discharge Valve
Z–106	Centrifuge Separator

Table 4.2. Preliminary Equipment Summary Table for HiPCO Process Model

Equipment	E–101	E–102	E–103	E–104	E–105	E–106
Type	Gas–Fired	Fixed Shell & Tube	Fixed Shell &Tube	Fixed Shell & Tube	Fixed Shell & Tube	Kettle Reboiler
Duty (kJ/hr)	26,943,517	2,349,417	24,100,964	4,395,044	23,582,209	4,261,155
Area (m^2)	215	18	116	107	92	42
Shell Side						
Max Temp (K)	1,400	707	533	323	393	533
Pressure (psia)	450	450	675	150	150	675
MOC	Nickel Alloy	Carbon Steel	Carbon Steel	Carbon Steel	Carbon Steel	Carbon Steel
Phase	Natural Gas	Gas	Steam	Liquid	Liquid	Steam
Tube Side						
Max Temp (K)	1,323	1,323	1,223	573	393	413
Pressure (psia)	450	450	450	450	150	150
MOC	Nickel Alloy	Nickel Alloy	Nickel Alloy	Carbon Steel	Carbon Steel	Carbon Steel
Phase	Gas	Gas	Gas	Gas	Liquid	Liquid

Table 4.2. (Continued)

Equipment	V–102	C–101	T–101	T–102	V–103	V–104
MOC	Nickel Alloy	Carbon Steel	Carbon Steel	Carbon Steel	Carbon Steel	Carbon Steel
Power (kW)	–	1,056	–	–	–	–
Efficiency	–	75 %	–	–	–	–
Type/Drive	–	Centrifugal	–	–	–	–
Temperature (K)	1,323	551	330	393	373	303
Pressure In (psia)	–	75	–	–	–	–
Pressure Out (psia)	–	450	–	–	–	–
Diameter (m)	0.65	–	1.1	0.7	0.97	0.9
Height (m)	7.7	–	11	11	3.9	3.6
Volume (m^3)	3.3	–	–	–	2.9	0.7
Orientation	Horizontal	–	Vertical	Vertical	Horizontal	Horizontal
Internals		–	15 Trays	15 Trays		
Pressure (psia)	–	–	–	–	–	–
	450	–	75	45	15	15

Table 4.2. (Continued)

Equipment	V–105	Z–101	Z–102	Z–103	Z–104	Z–105	Z–106
MOC	Carbon Steel	Carbon Steel	Stainless Steel	Stainless Steel	Carbon Steel	Carbon Steel	Carbon Steel
Power (MW)	–	–	–	–	–	–	–
Efficiency	–	–	–	–	–	–	–
Type/Drive	–	–	–	–	–	–	–
Temperature (K)	393	1,323	303	1,073	303	303	303
Pressure In (psia)	–	–	–	–	–	–	–
Pressure Out (psia)	–	–	–	–	–	–	–
Diameter (m)	0.8	–	–	0.97	0.5	–	1
Height (m)	3.2	–	–	3.9	2	–	0.6
Area (m^2)	–	5	9	–	–	–	–
Orientation	Horizontal	–	–	Vertical	Vertical	–	–
Internals	–	–	–	–	–	–	–
Pressure (psia)	15	450	15	15	15	15	15

In Table 4.2, there are six fixed shell and tube heat exchanger process units: the CO feed recycle gas–fired heater (E–101), two cross heat exchangers (E–102 and E–105), the waste heat boiler (E–103), the water cooler (E–104) and the kettle reboiler (E–106). The individual heat exchanger characteristics, such as material of construction, are dependent on the type and nature of the process fluids, the phase and temperature of process fluids, and the type of mechanical construction employed.

The energy required to increase the temperature of the carbon monoxide feed recycle from 707 K (SR18) to 1,323 K (SR04) in the gas–fired heater (E–101) is 26,944 MJ/hr. This energy is supplied by the heat of combustion of natural gas at 1,400 K and 450 psia. The area for heat transfer in the gas–fired heater is 215 m^2. The maximum temperature and preferred material of construction (MOC) for the shell and tube sides of the gas–fired heater is 1,400 K (nickel alloy), and 1,323 K (nickel alloy) respectively.

Heat exchange occurs between the mixed gas stream (SR07) from the gas–solid filter and the CO feed recycle stream (SR17) from the gas compressor in the cross heat exchanger (E–102). The heat duty in the cross heat exchanger (E–102) is 2,350 MJ/hr, and the heat transfer area is 18 m^2. The maximum temperature and preferred material of construction for the shell and tube sides of the cross heat exchanger is 707 K (carbon steel), and 1,323 K (nickel alloy) respectively.

The energy absorbed by the boiler feed water in the waste heat boiler (E–103) is 24,101 MJ/hr, and is used to convert the boiler feed water (BFW) supplied at 303 K to saturated steam (SSS) at 533 K. This energy is supplied by cooling the mixed gas stream exiting the cross heat exchanger from 1,223 K (SR08) to 573 K (SR09). The area for heat transfer in the waste heat boiler (E–103) is 116 m^2. The maximum temperature and material

of construction for the shell and tube sides of the waste heat boiler is 533 K (carbon steel) and 1,223 K (nickel alloy) respectively.

The energy liberated from cooling the mixed gas stream leaving the waste heat boiler from 573 K (SR09) to 330 K (SR10) in the water cooler (E–104) is 4,395 MJ/hr. Cooling water is supplied to the cooler at 303 K and leaves at 323 K. The area for heat transfer area in the water cooler (E–104) is 107 m^2. The maximum temperature and material of construction for the shell and tube sides of the water cooler is 323 K (carbon steel) and 533 K (carbon steel) respectively.

Heat exchange occurs between the solute rich MEA solution (SR19) from the gas absorption column and the lean MEA solution (SR21) from the stripping column in the cross heat exchanger (E–105). The heat duty in the cross heat exchanger is 23,582 MJ/hr, while the heat transfer area in the cross heat exchanger is 92 m^2. The maximum temperature for the shell and tube sides of the cross heat exchanger (E–105) is 393 K, and the material of construction is carbon steel.

The energy supplied by condensing steam in the reboiler (E–106) is 4,261 MJ/hr. This energy is transmitted to evaporate the aqueous fraction of the MEA solution. The area for heat transfer area in the kettle boiler (E–106) is 42 m^2. The maximum temperature and material of construction for the shell and tube sides of the reboiler is 533 K (carbon steel) and 413 K (carbon steel) respectively.

The process vessels and separators in the HiPCO preliminary equipment summary table include: the high pressure flow reactor (V–102), the gas compressor (C–101), gas absorption column (T–101), gas stripping column (T–102), and the flash drum (V–105). Other process vessels include the air oxidizer (V–103), the acid–treatment tank (V–104), the

gas–solid filter (Z–101), the liquid–solid filter (Z–102), the product drier (Z–103), the acid regeneration column (Z–104), and the centrifuge separator (Z–106).

The operating pressure and temperature in the flow reactor (V–102) is 450 psia and 1,323 K respectively. Due to the corrosive nature of the reactants, and the high operating temperature and pressure of the carbon nanotube reaction, nickel alloy is used as the material of construction for the HiPCO flow reactor. The size of the reactor, determined by geometrical scale–up of the laboratory–scale HiPCO reactor, was based on the residence time of the reactant gas in the flow reactor. The volume for the commercial scale HiPCO flow reactor was estimated to be 3.3 m^3, with a diameter of 0.65 m and a height of 7.7 m.

The gas compressor (C–101) increases the pressure of the CO feed recycle stream from 75 psia (SR16) to 450 psia (SR17) through adiabatic compression. Consequently the temperature of the CO feed recycle stream increases from 330 K (SR16) to 551 K (SR17). The compressor power, which is the rate at which the gas compressor delivers work in the process, was estimated to be 1,056 kW at 75% efficiency. Due to the high and constant delivery pressure requirements of the HiPCO process, centrifugal compressor constructed with carbon steel is selected and used for the HiPCO process.

The gas–absorption column (T–101) and gas stripping column (T–102) consists of 15 trays each, with a stage separation distance of 0.61 m and a 15% allowance for vapor disengagement and liquid sump. In the gas absorption column, carbon dioxide produced in the reactor is absorbed in a counter current flow of 20% MEA solution at 330 K and 75 psia. The unconverted CO flows up the column as an inert, and is recycled back to the reactor. The carbon dioxide absorbed in the gas absorber is stripped from the MEA solution by pure steam in the gas stripping column at 393 K and 45 psia.

The diameter and height of the gas absorption column (T–101) was estimated to be 1.08 m and 11 m respectively, whereas, the diameter and height for the gas stripping column (T–102) was calculated to be 0.70 m and 11 m respectively. Due to the moderate absorption and stripping temperatures of the HiPCO process, carbon steel is the preferred material of construction for both columns. The flash drum (V–105) is designed as an isothermal flash unit with operating temperature and pressure of 393 K and 15 psia respectively. The diameter and height of the flash drum is 0.8 m and 3.2 m respectively, with carbon steel as the preferred material of construction.

Selective low temperature oxidation of amorphous carbon and iron to carbon dioxide and iron (II) oxide is carried out in the air oxidizer (V–103) at 373 K. The diameter and height of the air oxidizer is 0.97 m and 3.9 m respectively. The equipment size was based on an average residence time of 3,600s for the carbon nanotube product in the air oxidizer (Chiang, et al, 2001).

In the acid treatment tank (V–104), residual iron oxide particles in the carbon nanotube product from the oxidizer are removed as iron chloride by dissolution in 12% hydrochloric acid solution. The ratio of the amount of HCl acid required to remove the iron oxide formed is based on the reaction between HCl and iron oxide. The diameter and length of the acid treatment tank is 0.90 m and 3.6 m respectively.

The gas–solid filter (Z–101) separates the raw carbon nanotube product (SR06) from the hot, mixed gaseous effluent (SR05) from the reactor, while the liquid–solid filter (Z–102) separates the purified carbon nanotube product (SR13) from the iron chloride solution from the acid treatment tank. The area for the gas–solid filter (Z–101) and the liquid–solid filter (Z–102) is 5 m^2 and 9 m^2 respectively.

The wet carbon nanotube product (SR13) from the liquid–solid filter is sent to the product drier (Z–103), where the residual water in the carbon nanotube product is removed. The final, dried carbon nanotube product (SR30) from the drier is subsequently sent for packaging, storage or sales. The drier size was based on an average residence time of 3600 s for the carbon nanotube product in the product drier. The diameter and height of the product drier (Z–103) is 1 m and 3.9 m respectively.

In the acid regeneration column (Z–104), the iron chloride solution is oxidized to produce hydrochloric acid and iron (III) oxide. The saturated iron oxide is removed from the regenerated hydrochloric acid in the centrifuge separator (Z–106). The hydrochloric acid recovered from the centrifuge separator is recycled back to the acid treatment tank for another reaction cycle. The diameter and height of the acid regeneration column (Z–104) is 0.5 m and 2.0 m respectively. The diameter and height of the centrifugal separator (Z–106), based on the average range of disk centrifuge sizes, are 1 m and 0.6 m respectively (Ulrich, 1984)

The flow summary for the process streams and utility streams in the HiPCO process flow diagram is given in Table 4.3 and Table 4.4 respectively. In Table 4.3, the temperature, pressure, component mass flow rates and total mass flow rates of each process streams is specified. Furthermore, the total mass flow rates, inlet and outlet temperatures of the utility streams for the gas–fired heater (E–101), waste heat boiler (E–103), water cooler (E–104), kettle reboiler (E–106) and air oxidizer (V–102) are given in Table 4.4.

The mass flow rate of fresh CO (SR01) and iron pentacarbonyl (SR02) to the mixer is 2,637 kg/hr and 627 kg/hr respectively. The iron pentacarbonyl vapor from the mixer decomposes in the reactor (V–102) to produce 448 kg/hr CO and 179 kg/hr catalytic

Table 4.3. Flow Summary Table for HiPCO Process Model

Stream No.	SR01	SR02	SR03	SR04	SR05	SR06	SR07	SR08
Temperature (K)	303	303	303	1,323	1,323	1,323	1,323	1,223
Pressure (psia)	15	15	15	450	450	15	450	450
Mass Flow (kg/hr)	2,637	627	3,264	12,340	15,604	840	14,764	14,764
Component Mass Flow Rate kg/hr								
CO_5	2,637	–	2,637	12,340	12,340	–	12,340	12,340
$Fe(CO)_2$	–	627	627	–	–	–	–	–
CO	–	–	–	–	2,424	–	2,424	2,424
MEA_2O	–	–	–	–	–	–	–	–
H	–	–	–	–	–	–	–	–
HCl	–	–	–	–	–	–	–	–
Fe	–	–	–	–	179	179	–	–
FeO	–	–	–	–	–	–	–	–
Carbon Nanotubes	–	–	–	–	66	66	–	–
Carbon Amorphous	–	–	–	–	595	595	–	–

Table 4.3. (Continued)

Stream No.	SR09	SR10	SR11	SR12	SR13	SR14	SR15	SR16
Temperature (K)	573	330	303	303	303	303	303	330
Pressure (psia)	450	450	15	15	15	15	15	75
Mass Flow (kg/hr)	14,764	14,764	825	2,793	850	1,943	1,967	12,340
Component Mass Flow Rate kg/hr								
	12,340	12,340						12,340
CO	–	–	–	–	–	–	–	–
$Fe(CO)_5$	2,424	2,424	–	–	–	–	–	–
CO_2	–	–	–	–	–	–	–	–
MEA	–	–	–	–	–	–	–	–
H_2O	–	–	–	1,789	255	1,534	1,731	–
HCl	–	–	–	–	–	–	236	–
FeO	–	–	230	–	–	–	–	–
$FeCl_2$	–	–	–	409	0.07	408.93	–	–
Amorphous Carbon	–	–	–	–	–	–	–	–
Carbon Nanotubes	–	–	595	595	595	–	–	–

Table 4.3. (Continued)

Stream No.	SR17	SR18	SR19	SR20	SR21	SR23	SR24	SR25
Temperature (K)	551	707	330	393	393	330	393	393
Pressure (psia)	450	450	15	15	15	15	45	15
Mass Flow (kg/hr)	12,340	12,340	64,032	64,032	61,608	61,608	4,187	1,763
Component Mass Flow Rate (kg/hr)								
CO	12,340	12,340	–	–	–	–	–	–
$Fe(CO)_5$	–	–	–	–	–	–	–	–
CO_2	–	–	2,424	2,424	–	–	2,424	–
MEA	–	–	12,322	12,322	12,322	12,322	–	–
H_2O	–	–	49,286	49,286	49,286	49,286	1,763	1,763
H	–	–	–	–	–	–	–	–
HCl	–	–	–	–	–	–	–	–
Fe	–	–	–	–	–	–	–	–
Fe_2O_3	–	–	–	–	–	–	–	–
Amorphous Carbon	–	–	–	–	–	–	–	–
Carbon Nanotubes	–	–	–	–	–	–	–	–

Table 4.3. (Continued)

Stream No.	SR26	SR27	SR28	SR29	SR30	SR31	SR32
Temperature (K)	393	393	393	398	1,073	1,073	303
Pressure (psia)	15	15	15	15	15	15	15
Mass Flow (kg/hr)	2,424	2,424	2,204	2,204	595	255	2,223
Component Mass Flow Rate kg/hr							
CO	–	–	–	–	–	–	–
$Fe(CO)_5$	–	–	–	–	–	–	–
CO_2	2,424	2,424	–	–	–	–	–
MEA	–	–	441	441	–	–	–
H_2O	–	–	1,763	1,763	–	255	1,731
H_2	–	–	–	–	–	–	–
O_2	–	–	–	–	–	–	–
$FeCl_2$	–	–	–	–	0.07	–	–
Fe_2O_3	–	–	–	–	–	–	256
Fe	–	–	–	–	–	–	236
HCl	–	–	–	–	–	–	–
Carbon Nanotubes	–	–	–	–	595	–	–

Table 4.3. (Continued)

Stream No.							
Temperature (K)	ARin	ARout	RG1	RG2	_	_	_
Pressure (psia)	423	423	303	303	_	_	_
Mass Flow (kg/hr)	15	15	15	15	_	_	_
Component Mass Flow Rate kg/hr							
	227	242	281	256	_	_	_
CO	_	_	_	_	_	_	_
$Fe(CO)_5$	_	_	_	_	_	_	_
$_2$	_	_	_	_	_	_	_
CO	_	242	_	_	_	_	_
MEA	_	_	_	_	_	_	_
$_2O$	_	_	255	_	_	_	_
H $_2$	227	_	26	_	_	_	_
O $_2$	_	_	_	_	_	_	_
FeCl	_	_	_	256	_	_	_
$_2O_3$	_	_	_	_	_	_	_
Fe	_	_	_	_	_	_	_
HCl	_	_	_	_	_	_	_
Carbon Nanotubes							

Table 4.4. Utility Flow Summary Table for HiPCO Process Model

	Natural Gas	Boiler Feed Water	Cooling Water			
Utility Equipment				Steam		
Temperature In	E–101	E–103	E–104	E–106	V–103 Oxygen	Z–104
Temperature (K)	1,400	303	303	533	423	303
Outlet Temperature (K)	1,400	533	323	513	423	303
Mass Flow (kg/hr)	486	6,517	52,522	2,565	227	26

iron particles. The total CO converted in the flow reactor is supplied by the make–up CO feed and the CO from the thermal decomposition of $Fe(CO)_5$. The mass flow rate of the CO feed recycle (SR04) to the flow reactor is 12,340 kg/hr at 1,323 K and 450 psi.

Carbon monoxide is converted to carbon nanotubes, amorphous carbon and carbon dioxide in the flow reactor (V–102). The conversion and selectivity of CO reactant to form carbon nanotube in the HiPCO process is 20 mol% and 90% respectively. The production rate of amorphous carbon, carbon dioxide and unconverted CO in the reactor were based on the carbon nanotubes produced. The effluent stream (SR05) from the reactor consists of: 595 kg/hr of carbon nanotubes, 66 kg/hr of amorphous carbon, 2,424 kg/hr CO_2, 179 kg/hr residual iron and 12,340 kg/hr of unconverted CO.

The mixed gas stream from the flow reactor, which consists of 12,340 kg/hr of unconverted CO and 2,424 CO_2, flows through the cross heat exchanger (E–102), waste heat boiler (E–103) and the water cooler (E–104) successively. The carbon dioxide in the mixed stream is absorbed in the counter flow of monoethanol amine (MEA) solution in the gas absorption column (T–101) at 330 K and 75 psia.

The monoethanol amine liquid absorbent feed (SR23) into the gas absorption column consists of 12,322 kg/hr MEA and 49,286 kg/hr water. The unconverted CO (SR16) flows up through the absorption column as an inert and is recycled back to the flow reactor. In the gas stripping column (T–102), the absorbed carbon dioxide is stripped from the solute rich MEA solution. The gas stream (SR24) leaving the top of the gas stripping column contains 2,424 kg/hr CO_2 and 1,763 kg/hr water.

The vapor leaving the gas stripper is sent to a flash drum (V–105), where it is flashed and separated to gas and liquid fractions. The vapor fraction (SR26), which consists

of 2,424 kg/hr CO_2, is sent through a discharge valve to the atmosphere or to carbon dioxide consuming processes. However, the liquid condensate (SR25), consisting of 1,763 kg/hr water is recovered and recycled to the gas stripping column.

The carbon nanotube product (SR06) from the gas–solid filter (Z–101), which contains amorphous carbon and residual iron particles, is sent to the air oxidizer (V–103) for low–temperature, selective oxidation at 373 K. In the air oxidizer, the amorphous carbon and residual iron particles are oxidized to carbon dioxide and iron (II) oxide respectively. The effluent streams from the oxidizer consist of 595 kg/hr carbon nanotubes (SR11), and 230 kg/hr iron oxide (SR11), and 242 kg/hr CO_2 (AR_{out}). Oxygen is supplied to the oxidizer for amorphous carbon and residual iron oxidation at 227 kg/hr (AR_{in}).

The iron oxide in the carbon nanotube product from the oxidation step is removed by dissolution in 12% hydrochloric acid solution. The ratio of the amount of hydrochloric acid required to remove the iron (II) oxide formed is based on the reaction between hydrochloric acid and iron oxide. The iron (II) oxide reacts with hydrochloric acid to form iron (II) chloride solution. The hydrochloric acid solution (SR15) supplied to the acid treatment tank consists of 236 kg/hr HCl and 1,731 kg/hr H_2O.

The liquid–solid filter (Z–102) separates the carbon nanotube product from the iron chloride solution. The wet carbon nanotube product (SR13) from the liquid–solid filter (Z–102) consists of 595 kg/hr carbon nanotube, 0.07 kg/hr residual iron chloride and 255 kg/hr water. The water contained in the wet carbon nanotube product is evaporated as steam (SR31) in the product drier/annealer (Z–103). The final carbon nanotube product (SR 30), from the product drier, consists of 595 kg/hr carbon nanotube and 0.07 kg/hr residual iron chloride.

Natural gas is supplied to the CO feed recycle gas–fired heater (E–101) at 1,400 K, and at a mass flow rate of 486 kg/hr. The heat energy is supplied by the heat of combustion of the natural gas. High pressure steam is supplied to the reboiler (E–106) at 533 K and leaves at 513 K respectively. The mass flow rate of high pressure steam through the kettle reboiler (E–106) 2,565 kg/hr respectively.

Boiler feed water is supplied to the waste heat boiler (E–103) at 303 K and gets converted to saturated steam at 533 K. The mass flow rate of boiler feed water to the waste heat boiler (E–103) is 6,517 kg/hr. Cooling water is supplied to the water cooler heat exchanger (E–104) at 303 K, and leaves at 323 K. The mass flow rate of cooling water into and out of the water cooler heat exchanger (E–104) is 52,522 kg/hr. The total flow rate of oxygen to the air oxidizer (V–102) and the acid regeneration column (Z–104) is 227 kg/hr and 26 kg/hr respectively.

Sample calculations showing the detailed analysis of the material and energy balance equations, size, preliminary design criteria and data for the individual process equipment in the HiPCO process flow diagram and the overall HiPCO production process are given in Appendix C.

4.2 ANALYSIS OF CoMoCAT PROCESS MODEL

Carbon nanotubes are formed from the disproportionation of CO over silica supported Co–Mo bimetallic catalysts according to the Boudouard reaction given by Equation (4.5):

$$xCO_{(g)} \xrightarrow{Co/Mo/SiO_2} CNT_{(s)} + \frac{x}{2} CO_{2(g)} \qquad (4.5)$$

The stoichiometrically balanced form of the Boudouard reaction based on an average – sized

carbon nanotube molecule containing 3,000 carbon atoms is given below:

$$6000CO_{(g)} \xrightarrow{Co/Mo/SiO_2} C_{3000} + 3000CO_{2(g)} \qquad (4.6)$$

The carbon monoxide conversion is 20 mol% and the CO selectivity to form carbon nanotube is 80%. In addition, carbon monoxide is converted to amorphous carbon at 20% selectivity according to Equation (4.7):

$$2CO_{(g)} \longrightarrow C_{(s)} + CO_{2(g)} \qquad (4.7)$$

Typically, the growth of the carbon nanotubes in the CoMoCAT process is nucleated by the Co–Mo bimetallic catalysts, such that the carbon nanotubes are grown and attached to the silica–supported bimetallic catalyst particles. Consequently, post–carbon nanotube synthesis purification processes will be required to detach the carbon nanotube product from the silica supports, remove amorphous carbon, and extract residual cobalt–molybdenum bimetallic particles in the final product.

The carbon nanotube product–bimetallic catalyst support interaction is broken by treating the carbon nanotubes grown on the bimetallic catalyst support in sodium hydroxide solution. The breaking of the nanotube–support interaction with alkali solution is known as silica leaching (Pisan, et al, 2004). In addition, the alkali treatment removes amorphous carbon and some of the residual cobalt and molybdenum catalysts from the carbon nanotube product. The silica supports, amorphous carbon, residual cobalt and molybdenum particles that get detached during the silica leaching process are separated from the carbon nanotube product separated in a surfactant–filled froth flotation column.

The froth flotation purification technique uses air, as the separation medium, to trap the carbon nanotube product at the air–water interface as a result of reduced surface

tension at the surfactant surface. However, the purity of the carbon nanotube product obtained from the froth flotation column is 80%, as the carbon nanotubes still contain significant amount of residual cobalt and molybdenum particles. Consequently, additional purification processes are required to remove the residual metal particles and increase the purity of the final carbon nanotube product close to 100%.

The bulk of these residual cobalt and molybdenum metal particles are subsequently removed by dissolution in 12% hydrochloric acid. The hydrochloric dissolves and extracts the residual Co and Mo particles as cobalt and molybdenum chlorides respectively. The final carbon nanotube product contains 97 mol% carbon nanotubes, 1.5 mol% cobalt metal and 1.5 mol% molybdenum metal particles (Resasco, et al, 2001).

The plant capacity for the CoMoCAT process design is 5,000 metric tons per year of 97 mol% carbon nanotubes (595 kg/hr). The proposed design is based on the production capacity of a carbon nanofiber production facility operated by Grafil, a California–based Mitsubishi Rayon subsidiary (C & EN, 2005). The stream factor used in this design is 0.96 (8,400 hr/yr), based on the production plant being shut down for two weeks in a year for scheduled maintenance.

The process flow diagram for the CoMoCAT carbon nanotube production process is shown in Figure 4.2. The description of the process units in the CoMoCAT process flow diagram is given in Table 4.5. The conversion and selectivity of carbon monoxide feed reactant to produce carbon nanotubes in the CoMoCAT process is 20 mol% and 80% respectively. The unconverted CO from the process is recovered, and recycled to the fluidized bed reactor, as shown in Figure 4.2.

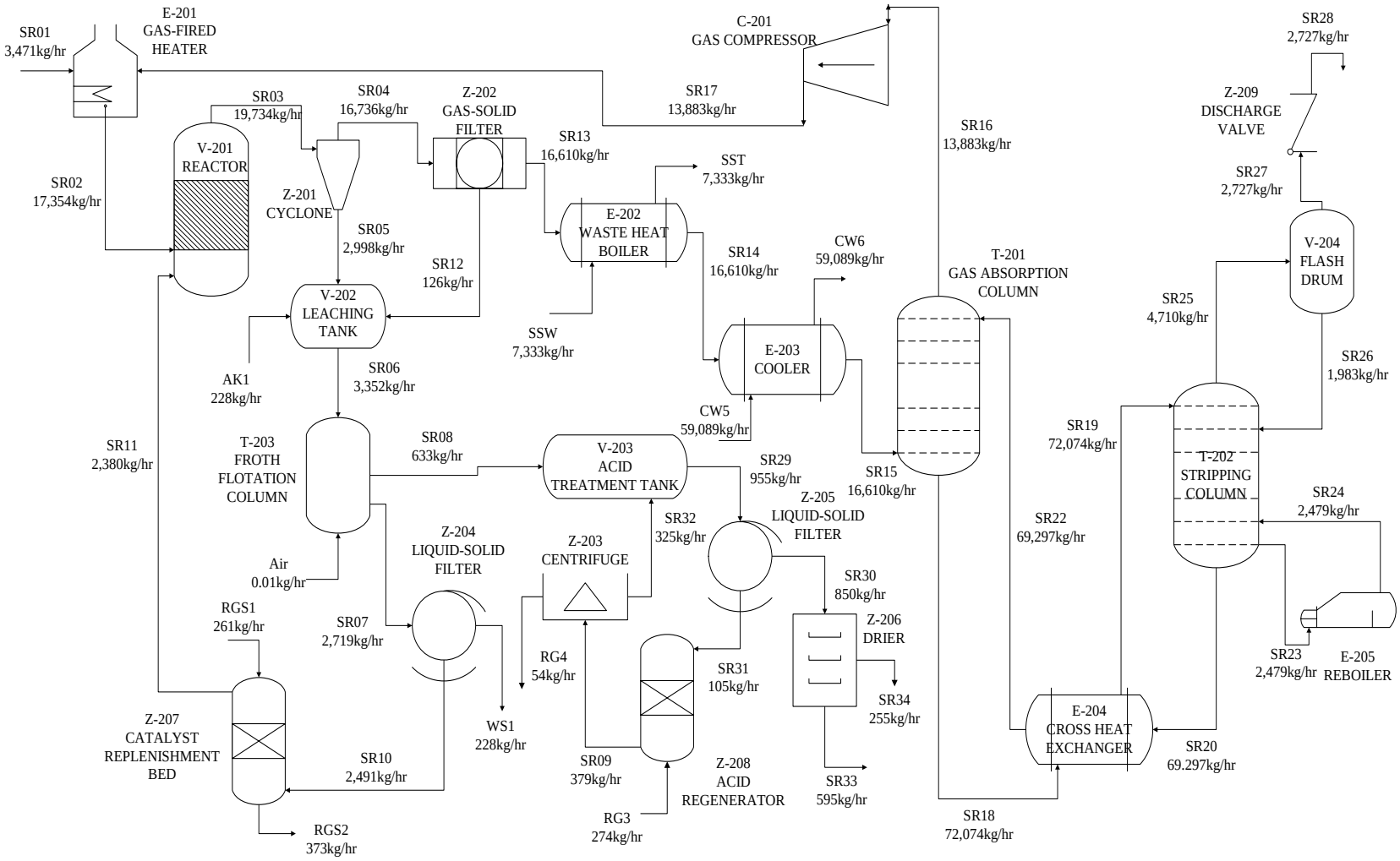

Figure 4.2. Process Flow Diagram for the CoMoCAT Carbon Nanotube Production Process

Table 4.5 Process Units for the CoMoCAT Process Model (Refer to Figure 4.2)

Name of Unit	Process Unit Description
Heat Exchangers	
E–201	CO Feed and Recycle Gas–Fired Heater
E–202	Waste Heat Boiler
E–203	Heat Exchanger Water Cooler 1
E–204	Solute Rich–Lean Solvent Cross Heat Exchanger
E–205	Kettle Reboiler
Process Vessels	
V–201	Fluidized Bed Reactor
V–202	Alkali Leaching Tank
V–203	Acid Treatment Tank
V–204	Flash Drum
T–201	Gas Absorption Column
T–202	Gas Stripping Column
T–203	Froth Flotation Column
C–201	Gas Compressor
Z–201	Cyclone Separator 1
Z–202	Gas–Solid Filter
Z–203	Centrifuge Separator
Z–204	Liquid–Solid Filter 1
Z–205	Liquid–Solid Filter 2
Z–206	Product Drier
Z–207	Catalyst Replenishment Bed
Z–208	Acid Regeneration Column
Z–209	Discharge Valve

The supported catalysts separated from the carbon nanotube in the froth flotation column is recovered and sent to a regeneration unit. In the catalyst regeneration unit, the amorphous carbon particles in the spent supported catalysts are oxidized by high pressure steam to carbon dioxide. Furthermore, fresh cobalt and molybdenum particles are added to the spent supported catalysts during regeneration to compensate for the cobalt and molybdenum losses in the acid dissolution step and with the final carbon nanotube product.

The summary of the preliminary process equipments in the CoMoCAT process flow diagram is given in Table 4.6. In Table 4.6, there are five fixed shell and tube heat exchanger process units: the CO feed and recycle gas–fired heater (E–201), the waste heat boiler (E–202), the water cooler (E–203), the cross heat exchangers (E–204), and the reboiler (E–205). The individual heat exchanger characteristics, such as material of construction, are dependent on the type and nature of the process fluids, the phase and temperature of the process fluids, and the type of mechanical construction employed.

The energy required for increasing the make–up CO feed (SR01) and the CO feed recycle (SR17) from 402 K to 1,223 K (SR02) in the gas- fired heater (E–201) is 34,191 MJ/hr. This energy is supplied by natural gas at 1,400 K and 150 psia. The heat transfer area of the gas–fired heater (E–201) is 205 m^2. The maximum temperature and preferred material of construction for the shell and tube sides of the gas–fired heater is 1,400 K (nickel alloy) and 1,323 K (nickel alloy) respectively.

The energy absorbed by the boiler feed water in the waste heat boiler (E–202) is 23,630 MJ/hr. The energy is used to convert the boiler feed water (BFW) supplied at 303 K to saturated steam (SST) at 533 K. This energy is supplied by cooling the mixed gas stream leaving the gas–solid filter from 1,223 K (SR13) to 573 K (SR14). The heat transfer area in

Table 4.6. Preliminary Equipment Summary Table for CoMoCAT Process Model

Equipment	E–201	E–202	E–203	E–204	E–205
Type	Gas–Fired	Fixed Shell & Tube	Fixed Shell &Tube	Fixed Shell & Tube	Kettle Reboiler
Duty (kJ/hr)	34,190,688	23,629,901	4,944,574	26,497,965	4,792,884
Area (m^2)					
Shell Side					
Max Temp (K)	1,400	533	323	393	533
Pressure (psia)	150	675	150	150	675
MOC	Nickel Alloy	Carbon Steel	Carbon Steel	Carbon Steel	Carbon Steel
Phase	Natural Gas	Liquid	Liquid	Liquid	Steam
Tube Side					
Max Temp (K)	1,223	1,223	573	393	513
Pressure (psia)	150	150	150	150	150
MOC	Nickel Alloy	Nickel Alloy	Carbon Steel	Carbon Steel	Carbon Steel
Phase	Gas	Gas	Gas	Liquid	Liquid

Table 4.6. (Continued)

Equipment	V–201	C–201	T–201	T–202	T–203	V–202
MOC	Nickel Alloy	Carbon Steel	Carbon Steel	Carbon Steel	Carbon Steel	Carbon Steel
Power (kW)	–	387	–	–	–	–
Efficiency	–	75 %	–	–	–	–
Type/Drive	–	Centrifugal	–	–	–	–
Temperature (K)	1,223	402	330	393	303	303
Pressure In (psia)	–	75	–	–	–	–
Pressure Out (psia)	–	150	–	–	–	–
Diameter (m)	1.2	–	1.2	0.8	1.9	0.9
Height (m)	2.5	–	11	11	5.9	3.6
Volume (m^3)	2.9	–	–	–	–	–
Orientation	Horizontal	–	Vertical	Vertical	Vertical	Horizontal
Internals	–	–	15 Trays	15 Trays	–	–
Pressure (psia)	150	–	75	45	15	15

Table 4.6. (Continued)

Equipment	V–203	V–204	Z–202	Z–203	Z–204	Z–205
MOC	Carbon Steel	Carbon Steel	Carbon Steel	Carbon Steel	Carbon Steel	Carbon Steel
Power (kW)	–	–	–	–	–	–
Efficiency	–	–	–	–	–	–
Type/Drive	–	–	–	–	–	–
Temperature (K)	303	393	1,223	303	303	303
Pressure In (psia)	–	–	–	–	–	–
Pressure Out (psia)	–	–	–	–	–	–
Diameter (m)	0.9	0.8	–	1	–	–
Height (m)	3.6	3	–	0.6	–	–
Area (m^2)	–	–	14	–	35	9
Orientation	Horizontal	–	–	–	–	–
Internals	–	–	–	–	–	–
Pressure (psia)	15	15	15	15	15	15

Table 4.6. (Continued)

Equipment						
	Z–206	Z–207	Z–208	Z–209	–	–
MOC	Stainless Steel	Ni Alloy	Carbon Steel	Carbon Steel		
Power (kW)					–	–
Efficiency	–	–	–	–	–	–
Type/Drive	–	–	–	–	–	–
Temperature	–	–	–	–	–	–
Pressure In (psia)	1,073 (K)	1,223	303	303	–	–
Pressure Out (psia)	–	–	–	–	–	–
Diameter (m)	–	–	–	–	–	–
Height (m)	0.9	1.3	0.9	–	–	–
Area (m^2)	3.6	5.2	3.6	–	–	–
Orientation	– Horizontal	–	–	–	–	–
Internals		–	–	–	–	–
Pressure (psia)	–	–	–	–	–	–
	15	150	15	15	–	–

the waste heat boiler (E–202) is 113 m^2. The maximum temperature and preferred material of construction for the shell and tube sides of the waste heat boiler is 533 K (carbon steel) and 1,223 K (nickel alloy) respectively.

The energy liberated from cooling the mixed gas stream leaving the waste heat boiler from 573 K (SR14) to 330 K (SR15) in the water cooler (E–203) is 4,945 MJ/hr. Cooling water is supplied to the water cooler heat exchanger at 303 K and leaves at 323 K. The heat transfer area in the water cooler (E–203) is 106 m^2. The maximum temperature and preferred material of construction for the shell and tube sides of the water cooler is 323 K (carbon steel) and 573 K (carbon steel) respectively.

Heat exchange occurs between the solute rich MEA solution (SR18) from the gas absorption column and the lean MEA solution (SR20) from the gas stripping column in the cross heat exchanger (E–204). The heat duty in the cross heat exchanger is 26,498 MJ/hr and the heat transfer area is 103 m^2. The maximum temperature and preferred material of construction for the shell and tube sides of the cross heat exchanger is 393 K (carbon steel) and 393 K (carbon steel) respectively.

The energy supplied by condensing steam in the reboiler (E–205) is 4,793 MJ/hr. This energy is used to evaporate the aqueous fraction of the MEA solution. The heat transfer area for the kettle boiler (E–205) was estimated to be 47 m^2. The maximum temperature and material of construction for the shell and tube sides of the kettle reboiler is 533 K (carbon steel) and 413 K (carbon steel) respectively.

The process vessels and separators in the CoMoCAT preliminary equipment summary table include: the fluidized bed reactor (V–201), the gas compressor (C–201), the gas absorption column (T–201), the gas stripping column (T–202), the flash drum (V–204)

and the froth flotation column (T–203). Other process vessels in the CoMoCAT model include: the silica leaching tank (V–202), the acid–dissolution tank (V–203), the gas–solid filter (Z–202), the liquid–solid filters (Z–204 and Z–205), the product drier (Z–206), the catalyst regeneration bed (Z–207), the acid regeneration column (Z–208), and the centrifuge separator (Z–203).

The operating pressure and temperature in the CoMoCAT fluidized bed reactor (V–201) is 150 psia and 1,223 K respectively. Due to the abrasive nature of the catalyst particles and the high operating temperature and pressure in the fluidized bed reactor, nickel alloy is used as the preferred material of construction for the CoMoCAT reactor. The size of the reactor was determined from the average residence time of the supported catalyst particles in the fluidized bed reactor. The average residence time used is 7,200 seconds, based on laboratory experiments (Resasco, et al, 2001). The diameter and height of the fluidized bed reactor (V–201) is 1.2 m and 2.5 m respectively.

The gas compressor (C–201) increases the pressure of the CO feed recycle stream from 75 psia (SR16) to 150 psia (SR17) by adiabatic compression. Consequently the temperature of the recycle stream increases from 330 K (SR16) to 402 K (SR17). The compressor power, which is the rate at which the gas compressor delivers work in the process, is 387 kW at 75% efficiency. Due to the high and constant delivery pressure requirements of the CoMoCAT process, centrifugal compressor with carbon steel as the preferred material of construction is selected for use in the CoMoCAT process.

The gas–absorption column (T–201) and gas stripping column (T–202) consists of 15 trays with a stage separation distance of 0.61 m and a 15% allowance for vapor disengagement and liquid sump. Carbon dioxide in the mixed gas stream (SR15) is absorbed

in the counter current flow of 20% MEA solution at 330 K and 75 psia. In the gas stripping column, the carbon dioxide absorbed in the gas absorber is stripped from the MEA solution by pure steam at 393 K and 45 psia.

The diameter and height of the gas absorption column (T–201) is 1.08 m and 11 m respectively, whereas, the diameter and height of the gas stripping column (T–202) is 0.70 m and 11 m respectively. Since gas absorption and gas stripping takes place at moderate temperatures of 330 K and 398 K respectively, carbon steel is used as the material of construction for both columns. The flash drum (V–204) is designed as an isothermal unit with operating temperature and pressure of 393 K and 15 psia respectively. The diameter and height of the flash drum is 0.8 m and 3.2 m respectively, and carbon steel is used as the material of construction.

In the silica leaching tank (V–202), the carbon nanotube–silica interaction is broken by treating the solid products from the reactor with (2M) sodium hydroxide solution (Resasco, et al, 2001). This process, which is referred to as silica leaching, breaks the carbon nanotube–silica attachment without removing the Co–Mo catalyst present on the silica substrate. The diameter and height of the silica leaching tank, based on an average residence time of 3,600s, is 1.2 m and 4.8 m respectively. The slurry from the leaching tank is then sent to the froth flotation column (T–203).

In the froth flotation column (T–203), the carbon nanotube product is separated from the silica supports, amorphous carbon, cobalt and molybdenum particles. However, the purity of the carbon nanotube product from the flotation column is about 80%, and thus additional purification steps are required to increase the purity close to 100%. The diameter and height of the flotation column is 1.9 m and 5.9 m respectively.

In the acid dissolution tank (V–203), residual cobalt and molybdenum particles in the carbon nanotube product are removed by dissolution in 12% hydrochloric acid. The ratio of the amount of HCl acid required to remove the residual metals is based on the reaction between hydrochloric acid, cobalt, and molybdenum respectively. The diameter and length of the acid treatment tank was estimated based on an average solid residence time of 3,600 s to be 0.90 m and 3.6 m respectively.

The gas–solid filter (Z–202) separates the raw carbon nanotube product from the hot mixed gas effluent from the fluidized bed reactor, while the liquid–solid filters (Z–204 and Z–205) separate the solid products from the sodium hydroxide and other process streams respectively. The area for the gas –solid filter (Z–202), is 14 m^2, whereas, the area for the liquid–solid filters Z–203 and Z–204 is 35 m^2, and 9 m^2 respectively.

The wet carbon nanotube product from the filter (Z–205) is sent to the product drier (Z–206), where residual water in the nanotube product is evaporated. The dried carbon nanotube product is subsequently sent to packaging, storage or sales. The size of the product drier was based on an average residence time of 3600 s for the carbon nanotube product in the product drier. The diameter and height of the product drier was estimated to be 1 m and 3.9 m respectively.

In the catalyst replenishment bed (Z–207), the amorphous carbon particles present in the spent supported catalyst is removed by high pressure steam. Furthermore, fresh cobalt and molybdenum metal catalysts are added to make up for the cobalt and molybdenum losses in the acid purification step and/or in the final carbon nanotube product. The diameter and height of the catalyst replenishment bed (Z–207), based on a regeneration time of 3,600 seconds per reaction cycle was estimated to be 1.3 m and 5.2 m respectively.

In the acid regeneration column (Z–208), cobalt chloride and molybdenum chloride solution is oxidized to produce hydrochloric acid, cobalt oxide and molybdenum oxide. The saturated cobalt and molybdenum oxides are removed from the regenerated hydrochloric acid in the centrifuge separator (Z–203). The hydrochloric acid recovered from the centrifuge separator is recycled back to the acid dissolution tank for another reaction cycle. The diameter and height of the acid regeneration column (Z–208) is 0.9 m and 3.6 m respectively.

The flow summary for the process streams and utility streams in the CoMoCAT process flow diagram is given in Table 4.7 and Table 4.8 respectively. In Table 4.7, the temperature, pressure, component mass flow rates and total mass flow rate of each process streams is specified. Similarly, the total mass flow rates, inlet and outlet temperatures of the utility streams for the CO recycle gas–fired heater (E–201), waste heat boiler (E–202), water cooler (E–203), and the kettle reboiler (E–205) are given in Table 4.8.

The mass flow rate of fresh CO (SR01) and CO feed recycle (SR17) to the gas–fired heater (E–201) is 3,471 kg/hr and 13,883 kg/hr respectively. The total CO supplied to the fluidized bed reactor (V–201) is 17,354 kg/hr at 1,223 K and 150 psia. The supported Co–Mo bimetallic catalyst (SR11) supplied to the fluidized bed reactor is 2,380 kg/hr at 1,223 K and 150 psia. The silica supported bimetallic catalyst, which consists of 2,190 kg/hr silica, 95 kg/hr Co and 95 kg/hr Mo, is fluidized in the hot CO reactant stream to produce carbon nanotube, amorphous carbon and carbon dioxide.

The conversion and selectivity of CO reactant to form carbon nanotube is 20 mol% and 80% respectively. The production rate of amorphous carbon, carbon dioxide and unconverted CO in the reactor were based on the amount of carbon nanotubes produced. The

Table 4.7. Flow Summary Table for CoMoCAT Process Model

Stream No.	SR01	SR02	SR03	SR04	SR05	SR06	SR07	SR08
Temperature (K)	303	1,223	1,223	1,223	1,223	303	303	303
Pressure (psia)	15	150	150	150	15	15	15	15
Mass Flow (kg/hr)	3,471	17,354	19,734	16,736	2,998	3,352	2,719	633
Component Mass Flow Rate kg/hr								
CO_2	3,471	17,354	13,883	13,883	–	–	–	–
SiO	–	–	2,190	88	2,102	2,190	2,190	–
Co	–	–	95	4	91	95	76	19
Mo_2	–	–	95	4	91	95	76	19
CO	–	–	2,727	2,727	–	–	–	–
HCl	–	–	–	–	–	–	–	–
NaOH	–	–	–	–	–	228	228	–
H_2O	–	–	–	–	–	–	–	–
Amorphous Carbon	–	–	149	6	143	149	149	–
Carbon Nanotubes	–	–	595	24	571	595	–	595

Table 4.7. (Continued)

Stream No.	SR09	SR10	SR11	SR12	SR13	SR14	SR15	SR16
Temperature (K)	303	303	1,223	1,223	1,223	573	330	330
Pressure (psia)	15	15	15	15	150	150	150	75
Mass Flow (kg/hr)	37	2,491	2,380	126	16,610	16,610	16,610	13,883
Component Mass Flow Rate (kg/hr)								
						13,883	13,883	13,883
CO_2	–	–	–	–	13,883			
SiO	–	2,190	2,190	88	–	–	–	–
Co	–	76	95	4	–	–	–	–
Mo_2	–	76	95	4	–	–	–	–
CO	–	–	–	–	2,727	2,727	2,727	–
HCl_2O	39	–	–	–	–	–	–	–
H_3	286	–	–	–	–	–	–	–
MoO_2O_3	28	–	–	–	–	–	–	–
Ca	Amorphous 26	–	–	–	–	–	–	–
Carbon	–	149	–	6	–	–	–	–
Carbon Nanotubes	–	–	–	24	–	–	–	–

Table 4.7. (Continued)

Stream No.	SR17	SR18	SR19	SR20	SR22	SR23	SR24	SR25
Temperature (K)	402	330	393	393	330	393	398	393
Pressure (psia)	150	15	15	15	15	15	15	45
Mass Flow (kg/hr)	13,883	72,074	72,074	69,297	69,297	2,479	2,479	4,710
Component Mass Flow Rate (kg/hr)								
	13,883							
CO_2	–	–	–	–	–	–	–	–
SiO_2	–	–	–	–	–	–	–	–
Co	–	–	–	–	–	–	–	–
Mo_2C	–	–	–	–	–	–	–	–
CO_2	–	2,727	2,727	–	–	–	–	2,727
HCl	–	–	–	–	–	–	–	–
MEA	–	13,859	13,859	13,859	13,859	496	496	–
H_2O	–	55,438	55,438	55,438	55,438	1,983	1,983	1,983
Amorphous Carbon	–	–	–	–	–	–	–	–
Carbon Nanotubes	–	–	–	–	–	–	–	–

Table 4.7. (Continued)

Stream No.	SR26	SR27	SR28	SR29	SR30	SR31	SR32	SR33
Temperature (K)	393	393	393	303	303	303	303	1,073
Pressure (psia)	15	15	15	15	15	15	15	15
Mass Flow (kg/hr)	1,983	2,727	2,727	955	850	105	325	595
Component Mass Flow Rate (kg/hr)								
H_2	–	–	–	41	0.04	40.96	–	0.04
$CoCl_2$	–	–	–	33	0.05	32.95	–	0.05
$MoCl_2O_3$	–	–	–	–	–	–	–	–
Co	–	–	–	–	–	–	–	–
Co_3	–	–	–	–	–	–	–	–
MoO_2	–	2,727	2,727	–	–	–	–	–
CO	–	–	–	–	–	–	39	–
HCl	–	–	–	–	–	–	–	–
NaOH	–	–	–	–	–	–	286	–
H_2O	1,983	–	–	286	255	31	–	–
Amorphous Carbon	–	–	–	–	–	–	–	–
Carbon Nanotubes	–	–	–	595	595	–	–	595

Table 4.7. (Continued)

Stream No.	SR34	AK1	RGS1	RGS2	RG3	RG4	WS1	Air
Temperature (K)	1,073	303	1,223	1,223	303	303	303	303
Pressure (psia)	15	15	150	150	15	15	15	15
Mass Flow (kg/hr)	255	228	261	373	274	54	228	0.01
Component Mass Flow Rate (kg/hr)								
Co	–	–	19	–	–	–	–	–
Mo_2O_3	–	–	19	–	–	–	–	–
Co_3	–	–	–	–	–	26	–	–
MoO	–	–	–	–	–	28	–	–
CO_2	–	–	–	348	–	–	–	–
H	–	–	–	25	–	–	–	–
NaOH	–	228	–	–	–	–	228	–
H_2O	255	–	223	–	265	–	–	–
H	–	–	–	–	9	–	–	–
O	–	–	–	–	–	–	–	–
Carbon Nanotubes	–	–	–	–	–	–	–	–

Table 4.8. Utility Flow Summary Table for CoMoCAT Process Model

	Natural Gas	Boiler Feed Water	Cooling Water		Oxygen	Air
Utility Equipment				Steam		
Temperature In	E–201	E–202	E–203	E–205	Z–208	T–203
Temperature (K)	1,400	303	303	533	303	303
Outlet Temperature (K)	1,400	533	323	513	303	303
Mass Flow (kg/hr)	616	7,333	59,089	2,885	9	0.01

effluent stream (SR03) from the fluidized bed reactor consists of: 595 kg/hr of carbon nanotubes, 149 kg/hr of amorphous carbon, 2,727 kg/hr CO_2, 13,833 kg/hr of unconverted CO, 95 kg/hr of residual cobalt, 95 kg/hr of residual molybdenum, and 2,190 kg/hr of silica particles.

The effluent stream from the fluidized bed reactor is sent to a cyclone separator, where the mixed gas stream containing unconverted CO and CO_2 is separated from the solid reactor products. The mixed gas stream (SR04) from the cyclone contains entrained solids, which are removed from the gas stream by the gas–solid filter (Z–202). The entrained solids are recombined with the solids (SR05) removed by the cyclone separator in the silica leaching tank (V–201). The solid entrainment fraction in the mixed gas stream depends on the efficiency of the cyclone separator.

The mixed gas stream (SR13) from the gas–solid filter (Z–202), which consists of 13,883 kg/hr of unconverted CO and 2,727 kg/hr CO_2 is passed through the waste heat boiler (E–202) where the mixed stream is cooled from 1,223 K to 573 K. The mixed gas stream leaving the waste heat boiler is then passed through the water cooler (E–203), with a decrease in the stream temperature from 573 K (SR14) to 330 K (SR15) in the water cooler.

The carbon dioxide in the mixed stream (SR15) is absorbed in counter flow of MEA solution in the gas absorption column at 330 K and 75 psia. The MEA liquid absorbent feed (SR22) into the absorption column consists of 13,859 kg/hr MEA and 55,438 kg/hr of water. The unconverted CO (SR16) flows up through the absorption column as an inert and is recycled back to the fluidized bed reactor. In the gas stripping column, the absorbed CO_2 is stripped from the solute rich MEA solution. The gas stream (SR25) leaving the top of the gas stripper contains 2,727 kg/hr CO_2 and 1,983 kg/hr of water.

The vapor leaving the gas stripping column is sent to a flash drum, where it is flashed and separated to gas and liquid fractions. The vapor fraction (SR27), consisting of 2,727 kg/hr CO_2 is passed through a vent valve to other CO_2 consuming processes, while the liquid condensate (SR25), consisting of 1,983 kg/hr water is returned to the gas stripping column. Carbon dioxide is removed from the solute rich MEA solution by pure steam in the gas stripping column.

The carbon nanotube is separated from the silica supports and amorphous carbon in the froth flotation column (T–203). The purity of the solid product from the froth flotation column is 80%, and hence, the carbon nanotube product (SR08) from the froth flotation column contains 595 kg/hr of carbon nanotubes, 19 kg/hr of residual cobalt and 19 kg/hr of residual molybdenum particles.

The residual cobalt and molybdenum particles in the carbon nanotube product from the flotation column are removed by dissolution in 12% hydrochloric acid, in the acid dissolution tank (V–203). The ratio of the amount of hydrochloric acid required to remove the residual cobalt and molybdenum metals is based on the reaction between hydrochloric acid, cobalt and molybdenum. The 12% hydrochloric acid solution required to dissolve the residual metals, based on the stoichiometric ratios of reactants in the reaction between HCl and the metals, consists of 39 kg/hr HCl and 286 kg/hr H_2O.

The wet carbon nanotube product, which contains 595 kg/hr carbon nanotube, 0.04 kg/hr cobalt chloride, 0.05 kg/hr of molybdenum chloride and 255 kg/hr H_2O, is separated from the cobalt and molybdenum chloride solution by the filter (Z–205). The water in the final product is evaporated in the drier (Z–206). Residual Co and Mo metals in the final product were estimated to be 0.02 kg/hr and 0.03 kg/hr respectively.

In the catalyst replenishment bed (Z–207), fresh cobalt and molybdenum metals are added to replenish the metal catalysts losses in the acid dissolution step and with the final carbon nanotube product. In addition, high pressure steam is supplied to the catalyst regeneration bed to oxidize amorphous carbon to carbon monoxide and hydrogen. The amount of fresh cobalt (19 kg/hr) and molybdenum (19 kg/hr) metals added were based on the amount of cobalt and molybdenum metals contained in the final carbon nanotube product (SR 33) and the metal oxides (RG4) leaving the centrifuge separator (Z–203). The cobalt and molybdenum oxides removed in the centrifuge separator are sent to the catalyst manufacturer to reuse the cobalt and molybdenum metals.

Natural gas is supplied to the CO feed and feed recycle gas–fired heater (E–201) at 1,400 K, and at a mass flow rate of 616 kg/hr. High pressure steam is supplied to the kettle reboiler (E–205) at 533 K, and leaves at 513 K. The mass flow rate of HP steam into and out of the reboiler is 2,885 kg/hr.

Boiler feed water is supplied to the waste heat boiler (E–202) at 303 K and gets converted to saturated steam at 533 K. The mass flow rate of boiler feed water to the waste heat boiler is 7,333 kg/hr. Cooling water is supplied to the heat exchanger water cooler (E–203) at 303 K and leaves at 323 K. The mass flow rate of cooling water into and out of the heat exchanger water cooler is 59,089 kg/hr.

Sample calculations showing the detailed analysis of the material and energy balance equations, size, preliminary design criteria and data for the individual process equipments in the CoMoCAT process flow diagram are given in Appendix C. In addition, the input–output component structure for the overall CoMoCAT process is given in Appendix C.

4.3. SUMMARY

The results of the analysis of the HiPCO and CoMoCAT carbon nanotube production processes were presented in this chapter. The temperature, total mass flow rates, and component mass flow rates of individual streams were determined and specified. In addition, the size, design criteria and data for the specification of the process equipments were given in this chapter.

The HiPCO process is a homogeneous gas–phase production process, where the iron pentacarbonyl catalyst precursor is in the gas phase. The iron pentacarbonyl decomposes to form carbon monoxide and catalytic iron particles, which nucleate the growth of carbon nanotubes by Boudouard reaction mechanism. The HiPCO reactor is a high pressure flow reactor maintained at operating pressure of 450 psia and temperature of 1,323 K. The CO conversion and selectivity to carbon nanotubes in the HiPCO reactor is 20 mol%, and 90% respectively.

The CoMoCAT process is a heterogeneous process involving the disproportionation of CO over silica–supported cobalt and molybdenum bimetallic catalysts. The reactor used in the CoMoCAT process is a fluidized bed reactor, whereby the supported catalysts are fluidized in hot carbon monoxide reactant gas stream. The operating temperature and pressure for the fluidization regime is1,223 K and 150 psia respectively. The carbon monoxide conversion and selectivity to carbon nanotubes in the CoMoCAT process is 20 mol%, and 80% respectively.

The reaction products, byproducts and other emission products from the overall HiPCO and CoMoCAT processes are given in Table 4.9 and Table 4.10 respectively. In Table 4.9, the final carbon nanotube product (SR30) consists of carbon nanotubes, and iron

Table 4.9. Reaction Products, Byproducts and Emission Products of HiPCO process

Effluent Stream	Components
SR30	Carbon Nanotubes, CNT
	Iron Chloride, $FeCl_2$
SR31	Steam, H_2O
SR27	Carbon dioxide, CO_2
ARout	Carbon dioxide, CO_2
RG2	Iron (III) Oxide, Fe_2O_3

Table 4.10. Reaction Products, Byproducts and Emission Products of CoMoCAT process

Effluent Stream	Components
SR33	Carbon Nanotubes, CNT
	Cobalt Chloride, $CoCl_2$
	Molybdenum Chloride, $MoCl_2$
SR34	Steam, H_2O
SR28	Carbon dioxide, CO_2
RGS2	Carbon monoxide, CO
	Hydrogen, H_2
WS1	Sodium Hydroxide, NaOH
RG4	Cobalt Oxide, Co_2O_3
	Molybdenum Oxide, MoO_3

chloride. The residual water (SR31) present in the wet carbon nanotube product is removed as steam by evaporation in the product drier (Z–103). The two sources of carbon dioxide emission in the HiPCO process include the carbon dioxide byproduct (SR27), which leaves through the back pressure control discharge valve (Z–105), and the carbon dioxide (ARout)

produced from the oxidation of amorphous carbon in the air oxidizer (V–103). Another source of residual iron in the HiPCO process is the Fe_2O_3 (RG2) leaving the centrifuge separator (Z–106).

In Table 4.10, the final carbon nanotube product (SR33) consists of carbon nanotubes, cobalt chloride and molybdenum chloride. The residual water (SR34) present in the wet carbon nanotube product is removed by evaporation in the product drier (Z–206). The sources of CO_2 and CO emission in the CoMoCAT process include the carbon dioxide byproduct (SR28), which leaves through the discharge valve (Z–209), and the carbon monoxide (RGS2) produced from the oxidation of amorphous carbon by high pressure steam in the catalyst regeneration bed (Z–207). In addition, hydrogen gas is liberated during the oxidation of amorphous carbon in the catalyst regeneration bed (Z–207).

The waste stream (WS1) leaving the filter (Z–204) contains sodium hydroxide solution used to break the silica–carbon nanotube interaction in the leaching tank (V–202). The waste stream can be sent to a solvent recovery unit to recover the sodium hydroxide solution for reuse in the silica leaching tank. Another source of residual cobalt and molybdenum in the CoMoCAT process is the cobalt and molybdenum oxide (RG4) leaving the centrifuge separator (Z–203).

The carbon dioxide produced in the HiPCO and CoMoCAT processes are sent to carbon dioxide consuming processes. The hydrogen gas byproduct from the oxidation of amorphous carbon in the CoMoCAT process can be separated from the carbon monoxide and sent to hydrogen consuming processes. The residual water removed as steam in the product driers of the HiPCO and CoMoCAT processes can be used to supply steam or heat to other process equipments such as the waste heat boiler, and/or the reboiler. Consequently,

these byproducts from the HiPCO and CoMoCAT processes are used as raw materials for other processes.

The cobalt oxide and molybdenum oxide residues, leaving the centrifuge separator (Z–203) in the CoMoCAT process, are sent to the catalyst manufacturer, where the cobalt and molybdenum metals can be recovered and reused. The iron oxide residues, leaving the centrifuge separator (Z–106) in the HiPCO process, can be used as catalysts for other process or as color pigment additive to color concrete products, paints and plastics.

In the next chapter, economical decision and profitability analysis principles will be used to evaluate and determine the total cost, scalability, economic feasibility and viability of the HiPCO and CoMoCAT production processes. The total capital costs, total product costs, and net present value economics for the HiPCO and CoMoCAT production technologies will be evaluated, also.

CHAPTER FIVE: ECONOMIC ANALYSIS OF HiPCO AND CoMoCAT PROCESS MODELS

The conceptual design and development of two potentially scalable carbon nanotube production processes: HiPCO and CoMoCAT, with a proposed production capacity of 5,000 metric tons of carbon nanotubes per year (595 kg/hr) each were discussed in the last chapter. The solution to the material and energy balance equations in the HiPCO and CoMoCAT process models, the size of process equipments, preliminary design criteria and data for equipment selection, were specified, also.

In this chapter, economic decision analysis will be used to estimate the total capital cost requirements for the HiPCO and CoMoCAT process models. In addition, elements of profitability analysis, such as the net present value, will be used to determine the economic feasibility and viability of the HiPCO and CoMoCAT production processes respectively.

5.1. ECONOMIC DECISION ANALYSIS

Economic decision analysis provides the framework for economic feasibility studies, which is essential for making informed decision on: (a) the profitability of the production venture, (b) systematic evaluation of alternative designs or investments, and (c) project planning and evaluation. Economic decisions aid in the allocation of available resources, which are limited, for a maximum return on investments.

An economic evaluation of any proposed capital investment, such as construction of a new production plant or expansion of existing facilities, involves the determination of the capital expenditures and the expected profit. The application of economic decision analysis, in the development of preliminary capital cost estimates for the HiPCO and

CoMoCAT process models, are based on standard economic concepts and production features of a chemical plant. The preliminary estimates of the total capital investment, total production cost, and other economic cost indices, will be discussed.

Some terms employed in economic decision analysis on an annual basis standard, are given in Table 5.1. Sales, S, refer to the income or revenue generated from selling the plant's product and/or byproducts to its customers. The total annual revenue from product sales is the sum of the unit price of each product multiplied by its rate of sales. The total capital investment (*TCI*), and the total production cost, C_T, are estimated based on delivered equipment cost and other related information.

5.1.1 Total Plant Costs

The total plant cost or total capital investment for a chemical process plant consists of the installed equipment costs, offsite facilities costs, start–up costs and the working capital for the plant. The installed equipment costs for the HiPCO and CoMoCAT process models were estimated by CAPCOST, a computer program that uses the equipment module approach for capital cost estimation (Turton et. al., 2003).

The offsite facilities, start–up costs and working capital for the plant are estimated as a percentage of the installed equipment cost. The offsite facilities costs are related to auxiliary or non processing facilities, whereas working capital refers to a certain amount of capital that is made available to sustain the production operation before sales of products, or receipt of payment for products sold. The start–up costs refer to the cost of starting the plant and bringing it to maximum production. The breakdown of these capital cost elements as a a percentage of the total fixed capital investment is given in Table 5.2.

The installed equipment costs for the carbon nanotube production processes are

Table 5.1 Terms Used in Economic Decision Analysis on an Annual Basis

Sales (Sales Price, S_p x Product mass flow rate/yr, m)	$\boldsymbol{S = S_p * m}$
Manufacturing Expenses	$\boldsymbol{C_M}$
General Expenses	$\boldsymbol{C_G}$
Total Production or Annual Expenses	$\boldsymbol{C_T = C_M + C_G}$
Purchased Equipment Cost	$\boldsymbol{C_{purchase}}$
Installed Equipment Cost or Fixed Capital Investment	$\boldsymbol{C_{installed}}$
Total Plant cost or Total Capital Investment	$\boldsymbol{C_{total\ plant}}$
Annual Capital Expenditure	$\boldsymbol{C_{cap}}$
Depreciation and Allowance for Tax Purposes	$\mathbf{D \sim C_{installed}/Economic\ life}$
Gross Profit	$\boldsymbol{P_G = S - C_M - D}$
Net Annual Income before Taxes	$\boldsymbol{I_{Net} = S - C_T}$
Net Annual Profit before Taxes	$\boldsymbol{P_{Net} = P_G – C_G}$
Net Annual Cash Flow before Taxes	$\boldsymbol{C_{Flow} = I_{Net} - C_{cap}}$
Taxable Income	$\boldsymbol{I_{taxable} = I_{Net} - D}$
Taxes (tax rate, t ~ 35% of taxable income)	$\boldsymbol{T = t\ (I_{Net} – D)}$
Net Annual Income after Taxes	$\boldsymbol{I_{xt} = I_{Net} - T}$
Net Annual Profit after Taxes	$\boldsymbol{P_{xt} = I_{xt} - D}$
Net Annual Cash Flow after Taxes	$\boldsymbol{C_{Flow\ xt} = I_{xt} - C_{cap}}$
Value Added (Sales – Raw materials cost – Utilities)	$\boldsymbol{P_{value\ added} = S - C_{raw\ materials} - C_{utl}}$
Profit Margin (After Tax Earnings as a % of Sales)	$\boldsymbol{P_{margin}}$

Table 5.2 Partial List of Elements in a Plant Cost Estimate, from Garrett, 1989

Capital Requirements	Percentage of Fixed Capital Investment
Offsite Facilities: Utilities : Boilers, Water systems, Generators, Fuel storage and distribution facilities, Air–conditioning, Power stations, Emergency communication systems, Fire fighting systems, Sewage collection (and treatment), etc Service Buildings and Related Facilities: Office buildings (management, sales, accounting), Shops, Technical service facilities, Analytical laboratory, Supply warehouse, Inventory (raw materials, products, supplies) storage, Engineering, Research and Development, Environment, Maintenance buildings, etc Product Sales: Packaging facilities, Loading, Forklifts, Loaders, Warehouses, etc Environment: Water treating and reuse facilities, Incineration equipment, Solid waste or liquid waste processing, Handling equipment, etc	30%
Start–up Costs: Labor, Materials, Overhead expenses, Minor equipment, Piping, Controls, Modification, Engineering, etc	10%
Working Capital: Cash for wages, fringe benefits, local taxes, Inventories for raw materials, maintenance, and operating supplies, etc	15%

based on the process equipment, as shown in the HiPCO process flow diagram (Figure 4.1) and the CoMoCAT process flow diagram (Figure 4.2). Equipment in the process flow diagrams that are not listed on the CAPCOST program were added as user equipment and the purchased equipment costs obtained from the literature. The total capital cost estimates

were based on the chemical engineering plant cost index (CEPCI – 2005 value) CEPCI = 468, (CE, 2005). The total plant cost estimates for the HiPCO and CoMoCAT production processes are given in Table 5.3 and Table 5.4 respectively.

In Table 5.3, the total capital investment (TCI) or total plant costs for the HiPCO production process is $4.6 million. The components of the total plant costs include: the fixed capital investment (FCI – $2.97 million), the offsite facilities cost (30% FCI – $0.9 million), the start–up costs (10% FCI – $0.3 million) and the plant working capital (15% FCI – $0.45 million).

The fixed capital investment (FCI) is the total installed equipment cost for all the process equipment in the HiPCO production process. The installed equipment costs for the process equipment in the HiPCO production process include: heat exchangers ($1.04 million), process vessels ($0.26 million), towers ($0.26 million), user added equipment ($0.47 million), and gas compressor ($0.95 million).

In Table 5.4, the total capital investment (TCI) or total plant cost for the CoMoCAT process is $4.4 million. The components of the total plant costs include: the fixed capital investment (FCI – $2.8 million), the offsite facilities cost (30% FCI – $0.84 million), the start–up costs (10% FCI – $0.28 million) and the plant working capital costs (15% FCI – $0.42 million).

The fixed capital investment (FCI) is the total installed equipment cost for all the equipment in the CoMoCAT process. The installed equipment costs for the equipment in the CoMoCAT process include: heat exchangers ($0.97 million), process vessels ($0.21 million), towers ($0.37 million), user added equipments ($0.78 million) and gas compressor ($0.48 million).

Table 5.3 Total Plant Cost Estimates for HiPCO Process

Production Rate = 5,000 metric tons of carbon nanotube/yr (595 kg/ hr)
Chemical Engineering Plant Cost Index (CEPCI – 2005) for CAPCOST = 468
Installed Costs: CAPCOST's bare module cost is installed cost

Equipment Designation	**Installed Equipment Cost ($)**	
Heat Exchangers		
E–101	327,000	
E–102	125,000	
E–103	204,000	
E–104	100,000	
E–105	90,000	
E–106	191,000	
	Total	$1,040,000
Process Vessels		
V–102	204,000	
V–103	20,000	
V–104	18,000	
V–105	19,000	
	Total	$261,000
Towers		
T–101	155,000	
T–102	106,000	
	Total	$261,000
User Added Equipment		
Z–101	119,000	
Z–102	163,000	
Z–103	57,500	
Z–104	16,500	
Z–105	51,000	
Z–106	62,000	
	Total	$469,000
Gas Compressor		
C–101		$940,000
Installed Equipment / Fixed Capital Cost (FCI)		$2,971,000
Offsite Facilities Cost (30% FCI)		$892,000
Start–up Costs (10% FCI)		$297,000
Working Capital (15% FCI)		$450,000
Total Plant Cost or Total Capital Investment (TCI)		**$4,600,000**

Table 5.4. Total Plant Cost Estimates for CoMoCAT Process

Production Rate = 5,000 metric tons of carbon nanotube/yr (595 kg/ hr)
Chemical Engineering Plant Cost Index (CEPCI–2005) for CAPCOST = 468
Installed Costs: CAPCOST's bare module cost is installed cost

Equipment Designation	**Installed Equipment Cost ($)**	
Heat Exchangers		
E–201	294,000	
E–202	202,000	
E–203	175,000	
E–204	94,000	
E–205	208,000	
	Total	$973,000
Process Vessels		
V–201	156,000	
V–202	18,000	
V–203	18,000	
V–204	18,000	
	Total	$210,000
Towers		
T–201	172,000	
T–202	115,000	
T–203	77,000	
	Total	$364,000
User Added Equipments		
Z–202	136,000	
Z–203	62,000	
Z–204	252,000	
Z–205	153,000	
Z–206	85,000	
Z–207	24,000	
Z–208	14,000	
Z–209	51,000	
	Total	$777,000
Gas Compressor		
C–201		$484,000
Installed Equipment / Fixed Capital Cost (FCI)		$2,810,000
Offsite Facilities Cost (30% FCI)		$843,000
Start–up Costs (10% FCI)		$281,000
Working Capital (15% FCI)		$422,000
Total Plant Cost or Total Capital Investment (TCI)		**$4,400,000**

5.1.2 Total Product Cost

The total product cost estimates consist of the manufacturing costs and general expenses or sales related costs. The manufacturing costs predict the expense of producing the desired product, and can be further categorized into direct and indirect manufacturing expenses. The direct manufacturing costs, which include raw material costs, utilities costs, and labor costs, can be estimated from the material and energy balances around the process units included in the process flow diagrams. Other indirect manufacturing expenses such as plant overhead costs, property insurance, environmental costs, etc can be estimated as a percentage of the labor costs, plant costs and sales revenue accordingly.

In addition to the manufacturing costs, there are other general expenses or sales related costs that make up the total product costs. These general expenditures, which include administrative costs, distribution and marketing costs, research and development costs, are relatively constant with little or no variation with the plant's production capacity. The general expenses or sales related costs are typically between 20–30% of the direct production costs. The list of components in the total product estimates is given in Table 5.5.

The raw materials and utilities costs used in the total product cost estimates for the HiPCO process and CoMoCAT process were obtained from the literature: Research Chemicals, Metals, and Materials Catalogue, Alfa Aesar (2003–2004), Petroleum Technology Quarterly Catalysis Review (2005), Turton, et al., 1998, and Turton, et al, 2003.

The plant production capacities were based on the projected size of a carbon nanofiber production plant operated by Grafil, a California–based Mitsuibishi Rayon subsidiary (C & EN, 2005). The proposed plant capacity compares reasonably with the production capacity of other carbon nanofiber plants in the United States.

Table 5.5. List of Components in Total Product Cost Estimate, from Peters, et al, 1991.

Raw Materials		Direct Production Costs	Manufacturing Costs C_M	Total Product Costs C_T
Operating Labor				
Operating Supervision				
Steam	Power and Utilities			
Cooling Water				
Electricity				
Fuel				
Refrigeration				
Maintenance and Repairs				
Operating Supplies				
Laboratory Charges				
Catalysts and Solvents				
Depreciation		Fixed Costs		
Property Taxes				
Insurance				
Rent				
Royalties, Interest, Fringe Benefits		Plant Overhead Costs		
Indirect Labor Charges, Medical				
Safety and Protection, Packaging				
Payroll Overhead,				
Recreation, Restaurant				
General plant Overhead				
General Plant Overhead,				
Control Laboratories,				
Storage Facilities				
Executive Salaries		Administrative Expenses	General Expenses C_G	
Clerical Wages				
Engineering and Legal Costs				
Office Maintenance				
Communications				
Sales Offices		Distribution and Marketing Expenses		
Salesmen Expenses				
Shipping				
Advertising				
Technical Sales Service				
Research and Development				
Gross – Earnings Expense				

The raw material cost for CO was not available from the Chemical Market Reporter, and thus, the cost of CO was based on its heating value as a fuel. The cost of CO was estimated to be $0.031/kg (Indala, 2003). The raw material cost for the iron pentacarbonyl catalyst precursor used in the HiPCO process was not available from the Chemical Market Reporter, also. However, the cost of the iron pentacarbonyl was obtained from Alfa Aesar Research Chemicals, Metals and Materials Price Catalogue (2003–2004) to be $26.40 per kg.

The raw material cost for the silica–supported cobalt and molybdenum bimetallic catalysts used in the CoMoCAT process was not available from the Chemical Market Reporter or other catalyst vendor price catalogues. The cost of the supported Co–Mo bimetallic catalysts was estimated from the average value of a typical Fischer Tropsch bimetallic (Co–Pt) catalyst to be $26 per kg (Brumby, et al., 2005). The costs of regenerating the spent catalysts by replenishing the Co and Mo particles lost in the acid dissolution step and in the final nanotube product were obtained from Petroleum Technology Quarterly Catalysis Review. The direct cost for catalyst regeneration is usually $0.80 – $1.00 per kg of spent catalysts (Llorens, 2005).

The carbon nanotube market for industrial–scale applications is characterized by high prices and low–volume production methods. The sales price for the carbon nanotube product was based on the market price of large–scale, low–cost, vapor grown carbon nanofibers. The market price for the vapor grown carbon nanofibers is presently $90–$170 per kilogram (www.atp.nist.gov). However, the market price for carbon nanofibers is projected to reach $60/kg by 2006, and $30/kg by 2008. In this design, the revenue from product sales was based on a market price of $90/kg carbon nanotube (www.atp.nist.gov).

The major elements of the utilities costs in the HiPCO and CoMoCAT processes are the steam costs, natural gas costs, cooling water costs, and electricity costs. The steam requirements for the HiPCO and CoMoCAT processes were supplied in the form of high–pressure (HP) steam for process heating. The heat of vaporization for steam and heat of combustion for natural gas were used to supply the process energy requirements. The cost of HP steam and natural gas used in the total product cost estimates is $8.65 per 1000 kg (Turton, et. al, 1998), and $0.172/kg (Indala, 2003).

Boiler feed water was supplied to the waste heat boilers at 303 K to generate saturated steam at 533 K. The saturated steam generated is used for process heating in units such as the stripping column for steam stripping. The cost of boiler feed water is $2.45 per 1000 kg (Turton, et al., 2003). Cooling water was supplied to the heat exchanger water coolers, where energy was removed from process streams. The cooling water was heated from 303 K to 323 K. Excess scaling occurs above this temperature (Turton, et al, 1998). The cost of cooling water is $0.067 per 1000 kg (Turton, et al, 2003).

The economic data for the raw materials, products, boiler feed water, cooling water and high pressure steam consumed in the HiPCO and CoMoCAT processes are given in Table 5.6 and Table 5.7 respectively. The mass flow rate of raw materials, products, boiler feed water, cooling water and high pressure steam were obtained from the analysis of the material and energy balance equations for the HiPCO and CoMoCAT processes given in Appendix C. The total mass flow rates and yearly cost of the raw materials consumed in the HiPCO and CoMoCAT processes are given in Appendix D.

The annual costs of process fluids consumed, recovered and re–used, such as monoethanol amine in the HiPCO and CoMoCAT processes are included in the installed

Table 5.6. Economic Data Summary for the HiPCO Process

Product/Raw Material	Flow Rate (kg/hr) (Appendix C and D)	Price ($/kg)	Source
Carbon monoxide	2,637	0.031	Indala, 2003
Iron Pentacarbonyl	627	26.40	Alfa Aesar, 2003–2004
Carbon dioxide	2,424	0.003	Indala, 2003
Oxygen	227	0.06	Kobayashi, et al, 2005
Hydrochloric acid	236	0.015	www.basf.com
Monoethanol amine	12,322	1.606	Indala, 2003
Boiler Feed Water	6,517	2.5×10^{-3}	Turton, et al, 2003
Cooling Water	53,228	6.7×10^{-5}	Turton, et. al., 2003
HP Steam	12,000	0.00865	Turton, et. al., 1998
Natural Gas	486	0.172	Indala, 2003
Carbon Nanotube	595	90.00	www.atp.nist.gov/eao

Table 5.7. Economic Data Summary for the CoMoCAT Process

Product/Raw Material	Flow Rate (kg/hr) (Appendix C and D)	Price ($/kg)	Source
Carbon monoxide	3,471	0.031	Indala, 2003
Co–Mo Catalyst	2,380	26.00	Ptqcatalysis, 2005
Carbon dioxide	2,727	0.003	Indala, 2003
Hydrochloric acid	39	0.015	www.basf.com
Monoethanol amine	13,859	1.606	Indala, 2003
Sodium hydroxide	228	0.40	Chemical Market Reporter, 2005
Boiler Feed Water	7,333	2.5×10^{-3}	Turton, et al., 2003
Cooling Water	59,089	6.7×10^{-5}	Turton et al., 2003
HP Steam	14,000	0.00865	Turton, et. al., 2003
Natural Gas	616	0.172	Indala, 2003
Catalyst Regeneration	2,380	0.90	Ptqcatalysis, 2005
Carbon Nanotubes	595	90.00	www.atp.nist.gov/eao

costs for the production plants. The annual cost for make–up fluids supplied to compensate for fluid losses was not considered. The major electricity costs in the total product costs estimate are due to the electrical power requirements of the gas compressors. The power requirements for the gas compressors used in the HiPCO and CoMoCAT processes are 1,056 kW and 387 kW respectively. The cost of the electrical power consumed by the gas compressors were estimated at $0.06 per kWh (Turton et al., 2003).

The operating labor costs used in the total product estimates for the HiPCO and CoMoCAT production processes were based on the operating labor requirements for chemical processes given by Equation (5.1), (Turton, et al., 2003):

$$N_{OL} = (6.29 + 31.7P^2 + 0.23N_{np})^{0.5} \qquad (5.1)$$

where N_{OL} is the number of operators per shift, P is the number of processing steps that involves the handling of particulate solids, N_{np} is the number of non–particulate processing steps, which include compression, mixing, heating, cooling, and reaction (Turton, et al, 2003).

An operator typically works on the average 49 weeks per year, five 8–hour shifts a week, which translates to 245 shifts per operator per year. Since a chemical plant usually operates 24 hours/day (365days/year), nearly 1,095 shifts are required per year. Consequently, the number of operators required to provide this number of shifts can be estimated as: [(1,095 shifts per yr) / (245 shifts per operator per yr)] or 5 operators (Turton, et al., 2003).

The average hourly wage of an operator in 2001, obtained from the Bureau of Labor and Statistics in the Gulf Coast region was $25.00. This corresponds to nearly $50,000 for a 2,000–hour year, and was used to estimate the operating labor costs (Turton et

al, 2003). The sample calculations for estimating the operating labor requirements for the HiPCO and CoMoCAT processes are given in Appendix D. Other support and supervisory labor cost are estimated as a percentage of the operating labor costs.

The total product estimates for the HiPCO process and the CoMoCAT process are given in Table 5.8 and Table 5.9 respectively. The direct production costs include: raw materials costs, utility costs and labor costs. The indirect production costs include capital related costs, and general related expenses or sales related costs. The capital related costs is estimated as a percentage (25%) of the fixed capital investment, while the general expenses or sales related costs is estimated as a percentage (20%) of the direct production costs. The annual production cost ($/kg) is estimated as the annual production costs ($/yr) per annual production rate (kg/yr).

In Table 5.8, the total product costs for the HiPCO process is $187 million. The direct production cost is $154 million, which include: raw materials costs ($140 million), utilities costs ($2.4 million), and operating labor costs ($12 million). The indirect production costs include capital related costs ($1.2 million) and sales related costs ($31 million). Sample calculations for the raw materials and utility costs for the HiPCO process are given in Appendix D.

In Table 5.9, the total product costs for the CoMoCAT production process is $124 million. The direct production cost is $102 million, which include: raw materials costs ($84 million), utilities costs ($2.5 million), and labor costs ($16 million). The indirect production costs include capital related costs ($1.1 million) and general expenses or sales related costs ($21 million). Sample calculations for the raw materials and utility costs for the CoMoCAT production process are given in Appendix D.

Table 5.8. Total Product Costs Estimates for the HiPCO Process

Production Costs			**Cost ($) /yr**
A. Raw Materials	kg/hr	$ / kg	
Carbon Monoxide	2,637	0.031	688,000
Iron Pentacarbonyl	627	26.40	139,000,000
Oxygen	227	2.90	115,000
		Total (A)	**140,000,000**
B. Utilities	kg/hr	$ / kg	
HP Steam	12,000	0.00865	1,000,000
Natural Gas	486	0.172	700,000
Electricity	kW	$/kW-h	
Gas Compressor (75% efficiency)	1,056	0.06	533,000
Water	kg/hr	$ / 1000 kg	
Boiler Feed Water	6,517	2.5	140,000
Cooling Water	53,228	0.067	30,000
		Total (B)	**2,400,000**
C. Labor			
Operating Labor Costs (for 178 Operators at $50,000.00/yr)			8,900,000
Supervisor/Support (35% Operating Labor Costs)			3,100,000
		Total (C)	**12,000,000**
Capital Related Costs (25% Plant Cost, FCI)			1,200,000
General Expenses or Sales Related Costs [20% of (A+B+C)]			31,000,000
Total Product Costs			**$186,000,000**

Table 5.9 Total Product Costs Estimates for the CoMoCAT Process

Production Costs			**Cost ($) /yr**
A. Raw Materials	kg/hr	$ / kg	
Carbon Monoxide	3,471	0.031	905,000
Silica based Co–Mo Catalyst	2,380	26.00	65,000,000
Catalyst Regeneration	2,380	0.90	18,000,000
		Total (A)	**84,000,000**
B. Utilities	kg/hr	$ / kg	
HP Steam	13,000	0.00867	1,100,000
Natural Gas	616	0.172	900,000
Electricity	kW	$/kW-h	
Gas Compressor (75% Efficiency)	387	0.06	200,000
Water	kg/hr	$ / 1000 kg	
Boiler Feed Water	7,333	2.5	200,000
Cooling Water	59,089	0.067	33,000
		Total (B)	**2,500,000**
C. Labor			
Operating Labor Costs (229 Operators at $50,000.00)			12,000,000
Supervisor/Support (35% Operating Labor Costs)			4,000,000
		Total (C)	**16,000,000**
Capital Related Costs (25% Plant Cost, FCI)			1,100,000
General Expenses or Sales Related Costs [20% of (A+B+C)]			21,000,000
Total Product Costs			**$124,000,000**

5.2 PROFITABILITY ANALYSIS

The basis for profitability analysis used by private corporations is the net present value (NPV) and the rate of return (ROR). The net present value is the sum of all of the cash flows for the project discounted to the present value, usually using the company's minimum attractive rate of return (MARR), and the capital investment required. The rate of return is the interest rate in the net present value analysis that gives a zero net present value.

The net present value analysis usually take into account the profit, capital expenditures, cash flow information, and the time value of money. The time value of money refers to the growth with time for funds committed in the present with some assurance that a larger amount of money will be returned in the future. The net present value analysis is one of the key profitability indices used to measure the economic viability and feasibility of a production process.

The minimum attractive rate of return (MARR) is the interest rate that usually reflects the average return on investment for a particular corporation. Consequently, the appropriate MARR is a corporate policy matter. However, from an economist view point, an investment is attractive as long as the marginal rate of return is equal to or greater than the marginal cost of total capital invested. In this analysis, a minimum attractive rate of 25% is used in the net present value (NPV) analysis of the HiPCO and CoMoCAT process economics.

The economic life of a plant is estimated based on the length of time that the plant can be operated profitably. New more efficient technology to produce the product, new environmental restrictions and a new product from another process that displaces the current product will end the economic life of the plant. The economic life proposed for the new

HiPCO and CoMoCAT processes is based on the IRS guidelines for the write–off life of plant equipment, which is about ten years. Thus, the economic analysis for the proposed HiPCO and CoMoCAT production plants are based on an economic life of ten years for the plants. The straight line method with no salvage value is used to compute the depreciation of the plants equipments according to Equation (5.2):

$$\text{Depreciation, D} = \frac{FCI}{n} \qquad (5.2)$$

where FCI is the fixed capital investment, and n refers to the economic life of the plant.

The economic price is the price required to sell a product in order to make the projected rate of return. The economic price is estimated from the total product cost, C_T, the annual cost of capital, EUAC and annual capital expenditure, C_{cap} based on the rate of return on investment. The economic price is computed from Equation (5.3):

$$\text{Economic Price} = (\text{Total Product Cost, } C_T + \text{Annual Cost of Capital, EUAC} + \text{Annual Capital Expenditure, } C_{cap}) / \text{Product Rate} \qquad (5.3)$$

The annual cost of capital, EUAC is computed from Equation (5.4):

$$EUAC = TCI * \left(\frac{i}{[1-(1+i)^{-n}]} \right) \qquad (5.4)$$

where *TCI* is the total capital investment, *i* is the minimum attractive rate of return, and *n* is the economic life of the plant.

The net present value (NPV) analysis for the HiPCO process at a minimum attractive rate of return of 25% and an economic life of 10 years is given in Table 5.10. The annual cost of capital (EUAC) for the HiPCO process, based on a market price of $90/kg of carbon nanotube, was estimated to be $1.3 million. The annual expenditure for worn out equipments was estimated as a percentage (15%) of the fixed capital investment.

Table 5.10. Net Present Value Analysis for the HiPCO Process

Plant Capacity (kg carbon nanotubes per year)	5,000,000
Plant Installed Cost or Fixed Capital Investment, FCI	$2,971,000
Total Plant Cost or Total Capital Investment, TCI	$4,600,000
Total Product Cost, C_T	$186,000,000
Annual Expenditure for worn out equipment, C_{cap}	$450,000
Economic Life, n (years)	10
Tax Rate, 35%	0.35
Minimum Attractive Rate of Return, 25%	0.25
Depreciation, straight line with no salvage value	
Market Price (www.atp.nist.gov)	$90/kg CNT
Annual Sales, S	$450,000,000
Net Annual Income before taxes, $I_{net} = S - C_T$	$264,000,000
Net Annual Cash Flow before taxes, $CF = I_{net} - C_{cap}$	$263,500,000
Depreciation, D = Plant Installed Cost/Economic Life	$297,000
Taxable Income = $I_{net} - D$	$263,200,000
Taxes Rate = 0.35	$92,120,000
Net Income after taxes, $I_{xt} = I_{net} - taxes$	$171,880,000
Net Annual Cash Flow after taxes, $CF_{xt} = I_{xt} - C_{cap}$	$171,430,000
$i = 0.25$	
Net Present Value = $\left[-TCI + I_{xt} * \left(\frac{1-(1+i)^{-n}}{i} \right) \right]$	**$609,000,000**
$EUAC = \left[TCI * \left(\frac{i}{(1-(1+i)^{-n}} \right) \right]$	**$1,300,000**
Economic Price ($/kg) = $\frac{\$(C_T + EUAC + C_{cap})}{5{,}000{,}000 kg}$	**$38/kg**
Rate of Return, ROR (NPV = 0)	**37.4%**

The net present value for the HiPCO process was estimated from Equation (5.5):

$$\text{NPV} = \left[-TCI + I_{xt} * \left(\frac{1-(1+i)^{-n}}{i} \right) \right] \qquad (5.5)$$

The net present value calculated for the HiPCO production process, based on minimum attractive rate of return (MARR) of 25% and an economic life of ten years, was calculated to be $609 million. The ‘‘production cost’’ or economic price for carbon nanotubes produced by the HiPCO process was calculated to be $38 per kg. The rate of return (NPV = 0) on investment for the HiPCO production process was estimated from Equation (5.6):

$$\left[-TCI + I_{xt} * \left(\frac{1-(1+i)^{-n}}{i} \right) \right] = 0 \qquad (5.6)$$

The rate of return (ROR) calculated for the HiPCO production process, based on an economic life of ten years (n = 10) for the plant, was estimated to be 37.4%

The annual revenue from the HiPCO production process, based on the market price of $90/kg of carbon nanotubes and a production rate of 5 million kg of carbon nanotube per year was estimated to be $450 million. The net annual income before taxes, I_{net}, which is the difference between the annual sales revenue and the total product cost, was calculated to be $264 million. The straight line depreciation with no salvage value for the HiPCO plant over an economic life of ten years was estimated to be $0.30 million. The taxable income (35% taxes rate) was calculated to be $263 million, and the net income after taxes, I_{xt} was estimated to be $172 million.

The net present value (NPV) economic analysis for the CoMoCAT production process is given in Table 5.11. The annual cost of capital, *EUAC* for the CoMoCAT process was estimated from Equation (5.4) to be $1.2 million. The annual expenditure for worn out

Table 5.11. Net Present Value Analysis for the CoMoCAT Process

Plant Capacity (kg carbon nanotube per year)	5,000,000
Plant Installed Cost or Fixed Capital Investment, FCI	$2,810,000
Total Plant Cost or Total Capital Investment, TCI	$4,400,000
Total Product Cost, C_T	$124,000,000
Annual Expenditure for worn out equipment, C_{cap}	$420,000
Economic Life, n (years)	10
Tax Rate, 35%	0.35
Minimum Attractive Rate of Return, 25%	0.25
Depreciation, straight line with no salvage value	
Sales Prices (www.atp.nist.gov)	$90/kg CNT
Estimated Annual Sales, S	$450,000,000
Net Annual Income before taxes, $I_{net} = S - C_T$	$326,000,000
Net Annual Cash Flow before taxes, $CF = I_{net} - C_{cap}$	$325,600,000
Depreciation, D = Plant Installed Cost/Economic Life	$280,000
Taxable Income = $I_{net} - D$	$325,700,000
Taxes Rate = 0.35	$114,000,000
Net Income after taxes, $I_{xt} = I_{net} - taxes$	$212,000,000
Net Annual cash Flow after taxes, $CF_{xt} = I_{xt} - C_{cap}$	$211,600,000
$i = 0.25$	
Net Present Value = $\left[-TCI + I_{xt} * \left(\frac{1-(1+i)^{-n}}{i} \right) \right]$	**$753,000,000**
$EUAC = \left[TCI * \left(\frac{i}{(1-(1+i)^{-n}} \right) \right]$	**$1,230,000**
Economic Price ($/kg) = $\frac{\$(C_T + EUAC + C_{cap})}{5{,}000{,}000 kg}$	**$25/kg**
Rate of Return, ROR (NPV = 0)	**48.2%**

equipment was estimated to be $0.42 million. The annual revenue for the CoMoCAT production process, based on a market price of $90/kg of carbon nanotubes produced rate was estimated to be $450 million. The net annual income before taxes, I_{net} for the CoMoCAT process was calculated to be $326 million. The straight line depreciation, with no salvage value, for the CoMoCAT production plant over an economic life of ten years was calculated to be $0.28 million. The taxable income (35% taxes rate) was calculated to be $325.7 million and the net income after taxes, I_{xt} was calculated to be $212 million.

The "production cost" or economic price predicted for carbon nanotube produced by the CoMoCAT process was calculated to be $25 per kg. The net present value (NPV) for the CoMoCAT production process was computed from Equation (5.5) to be $753 million. The NPV analysis was based on a minimum attractive rate of return of 25% and an economic life of ten years. The rate of return (NPV = 0) for the CoMoCAT production process was estimated from Equation (5.6) to be 48.2%

5.3 COMPARISON OF ENERGY CONSUMPTION AND EMISSIONS FROM HiPCO AND CoMoCAT PROCESSES

The raw materials, products, energy requirements and the emissions from the HiPCO and CoMoCAT processes are given and compared in Table 5.12. The total flow rate of raw materials, which consists of the feed and other reactants, into the HiPCO and CoMoCAT processes, is 3,772 kg/hr and 4,234 kg/hr respectively. The total flow rate of carbon nanotube product and other emissions from the HiPCO and CoMoCAT production processes is 3,772 kg/hr and 4,234 kg/hr respectively.

The energy consumed by the HiPCO and CoMoCAT production processes is in the form HP steam, natural gas and electricity. The HP steam consumed by the HiPCO and

Table 5.12 Comparison of Raw Materials, Energy Consumption and Emissions from HiPCO and CoMoCAT Processes

HiPCO Process									
Material Balance									
Feed	kg/hr		**Other Reactants**	kg/hr		**Product**	kg/hr		**Emissions**	kg/hr
CO	2,637								CO_2	0.07
$Fe(CO)_5$	627		Oxygen	253		CNT	595		$FeCl_2$	2,666
			Water	255					CO_2	256
									Water	255
			3,772 kg/hr			Total (Product + Emissions) = **3,772 kg/hr**				
Total (Feed + Other Reactants) =										
Energy Consumption										
HP Steam	**12,000 kg/hr**					**486 kg/hr**			Electricity	**1,056 kW**
CoMoCAT Process										
Material Balance										
Feed	kg/hr		**Other Reactants**	kg/hr		**Product**	kg/hr		**Emissions**	kg/hr
CO	3,471								CO_2	2,727
Mo	19		Oxygen	488		CNT	595			
Co	19		Water	228					CO_2	349
			NaOH	0.01					CO	25
									Water	255
			Air						H_2O_3	26
									CO	28
									MoO_3	228
									NaOH	0.05
									$MoCl_2$	0.04
			4,234 kg/hr			Total (Product + Emissions) = **4,234 kg/hr**				
Total (Feed + Other Reactants) =										
Energy Consumption										
HP Steam	**14,000 kg/hr**					**616 kg/hr**			Electricity	**387 kW**

CoMoCAT processes is 12,000 kg/hr and 14,000 kg/hr respectively. The natural gas requirement for the HiPCO process is 486 kg/hr, and 616 kg/hr for the CoMoCAT process. Furthermore, the electrical energy consumed by the HiPCO and CoMoCAT production processes is 1,056 kW and 387 kW respectively.

The power requirement for the gas compressor in the HiPCO process is significantly higher than that of the CoMoCAT process. This is due to the higher operating pressure of the HiPCO process (450 psia) compared to the operating pressure of the CoMoCAT process (150 psia).

In addition to the production processes being economically feasible and viable, the proposed HiPCO and CoMoCAT production processes have to be environmentally acceptable. The HiPCO and CoMoCAT processes, being high temperature and high pressure processes are energy intensive with significant carbon dioxide emissions. Carbon dioxide accounts for 83% of United States greenhouse gas emissions in 1998 (EIA, 1998). Any increase in the concentration of greenhouse gases in the atmosphere increases the greenhouse effect, and the consequent adverse effect on climatic changes and in achieving sustainable development.

Sustainable development is the concept that development should meet the needs of the present without compromising of the future to meet its needs (Hertwig, et al., 2000). In order to ensure the sustainability of the proposed production processes, the carbon dioxide emissions from the HiPCO and CoMoCAT processes can be utilized as raw materials in other carbon dioxide consuming processes, such as the production of urea, and methanol.

Sustainable development is focused on economic, social and environmental areas, which are often referred to as the “triple bottom line”. The economic factors include

shareholder value and capacity for development. The social factors include human and workers rights, corporate policies, ethics, poverty alleviation and governance. The environmental factors include climate change, depletion of natural resources, and ecosystem destruction.

A comparison of these processes can be made using total cost assessment which includes the evaluation of the "triple bottom line" or the sum of economic, environmental and sustainable costs. Estimates of the sustainable cost carbon dioxide are of the order of $50 per ton. The results of this work will be used in future research to assess the best design that minimizes the "triple bottom line".

5.4 SUMMARY

In this chapter, economic decision analysis and profitability analysis measures were used to evaluate and determine the economic feasibility and viability of the proposed HiPCO and CoMoCAT carbon nanotube production technologies. The economic decision and profitability analysis measures include the total plant costs, the total product costs, the annual sales revenue, economic price, the net present value, and the rate of return. These economic decision analysis and profitability analysis measures for the HiPCO and CoMoCAT production processes are listed and compared in Table 5.13.

In Table 5.13, the total plant costs for the HiPCO and CoMoCAT production processes are $4.6 million and $4.4 million respectively. The total product costs for the HiPCO process is $186 million, whereas, the total product cost for the CoMoCAT process is $124 million dollars. The total product costs for the CoMoCAT process is significantly lower than the total capital costs of the HiPCO because of the recovery, regeneration and recycling of the silica supported bimetallic Co–Mo catalyst in the CoMoCAT process. The

Table 5.13. Economic and Profitability Analysis of HiPCO and CoMoCAT Processes

Economic Analysis Index	HiPCO Process	CoMoCAT Process
Total Plant Costs	$4.6 million	$4.4 million
Total Product Costs	$186 million	$124 million
Annual Sales Revenue	$450 million	$450 million
Economic Price	$38/kg	$25/kg
Net Present Value (NPV)	$609 million	$753 million
Rate of Return (ROR)	37.4%	48.2%

gas–phase iron pentacarbonyl catalyst precursor used in the HiPCO carbon nanotube process decomposes and cannot be recovered or recycled for another reaction cycle.

The annual sales revenue for the HiPCO and CoMoCAT production processes, based on a market price of $90/kg of carbon nanotubes and a product rate of 5 million kg of carbon nanotubes /yr is $450 million. The “production cost” or economic price calculated for carbon nanotubes produced by the HiPCO and CoMoCAT production processes are $38/kg carbon nanotube and $25/kg carbon nanotube respectively.

The net present value (NPV) for the HiPCO carbon nanotube production process is $609 million, whereas the net present value (NPV) for the CoMoCAT carbon nanotube production process is $753 million. Consequently, since the net present values for the HiPCO and CoMoCAT production processes are both positive, the proposed investment in the production of 5,000 metric tons of carbon nanotubes per year, based on the HiPCO and the CoMoCAT production technologies is economically feasible and viable, if funds are available.

Furthermore, the rate of return (NPV = 0) on investment for the HiPCO and CoMoCAT production processes, based on an economic life of 10 years, were estimated to be 37.4% and 48.2% respectively. Since the rate of return (ROR) calculated for the HiPCO and CoMoCAT production processes is greater than the minimum attractive rate of return (MARR) of 25% used in the profitability analysis, the HiPCO and CoMoCAT production processes are considered to be profitable.

The conclusions for this research will be given and the recommendations for future work will also be made in the next chapter.

CHAPTER SIX: CONCLUSIONS AND RECOMENDATIONS FOR FUTURE RESEARCH

The various production processes for the synthesis of carbon nanotubes and post – synthesis purification methods were reviewed and compared to identify scalable carbon nanotube production technologies. The selection criteria used include process operating conditions such as temperature and pressure, catalyst performance, continuous operation, carbon source, cost and availability of raw materials, product yield and reactant selectivity to form carbon nanotubes.

The chemical vapor deposition technique was identified to offer a more promising route to developing scalable carbon nanotube production technologies. Two potentially scalable carbon nanotube production technologies; HiPCO and CoMoCAT processes, were selected, and used as a basis for the conceptual design of two commercial–scale plants. The proposed carbon nanotube production plants have a design capacity of 5,000 metric tons of carbon nanotubes per year each.

The process models for the HiPCO and CoMoCAT carbon nanotube production technologies were developed and formulated in Chapter Three. The material and energy balance equations for the HiPCO and CoMoCAT processes were evaluated and their results analyzed in Chapter Four.

Furthermore, economic decision and profitability analysis were used to determine the economic feasibility and viability of the proposed carbon nanotube production technologies. The economic decision and profitability analysis for the HiPCO and CoMoCAT production processes were presented in Chapter Five.

In this chapter, the conclusions of this research work and suggestions for future research work will be presented.

6.1 CONCLUSIONS

The conceptual design of two scalable carbon nanotube production technologies, based on the chemical vapor deposition technique, was carried out. The two production technologies are: the high pressure carbon monoxide (HiPCO) process, and the cobalt–molybdenum catalyst (CoMoCAT) process. The design capacity for the proposed carbon nanotube production plants was 5,000 metric tons (595 kg/hr) of carbon nanotubes per year.

The HiPCO and CoMoCAT production technologies were designed and developed as continuous production processes, with continuous recovery and recycle of unconverted carbon monoxide reactant. Furthermore, post–synthesis purification processes were also developed to separate and purify the desired carbon nanotube product from other reaction products, byproducts and/or non–products.

The high–pressure carbon monoxide (HiPCO) process is a gas–phase homogeneous process that employs a floating catalyst approach, whereby the growth catalyst is formed *in situ* during the growth process. Carbon nanotubes are produced in the HiPCO process from the disproportionation of carbon monoxide over catalytic iron nanoparticles at 1,323 K and 450 psia. The catalytic iron nanoparticles are formed *in situ* by the decomposition of the iron pentacarbonyl catalyst precursor. The CO conversion and selectivity to carbon nanotubes used is 20 mol% and 90% respectively. The carbon nanotubes produced contain amorphous carbon and residual iron particles.

In order to remove the amorphous carbon and residual iron impurities from the carbon nanotube product, a multi–step purification processes, which include oxidation, acid treatment, and filtration, was adopted for the HiPCO process. The amorphous carbon and residual iron particles in the nanotube product are selectively oxidized in air to carbon

dioxide and iron oxides. The iron oxides formed are subsequently removed by dissolution in concentrated hydrochloric acid solution.

However, due to the organometallics source of the catalyst particles, the final carbon nanotube product still contains iron chloride. The final product contains 97 mol% carbon nanotubes (595 kg/hr), and 3 mol% residual iron metal particles (0.03 kg/hr).

The cobalt–molybdenum catalyst (CoMoCAT) process is a heterogeneous gas–phase process that involves the catalytic decomposition of carbon monoxide on silica–supported Co–Mo bimetallic catalyst particles. The CoMoCAT process employs a fluidized bed reactor in which the supported catalysts are fluidized in a hot stream of carbon monoxide at 1,223 K and 150 psia.

The carbon monoxide conversion and selectivity to carbon nanotube for the CoMoCAT production process is 20 mol% and 80% respectively. The carbon nanotube and amorphous carbon produced are grown and remain attached to the supported catalysts particles. The carbon nanotubes–silica support interaction is broken by treating the reactor product with sodium hydroxide.

The carbon nanotube is subsequently separated from amorphous carbon, silica, and the bulk of the cobalt and molybdenum particles by the froth flotation purification process. However, the purity of the carbon nanotubes produced from the froth flotation process is 80%, as the nanotube product still contains significant residual cobalt and molybdenum particles.

The bulk of the residual cobalt and molybdenum particles in the nanotube product from the flotation column are subsequently removed by dissolution in concentrated hydrochloric acid. The final carbon nanotube product from the acid treatment purification

step contains 97 mol% carbon nanotubes (595 kg/hr), 1.5 mol% cobalt (0.02 kg/hr) and 1.5 mol% molybdenum particles (0.03 kg/hr).

Economic decision and profitability analysis for the HiPCO and CoMoCAT production processes showed that both production technologies are economically feasible and viable. The net present value economics for both plants were based on a minimum attractive rate of return of 25% and an economic life of ten years.

The net present value for the HiPCO production process was calculated to be $609 million, and the economic price calculated for carbon nanotubes produced by the HiPCO process was $38 per kg of carbon nanotube. The net present value for the CoMoCAT production process was calculated to be $753 million, and the economic price calculated for carbon nanotubes produced by the CoMoCAT process was $25 per kg of carbon nanotube.

The rate of return (NPV = 0) on investment for the HiPCO and CoMoCAT production processes, based on an economic life of 10 years were estimated to be 37.4% and 48.2% respectively. The rate of return calculated for the HiPCO and CoMoCAT processes is greater than the minimum attractive rate of return (MARR) of 25% used in the profitability analysis. Consequently, both the HiPCO and CoMoCAT production processes are considered to be profitable.

The economic feasibility and viability of the HiPCO and CoMoCAT production technologies with a design capacity of 5,000 metric tons of carbon nanotubes each have been demonstrated in this research. The economic price proposed for the HiPCO and CoMoCAT production processes are orders of magnitude less than the prevalent market price of carbon nanotubes. Based on these results, the route to multi tons production of high

purity carbon nanotubes at affordable prices could soon become a reality and not hype as once touted in some circles.

6.2 RECOMMENDATIONS FOR FUTURE RESEARCH

Since both the HiPCO and CoMoCAT production processes occur at high temperatures and pressures, the production costs can be greatly reduced by exploring low–temperature synthesis of carbon nanotubes at moderate pressures. This can be achieved by improved catalyst specificity and selectivity. Carbon nanotubes have been reportedly synthesized via a single–source precursor route at 750 K (Liu, et. al., 2003).

The carbon monoxide conversion to carbon nanotubes in the HiPCO and CoMoCAT reactors is low (20 mol%). The CO conversion to carbon nanotubes in the HiPCO and CoMoCAT processes can be improved by more accurate modeling and parameter estimation of the carbon nanotube reaction kinetics. Presently, the kinetic model of the Boudouard reaction mechanism is not fully understood, while the catalyst decomposition and growth nucleation process is still being explored.

It has been suggested that the addition of methane to the carbon monoxide feedstock increases the carbon nanotube yield in the HiPCO process. Consequently, the use of alternative feedstock as carbon source should be considered in future work. Some possible alternative feedstock that can be used as carbon sources include: acetylene, coal, toluene, etc. Furthermore, less toxic and less expensive catalyst precursors should be substituted for iron pentacarbonyl in the HiPCO process.

It has been reported in the literature that the use of co–catalysts such as palladium, chromium and platinum can be used to decrease the growth temperature of carbon nanotubes to 500–550 ^{o}C (Han, et al, 2001). Consequently, different combination

metal catalyst particles such as iron, alumina, nickel, yttrium, palladium, etc, on various substrates should be investigated in the CoMoCAT production process.

The carbon dioxide produced as a byproduct of the CO disproportionation reaction can be captured and used as raw material to produce other industrially important products. Consequently, alternative absorption technologies like the use of molecular sieves to capture the carbon dioxide from the process streams should be considered in future work.

In future work, an assessment of these processes should be carried out to develop the best process design that is economically viable and environmentally acceptable. This assessment can be made by using the “triple bottom line” incorporating economic, environmental and sustainable costs.

REFERENCES

Ajayan, P. M., 2000, "Carbon Nanotubes", *Handbook of Nanostructured Materials and Nanotechnology*, 5, 375–403.

Ajayan, P.M., Charlier, J.C., Rinzler, A.G., 1999, *Fifth Annual German–American Frontiers of Science Symposium*, PNAS 96:14199–14200.

Alexandrou, I., Wang, H., Sano, N., Amaratunga, G.A.J., 2003, "Structure of carbon onions and nanotubes formed by arc in liquids", Journal of Chemical Physics, 120(2), 1055-1058.

Alfa Aesar, 2004, "*Research Chemicals, Metals, and Materials Catalogue*" .

Andrews, R., Jacques, D., Qian, D., Rantell, T., 2002, "Multi-wall Carbon Nanotubes: Synthesis and Application", *Account of Chemical Research*, 35 (12):1008–1017.

Bandow, S., Rao, A. M., Williams, K.A., Thess, A., Smalley, R. E., Eklund, P. C., 1997, "Purification of Single–Wall Carbon Nanotubes by Microfiltration", Journal of Physical Chemistry B, 101, 8839–8842.

Baughman, R. H., Zakhidov, A., A., de Heer, W., A., 2002 "Carbon Nanotubes– The Route Toward Applications", Science Compass Review, 297, 787–792.

Branan, C., 2002, "*Rules of Thumb for Chemical Engineers*", Third Edition, Gulf Professional Publishing, New York.

Bronikowski, M., J., Willis, P., A., Colbert, T., D., Smith, K. A., Smalley, R. E., 2001, "Gas Phase Production of Carbon Single Walled Nanotubes from Carbon Monoxide via the HiPCO Process: A Parametric Study", Journal Vacuum Science Technology A, 19(4), 1800–1805.

Brumby, H. A., Verhelst, M. P., 2005, "Recycling of GTL Catalysts", *ptqcatalysis*, Petroleum Technology Quarterly Review, p. 15.

C & EN, 2005, "Chemical Engineering Product Cost Index", *Chemical & Engineering News*, June, 2005

CEP, 2003, "Nanotechnology", *Chemical Engineering Progress*, November, 2003

Chemical Market Reporter, 2005, "Sodium Hydroxide", *Chemical Market Reporter*, September, 2005

Cheung, C.L., Kurtz, A., Park, H., Lieber, C.M., 2002, "Diameter–controlled synthesis of carbon nanotubes", Journal Physical Chemistry B, 106, 2429–2433.

Chiang, I. W., Brinson, B. E., Smalley, R. E., Margrave, J. L., Hauge, R. H., 2001, "Purification and Characterization of Single–Wall Carbon Nanotubes", Journal of Physical Chemistry B, 105, 1157–1161.

Chiang, I. W., Brinson, B. E., Huang, A. Y., Willis, P. A., Bronikowski, M. J., Smalley, R. E., Margrave, J. L., Hauge, R. H., 2001, "Purification and Characterization of Single–Wall Carbon Nanotubes (SWNTs) Obtained from the Gas–Phase Decomposition of CO (HiPCO Process)", Journal of Physical Chemistry B, 105, 8297–8301.

Choi, H.C., Kim, W., Wang, D., Dai, H., 2002, "Delivery of Catalytic Metal Species onto Surfaces with Dendrimer Carriers for the Synthesis of Carbon Nanotubes with Narrow Diameter Distribution", Journal of Physical Chemistry B, 106(48), 12361–12365.

Corrias, M., Caussat, B., Ayral, A., Durand, J., Kihn, Y., Kalck, Ph. Serp, Ph., 2003, "Carbon Nanotubes Produced by Fluidized Bed Catalytic CVD: First Approach of the Process", Chemical Engineering Science, 58, 4475–4482.

Coquay, P., Vandenberghe, R. E., De Grave, E., Fonseca, A., Piedigrosso, P., Nagy, J. B., 2002, "X–ray Diffraction and Mossbauer characterization of an Fe/SiO2 Catalyst for the Synthesis of Carbon Nanotubes", Journal of Applied Physics, 92 (3), 1286–1291.

Coulson, J. M., Richardson, J. F., 1996, "Chemical Engineering Design", Chemical Engineering, Volume 6, Second Edition.

Daenen, M., De Fouw, R.D., Hamers, B., Janssen, P.G.A., Schouteden, K., Veld, M.A.J., 2003, *The Wondrous World of Carbon Nanotubes*, Eindhoven University of Technology.

Dateo, C. E., Gokcen, T., Meyyappan, M., 2002, "Modeling of the HiPCO Process for Carbon Nanotube Production 1: Chemical Kinetics", Journal of Nanoscience and Nanotechnology, 2 (5), 523–534.

Davis, V. A., 2005, Carbon Nanotechnology Laboratory, Chemical Engineering Department, Rice University, Private Communication, January, 2005.

De Jong, K. P., Geus, J. W., 2002, "Carbon Nanofibers", 497 – 510.

Douglas, J. M., 1988, "*Conceptual Design of Chemical Processes*", McGraw–Hill Chemical Engineering Series.

Dresselhaus, M., Dresselhaus, G., Eklund, P.C., Riico, 1998, Carbon Nanotubes, *Physics World* (http: physicsweb.org/article/world/11/1/9).

Dresselhaus, M.S., Dresselhaus, G., Eklund, P.C., 1996, "*Science of Fullerenes and Carbon Nanotubes*", Academy Press.

Ebbesen, T.W., Ajayan, P.M., 1992, “Large scale Synthesis of Carbon Nanotubes”, Nature, 358, 220-222

EIA, 1998, Greenhouse Gases, Global Climate Change, and Energy http://www.eia.doe.gov/oiaf/1605/ggccebro/chapter1.html (accessed August, 2005).

Eklund, P. C., Pradhan, B. K., Kim, U. J., Xiong, Q., 2002, “Large–Scale Production of Single–Walled Carbon Nanotubes using Ultrafast Pulses from a Free Electron Laser”, Nanoletters, 2 (6), 561–566.

Emmenegger, C., Bonard, J.M., Mauron, P., Sudan, P., Lepora, A., Groberty, B., Zuttel, A., Schlapbach, L., 2003, “Synthesis of Carbon Nanotubes over Fe Catalyst on Aluminum and Suggested Growth Mechanism”, Carbon, 41, 539–547.

Felder, R. M., Rousseau, R. W., 2000, “*Elementary Principles of Chemical Processes*”, Third Edition, John Wiley, New York.

Garrett, D. E., 1989, “*Chemical Engineering Economics*”, Fifth Edition, McGraw – Hill, New York.

Georgakilas, V., Voulgaris, D., Vasquez, E., Prato, M., Guldi, D. M., Kukovecz, A., Kuzmany, H., 2002, “Purification of HiPCO Carbon Nanotubes via Organic Functionalization”, Journal of American Chemical Society, 124, 14318–14319.

Guillard, T., Cetout, S., Flamant, G., Laplaze, D., 2000, “Solar Production of Carbon Nanotubes; Structure, Evolution with Experimental Conditions”, Journal of Materials Science, 35, 419–425.

Guo, T., Nikolaev, P., Thess, A., Colbert, D. T., Smalley, R. E., 1995, “Catalytic Growth of Single–Walled Carbon Nanotubes by Laser Vaporization”, Chemical Physics Letters, 243, 49–54.

Han, H. J., Yoo, J., 2002, “Low Temperature Synthesis of Carbon Nanotubes by Thermal Chemical Vapor Deposition using Co–Catalyst”, Journal of the Korean Physical Society, 39, S116–S119.

Harutyunyan, A. R., Pradhan, B. K., Chang, J., Chen, G., Eklund, P. C., 2002, “Purification of Single–Wall Carbon Nanotubes by Selective Microwave Heating of Catalyst Particles”, Journal of Physical Chemistry B, 106, 8671–8675.

Height, M.J., Howard, J.B., Tester, J.W., 2003, “Flame Synthesis of Carbon Nanotubes”, Materials Research Society Symposia Proceedings, 772, 55–61.

Hernadi, K., Fonseca, A., Nagy, J. B., Bernaerts, D., Riga, J., Lucas, A., 1996, “Catalytic Synthesis and Purification of Carbon Nanotubes”, Synthetic Metals, 77, 31–34.

Hertwig, T. A., Xu, A., Nagy, B., Pike, R. W., Hopper, J. R., Yaws, C. L., 2002, "A Prototype System for Economic, Environmental and Sustainable Optimization of a Chemical Complex", *Tools for Sustainable Session, AIChE Annual Meeting*, Los Angeles.

Hlavaty, J., Kavan, L., Kasahara, N., Oya, A., 2001, "Polymerization of 1–iodohexa–1,3,5–triyne and hexa–1,3,5–triyne: A New Synthesis of Carbon Nanotubes at Low Temperatures", Chemical Communication, 737–738.

Hong, E. H., Lee, K., Oh, S. O., Park, C., 2003, "Synthesis of Carbon Nanotubes using Microwave Radiation", Advanced Functional Materials, 13(12), 961–966.

Hou, P. X., Bai, S., Yang, Q. H., Liu, C., Cheng, H. M., 2002, "Multi–step Purification of Carbon Nanotubes", Carbon, 40, 81–85.

Hsu, W. K., Terrones, M., Hare, J. P., Terrones, H., Kroto, H. W., Walton, D. R. M., 1996, "Electrolytic Formation of Carbon Nanostructures", Chemical Physics Letters, 262, 161–166.

Hu, G., Cheng, M., Ma, D., Bao, X., 2003, "Synthesis of Carbon Nanotube Bundles with Mesoporous Structure by a Self–Assembly Solvothermal Route", Chemical Materials, 15, 1470–1473.

Hydrochloric Acid Market Price: http://www.basf.com (accessed July, 2005)

Hydrochloric Acid Recovery: http://www.acidrecovery.com (accessed May, 2005)

Igbinoghene, D.C., 2004, "*Chemical Process Calculations Manual*", McGraw-Hill, New York.

Iijima, S., Ajayan, P. M., Ichiashi, T., 1992, "Growth Model for Carbon Nanotubes", Physical Review Letters, 69 (21), 3100–3103.

Indala, S., 2004, "Development and Integration of New Processes Consuming Carbon Dioxide In Multi Plant Chemical Production", M.S. Thesis, Chemical Engineering Department, Louisiana State University.

Jeong, S.H., Lee, O.J., Lee, K. H., 2003, "Synthesis of Carbon Nanotubes with Prescribed Dimensions", Presentation at 2003 AIChE Annual Meeting.

Journet, C., Maser, W.K., Bernier, P., Loiseau, A., Lamy de la Chapelle, M., Lefrant, S., Denlard, P., Lee, R., Fischer, J.E., 1997, "Large–scale Production of Single–walled Carbon Nanotubes by Electric–Arc Technique", Nature, 388, 756– 758.

Jung, S.H., Kim, M. R., Jeong, S. H., Kim, S. U., Lee, O. J., Lee, K. H., Suh, J. H., Park, C.K., 2003, "High–Yield Synthesis of Multi–Walled Carbon Nanotubes by Arc Discharge in Liquid Nitrogen", Applied Physics A 76, 285-286.

Kobayashi, H. S., Hassel, B. V., 2005 "CO_2 Reduction by Oxy–Fuel Combustion: Econnomics and Opportunities", GCEP Advance Coal Workshop, Provo, Utah.

Komatsu, T., Inoue, H., 2002, "Synthesis of Thin Wall Multi–Walled Carbon Nanotubes by Catalytic Decomposition of Hydrocarbon using Metallophtalocyanine as Catalyst", Molecular Crystal Liquid Crystal, 387, (337)/113–(340)/116.

Kunii, D., Levenspiel, O., 1968, "*Fluidization Engineering*", Chemical Engineering Series, First Edition, Butterworth-Heinemann.

Lee, D. C., Mikulev, F. V., Korgel, B. A., 2004, "Carbon Nanotube Synthesis in Supercritical Toluene", Journal of American Chemical Society, 126, 4951–4957.

Lee, S.J., Baik, H.K., Yoo, J., Han, J.H., 2002, "Large Scale Synthesis of Carbon Nanotubes by Plasma Rotating Arc Discharge Technique", Diamond and Related Materials, 11, 914–917.

Li, M., Hu, Z, Wang, X., Wu, Q., Chen, Y., Tian, Y., 2004, "Low Temperature Synthesis of Carbon Nanotubes using Corona discharge Plasma at Atmospheric Pressure", Diamond and Related Materials, 13, 111–115.

Liu, X., Huang, B., Coville, N.J., 2002, "The Influence of Synthesis Parameters on the Production of Multiwalled Carbon Nanotubes by the Ferrocene Catalyzed Pyrolysis of Toluene", Fullerenes, Nanotubes and Nanostructures, 10(4), 339–352.

Liu, J., Shao, M., Chen, X., Yu, W., Liu, X., Qian, Y., 2003, "Large–Scale Synthesis of Carbon Nanotubes by an Ethanol Thermal Reduction Process", Journal of American Chemical Society", 125, 8088–8089.

Liu, J., Shao, M., Xie, Q., Kong, L., Yu, W., Qian, Y., 2003, "Single–Source Precursor Route to Carbon Nanotubes at Mild Temperature", Carbon, 41, 2101–2104.

Llorens, D. 2005, "Reformer Catalyst Regeneration", *ptqcatalysis*, Petroleum Technology Quarterly Review, p.18.

Luyben, W., L., Wenzel, L., A., 1988, "*Chemical Process Analysis: Mass and Energy Balances*", Prentice Hall Series.

Lyu, S.C., Liu, B.C., Lee, S.H., Park, C.Y., Kang, H.K., Yang, C.W., Lee, C.J., 2004, "Large–scale Synthesis of High–Quality Single–walled Carbon Nanotubes by Catalytic Decomposition of Ethylene", Journal of Physical Chemistry B, 108, 1613–1616.

Lyu, S.C., Liu, B. C., Lee, S. H., Park, C. Y., Kang, H. K., Yang, C.W., Lee, C. J., 2003, "Large–Scale Synthesis of High–Quality Double–Walled Carbon Nanotubes by Catalytic Decomposition of n–Hexane", Journal of Physical Chemistry B, 108, 2192–2194.

Maruyama, S., Marukami, Y., Miyauchi, Y., Chashi, S., 2003, "Catalytic CVD Generation and Optical Characterization of Single–Walled Carbon Nanotubes from Alcohol", Presentation at AIChE Annual Meeting, San Francisco, CA.

Maser, K.W., Benito, A.M., Munoz, E., Marta de Val, G., Martinez, M.T., Larrea, A., Fuente, G.F., 2001, "Production of Carbon Nanotubes by CO_2–laser Evaporation of various Carbonaceous Feedstock Materials", Nanotechnology, 12, 147–151.

Mauron, Ph., Emmenegger, Ch., Sudan, P., Wenger, P., Rentsch, S., Zuttel, A., 2003, "Fluidized–bed CVD Synthesis of Carbon Nanotubes on Fe_2O_3/MgO", Diamond and Related Materials, 12, 780–785.

McBride, B. J., Zehe, M., Gordon, S., 2002, "NASA Glenn Coefficients for Calculating Thermodynamic Properties", NASA/TP – 2002 – 211556.

Meyyappan, W., Srivasta, D., 2003, "*Handbook of Nanoscience, Engineering and Technology*", *18*:18-1–18-26.

Meyyappan, M., 2005, "Growth: CVD and PECVD", *Carbon Nanotubes: Science and Applications*, 99–116.

Moravsky, A. P., Wexler, E. U., Loutfy, R. O., 2005, "Growth of Carbon Nanotubes by Arc Discharge and Laser Ablation", *Carbon Nanotubes: Science and Applications*, 65–98

Motiei, M., Hacohen, Y.R., Calderon–Moreno, J., Gedanken, A., 2001, "Preparing Carbon Nanotubes and Nested Fullerenes from Supercritical CO_2 by a Chemical Reaction", Journal of American Chemical Society, 123, 8624–8625.

Munoz, E., Maser, W.K., Benito, A.M., Fuente, G.F., Righi, A., Sauvajol, J.L., Anglaret, E., Maniette, Y., 2000, "Single–walled Carbon Nanotubes Produced by cw CO_2–laser Ablation: Study of Parameters Important for their Formation", Applied Physics A, Material Science and Processing, 70, 145–151.

Nerushev, O. A., Dittmar, S., Morjan, R. E., Rohmund, F., Campbell, E. E. B., 2003, "Particle Size Dependence and Model for Iron–catalyzed Growth of Nanotubes by Thermal Chemical Vapor Deposition", Journal of Applied Physics, 93(7), 4185–4190.

Nikolaev, P, 2004, "Gas–Phase Production of Single–Walled Carbon nanotubes from Carbon Monoxide: A Review of the HiPCO Process", Journal of Nanoscience and Nanotechnology, 4 (4), 307–316.

Nikolaev, P., Bronikowski, M. J., Bradley, R. K., Rohmund, F., Colbert, D. T., Smith, K. A., Smalley, R. E., 1999, "Gas–phase Catalytic Growth of Single–walled Carbon Nanotubes from Carbon Monoxide", Chemical Physics Letters, 313, 91–97.

Niyogi, S., Hu, H., Hamon, M. A., Bhowmik, P., Zhao, B., Rozenzhak, S. M., Chen, J., Itkis, M. E., Meier, M. S., Haddon, R. C., 2001, "Chromatographic Purification of Soluble Single–Walled Carbon Nanotubes (s–SWNTs)", Journal American Chemical Society, 123, 733–734.

O'Loughlin, J.L., Kiang, C.H., Wallace, C.H., Reynolds, T.K., Rao, L., Kaner, R.B., 2001, "Rapid Synthesis of Carbon Nanotubes by Solid–State Metathesis Reactions", Journal of Physical Chemistry B, 105, 1921–1924.

Park, Y. S., Choi, Y. C., Kim, K. S., Chung, D. C., Bae, D. J., An, K.H., Lim, S. C., Zhu, X., Y., Lee, Y. H., 2001, "High Yield Purification of Multi–walled Carbon Nanotubes by Selective Oxidation during Thermal Annealing", Carbon, 39, 655–661.

Perez–Cabero, M., Rodriguez–Ramos, I., Guerrero–Ruiz, A., 2003, "Characterization of carbon nanotubes and carbon nanofibers prepared by catalytic decomposition of acetylene in a fluidized bed reactor", Journal of catalysis, 215, 305–316.

Perry, R. H., Green, D., 1984, "*Perry's Chemical Engineers Handbook*", Fifth Edition, McGraw Hill, New York, NY

Peters, M. S., Timmerhaus, K. D., West, R., E., 2003, "*Plant Design and Economics for Chemical Engineers*", Fifth Edition, McGraw–Hill, New York.

Pisan, C., Chavadej, S., Kitiyana, B., Scamehorn, J. F., Resasco, D. E., 2004, "Separation of Single – walled Carbon nanotubes from Silica by Froth Flotation Technique"

Qian, D., Wagner, G. J., Liu, W.K., Yu, M., Ruoff, R.S., 2003, *Handbook of Nanoscience, Engineering and Technology* 19:19-1–19-63.

Resasco, D.E., Alvarez, W.E., Pompeo, F., Balzano, L., Herrera, J.E., Kitiyanan, B., Borgna, A., 2001, "A Scalable Process for Production of Single Walled Carbon Nanotubes (SWNTs) by Catalytic Disproportionation of CO on a Solid Catalyst", Journal of Nanoparticle Research, 4, 1 – 6.

Roman, C., Holister, P., Harper, T., 2004 "Nanotubes", Cientifica

Rinzler, A. G., Liu, J., Dai, H., Huffman, C.B., Rodriguez–Macias, F. J., Boul, P. J., Lu, A. H., Heymann, D., Colbert, D. T., Lee, R. S., Fischer, J. E., Rao, A. M., Eklund, P. C.,

Smalley, R. E., 1998, “Large–scale purification of single–wall carbon nanotubes: process, product, and characterization”, Applied Physics A, 67, 29–37.

Scott, C. D., Povitsky, A, Dateo, C., Willis, P. A., Smalley, R. E., 2003, “Iron Catalyst Chemistry in Modeling a High–Pressure Carbon Monoxide Reactor”, Journal of Nanoscience and Nanotechnology, 3, 63–73.

Shah, N., Wang, Y., Panjala, D., Huffman, G.P., 2004, Energy and Fuels, A–I.

Shao, M., Wang, D., Yu, G., Hu, B., Yu, W., Qian, Y., 2004, “The Synthesis of Carbon Nanotubes at Low Temperature via Carbon Suboxide Disproportionation”, Carbon, 42, 183–185.

Shelimov, K. B., Esenaliev, R. O., Rinzler, A. G., Huffman, C. B., Smalley, R.E., 1998, “Purification of single–wall carbon nanotubes by ultrasonically assisted filtration”, Chemical Physics Letters, 282, 429–434.

Smith, J., M., Van Ness, H. C., Abbott, M. M., 1996, *Introduction to Chemical Engineering Thermodynamics*, Fifth Edition, McGraw–Hill, New York.

Thien–Nga, L., Hernadi, K., Ljubovic, E., Garaj, S., Forro, L., 2002, “Mechanical Purification of Single–walled Carbon Nanotube Bundles from Catalytic Particles”, Nano Letters, 2(12), 1349–1352.

Terrones, M, 2003, “Science and Technology of the Twenty – First Century: Synthesis, Properties and Applications of Carbon Nanotubes”, Annual Review of Materials Research, 33, 419–509.

Traceski, F. T., 1999, “Assessing Industrial Capabilities for Carbon Fiber Production”, Acquisition Review Quarterly, 179–194.

Turton, R., Bailie, R., C., Whiting, W., B., Shaeiwitz, J.A., 2003, “*Analysis, Synthesis and Design of Chemical Processes*”, Second Edition, Prentice Hall Series.

Turton, R., Bailie, R., C., Whiting, W., B., Shaeiwitz, J.A., 1998, “*Analysis, Synthesis and Design of Chemical Processes*”, Second Edition, Prentice Hall Series.

Ulrich, G. D., 1984, “*A Guide To Chemical Engineering Process Design and Economics*”, John Wiley and Sons, New York.

Vasquez, E., Georgakilas, V., Prato, M., 2002, “Microwave–Assisted Purification of HiPCO Carbon Nanotubes”, Chemical Communications, 20, 2308–2309.

Vapor Grown Carbon Fiber Case Study, http://www.atp.nist.gov/eao/grc04-863/chapt3.html (accesses November, 2004)

Wark, K., Warner, C. F., Davis, W. T., 1998, “Air Pollution: Its Origin and Control”, Third Edition.

Weizhog, Q., Fei, W., Zhanwen, W., Tang, L., Hao, Y., Guohua, L., Lan, X., Xiangyi, D., 2003, “Production of Carbon Nanotubes in a Packed Bed and a Fluidized Bed”, AIChE Journal, 49(3), 619–625.

Yates, J., G., 1983, “Fundamentals of Fluidized Bed Chemical Processes”, Butterworths.

Yu, J., Lucas, J., Strezov, V., Wall, T., 2003, “Coal and Carbon Nanotube Production”, Fuel, 82, 2025–2032.

APPENDIX A

THERMODYNAMIC DATA OF PROCESS STREAMS

The reference condition for enthalpy is the elements that constitute the reactants and products at 298 K and the non–reactive molecular species at any convenient temperature. The specific enthalpy, $h_k^{(i)}$ and specific heat capacity, $C_p^{(i)}$ of component, *i* in stream *k*, is represented as a function of temperature in terms of thermodynamic data coefficients, $a_1, a_2, a_3, a_4, a_5,$ and b_1 as given by McBride et. al., 2002:

$$h_k^{(i)}(T) = R*(a_1^{(i)}T + \frac{a_2^{(i)}}{2}T^2 + \frac{a_3^{(i)}}{3}T^3 + \frac{a_4^{(i)}}{4}T^4 + \frac{a_5^{(i)}}{5}T^5 + \frac{b_1^{(i)}}{T}) \text{ kJ/kgmol}$$

$$C_p^{(i)}(T) = R*(a_1^{(i)} + a_2^{(i)}T + a_3^{(i)}T^2 + a_4^{(i)}T^3 + a_5^{(i)}T^4) \text{ kJ/kgmol K}$$

Universal Gas Constant, $R = 8.314$ kJ/kgmol K

T = Temperature, K

The superscript '*i*' and subscript '*k*' refer to the component species and stream numbers respectively. The thermodynamic coefficients, $a_1, a_2, a_3, a_4, a_5,$ and b_1 in the specific enthalpy and specific heat capacity functions for individual component reaction species are given in Table A.1.

The enthalpy of other reaction species that is not available as a function of temperature is estimated from the mean specific heat capacity and the enthalpy of formation at the reference states. The mean specific capacity and the corresponding enthalpy of formation at 298 K for these reaction species are given in Table A.2.The mean specific heat capacity for carbon nanotube is presently not available in the literature. However, since carbon nanotubes structures are based on hexagonal lattice of

Table A.1 Thermodynamic Coefficient Data for Specific Enthalpy and Specific Heat Capacity, from McBride, et al., 2002

Component	Temperature (K)	a_1	a_2	a_3	a_4	a_5	b_1
CO (g)	1000–6000	5.9167E+00	-5.6643E-04	1.3988E-07	-1.7876E-11	9.6209E-16	-1.2466E+03
	200–1000	5.7245E+00	-8.1762E-03	1.4569E-05	-1.0877E-08	3.0279E-12	-1.3031E+04
CO_2 (g)	1000–6000	8.2915E+00	-9.2231E-05	4.8636E-09	-1.8910E-12	6.3300E-16	-3.9083E+04
	200–1000	5.3017E+00	2.5038E-03	-2.1273E-07	-7.6899E-10	2.8496E-13	-4.5281E+04
Fe_2O_3(s)*	273–1100	1.0340E-01	6.7110E-05	-1.7720E+03	0.0000E+00	0.0000E+00	0.0000E+00
$Fe(CO)_5$(g)	200–600	5.4002E+01	-6.9354E-02	1.0267E-04	-7.2073E-08	1.9589E-11	-5.8545E+04
NaOH	594–1000	1.0778E+01	-7.1117E-04	0.0000E+00	0.0000E+00	0.0000E+00	-5.3083E+04
H_2	200–1000	3.7824E+00	-2.9967E-03	9.8473-06	-9.6813E-09	3.2437E+00	-1.0639E+03
O	200–1000	3.7824E+00	-2.9967E-03	9.8473-06	-9.6813E-09	3.2437E+00	-1.0639E+03
H_2O (l)	273–373	7.2558E+01	-6.6244E-01	2.5620E-03	-4.3659E-06	2.7818E-09	-4.1886E+04
H_2O(g)	373–600	4.1986E+00	-2.0364E-03	6.5204E-06	-5.4880E-09	1.7720E-12	3.0294E+04
H	273–600	9.3110E+00	3.00095E-01	-1.8180E-04	4.6557E-08	0.0000E+00	0.0000E+00
MEA#							

* Coulson, et al, 1996

Felder, et al, 2000

Table A.2. Mean Specific Heat Capacities and Enthalpy of Formation (Perry, 1984)

Reference Temperature T_{ref} : 298 K, 1 bar

Component	$\Delta H_f^o\,(kJ/kgmol)$	$C_{p(mean)}\,(kJ/kgmol*K)$
Carbon Nanotube*	517,208	19.6
Amorphous Carbon	0	19.4
Silica	– 849.8	79.4
Iron	0	31.9
Carbon monoxide	– 110.5	–
Carbon dioxide	– 393.5	–
Iron Oxide	– 266.5	51.8
Oxygen	0	–
Monoethanol amine	– 201.72	–
* $C_{p(mean)}$ data for Graphite used for Carbon Nanotubes		

carbon atoms that form crystalline graphite, the mean specific heat capacity of graphite is used in calculating the enthalpy values for carbon nanotubes.

Enthalpy Calculation:

$$h(T) = \Delta H_f^o(T_{ref}) + C_{p(mean)}(T - T_{ref}) \qquad \text{(Felder, et al, 2000)}$$

$$h(T) = \Delta H_f^o(T_{ref}) + \int_{T_{ref}}^{T} C_p(T)dT$$

$$H(T) = \frac{h(T)kJ/kgmol}{MW(kg/kgmol)}$$

The heat of formation of the carbon nanotube product is estimated from Equation (A1.1), which relates the heat of reaction in terms of the standard heat of formation of the reactants and products:

$$\Delta H_{rxn} = \sum_{products} \nu_i \Delta H^o_{fi} - \sum_{reac\,tan\,ts} \nu_i \Delta H^o_{fi} \qquad \text{(A1.1)}$$

The stoichiometrically balanced form of the carbon nanotube reaction is:

$$6000CO_{(g)} \xrightarrow{Fe} C_{3000} + 3000CO_{2(g)}$$

ΔH_{rxn} = – 172.5 kJ/kgmol (Dateo, et al, 2002)

Heat of Formation for Carbon Nanotube, $\Delta H^o_{f(CNT)}$ (Equation A1.1):

$$-172.5\frac{kJ}{kgmol} = (3{,}000 * \Delta H^o_{f(CO_2)} + \Delta H^o_{f(CNT)}) - (6{,}000 * \Delta H^o_{f(CO)})$$

$$\Delta H^o_{f(CNT)} = -172.5\frac{kJ}{kgmol} - (3{,}000 * \Delta H^o_{f(CO_2)}) + (6{,}000 * \Delta H^o_{f(CO)})$$

$\Delta H^o_{f(CNT)}$ = 517,208 kJ/kgmol

Sample Enthalpy Calculation for Carbon Nanotube at 1,323K:

$$h(1{,}323K) = 517{,}208kJ/kgmol + 19.6\frac{kJ}{kgmolK} * (1{,}323K - 298K)$$

$h(1{,}323K)$ = 537,298 kJ/kgmol

$$H(1{,}323K) = 537{,}298\frac{kJ}{kgmol} * \frac{1kgmolCNT}{36{,}000kgCNT} = \textbf{14.93 kJ/kg}$$

Molecular Weight

The average molecular weight estimate is based on the Ames preliminary model, which assumes that an average–sized carbon nanotube is 3,000 carbon atoms long (Scott, et al, 2003).

Average Molecular Weight of Carbon Nanotube ($CNT = C_{3000}$):

$$MW^{(CNT)} = 3{,}000 \text{ x } 12 \text{ kg/kgmol}$$

$$MW^{(CNT)} = \mathbf{36{,}000 \text{ kg CNT/kgmol CNT}}$$

The molecular weight of all the reaction components in the HiPCO and CoMoCAT production processes are listed in Table A.3

Table A.3 Molecular Weights of Component Species in HiPCO and CoMoCAT Processes

Component	$MW\,(kg/kgmol)$
CO	28
CO_2	44
SiO_2	60
Fe_2O_3	160
HCl	37
Co	59
Mo	96
$Fe(CO)_5$	196
Fe	56
MEA	61
C	12
CNT	36,000
H_2O	18
O_2	32
$FeCl_2$	128
$CoCl_2$	131
$MoCl_2$	168

APPENDIX B

MATERIAL AND ENERGY BALANCE EQUATIONS

The material and energy balance equations for individual process units in the carbon nanotube HiPCO production and CoMoCAT production process models are listed in this section. The material and energy balance equations for the HiPCO process model are listed in Table B1.1 to Table B1.19, whereas the material and energy balance equations for the CoMoCAT process model are given in Table B2.1 to Table B2.23.

B1. HiPCO Process Model

Table B1.1. Material and Energy Balance Equations for Mixer (V–101)

Description	Input Streams SR01: CO SR02: $Fe(CO)_5$	Output Streams SR03: CO, $Fe(CO)_5$
Material Balances:		
Overall	$F_{01} + F_{02} - F_{03} = 0$	
Species	CO: $F_{03}^{(CO)} - F_{01}^{(CO)} = 0$ $Fe(CO)_5$: $F_{03}^{(Fe(CO)_5)} - F_{02}^{(Fe(CO)_5)} = 0$	
Energy Balances	$i = CO, Fe(CO)_5, k = 01,02,03$	
Overall	$T_{01} = T_{02} = T_{03}$ T_k is the temperature of stream, k	

Table B1.2. Material and Energy Balance Equations for Reactor (V–102)

Description	Inlet Streams SR03: CO, $Fe(CO)_5$ SR04: CO	Outlet Stream SR05: CO, CO_2, CNT, Fe, C
Material Balances	$conv1 = 0.20$ kgmol CO Converted/kgmol CO Fed $selc1 = 0.90$ kgmol CO Reacted to CNT/kgmol CO Reacted	
Overall	$F_{05} - (F_{03} + F_{04}) = 0$	
Species	Total CO from Thermal Decomposition of $Fe(CO)_5$: $= \frac{5 kgmol CO}{1 kgmol Fe(CO)_5} * \frac{MW^{(CO)}}{MW^{(Fe(CO)_5)}} * F_{03}^{(Fe(CO)_5)}$	
CO:	$F_{05}^{(CO)} - (1 - conv1) * (F_{03}^{(CO)} + F_{04}^{(CO)}) = 0$	
CO_2:	$F_{05}^{(CO_2)} - [F_{30}^{(CNT)} * \frac{MW^{(CO_2)}}{MW^{(CNT)}} * \frac{3000 kgmol CO_2}{1 kgmol CNT}]$ $- [F_{05}^{(C)} * \frac{MW^{(CO_2)}}{MW^{(C)}} * \frac{1 kgmol CO_2}{1 kgmol C}] = 0$	
CNT:	$F_{05}^{(CNT)} - \frac{1 kgmol CNT}{6000 kgmol CO} * \frac{MW^{(CNT)}}{MW^{(CO)}} * (conv1) * (selc1) * (F_{03}^{(CO)} + F_{04}^{(CO)}) = 0$	
Fe:	$F_{05}^{(Fe)} = \frac{1 kgmol Fe}{1 kgmol Fe(CO)_5} * \frac{MW^{(Fe)}}{MW^{(Fe(CO)_5)}} * F_{03}^{(Fe(CO)_5)}$	
C:	$F_{05}^{(C)} - \frac{1 kgmol C}{2 kgmol CO} * \frac{MW^{(C)}}{MW^{(CO)}} * (conv1) * (1 - selc1) * (F_{03}^{(CO)} + F_{04}^{(CO)}) = 0$	
Energy Balance	$T_{ref} = 298K$; 1 bar; $i = CO, CO_2, CNT, Fe, C$; $k = 03,04,05$	
Overall	$\sum_i F_{03}^{(i)} H_{03}^{(i)} + \sum_i F_{04}^{(i)} H_{04}^{(i)} - \sum_i F_{05}^{(i)} H_{05}^{(i)} + Q_{V-102} = 0$ Q_{V-102} = Heat Added to Reactor $H_k^{(i)}$ (kJ/kg) is the enthalpy of component '*i*' in stream, *k* $F_k^{(i)}$ is the mass flow rate (kg/hr) respectively	

Table B1.3. Material and Energy Balance Equations for Reactor Gas Effluent–Feed Recycle Cross Heat Exchanger (E–102).

Description	Input Streams SR07: CO, CO_2, SR17: CO	Output Streams SR08: CO, CO_2, SR18: CO
Material Balances		
Overall	$F_{07} - F_{08} = 0$ $F_{17} - F_{18} = 0$	
Species	CO: $F_{08}^{(CO)} - F_{07}^{(CO)} = 0$ $F_{18}^{(CO)} - F_{17}^{(CO)} = 0$ CO_2: $F_{08}^{(CO_2)} - F_{07}^{(CO_2)} = 0$	
Energy Balances	$i = CO, CO_2; k = 07,08,17,18$	
Overall	$\Delta H = \sum_{output} F_k^{(i)} H_k^{(i)} - \sum_{input} F_k^{(i)} H_k^{(i)}$ $(\sum_i F_{18}^{(i)} H_{18}^{(i)} - \sum_i F_{17}^{(i)} H_{17}^{(i)}) - (\sum_i F_{08}^{(i)} H_{08}^{(i)} - \sum_i F_{07}^{(i)} H_{07}^{(i)}) = 0$ $H_k^{(i)}(kJ/kg) = \frac{h_k^{(i)}(kJ/kgmol)}{MW^{(i)}(kg/kgmol)}$ $h_k^{(i)}(T) = R*(a_1^{(i)}T + \frac{a_2^{(i)}}{2}T^2 + \frac{a_3^{(i)}}{3}T^3 + \frac{a_4^{(i)}}{4}T^4 + \frac{a_5^{(i)}}{5}T^5 + \frac{b_1^{(i)}}{T})\frac{kJ}{kgmol}$ $Q_{E-102} = \sum_i F_{18}^{(i)} H_{18}^{(i)} - \sum_i F_{17}^{(i)} H_{17}^{(i)}$ $Q_{E-102} - U_{E-102} A_{E-102} \Delta T_{lm} = 0$ $\Delta T_{lm} = \frac{(T_{07} - T_{18}) - (T_{08} - T_{17})}{\ln\left((T_{07} - T_{18})/(T_{08} - T_{17})\right)}$	

Table B1.4.Material and Energy Balance Equations for CO Feed Gas–Fired Heater (E–101)

Description	Input Streams SR18: CO	Output Streams SR04: CO
Material Balances		
Overall	$F_{18} - F_{04} = 0$	
Species	CO: $F_{04}^{(CO)} - F_{18}^{(CO)} = 0$	
Energy Balances	$i = CO; k = 04,18$	
Overall	$F_{04}H_{04} - F_{18}H_{18} - Q_{E-101} = 0$ where, $H_k^{(i)}(kJ/kg) = \frac{h_k^{(i)}(kJ/kgmol)}{MW^{(i)}(kg/kgmol)}$ $h_k^{(i)}(T) = R*(a_1^{(i)}T + \frac{a_2^{(i)}}{2}T^2 + \frac{a_3^{(i)}}{3}T^3 + \frac{a_4^{(i)}}{4}T^4 + \frac{a_5^{(i)}}{5}T^5 + \frac{b_1^{(i)}}{T})\frac{kJ}{kgmol}$ $Q_{E-101} = F_{04}H_{04} - F_{18}H_{18}$ H_k is the enthalpy of stream, k $F_k^{(i)}$ is the mass flow rate of component 'i' in stream, k $h_k^{(i)}$ is the specific enthalpy of component 'i' in stream k Q_{E-101} is the heat supplied to CO Recycle Heater (E–101)	

Table B1.5. Material and Energy Balance Equations for Waste Heat Boiler (E–103)

Description	Input Streams SR08: CO, CO_2 BFW: H_2O	Output Streams SR09: CO, CO_2 SSS: H_2O
Material Balances		
Overall	$F_{08} - F_{09} = 0$ $F_{SSS} - F_{BFW} = 0$ BFW – Boiler Feed Water SSS – Saturated Steam	
Species	CO: $F_{09}^{(CO)} - F_{08}^{(CO)} = 0$ CO_2: $F_{09}^{(CO_2)} - F_{08}^{(CO_2)} = 0$ H_2O: $F_{SSS} - F_{BFW} = 0$	
Energy Balances	$i = CO, CO_2, H_2O;\quad k = 08,09, BFW, SSS$	
Overall	$\sum_i F_{09}^{(i)} H_{09}^{(i)} - \sum_i F_{08}^{(i)} H_{08}^{(i)} - Q_{E-103} = 0$ $F_{SSS} H_{SSS} - F_{BFW} H_{BFW} - Q_{E-103} = 0$ $Q_{E-103} = F_{BFW} * (C_p^{(H_2O)} \Delta T + \lambda_s)$ $H_k^{(i)}$ is the enthalpy of component '*i*' in stream, *k* $F_k^{(i)}$ is the mass flow rate of component '*i*' in stream, *k* λ_s is the latent heat of steam = 2,260 kJ/kg (Luyben, et al., 1988) $Q_{E-103} - U_{E-103} A_{E-103} \Delta T_{lm} = 0$ where, $\Delta T_{lm} = \frac{(T_{08} - T_{SSS}) - (T_{09} - T_{BFW})}{\ln\left((T_{08} - T_{SSS}) / (T_{09} - T_{BFW}) \right)}$	

Table B1.6. Material and Energy Balance Equations for Water Cooler 1 (E–104)

Description	Input Streams SR09: CO, CO_2, CW1: H_2O	Output Streams SR10: CO, CO_2, CW2: H_2O
Material Balances		
Overall	$F_{09} - F_{10} = 0$ $F_{CW1} - F_{CW2} = 0$ CW – Cooling Water	
Species	CO: $F_{10}^{(CO)} - F_{09}^{(CO)} = 0$ CO_2: $F_{10}^{(CO_2)} - F_{09}^{(CO_2)} = 0$ H_2O: $F_{CW2} - F_{CW1} = 0$	
Energy Balances	$i = CO, CO_2; k = 09,10$	
Overall	$\sum_i F_{10}^{(i)} H_{10}^{(i)} - \sum_i F_{09}^{(i)} H_{09}^{(i)} - Q_{E-104} = 0$ $F_{CW2} H_{CW2} - F_{CW1} H_{CW1} - Q_{E-104} = 0$ $Q_{E-104} = F_{CW1} * C_p^{(H_2O)} * \Delta T$ $H_k^{(i)}$ is the enthalpy of component '*i*' in stream, *k* $F_k^{(i)}$ is the flow rate of component '*i*' in stream, *k* $h_k^{(i)}$ is the specific enthalpy of component '*i*' in stream *k* $Q_{E-104} - U_{E-104} A_{E-104} \Delta T_{lm} = 0$ $\Delta T_{lm} = \frac{(T_{09} - T_{CW2}) - (T_{10} - T_{CW1})}{\ln\left(\frac{(T_{09} - T_{CW2})}{(T_{10} - T_{CW1})}\right)}$	

Table B1.7. Material and Energy Balance Equations for Solute Rich–Lean Solvent Cross Heat Exchanger (E–105)

Description	Input Streams SR19: CO_2, MEA, H_2O SR21: MEA, H_2O	Output Streams SR20: CO_2, MEA, H_2O SR23: MEA, H_2O
Material Balances		
Overall	$F_{19} - F_{20} = 0$ $F_{21} - F_{23} = 0$	
Species	CO_2 : $F_{20}^{(CO_2)} - F_{19}^{(CO_2)} = 0$ MEA: $F_{20}^{(MEA)} - F_{19}^{(MEA)} = 0$; $F_{23}^{(MEA)} - F_{21}^{(MEA)} = 0$ H_2O: $F_{20}^{(H_2O)} - F_{19}^{(H_2O)} = 0$; $F_{23}^{(H_2O)} - F_{21}^{(H_2O)} = 0$	
Energy Balances	$i = CO_2, MEA, H_2O; k = 19,20,21,23$	
Overall	$\Delta H = \sum_{output} F_k^{(i)} H_k^{(i)} - \sum_{input} F_k^{(i)} H_k^{(i)}$ $(\sum_i F_{20}^{(i)} H_{20}^{(i)} - \sum_i F_{19}^{(i)} H_{19}^{(i)}) - (\sum_i F_{22}^{(i)} H_{22}^{(i)} - \sum_i F_{21}^{(i)} H_{21}^{(i)}) = 0$ $Q_{E-105} = \sum_i F_{20}^{(i)} H_{20}^{(i)} - \sum_i F_{19}^{(i)} H_{19}^{(i)}$ $H_k^{(i)}$ is the enthalpy of component '*i*' in stream, *k* $F_k^{(i)}$ is the mass flow rate of component '*i*' in stream, *k* $Q_{E-105} - U_{E-105} A_{E-105} \Delta T_{lm} = 0$ $\Delta T_{lm} = \frac{(T_{21} - T_{20}) - (T_{22} - T_{19})}{\ln\left((T_{21} - T_{20}) / (T_{22} - T_{19})\right)}$	

Table B1.8. Material and Energy Balance Equations for Gas–Solid Filter (Z–101)

Description	Inlet Stream SR05: CO, CO_2, CNT, Fe, C	Outlet Stream SR07: CO, CO_2 SR06: CNT, Fe, C
Material Balances		
Overall	$F_{05} - (F_{06} + F_{07}) = 0$	
Species	CO: $F_{07}^{(CO)} - F_{05}^{(CO)} = 0$ CO_2: $F_{07}^{(CO_2)} - F_{05}^{(CO_2)} = 0$ CNT: $F_{06}^{(CNT)} - F_{05}^{(CNT)} = 0$ Fe: $F_{06}^{(Fe)} - F_{05}^{(Fe)} = 0$ C: $F_{06}^{(C)} - F_{05}^{(C)} = 0$	
Energy Balances	$i = CO, CO_{2,} CNT, Fe, C$; $k = 05,06,07$	
Overall	$T_{05} = T_{06} = T_{07}$ T_k is the temperature of stream k	

Table B1.9. Material and Energy Balance Equations for Air Oxidizer (V–103)

Description	Inlet Streams SR06: CNT, Fe, C ARin: O_2	Outlet Stream SR11: CNT, FeO ARout: CO_2
Material Balances		
Overall	$(F_{05} + F_{ARin}) - (F_{09} + F_{ARout}) = 0$	
Species	CNT: $F_{11}^{(CNT)} - F_{06}^{(CNT)} = 0$ FeO: $F_{11}^{(FeO)} - \frac{1kgmolFeO}{1kgmolFe} * \frac{MW^{(FeO)}}{MW^{(Fe)}} * F_{06}^{(Fe)} = 0$ C: $F_{11}^{(C)} = 0$ Oxygen required for amorphous carbon and iron oxidation: $F_{ARin}^{(O_2)} = (\frac{1kgmolO_2}{1kgmolC} * \frac{MW^{(O_2)}}{MW^{(C)}} * F_{06}^{(C)} + \frac{1kgmolO_2}{2kgmolFe} * \frac{MW^{(O_2)}}{MW^{(Fe)}} * F_{06}^{(Fe)})$ CO_2: $F_{ARout}^{(CO_2)} - \frac{1kgmolCO_2}{1kgmolC} * \frac{MW^{(CO_2)}}{MW^{(C)}} * F_{06}^{(C)} = 0$	
Energy Balances		
Overall	$Q_{V-103} = \sum_i F_{outlet}^{(i)} H_{outlet}^{(i)} - \sum_i F_{inlet}^{(i)} H_{inlet}^{(i)}$ Q_{V-103} is the heat liberated in the air oxidizer	

Table B1.10. Material and Energy Balance Equations for Acid Treatment Tank (V–104)

Description	Inlet Streams SR11: CNT, FeO SR15: HCl, H_2O	Outlet Streams SR12: CNT, FeCl, H_2O
Material Balances		
Overall	$(F_{11} + F_{15}) - F_{12} = 0$	
Species	CNT: $F_{12}^{(CNT)} - F_{11}^{(CNT)} = 0$ HCl: $F_{15}^{(HCl)} - \frac{2kgmolHCl}{1kgmolFeO} * \frac{MW^{(HCl)}}{MW^{(FeO)}} * F_{11}^{(FeO)} = 0$ $FeCl_2$: $F_{12}^{(FeCl_2)} - \frac{1kgmolFeCl_2}{1kgmolFeO} * \frac{MW^{(FeCl_2)}}{MW^{(FeO)}} * F_{11}^{(FeO)} = 0$ H_2O: $F_{12}^{(H_2O)} - (F_{15}^{(H_2O)} + \frac{1kgmolH_2O}{1kgmolFeO} * \frac{MW^{(H_2O)}}{MW^{(FeO)}} * F_{11}^{(FeO)}) = 0$	
Energy Balances		
Overall	$T_{11} = T_{12} = T_{15}$ T_k is the temperature of stream, *k*	

Table B1.11. Material and Energy Balance Equations for Liquid–Solid Filter (Z–102)

Description	Inlet Streams SR12: CNT, $FeCl_2$, H_2O	Outlet Stream SR13: CNT, $FeCl_2$, H_2O SR14: $FeCl_2$, H_2O
Material Balances		
Overall	$F_{12} - (F_{13} + F_{14}) = 0$	
Species	CNT: $F_{13}^{(CNT)} - F_{12}^{(CNT)} = 0$ $FeCl_2$: $F_{12}^{(FeCl_2)} - (F_{13}^{(FeCl_2)} + F_{14}^{(FeCl_2)}) = 0$ H_2O: $F_{12}^{(H_2O)} - (F_{13}^{(H_2O)} + F_{14}^{(H_2O)}) = 0$	
Energy Balances		
Overall	$T_{12} = T_{13} = T_{14}$ T_k is the temperature of stream, k	

Table B1.12. Material and Energy Balance Equations for Gas Absorption Column (T–101)

Description	Input Streams SR10: CO, CO_2 SR23: MEA, H_2O	Output Streams SR16: CO SR19: MEA, H_2O, CO_2
Material balances		
Overall	$(F_{10} + F_{23}) - (F_{16} + F_{19}) = 0$	
Species	CO: $F_{16}^{(CO)} - F_{10}^{(CO)} = 0$ CO_2: $F_{19}^{(CO_2)} - F_{10}^{(CO_2)} = 0$ MEA: $F_{19}^{(MEA)} - F_{23}^{(MEA)} = 0$ H_2O: $F_{19}^{(H_2O)} - F_{23}^{(H_2O)} = 0$	
Energy Balances	$i = CO, CO_2, MEA, H_2O$; $k = 10,16,19,23$	
Overall	$T_{10} = T_{16} = T_{19} = T_{23}$ T_k is the temperature of stream, k	

Table B1.13. Material and Energy Balance Equations for Gas Stripping Column (T–102)

Description	Input Streams SR20: CO_2, MEA, H_2O SR25: H_2O SR29: MEA, H_2O	Output Streams SR24: CO_2 SR21: MEA, H_2O SR28: MEA, H_2O
Material balances		
Overall	$(F_{20} + F_{25} + F_{29}) - (F_{21} + F_{24} + F_{28}) = 0$	
Species	CO_2: $F_{24}^{(CO_2)} - F_{20}^{(CO_2)} = 0$ MEA: $(F_{21}^{(MEA)} + F_{28}^{(MEA)}) - (F_{20}^{(MEA)} + F_{29}^{(MEA)}) = 0$ H_2O: $(F_{21}^{(H_2O)} + F_{24}^{(H_2O)} + F_{28}^{(MEA)}) - (F_{20}^{(MEA)} + F_{25}^{(H_2O)} + F_{29}^{(MEA)}) = 0$	
Energy Balances		
Overall	$Q_{T-102} = \sum_i F_{outlet}^{(i)} H_{outlet}^{(i)} + \sum_i F_{inlet}^{(i)} H_{inlet}^{(i)}$ T_k is the temperature of stream, k	

Table B1.14. Material and Energy Balance Equations for Reboiler (E–106)

Description	Inlet Streams SR28: MEA, H_20	Outlet Streams SR29: MEA, H_20
Material Balances		
Overall	$F_{28} - F_{29} = 0$	
Species	MEA: $F_{29}^{(MEA)} - F_{28}^{(MEA)} = 0$ H_20: $F_{29}^{(H_2O)} - F_{28}^{(H_2O)} = 0$	
Energy Balances	$i = MEA, H_2O$; $k = 28,29$	
Overall	$\sum_i F_{29}^{(i)} H_{29}^{(i)} - \sum_i F_{28}^{(i)} H_{28}^{(i)} - Q_{E-106} = 0$ $H_k^{(i)}(kJ/kg) = \frac{h_k^{(i)}(kJ/kgmol)}{MW^{(i)}(kg/kgmol)}$ $H_k^{(i)}$ is the enthalpy of component '*i*' in stream, *k* $F_k^{(i)}$ is the flow rate of component '*i*' in stream, *k* $h_k^{(i)}$ is the specific enthalpy of component '*i*' in stream *k* $Q_{E-106} - U_{E-106} A_{E-106} \Delta T_m = 0$	

Table B1.15. Material and Energy Balance Equations for Flash Drum (V–105)

Description	Inlet Streams SR24: CO_2, H_2O	Outlet Streams SR25: H_2O SR26: CO_2
Material Balances		
Overall	$F_{24} - (F_{25} + F_{26}) = 0$	
Species	H_2O: $\frac{y_{24}^{(H_2O)}}{MW^{(H_2O)}} * F_{24} - x_{25}^{(H_2O)} * F_{25} = 0$ CO_2: $\frac{y_{24}^{(CO_2)}}{MW^{(CO_2)}} F_{24} - y_{26}^{(CO_2)} * F_{26} = 0$ $K_i = \frac{y_i}{x_i}; \sum_i x_i = 1; \sum_i y_i = 1$ $y_{24}^{(CO_2)} + y_{24}^{(H_2O)} = 1;$ $y_{26}^{(CO_2)} = 1; \quad y_{26}^{(H_2O)} = 0$ $x_{25}^{(H_2O)} = 1; \quad x_{25}^{(CO_2)} = 0$ $K_i \equiv$ Distribution Coefficient $x_i \equiv$ mole fraction of component '*i*' in the liquid phase $y_i \equiv$ mole fraction of component '*i*' in the gas phase	
Energy Balances	$i = H_2O, CO_2; \quad k = 24,25,26$	
Overall	$T_{24} = T_{25} = T_{26}$	

Table B1.16. Material and Energy Balance Equations for Gas Compressor (C–101)

Description	Input Streams SR16: CO	Output Streams SR17: CO
Material Balances		
Overall	$F_{16} - F_{17} = 0$	
Species	CO: $F_{17}^{(CO)} - F_{16}^{(CO)} = 0$	
Energy Balances	$i = CO; k = 16,17$	
Overall	$F_{17}H_{17} - F_{16}H_{16} + P_{C-101} = 0$ $T_{17} = T_{16}\left(\frac{P_{17}}{P_{16}}\right)^{\frac{(k-1)}{k}}$ where, $T_{17} \equiv$ Adiabatic Discharge Temperature; $T_{16} \equiv$ Suction Temperature $P_{17} \equiv$ Discharge Pressure; $P_{16} \equiv$ Suction Pressure $k \equiv$ Ratio of specific heat capacities $\left(c_p / c_v\right)$ H_k is the enthalpy of stream, k $F_k^{(i)}$ is the mass flow rate of component 'i' in stream, k $P_{C-101} \equiv$ Power supplied to the compressor	

Table B1.17. Material and Energy Balance Equations for Discharge Valve (Z–105)

Description	Inlet Streams SR26: CO_2	Outlet Streams SR27: CO_2
Material Balances		
Overall	$F_{26} - F_{27} = 0$	
Species	CO_2: $F_{27}^{(CO_2)} - F_{26}^{(CO_2)} = 0$	
Energy Balances		
Overall	$T_{27} = T_{26}$	

Table B1.18. Material and Energy Balance Equations for Acid Regenerator (Z–104)

Description	Inlet Streams SR14: $FeCl_2$, H_2O RG1: O_2, H_2O	Outlet Streams SR32: HCl, H_2O, Fe_2O_3
Material Balances		
Overall	$(F_{14} + F_{RG1}) - F_{32} = 0$	
Species	H_2O: $F_{32}^{(H_2O)} - (F_{14}^{(H_2O)} + F_{RG1}^{(H_2O)}) = 0$ HCl: $F_{32}^{(HCl)} - \frac{2 kgmol HCl}{1 kgmol FeCl_2} * \frac{MW^{(HCl)}}{MW^{(FeCl_2)}} * F_{14}^{(FeCl_2)} = 0$ Fe_2O_3: $F_{32}^{(Fe_2O_3)} - \frac{1 kgmol Fe_2O_3}{2 kgmol FeCl_2} * \frac{MW^{(Fe_2O_3)}}{MW^{(FeCl_2)}} * F_{14}^{(FeCl_2)} = 0$ O_2: $F_{RG1}^{(O_2)} - (\frac{1 kgmol O_2}{4 kgmol FeCl_2} * \frac{MW^{(O_2)}}{MW^{(FeCl_2)}} * F_{14}^{(FeCl_2)}) = 0$	
Energy Balances		
Overall	$T_{11} = T_{12} = T_{32}$ T_k is the temperature of stream, k	

Table B1.19. Material and Energy Balance Equations for Product Drier (Z–103)

Description	Inlet Streams SR13: CNT, $FeCl_2$, H_2O	Outlet Streams SR30: CNT, $FeCl_2$, H_2O
Material Balances		
Overall	$F_{13} - F_{30} = 0$	
Species	CNT: $F_{30}^{(CNT)} - F_{13}^{(CNT)} = 0$ $FeCl_2$: $F_{30}^{(FeCl_2)} - F_{13}^{(FeCl_2)} = 0$ H_2O: $F_{30}^{(H_2O)} - F_{13}^{(H_2O)} = 0$	
Energy Balances		
Overall	$T_{13} = T_{30}$	

Table B1.20. Material and Energy Balance Equations for Centrifuge Separator (Z–106)

Description	Inlet Streams SR32: HCl, H_2O, Fe_2O_3	Outlet Streams SR15: HCl, H_2O RG2: Fe_2O_3
Material Balances		
Overall	$F_{32} - (F_{15} + F_{RG2}) = 0$	
Species	H_2O: $F_{32}^{(H_2O)} - F_{15}^{(H_2O)} = 0$ HCl: $F_{32}^{(HCl)} - F_{15}^{(HCl)} = 0$ Fe_2O_3: $F_{32}^{(Fe_2O_3)} - F_{RG2}^{(Fe_2O_3)} = 0$	
Energy Balances		
Overall	$T_{15} = T_{32}$ T_k is the temperature of stream, *k*	

B2. CoMoCAT Process Model

Table B2.1. Material and Energy Balance Equations for CO Feed Gas–Fired Heater (E–201)

Description	Input Streams SR01: CO SR17: CO	Output Streams SR02: CO
Material Balances		
Overall	$F_{02}^{(CO)} - (F_{17}^{(CO)} + F_{01}^{(CO)}) = 0$	
Species	CO: $F_{02}^{(CO)} - (F_{17}^{(CO)} + F_{01}^{(CO)}) = 0$	
Energy Balances	$i = CO; k = 01,02,17$	
Overall	$F_{02}H_{02} - (F_{17}H_{17} + F_{01}H_{01}) - Q_{E-201} = 0$ where, $H_k^{(i)}(kJ/kg) = \frac{h_k^{(i)}(kJ/kgmol)}{MW^{(i)}(kg/kgmol)}$ H_k is the enthalpy of stream, k $F_k^{(i)}$ is the flow rate of component 'i' in stream, k $h_k^{(i)}$ is the specific enthalpy of component 'i' in stream k Q_{E-201} is the energy supplied to the Heater (E–201)	

Table B2.2 Material and Energy Balance Equations for Fluidized Bed Reactor (V–201)

Description	Inlet Streams SR02: CO SR11: Catalyst (*SiO_2, Co, Mo.*)	Outlet Stream SR03: CO, CO_2, CNT, C, *Cat.*
Material Balances	$conv2 = 0.20 kgmolCO / kgmolCO$; $selc2 = 0.80$	
Overall	$F_{03} - (F_{02} + F_{11}) = 0$	
Species CO:	$F_{03}^{(CO)} - (1 - conv2) * F_{02}^{(CO)} = 0$	
CO_2:	$F_{03}^{(CO_2)} - \frac{3000 kgmolCO_2}{6000 kgmolCO} * \frac{MW^{(CO_2)}}{MW^{(CO)}} * (conv2) * F_{02}^{(CO)} = 0$	
CNT:	$F_{03}^{(CNT)} - \frac{1 kgmolCNT}{6000 kgmolCO} * \frac{MW^{(CNT)}}{MW^{(CO)}} (conv2) * (selc2) * F_{02}^{(CO)} = 0$	
C:	$F_{03}^{(C)} - \frac{1 kgmolC}{2 kgmolCO} * \frac{MW^{(C)}}{MW^{(CO)}} * (conv2) * (1 - selc2) * F_{02}^{(CO)} = 0$	
Catalyst: (SiO_2, Co, Mo)	$F_{03}^{(SiO_2)} = F_{11}^{(SiO_2)}$; $F_{03}^{(Co)} = F_{11}^{(Co)}$; $F_{03}^{(Mo)} = F_{11}^{(Mo)}$	
Energy Balances	$i = CO, Cat, CO_2, CNT, C$; $k = 02,03,11$	
Overall	Energy In – Energy Out + Energy Generated = 0 $(F_{02}^{(CO)} H_{02}^{(CO)} + F_{11}^{(Cat)} H_{11}^{(Cat)}) - \sum_i F_{03}^{(i)} H_{03}^{(i)} + Q_{V-201} = 0$ Enthalpy, $H_k^{(i)}(kJ/kg) = \frac{h_k^{(i)}(kJ/kgmol)}{MW^{(i)}(kg/kgmol)}$ Q_{V-201} = Heat Added to Reactor $F_k^{(i)}$ is the mass flow rate of component '*i*' in stream, *k* $h_k^{(i)}$ is the specific enthalpy of component '*i*' in stream *k*	

Table B2.3. Material and Energy Balance Equations for the Cyclone Separator (Z–201)

Description	Inlet Streams SR03: CO, CO_2, CNT, C, *Cat*.	Outlet Stream SR04: CO, CO_2, CNT, C, *Cat*. SR05: CNT, *Cat*.
Material Balances	Collection Efficiency, $\eta_{Z-201} = 0.96$	
Overall	$F_{05} + F_{04} - F_{03} = 0$	
Species	CO: $F_{04}^{(CO)} - F_{03}^{(CO)} = 0$ CO_2: $F_{04}^{(CO_2)} - F_{03}^{(CO_2)} = 0$ CNT: $F_{05}^{(CNT)} + F_{04}^{(CNT)} - F_{03}^{(CNT)} = 0$ $F_{05}^{(CNT)} = \eta_{Z-201} * F_{03}^{(CNT)}$ $F_{04}^{(CNT)} = (1-\eta_{Z-201}) * F_{03}^{(CNT)}$ Cat: $F_{05}^{(Cat)} + F_{04}^{(Cat)} - F_{03}^{(Cat)} = 0$ $F_{05}^{(Cat.)} = \eta_{Z-201} * F_{03}^{(Cat.)}$ $F_{04}^{(Cat.)} = (1-\eta_{Z-201}) * F_{03}^{(Cat.)}$ C: $F_{05}^{(C)} + F_{04}^{(C)} - F_{03}^{(C)} = 0$ $F_{05}^{(C)} = \eta_{Z-201} * F_{03}^{(C)}$ $F_{04}^{(C)} = (1-\eta_{Z-201}) * F_{03}^{(C)}$	
Energy Balances		
Overall	$T_{03} = T_{04} = T_{05}$	

Table B2.4. Material and Energy Balance Equations for Waste Heat Boiler (E–202)

Description	Input Streams SR13: CO, CO_2 BFW: H_2O	Output Streams SR14: CO, CO_2 SST: H_2O
Material Balances		
Overall	$F_{14} - F_{13} = 0$ $F_{SST} - F_{BFW} = 0$ BFW – Boiler Feed Water SST – Saturated Steam from Waste Heat Boiler	
Species	CO: $F_{14}^{(CO)} - F_{13}^{(CO)} = 0$ CO_2: $F_{14}^{(CO_2)} - F_{13}^{(CO_2)} = 0$ H_2O: $F_{SST} - F_{BFW} = 0$	
Energy Balances	$i = CO, CO_2$; $k = 13,14$;	
Overall	Energy Liberated = Energy Absorbed $(\sum_i F_{14}^{(i)} H_{14}^{(i)} - \sum_i F_{13}^{(i)} H_{13}^{(i)}) - (F_{SST} H_{SST} - F_{BFW} H_{BFW}) = 0$ $Q_{E-202} = \sum_i F_{14}^{(i)} H_{14}^{(i)} - \sum_i F_{13}^{(i)} H_{13}^{(i)}$ $Q_{E-202} = F_{BFW} * (C_p^{(H_2O)} \Delta T + \lambda_s)$ $H_k^{(i)}(kJ/kg) = \frac{h_k^{(i)} kJ/kgmol}{MW^{(i)} kg/kgmol}$ λ_s is the latent heat of steam =2260 kJ/kg (Luyben, et al, 1988) $Q_{E-202} - U_{E-202} A_{E-202} \Delta T_{lm} = 0$ $\Delta T_{lm} = \frac{(T_{13} - T_{SST}) - (T_{14} - T_{BFW})}{\ln\left((T_{13} - T_{SST}) / (T_{14} - T_{BFW})\right)}$	

Table B2.5. Material and Energy Balance Equations for Water Cooler 1 (E–203)

Description	Input Streams SR14: CO, CO_2, CW5: H_2O	Output Streams SR15: CO, CO_2, CW6: H_2O
Material Balances		
Overall	$F_{15} - F_{14} = 0$ $F_{CW5} - F_{CW6} = 0$ CW – Cooling Water	
Species	CO: $F_{15}^{(CO)} - F_{14}^{(CO)} = 0$ CO_2: $F_{15}^{(CO_2)} - F_{14}^{(CO_2)} = 0$ H_2O: $F_{CW6} - F_{CW5} = 0$	
Energy Balances	$i = CO, CO_2; k = 14,15$	
Overall	$\sum_i F_{15}^{(i)} H_{15}^{(i)} - \sum_i F_{14}^{(i)} H_{14}^{(i)} - Q_{E-203} = 0$ $F_{CW6} H_{CW6} - F_{CW5} H_{CW5} - Q_{E-203} = 0$ where $H_k^{(i)} = \frac{h_k^{(i)}}{MW^{(i)}}$ and $H_k^{(i)}$ is the enthalpy of component 'i' in stream, *k* $F_k^{(i)}$ is the flow rate of component '*i*' in stream, *k* $h_k^{(i)}$ is the specific enthalpy of component '*i*' in stream *k* $Q_{E-203} - U_{E-203} A_{E-203} \Delta T_{lm} = 0$ $\Delta T_{lm} = \frac{(T_{14} - T_{CW6}) - (T_{15} - T_{CW5})}{\ln\left(\frac{(T_{14} - T_{CW6})}{(T_{15} - T_{CW5})}\right)}$	

Table B2.6. Material and Energy Balance Equations for Solute Rich–Lean Solvent Cross Heat Exchanger (E–204)

Description	Input Streams SR18: CO_2, MEA, H_2O SR20: MEA, H_2O	Output Streams SR19: CO_2, MEA, H_2O SR22: MEA, H_2O
Material Balances		
Overall	$F_{18} - F_{19} = 0$ $F_{20} - F_{22} = 0$	
Species	CO_2 : $F_{19}^{(CO_2)} - F_{18}^{(CO_2)} = 0$ MEA: $F_{19}^{(MEA)} - F_{18}^{(MEA)} = 0$; $F_{22}^{(MEA)} - F_{20}^{(MEA)} = 0$ H_2O: $F_{19}^{(H_2O)} - F_{18}^{(H_2O)} = 0$; $F_{22}^{(H_2O)} - F_{20}^{(H_2O)} = 0$	
Energy Balances	$i = CO_2, MEA, H_2O; k = 18,19,20,22$	
Overall	$(\sum_i F_{19}^{(i)} H_{19}^{(i)} - \sum_i F_{18}^{(i)} H_{18}^{(i)}) - (\sum_i F_{22}^{(i)} H_{22}^{(i)} - \sum_i F_{20}^{(i)} H_{20}^{(i)}) = 0$ $Q_{E-204} = \sum_i F_{19}^{(i)} H_{19}^{(i)} - \sum_i F_{18}^{(i)} H_{18}^{(i)}$ $H_k^{(i)} = \frac{h_k^{(i)}(kJ/kgmol}{MW^{(i)}(kg/kmol)}$ H_k is the enthalpy of stream, *k* $F_k^{(i)}$ is the flow rate of component '*i*' in stream, *k* $h_k^{(i)}$ is the specific enthalpy of component '*i*' in stream *k* $Q_{E-204} - U_{E-204} A_{E-204} \Delta T_m = 0$ $\Delta T_m = \frac{(T_{20} - T_{19}) - (T_{22} - T_{18})}{\ln\left((T_{20} - T_{19}) / (T_{22} - T_{18})\right)}$	

Table B2.7. Material and Energy Balance Equations for Gas–Solid Filter (Z–202)

Description	Inlet Stream SR04: CO, CO_2, CNT, C, SiO_2, Co, Mo	Outlet Stream SR13: CO, CO_2 SR12: CNT, SiO2, Co, Mo
Material Balances		
Overall	$F_{04} - (F_{12} + F_{13}) = 0$	
Species	CO: $F_{13}^{(CO)} - F_{04}^{(CO)} = 0$ CO_2: $F_{13}^{(CO_2)} - F_{04}^{(CO_2)} = 0$ CNT: $F_{12}^{(CNT)} - F_{04}^{(CNT)} = 0$ C: $F_{12}^{(C)} - F_{04}^{(C)} = 0$ SiO_2: $F_{12}^{(SiO_2)} - F_{04}^{(SiO_2)} = 0$ Co: $F_{12}^{(Co)} - F_{04}^{(Co)} = 0$ Mo: $F_{12}^{(Mo)} - F_{04}^{(Mo)} = 0$	
Energy Balances	$i = CO, CO_2, CNT, C, Cat.;\quad k = 04,12,13$	
Overall	$T_{04} = T_{12} = T_{13}$	

Table B2.8. Material and Energy Constraint Equations for Silica Leaching Tank (V–202)

Description	Inlet Streams SR05: CNT, C, SiO_2, Co, Mo SR12: CNT, C, SiO_2, Co, Mo AK1: NaOH	Outlet Stream SR06: CNT, C, SiO_2, Co, Mo NaOH
Material Balances		
Overall	$(F_{05} + F_{12} + F_{AK1}) - F_{06} = 0$	
Species	CNT: $F_{06}^{(CNT)} - (F_{05}^{(CNT)} + F_{12}^{(CNT)}) = 0$ C: $F_{06}^{(C)} - (F_{05}^{(C)} + F_{12}^{(C)}) = 0$ SiO_2: $F_{06}^{(SiO_2)} - (F_{05}^{(SiO_2)} + F_{12}^{(SiO_2)}) = 0$ Co: $F_{06}^{(Co)} - (F_{05}^{(Co)} + F_{12}^{(Co)}) = 0$ Mo: $F_{06}^{(Mo)} - (F_{05}^{(Mo)} + F_{12}^{(Mo)}) = 0$ NaOH: $F_{06}^{(NaOH)} - F_{AK1}^{(NaOH)} = 0$	
Energy Balances		
Overall	$T_{05} = T_{06} = T_{12}$	

Table B2.9. Material and Energy Balance Equations for Froth Flotation Column (T–203)

Description	Input Streams SR06: CNT, C, SiO_2, Co, Mo NaOH	Output Streams SR07: C, SiO_2, Co, Mo, NaOH SR08: CNT, Co, Mo
Material balances		
Overall	$F_{07} + F_{08} - F_{06} = 0$	
Species	CNT: $F_{08}^{(CNT)} - F_{06}^{(CNT)} = 0$ SiO_2: $F_{07}^{(SiO_2)} - F_{06}^{(SiO_2)} = 0$ C: $F_{07}^{(C)} - F_{06}^{(C)} = 0$ Co: $(F_{07}^{(Co)} + F_{08}^{(Co)}) - F_{06}^{(Co)} = 0$ Mo: $(F_{07}^{(Mo)} + F_{08}^{(Mo)}) - F_{06}^{(Mo)} = 0$ NaOH: $F_{07}^{(NaOH)} - F_{06}^{(NaOH)} = 0$	
Energy Balances		
Overall	$T_{06} = T_{07} = T_{08}$	

Table B2.10. Material and Energy Balance Equations for Liquid–Solid Filter (Z–204)

Description	Inlet Streams SR07: *SiO_2,, Co, Mo, C*	Outlet Stream SR10: *SiO_2, Co, Mo, C* WS1:
Material Balances		
Overall	$F_{07} - (F_{10} + F_{WS1}) = 0$	
Species	*SiO_2*: $F_{10}^{(SiO_2)} - F_{07}^{(SiO_2)} = 0$ Co: $F_{10}^{(Co)} - F_{07}^{(Co)} = 0$ Mo: $F_{10}^{(Mo)} - F_{07}^{(Mo)} = 0$ *C*: $F_{10}^{(C)} - F_{07}^{(C)} = 0$ NaOH: $F_{WS1}^{(NaOH)} - F_{07}^{(NaOH)} = 0$	
Energy Balances		
Overall	$T_{07} = T_{10}$	

Table B2.11. Material and Energy Balance Equations for Centrifuge Separator (Z–203)

Description	Input Streams SR09: Co_2O_3, MoO_3, HCl, H_2O	Output Streams SR32: HCl, H_2O RG4: Co_2O_3, MoO_3
Material balances		
Overall	$F_{09} - (F_{32} + F_{RG4}) = 0$	
Species	HCl: $F_{32}^{(HCl)} - F_{09}^{(HCl)} = 0$ H_2O: $F_{32}^{(H_2O)} - F_{09}^{(H_2O)} = 0$ Co_2O_3: $F_{RG4}^{(Co_2O_3)} - F_{09}^{(Co_2O_3)} = 0$ MoO_3: $F_{RG4}^{(MoO_3)} - F_{09}^{(MoO_3)} = 0$	
Energy Balances		
Overall	$T_{09} = T_{32}$	

Table B2.12. Material and Energy Balance Equations for Acid Dissolution Tank (V–203)

Description	Inlet Streams SR08: CNT, Co, Mo SR32: HCl, H_2O	Outlet Streams SR29: H_2O, CNT, $CoCl_2$, $MoCl_2$
Material Balances		
Overall	$(F_{08} + F_{32}) - F_{29} = 0$	
Species	CNT: $F_{29}^{(CNT)} - F_{08}^{(CNT)} = 0$ H_2O: $F_{29}^{(H_2O)} - F_{32}^{(H_2O)} = 0$ HCl: $F_{32}^{(HCl)} - \frac{2kgmolHCl}{1kgmolCo} * \frac{MW^{(HCl)}}{MW^{(Co)}} * F_{08}^{(Co)} - \frac{2kgmolHCl}{1kgmolMo} * \frac{MW^{(HCl)}}{MW^{(Mo)}} * F_{08}^{(Mo)} = 0$ $CoCl_2$: $F_{29}^{(CoCl_2)} - \frac{1kgmolCoCl_2}{1kgmolCo} * \frac{MW^{(CoCl_2)}}{MW^{(Co)}} * F_{08}^{(Co)} = 0$ $MoCl_2$: $F_{29}^{(MoCl_2)} - \frac{1kgmolMoCl_2}{1kgmolMo} * \frac{MW^{(MoCl_2)}}{MW^{(Mo)}} * F_{08}^{(Mo)} = 0$	
Energy Balances		
Overall	$T_{08} = T_{29} = T_{32}$	

Table B2.13. Material and Energy Balance Equations for Liquid–Solid Filter (Z–205)

Description	Inlet Streams SR29: CNT, H_2O, $CoCl_2$, $MoCl_2$	Outlet Stream SR30: CNT, $CoCl_2$, $MoCl_2$, H_2O SR31: H_2O, $CoCl_2$, $MoCl_2$
Material Balances		
Overall	$F_{29} - (F_{30} + F_{31}) = 0$	
Species	CNT: $F_{30}^{(CNT)} - F_{29}^{(CNT)} = 0$ H_2O: $F_{29}^{(H_2O)} - (F_{30}^{(H_2O)} + F_{31}^{(H_2O)}) = 0$ $CoCl_2$: $F_{29}^{(CoCl_2)} - (F_{30}^{(CoCl_2)} + F_{31}^{(CoCl_2)}) = 0$ $MoCl_2$: $F_{29}^{(MoCl_2)} - (F_{30}^{(MoCl_2)} + F_{31}^{(MoCl_2)}) = 0$	
Energy Balances		
Overall	$T_{29} = T_{30} = T_{31}$	

Table B2.14. Material and Energy Balance Equations for Gas Absorption Column (T–201)

Description	Input Streams SR15: CO, CO_2 SR22: MEA, H_2O	Output Streams SR16: CO SR18: MEA,H_2O CO_2
Material balances		
Overall	$(F_{16} + F_{18}) - (F_{15} + F_{22}) = 0$	
Species	CO: $F_{16}^{(CO)} - F_{15}^{(CO)} = 0$ CO_2: $F_{18}^{(CO_2)} - F_{15}^{(CO_2)} = 0$ MEA: $F_{18}^{(MEA)} - F_{22}^{(MEA)} = 0$ H_2O: $F_{18}^{(H_2O)} - F_{22}^{(H_2O)} = 0$	
Energy Balances	$i = CO, CO_2, MEA, H_2O$; $k = 15,16,18,22$	
Overall	$T_{15} = T_{22} = T_{16} = T_{18}$ T_k is the temperature of stream, k	

Table B2.15. Material and Energy Balance Equations for Gas Stripping Column (T–202)

Description	Input Streams SR19: CO_2, MEA, H_2O SR24: MEA, H_2O SR26: H_2O	Output Streams SR25: CO_2, H_2O SR20: MEA, H_2O SR23: MEA, H_2O
Material balances	$i = CO, CO_2, MEA, H_2O$; $k = 19,20,23,24,25,26$	
Overall	$(F_{19} + F_{24} + F_{26}) - (F_{20} + F_{23} + F_{25}) = 0$	
Species	CO_2: $F_{25}^{(CO_2)} - F_{19}^{(CO_2)} = 0$ MEA: $(F_{19}^{(MEA)} + F_{24}^{(MEA)}) - (F_{20}^{(MEA)} + F_{23}^{(MEA)}) = 0$ H_2O: $(F_{19}^{(H_2O)} + F_{24}^{(H_2O)} + F_{26}^{(H_2O)}) - (F_{20}^{(H_2O)} + F_{23}^{(H_2O)} + F_{25}^{(H_2O} = 0$	
Energy Balances		
Overall	$Q_{T-202} = \sum_i F_{outlet}^{(i)} H_{outlet}^{(i)} + \sum_i F_{inlet}^{(i)} H_{inlet}^{(i)}$	

Table B2.16. Material and Energy Balance Equations for Reboiler (E–205)

Description	Inlet Streams SR23: MEA, H_2O	Outlet Streams SR24: MEA, H_2O
Material Balances		
Overall	$F_{23} - F_{24} = 0$	
Species	MEA: $F_{24}^{(MEA)} - F_{23}^{(MEA)} = 0$ H_2O: $F_{24}^{(H_2O)} - F_{23}^{(H_2O)} = 0$	
Energy Balances	$i = CO_2, MEA, H_2O$; $k = 23,24$	
Overall	$F_{24}H_{24} - F_{23}H_{23} - Q_{E-205} = 0$ $H_k = \frac{h_k^{(i)}(kJ/kgmol)}{MW^{(i)}(kg/kgmol)}$ H_k is the enthalpy of stream, k $F_k^{(i)}$ is the flow rate of component 'i' in stream, k $h_k^{(i)}$ is the specific enthalpy of component 'i' in stream k $Q_{E-205} - U_{E-205} A_{E-205} \Delta T_m = 0$ where, $\Delta T_m = \frac{(T_{23} - T_{SS_{out}}) - (T_{24} - T_{SS_{in}})}{\ln\left(\frac{(T_{23} - T_{SS_{out}})}{(T_{24} - T_{SS_{in}})}\right)}$	

Table B2.17. Material and Energy Balance Equations for Flash Drum (V–204)

Description	Inlet Streams SR25: CO_2, H_2O	Outlet Streams SR26: H_2O SR27: CO_2
Material Balances		
Overall	$F_{25} - (F_{26} + F_{27}) = 0$	
Species	MEA: $\frac{y_{25}^{(H_2O)}}{MW^{(H_2O)}} * F_{25} - x_{26}^{(H_2O)} * F_{26} = 0$ CO_2: $\frac{y_{25}^{(CO_2)}}{MW^{(CO_2)}} * F_{25} - y_{27}^{(CO_2)} * F_{27} = 0$ $K_i = \frac{y_i}{x_i}; \sum_i x_i = 1; \sum_i y_i = 1$ $y_{25}^{(CO_2)} + y_{25}^{(H_2O)} = 1;$ $y_{27}^{(CO_2)} = 1; \quad y_{27}^{(H_2O)} = 0$ $x_{26}^{(H_2O)} = 1; \quad x_{26}^{(CO_2)} = 0$ $K_i \equiv$ Distribution Coefficient $x_i \equiv$ mole fraction of component 'i' in the liquid phase $y_i \equiv$ mole fraction of component 'i' in the gas phase	
Energy Balances	$i = H_2O, CO_2;$ $k = 25,26,27$	
Overall	$T_{25} = T_{26} = T_{27}$	

Table B2.18. Material and Energy Balance Equations for Gas Compressor (C–201)

Description	Input Stream SR16: CO	Output Stream SR17: CO
Material Balances		
Overall	$F_{16} - F_{17} = 0$	
Species	CO: $F_{17}^{(CO)} - F_{16}^{(CO)} = 0$	
Energy Balances	$i = CO; k = 16,17$	
Overall	$F_{17}H_{17} - F_{16}H_{16} + P_{C-201} = 0$ where $H_k^{(i)} = \frac{h_k^{(i)}(kJ/kgmol)}{MW^{(i)}(kg/kgmol)}$ H_k is the enthalpy of stream, k $F_k^{(i)}$ is the flow rate of component 'i' in stream, k $h_k^{(i)}$ is the specific enthalpy of component 'i' in stream k and $P_{C-201} \equiv$ Power supplied to the compressor $T_{17} = T_{16}\left(\frac{P_{17}}{P_{16}}\right)^{\frac{(k-1)}{k}}$ $T_{17} \equiv$ Adiabatic Discharge Temperature; $T_{16} \equiv$ Inlet Temperature $P_{17} \equiv$ Discharge Pressure; $P_{16} \equiv$ Inlet Pressure $c \equiv$ Ratio of specific heat capacities $\left(c_p / c_v\right)$	

Table B2.19. Material and Energy Balance Equations for Discharge Valve (Z–209)

Description	Inlet Stream SR27: CO_2	Outlet Stream SR28: CO_2
Material Balances		
Overall	$F_{27} - F_{28} = 0$	
Species	CO_2: $F_{28}^{(CO_2)} - F_{27}^{(CO_2)} = 0$	
Energy Balances		
Overall	$T_{28} = T_{27}$	

Table B2.20. Material and Energy Balance Equations for Product Drier (Z–206)

Description	Inlet Streams SR30: CNT, $CoCl_2$, $MoCl_2$, H_2O	Outlet Streams SR33: CNT, $CoCl_2$, $MoCl_2$, SR34: H_2O
Material Balances		
Overall	$F_{30} - (F_{33} + F_{34}) = 0$	
Species	CNT: $F_{33}^{(CNT)} - F_{30}^{(CNT)} = 0$ $CoCl_2$: $F_{33}^{(CoCl_2)} - F_{30}^{(CoCl_2)} = 0$ $MoCl_2$: $F_{33}^{(MoCl_2)} - F_{30}^{(MoCl_2)} = 0$ H_2O: $F_{34}^{(H_2O)} - F_{30}^{(H_2O)} = 0$	
Energy Balances		
Overall	$T_{30} = T_{33}$	

Table B2.21. Material and Energy Balance Equations for Acid Regenerator (Z–208)

Description	Inlet Streams SR31: $CoCl_2$, $MoCl_2$, H_2O RG3: O_2, H_2O	Outlet Streams SR09: HCl, H_2O, Co_2O_3, MoO_3
Material Balances		
Overall	$(F_{31} + F_{RG3}) - F_{09} = 0$	
Species	H_2O: $F_{09}^{(H_2O)} - (F_{31}^{(H_2O)} + F_{RG3}^{(H_2O)}) = 0$ HCl: $F_{09}^{(HCl)} - (\frac{2 kgmol HCl}{1 kgmol CoCl_2} * \frac{MW^{(HCl)}}{MW^{(CoCl_2)}} * F_{31}^{(CoCl_2)})$ $- (\frac{2 kgmol HCl}{1 kgmol MoCl_2} * \frac{MW^{(HCl)}}{MW^{(MoCl_2)}} * F_{31}^{(MoCl_2)}) = 0$ Co_2O_3: $F_{09}^{(Co_2O_3)} - (\frac{2 kgmol Co_2O_3}{4 kgmol CoCl_2} * \frac{MW^{(Co_2O_3)}}{MW^{(CoCl_2)}} * F_{31}^{(CoCl_2)}) = 0$ MoO_3: $F_{09}^{(MoO_3)} - (\frac{1 kgmol MoO_3}{1 kgmol MoCl_2} * \frac{MW^{(MoO_3)}}{MW^{(MoCl_2)}} * F_{31}^{(MoCl_2)}) = 0$ O_2: $F_{RG3}^{(O_2)} - (\frac{1 kgmol O_2}{4 kgmol CoCl_2} * \frac{MW^{(O_2)}}{MW^{(CoCl_2)}} * F_{31}^{(CoCl_2)})$ $- (\frac{1 kgmol O_2}{1 kgmol MoCl_2} * \frac{MW^{(O_2)}}{MW^{(MoCl_2)}} * F_{31}^{(MoCl_2)}) = 0$	
Energy Balances		
Overall	$T_{31} = T_{09}$ T_k is the temperature of stream, k	

Table B2.22. Material and Energy Balance Equations for Catalyst Regenerator (Z–207)

Description	Inlet Streams SR10: Co, Mo, SiO_2, C RGS1: Co, Mo, H_2O	Outlet Streams SR11: Co, Mo, SiO_2 RGS2: CO_2, H_2
Material Balances		
Overall	$(F_{10} + F_{RGS1}) - (F_{11} + F_{RGS2}) = 0$	
Species	SiO_2: $F_{10}^{(SiO_2)} - F_{11}^{(SiO_2)} = 0$ C: $F_{10}^{(C)} - F_{RGS2}^{(C)} = 0$ Co: $F_{11}^{(Co)} - (F_{10}^{(Co)} + F_{RGS1}^{(Co)}) = 0$ Mo: $F_{11}^{(Mo)} - (F_{10}^{(Mo)} + F_{RGS1}^{(Mo)}) = 0$ H_2O: $F_{RGS1}^{(H_2O)} - \frac{2kgmolH_2O}{1kgmolC} * \frac{MW^{(H_2O)}}{MW^{(C)}} * F_{10}^{(C)} = 0$ CO_2: $F_{RGS2}^{(H_2O)} - \frac{1kgmolCO_2}{1kgmolC} * \frac{MW^{(CO_2)}}{MW^{(C)}} * F_{10}^{(C)} = 0$ H_2: $F_{RGS2}^{(H_2)} - \frac{2kgmolH_2}{1kgmolC} * \frac{MW^{(H_2)}}{MW^{(C)}} * F_{10}^{(C)} = 0$	
Energy Balances		
Overall	$Q_{Z-207} = \sum_i F_{outlet}^{(i)} H_{outlet}^{(i)} + \sum_i F_{inlet}^{(i)} H_{inlet}^{(i)}$	

APPENDIX C

ANALYSIS OF HiPCO AND CoMoCAT PROCESS MODELS

C1. HiPCO Model

- **Production Rate of Carbon Nanotube**

Design Carbon Nanotube Production Capacity: 5,000 metric tons/year

Production Basis: 8,410 hrs/year

The proposed plant, designed to operate on a 24 hour continuous production basis, is shut down for two weeks in a year for scheduled maintenance.

Stream factor, SF = (Number of days plant operates per year)/365

$$\text{SF} = \frac{350}{365} = 0.96$$

Production Rate (kg/hr), $F_{30}^{(CNT)}$:

$$F_{30}^{(CNT)} = 5{,}000\frac{tonsCNT}{yr} * \frac{1{,}000kgCNT}{1tonCNT} * \frac{1yr}{365days} * \frac{1day}{24hr} * \frac{365days}{350days}$$

Final Carbon Nanotube Product, $F_{30}^{(CNT)}$ = **595 kg CNT/hr**

The final carbon nanotube product in the HiPCO process contains 97mol% carbon nanotubes and 3 mol% of residual iron particles (Bronikowski, et al, 2001). The amount of iron particles in the final product is estimated from the carbon nanotube produced.

Residual iron particles (3 mol%) in Final Product, $F_{30}^{(Fe)}$:

$$F_{30}^{(Fe)} = \frac{595kgCNT}{hr} * \frac{0.03kgmolFe}{0.97kgmolCNT} * \frac{1kgmolCNT}{36{,}000kgCNT} * \frac{56kgFe}{kgmolFe}$$

Residual iron in final product, $F_{30}^{(Fe)}$ = **0.03 kg Fe/hr**

The residual iron in the final carbon nanotube product is present in the form iron chloride. Thus, the amount of iron chloride in the final carbon nanotube product is estimated below:

$$F_{30}^{(FeCl_2)} = \frac{0.03 kgFe}{hr} * \frac{1 kgmolFeCl_2}{1 kgmolFe} * \frac{1 kgmolFe}{56 kgFe} * \frac{128 kgFeCl_2}{1 kgmolFeCl_2}$$

$$F_{30}^{(FeCl_2)} = \mathbf{0.07\ kg\ FeCl_2/hr}$$

The input–output structure for the overall HiPCO production process is shown in Figure C1.1:

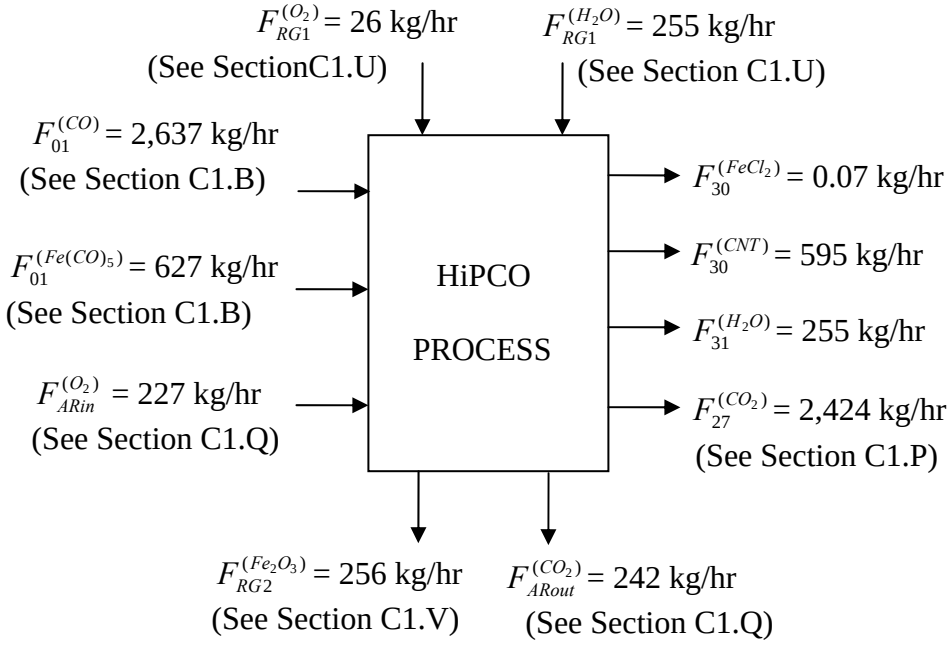

Figure C1.1. Input – Output Structure for the Overall HiPCO Process

There are four input streams into the overall HiPCO process diagram: the make–up CO feed stream ($F_{01}^{(CO)}$), the iron pentacarbonyl feed stream ($F_{02}^{(Fe(CO)_5)}$), the water added to the acid regeneration column to make up for the water loss in the product drier, $F_{RG1}^{(H_2O)}$, the oxygen supplied for the oxidation of amorphous carbon and iron in the air oxidizer,

$F_{ARin}^{(O_2)}$ and the oxygen supplied, $F_{RG1}^{(O_2)}$ for hydrochloric acid regeneration in the acid regeneration column.

There are five output streams from the HiPCO overall process diagram: the final product consisting of carbon nanotubes ($F_{30}^{(CNT)}$), and iron chloride ($F_{30}^{(FeCl_2)}$), the water loss from the wet product in the product drier, $F_{31}^{(H_2O)}$; the carbon dioxide produced in the flow reactor ($F_{28}^{(CO_2)}$); iron oxides residues formed during the hydrochloric acid regeneration process, $F_{RG2}^{(Fe_2O_3)}$; and carbon dioxide from the oxidation of amorphous carbon in the air oxidizer ($F_{ARout}^{(CO_2)}$).

C1.A. <u>Reactor (V–102)</u>: (Refer to Table B1.2)

The analysis of the input–output structure of the HiPCO flow reactor (V–102) is given in this section. The input–output structure, with the flow reactor as the control volume, is shown in Figure C1.2. There are two input streams: the mixed CO and iron pentacarbonyl feed stream (SR03) at 303 K, and the CO feed recycle stream (SR04) at 1,323 K. The output stream (SR05) leaves the flow reactor at 1,323 K. Heat is added to the reactor, Q_{V-102} to maintain the reaction temperature at 1,323 K, while the operating pressure is maintained at 450 psi (Bronikowski, et al, 2001).

The mixed stream (SR03) consists of two components: carbon monoxide, $F_{03}^{(CO)}$ and iron pentacarbonyl, $F_{03}^{(Fe(CO)_5)}$. The iron pentacarbonyl decomposes on heating to carbon monoxide and iron nanoparticles in the flow reactor. The CO feed recycle stream (SR04) consists of unconverted CO reactant, $F_{04}^{(CO)}$ recovered from and recycled to the flow reactor.

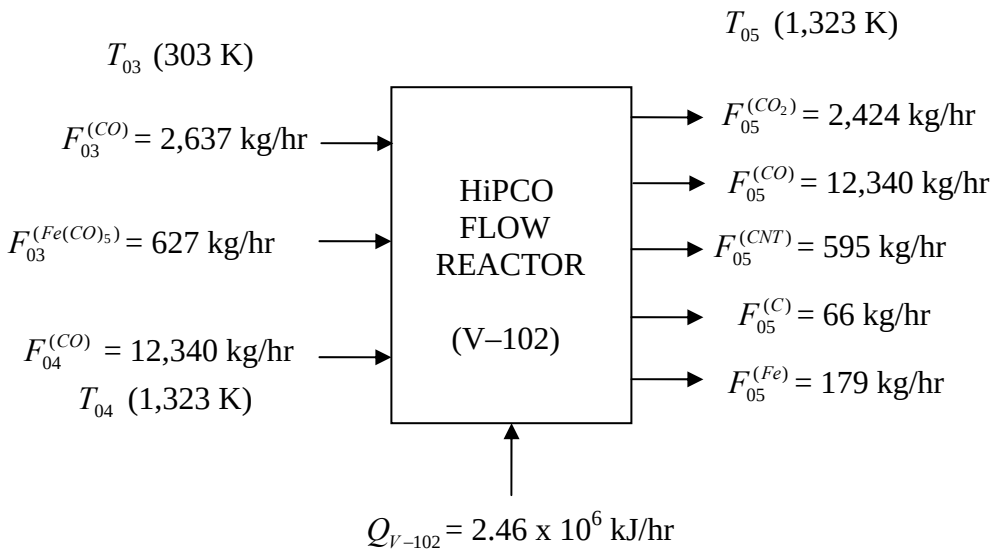

Figure C1.2. Input – Output Component Structure for HiPCO Flow Reactor (V–101)

The output stream (SR05) from the flow reactor consists of five components: the unconverted CO from the reactor, $F_{05}^{(CO)}$, carbon nanotube, $F_{05}^{(CNT)}$, amorphous carbon, $F_{05}^{(C)}$, CO_2 formed from the carbon nanotube and amorphous carbon reactions, $F_{05}^{(CO_2)}$, and residual iron particles formed from the decomposition of the catalyst precursor, $F_{05}^{(Fe)}$. The solution to the material and energy balance equations for the flow reactor (V–101), given in Table B1.2, and included in the input–output component structure of the HiPCO flow reactor in Figure C1.2 is given below:

Carbon Nanotube Reaction:

$$6000CO_{(g)} \xrightarrow{Fe} C_{3000} + 3000CO_{2(g)} \qquad \text{(C1.1)}$$

Conversion (*conv1*) = 20 mol%, i.e., 0.20 kgmol CO reacted to CNT per kgmol CO fed

Selectivity (*selc1*) = 90%, i.e., 0.9 kgmol CO reacted to CNT per kgmol CO reacted

Amorphous Carbon Reaction

$$2CO_{(g)} \rightarrow C + CO_{2(g)} \qquad \text{(C1.2)}$$

Selectivity = (1 – selc1) = 10%

Iron Particles from $Fe(CO)_5$ decomposition, $F_{03}^{(Fe)}$:

The iron pentacarbonyl catalyst precursor decomposes when heated to produce catalytic iron particles and carbon monoxide according to Equation (C1.3):

$$Fe(CO)_{5(g)} \xrightarrow{Heat} Fe + 5CO_{(g)} \qquad \text{(C1.3)}$$

The reaction stoichiometry shows that the number of moles of iron in the decomposition products equals the number of moles of iron pentacarbonyl in SR03:

Moles of Fe in Reactor = Moles of $Fe(CO)_5$ in SR03

Residual iron nanoparticles formed from the decomposition of iron pentacarbonyl in the reactor constitutes 30 weight% of the total carbon nanotube produced (Meyyappan, 2005). The amount of iron particles, $F_{05}^{(Fe)}$ in the effluent stream from the reactor is:

$$F_{05}^{(Fe)} = \frac{0.30 kgFe}{1 kgCNT} * F_{30}^{(CNT)} \qquad \text{(Meyyappan, 2005)}$$

$$F_{05}^{(Fe)} = \frac{0.30 kgFe}{1 kgCNT} * 595 \frac{kgCNT}{hr} = \mathbf{179\ kg\ Fe/hr}$$

$$F_{03}^{(Fe)} = F_{05}^{(Fe)} = \mathbf{179\ kg\ Fe/hr}$$

Iron Pentacarbonyl Feed Stream to Reactor, $F_{03}^{(Fe(CO)_5)}$:

The reaction stoichiometry for Equation (C1.3) shows that:

Moles of $Fe(CO)_5$ = Moles of Iron Particles Formed in Reactor

$F_{03}^{(Fe)}$ = 179 kg Fe/hr

$$F_{03}^{(Fe(CO)_5)} = \frac{1kgmolFe(CO)_5}{1kgmolFe} * \frac{196kgFe(CO)_5}{1kgmolFe(CO)_5} * \frac{179kgFe}{hr} * \frac{1kgmolFe}{56kgFe}$$

$F_{03}^{(Fe(CO)_5)}$ = **627 kg Fe(CO)$_5$/hr**

CO Produced from Thermal Decomposition of Iron Pentacarbonyl

The CO produced from the thermal decomposition of iron pentacarbonyl in the flow reactor is estimated from the stoichiometry ratios of the reactant and products according to Equation (C1.5):

CO from Thermal Decomposition of $Fe(CO)_5$:

$$= \frac{5kgmolCO}{1kgmolFe(CO)_5} * \frac{1kgmolFe(CO)_5}{196kgFe(CO)_5} * \frac{627kgFe(CO)_5}{hr} * \frac{28kgCO}{kgmolCO}$$

CO from Thermal Decomposition of $Fe(CO)_5$ = **448 kg CO/hr**

For material balance purposes and to prevent the build–up of CO in the reactor, the CO produced from the thermal decomposition of $Fe(CO)_5$ in the reactor forms part of the CO reactant consumed in the reactor. Consequently, the make–up CO reactant, $F_{03}^{(CO)}$ from the mixer is equal to the difference between the total CO converted in the reactor and the CO produced from the thermal decomposition of iron pentacarbonyl catalyst precursor.

CO Reactant Converted in Reactor:

The CO reactant consumed in the reactor is based on the carbon nanotube produced in the reactor (Equation C1.1). The amount of CO reactant converted in the reactor is calculated from Equation (C1.4):

Moles CO Converted = Moles CNT Formed / Selectivity (C1.4)

Selectivity = 90%, i.e., 0.9 kgmol CO reacted to form CNT/kgmol CO reacted

CO Consumed in Reactor:

$$= 595 \frac{kgCNT}{hr} * \frac{1 kgmolCNT}{36{,}000 kgCNT} * \frac{6{,}000 kgmolCO}{1 kgmolCNT} * \frac{1 kgmolCO}{0.9 kgmolCO} * \frac{28 kgCO}{kgmolCO}$$

CO Consumed in Reactor = **3,085 kg CO/hr**

Make–up CO Supplied to Reactor, $F_{03}^{(CO)}$:

The make–up CO supplied to the reactor from the mixer is equal to the difference between the total CO consumed in reactor and the CO produced during the thermal decomposition of iron pentacarbonyl:

$F_{03}^{(CO)}$ = CO Consumed in Reactor – CO from $Fe(CO)_5$ Decomposition

$F_{03}^{(CO)}$ = (3,085 – 448) kg CO/hr

Make–up CO Supplied to Reactor, $F_{03}^{(CO)}$ = **2,637 kg CO/hr**

Total CO Reactant Supplied to Reactor, $(F_{03} + F_{04})$:

The total CO supplied to the reactor consists of the make–up CO from the mixer, $F_{03}^{(CO)}$, the CO supplied from the decomposition of iron pentacarbonyl, and the unconverted CO feed recycle, $F_{04}^{(CO)}$. The single pass conversion in the flow reactor, based on the carbon nanotube produced, is given by Equation (C1.5), (Douglas, 1988):

Conversion = Moles CO Consumed in Reactor / Moles CO Fed to Reactor (C1.5)

CO Supplied to Reactor = Moles CO Consumed in Reactor / Conversion

Total CO Supplied to Reactor (based on carbon nanotube produced):

$$(F_{03} + F_{04}) = 3{,}085 \frac{kgCO}{hr} * \frac{1 kgmolCO}{28 kgCO} * \frac{1 kgmolCO}{0.20 kgmolCO} * \frac{28 kgCO}{1 kgmolCO}$$

Total CO Supplied to Reactor, $(F_{03} + F_{04})$ = **15,425 kg CO/hr**

The total CO supplied to the flow reactor as estimated above is based on carbon nanotube only, and consists of the make–up CO feed stream $F_{01}^{(CO)}$, CO feed recycle, $F_{04}^{(CO)}$ and CO from the thermal decomposition of $Fe(CO)_5$.

CO Feed Recycle, $F_{04}^{(CO)}$:

Since the CO from the thermal decomposition of iron pentacarbonyl is consumed in the reactor, the CO feed recycle to the reactor, $F_{04}^{(CO)}$ is estimated as the difference between the total CO supplied to the reactor and the CO consumed in the reactor. The CO consumed in the reactor includes the make–up CO feed and the CO from the thermal decomposition of iron pentacarbonyl. The CO feed recycle (SR04) is calculated thus:

$F_{04}^{(CO)}$ = Total CO Supplied – CO Consumed in Reactor

$F_{04}^{(CO)}$ = (15,425 – 3,085) kg CO/hr

CO Feed Recycle, $F_{04}^{(CO)}$ = **12,340 kg CO/hr**

Unconverted CO Reactant from Reactor, $F_{05}^{(CO)}$:

$$F_{05}^{(CO)} = (1 - conv1) * (F_{03} + F_{04})$$

$$F_{05}^{(CO)} = (1 - \frac{0.20 kgmolCO}{1 kgmolCO}) * 15{,}425 \frac{kgCO}{hr}$$

$F_{05}^{(CO)}$ = **12,340 kg CO/hr**

Carbon Nanotube Produced in Reactor, $F_{05}^{(CNT)}$

The stoichiometrically balanced form of the equation describing the formation of the carbon nanotube (CNT) in the HiPCO reactor is given by Equation (C1.1). The ratio of

the stoichiometric coefficients of the carbon nanotube product to the CO reactant is 1: 6,000. The single–pass CO conversion (20 mol%) and CO reactant selectivity (90%) to form carbon nanotubes are used to formulate the material balance equation:

$$F_{05}^{(CNT)} = \frac{1 kgmolCNT}{6{,}000 kgmolCO} * \frac{MW^{(CNT)}}{MW^{(CO)}} * (conv1) * (selc1) * (F_{03}^{(CO)} + F_{04}^{(CO)})$$

$$F_{05}^{(CNT)} = \frac{1 kgmolCNT}{6{,}000 kgmolCO} * \frac{36{,}000 \frac{kgCNT}{kgmolCNT}}{28 \frac{kgCO}{kgmolCO}} * \frac{0.2 kgmolCO}{1 kgmolCO} * \frac{0.9 kgmolCNT}{1 kgmolCO} * 15{,}425 \frac{kgCO}{hr}$$

Carbon Nanotube Produced in Reactor, $F_{05}^{(CNT)}$ = **595 kg CNT/hr**

Amorphous Carbon Produced in Reactor, $F_{05}^{(C)}$

Amorphous carbon is formed in the reactor according to Equation (C1.2):

$$2CO_{(g)} \longrightarrow C_{(s)} + CO_{2(g)}$$

The amount of amorphous carbon produced is based on the carbon nanotube produced in the flow reactor. In Equation (C1.2), the stoichiometric ratio of amorphous carbon produced to CO reactant consumed is 1: 2. The selectivity of the CO reactant to form amorphous carbon is 10%. The amount of amorphous carbon formed is calculated thus:

$$F_{05}^{(C)} = \frac{1 kgmolC}{2 kgmolCO} * \frac{MW^{(C)}}{MW^{(CO)}} * (conv1) * (1 - selc1) * (F_{03}^{(CO)} + F_{04}^{(CO)})$$

$$F_{05}^{(C)} = \frac{1 kgmolC}{2 kgmolCO} * \frac{12 \frac{kgC}{kgmolC}}{28 \frac{kgCO}{kgmolCO}} * \frac{0.20 kgmolCO}{1 kgmolCO} * \frac{0.1 kgmolC}{1 kgmolCO} * 15{,}425 \frac{kgCO}{hr}$$

Amorphous Carbon Produced in Reactor, $F_{05}^{(C)}$ = **66 kg C/hr**

Carbon dioxide Produced in Reactor, $F_{05}^{(CO_2)}$

Carbon dioxide is produced from the carbon nanotube reaction (Equation C1.1) and the amorphous carbon reaction (Equation C1.2). The total mass flow rate of carbon dioxide leaving the reactor is the sum of CO_2 produced from both reactions:

CO_2 from Carbon Nanotube Reaction (Equation C1.1):

$$= 595\frac{kgCNT}{hr} * \frac{1kgmolCNT}{36{,}000kgCNT} * \frac{3{,}000kgmolCO_2}{1kgmolCNT} * \frac{44kgCO_2}{1kgmolCO_2} = \mathbf{2{,}182\ kg\ CO_2/hr}$$

CO_2 from Amorphous Carbon Reaction (Equation C1.2):

$$= 66\frac{kgC}{hr} * \frac{1kgmolC}{12kgC} * \frac{1kgmolCO_2}{1kgmolC} * \frac{44kgCO_2}{1kgmolCO_2} = \mathbf{242\ kg\ CO_2/hr}$$

Carbon dioxide Produced in Reactor, $F_{05}^{(CO_2)}$

$$F_{05}^{(CO_2)} = (2{,}182 + 242) = \mathbf{2{,}424\ kg\ CO_2/hr}$$

The estimate of the CO_2 produced in both nanotube and amorphous carbon reaction is based on the production rate of carbon nanotube in the flow reactor.

Reactor Heat Effect, Q_{V-102}

The heat added to the reactor, Q_{V-102} is estimated from the reactor energy balance according to Equation (C1.6), (Felder, et al, 2000):

$$Q_{V-102} = \sum_i F_{inlet}^{(i)} H_{inlet}^{(i)} - \sum_i F_{outlet}^{(i)} H_{outlet}^{(i)} \qquad \text{(C1.6)}$$

The enthalpy data for the component streams into and out of the flow reactor (V–102) is given in Table C1.1. The heats of reaction are not required since the elements are chosen at their reference states: 298 K and 1 bar. The heats of reaction are implicitly included, when

Table C1.1. Enthalpy Data for HiPCO Flow Reactor (V–102)

	SR03		SR04		SR05	
Species	*F* (kg/hr)	*H* (303 K) kJ/kg	*F* (kg/hr)	*H* (1,323 K) (kJ/kg)	*F* (kg/hr)	*H* (1,323 K) (kJ/kg)
CO	2,637	– 3,432	12,340	– 5,118	12,340	– 5,118
$Fe(CO)_5$	627	– 1,877	–	–	–	–
CO_2	–	–	–	–	2,424	– 5,327
CNT	–	–	–	–	595	14.93
C	–	–	–	–	66	1,660
Fe	–	–	–	–	179	584

the heats of formation of the reactants are subtracted from those of the reaction products (Felder, et al, 2000).

Heat added to maintain the reactor at 1,323 K is calculated from Equation (C1.6):

$$Q_{V-102} = (-73{,}383{,}183 kJ/hr) - (-75{,}845{,}789 kJ/hr)$$

Heat added to the reactor, Q_{V-102} = **2,462,606 kJ/hr**

HP Steam Required to Supply Heat to Reactor (V–102):

$$F_{HPSteam}(kg/hr) = \frac{Q_{V-102}}{\Delta H_{vap}} = \frac{2{,}462{,}606 kJ/hr}{1{,}661.5 kJ/kg}$$

$$F_{HPSteam(V-102)} = \textbf{1,482 kg HP Steam/hr}$$

Reactor Size, V_{V-102}

The reactor size, V_{V-102} is related to the gas residence time, θ in the flow reactor by Equation (C1.7), (Ulrich, 1984):

$$\theta(s) = \frac{V_{V-102}(m^3) * \rho_g(kg/m^3)}{F_{total}^{(CO)}(kg/s)} \qquad \text{(C1.7)}$$

The reaction gas residence time, θ can be obtained from a theoretical analysis, the literature or laboratory–scale pilot plants. Since gas residence time in the laboratory scale reactor is equivalent to the residence time in the commercial scale reactor, the size of the commercial scale HiPCO reactor is determined by geometric scaling of the laboratory reactor:

$$\frac{V_{V-102}(m^3) * \rho_g(kg/m^3)}{F_{total}^{(CO)}(kg/s)} = \frac{V_{Lab}(m^3) * \rho_g(kg/m^3)}{F_{Lab}^{(CO)}(kg/s)}$$

$$V_{V-101} = \frac{F_{total}^{(CO)}(kg/s) * V_{Lab}(m^3)}{F_{Lab}^{(CO)}(kg/s)} \qquad \text{(C1.8)}$$

V_{Lab} = Volume of Laboratory scale HiPCO Reactor

$$V_{Lab} = \pi * \frac{(0.0762m)^2}{4} * 0.9144m = 0.0042 \text{ m}^3 \qquad \text{(Bronikowski, et al, 2001)}$$

$F_{Lab}^{(CO)}$ = Total Mass Flow Rate of CO in laboratory scale HiPCO Reactor

$F_{Lab}^{(CO)}$ = 0.0062 kg CO/s (Bronikowski, et al, 2001)

$F_{Total}^{(CO)}$ = Total Mass Flow Rate of CO in Reactor (V–102) = 4.3 kg CO/s

Reactor Size, $V_{V-102} = \frac{F_{total}^{(CO)}(kg/s) * V_{Lab}(m^3)}{F_{Lab}^{(CO)}(kg/s)}$

$$V_{V-102} = \frac{4.3kg/s * 0.0047m^3}{0.0062kg/s} = \mathbf{3.3\ m^3}$$

The length to diameter ratio in the commercial reactor is scaled geometrically as the laboratory reactor. The diameter of the laboratory scale reactor is one–twelfth of its length:

$$L_{V-102} = 12\ D_{V-102}$$

$$V_{V-102} = \pi \frac{D_{V-102}^2}{4} * 12 D_{V-102} = 3.3 \text{ m}^3$$

D_{V-102} = **0.65 m**

L_{V-102} = **7.68 m**

C1.B. <u>Mixer (V–101):</u> (Refer to Table B1.1)

The input–output structure for the mixer (V–101) is shown in Figure C1.3. There are two input streams: the make–up CO stream (SR01), $F_{01}^{(CO)}$ and the iron pentacarbonyl catalyst precursor vapor stream (SR02), $F_{02}^{(Fe(CO)_5)}$. The output stream (SR03) from the mixer is a two–component stream, consisting of carbon monoxide, $F_{03}^{(CO)}$, and iron pentacarbonyl catalyst precursor, $F_{03}^{(Fe(CO)_5)}$. The mass flow rate of carbon monoxide and iron pentacarbonyl into the mixer equals the mass flow rate of carbon monoxide and iron pentacarbonyl out of the mixer:

CO: $F_{01}^{(CO)} = F_{02}^{(CO)}$ = **2,637 kg CO/hr**

$Fe(CO)_5$: $F_{01}^{(Fe(CO)_5)} = F_{02}^{(Fe(CO)_5)}$ = **627 kg/hr**

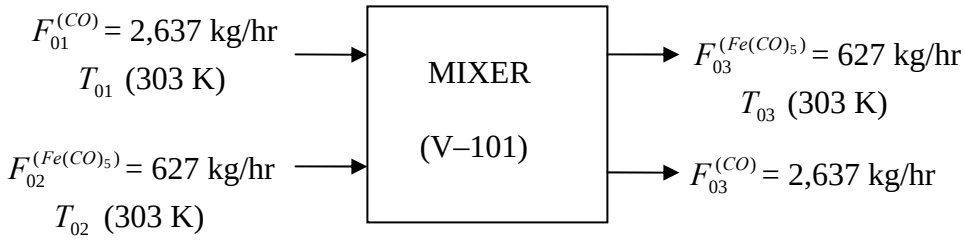

Figure C1.3. Input – Output Component Structure for Mixer (V–101)

C1.C. <u>Gas–Solid Filter, (Z–101)</u> (Refer to Table B1.8)

The input–output component structure of the gas–solid filter (Z–101) is shown in Figure C1.4. The input stream (SR05) to the filter from the reactor consists of five components; $F_{05}^{(CO)}$, $F_{05}^{(CO_2)}$, $F_{05}^{(CNT)}$, $F_{05}^{(C)}$, and $F_{05}^{(Fe)}$. There are two output streams from the filter: the mixed gas stream (SR07), and the solid product stream (SR06).

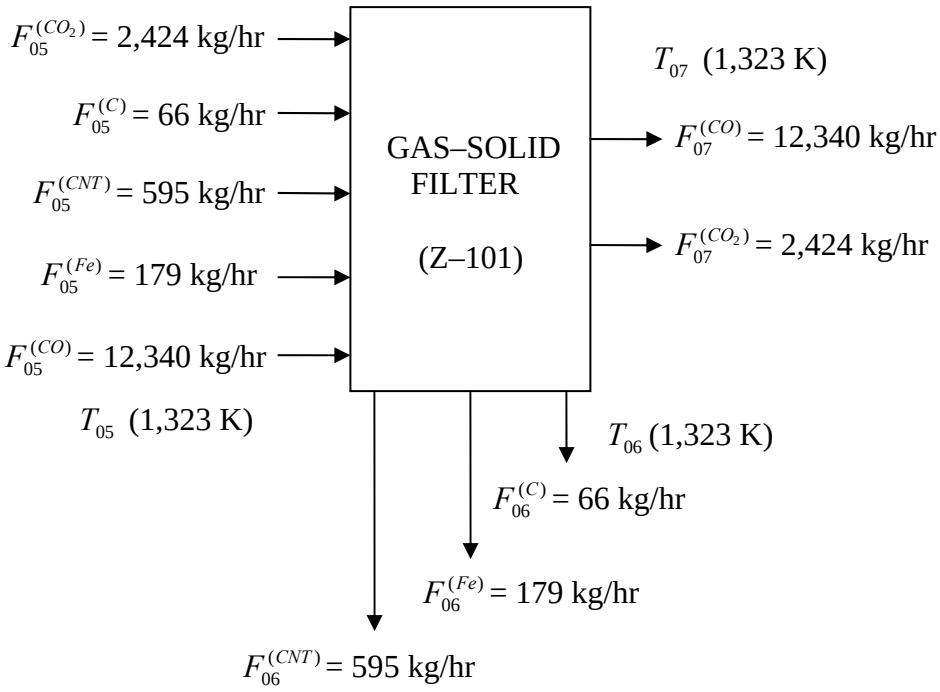

Figure C1.4. Input – Output Component Structure for Gas–Solid Filter (Z–101)

The mixed gas stream (SR07) consists of unconverted CO, $F_{07}^{(CO)}$ and carbon dioxide, $F_{07}^{(CO_2)}$. The solid product stream (SR06) consists of carbon nanotube, $F_{06}^{(CNT)}$, amorphous carbon, $F_{06}^{(C)}$, and iron particles, $F_{06}^{(Fe)}$.

CO: $F_{07}^{(CO)} = F_{05}^{(CO)} =$ **12,340 kg CO/hr**

CO_2: $F_{07}^{(CO_2)} = F_{05}^{(CO_2)} =$ **2,424 kg CO_2/hr**

CNT: $F_{06}^{(CNT)} = F_{05}^{(CNT)}$ = **595 kg CNT/hr**

C: $F_{06}^{(C)} = F_{05}^{(C)}$ = **66 kg C/hr**

Fe: $F_{06}^{(Fe)} = F_{05}^{(Fe)}$ = **179 kg Fe/hr**

Gas–Solid Filter Size, A_{Z-101}:

The filter size is estimated from preliminary design criteria for gas–solid filters, which relate the gas volumetric flow rate, q_g to the nominal area of the filter, A_{Z-101}, given by Equation (C1.9), (Ulrich,1984):

$$q_{gas} = 0.1 * A_{Z-101} \qquad \text{(C1.9)}$$

The gas volumetric flow rate, q_g is calculated from Equation (C1.10):

$$q_g(m^3/s) = \frac{Flowrate(kg/hr)}{Density(kg/m^3)} * \frac{1hr}{3600s} \qquad \text{(C1.10)}$$

Total Gas Flow Rate, $F_{07} = F_{07}^{(CO)} + F_{07}^{(CO_2)}$ = 14,764 kg/hr

The average gas density, ρ_g is calculated from the ideal gas law requirement that 1kgmol of an ideal gas at standard conditions of temperature (298 K) and pressure (15 psi) occupies a molar volume of 22.4 m^3:

Gas density at standard conditions (298 K, 15 psi), ρ_g^{std}

$$\rho_g^{std} = MW^{(g)} * \frac{1kgmol}{22.4m^3}$$

$$\rho_{CO}^{std} = 28\frac{kgCO}{kgmolCO} * \frac{1kgmolCO}{22.4m^3CO} = 1.25 \text{ kg/m}^3$$

$$\rho_{CO_2}^{std} = 44 \frac{kgCO_2}{kgmolCO_2} * \frac{1kgmolCO_2}{22.4m^3CO_2} = 1.96 \text{ kg/m}^3$$

Gas density at temperature, T_o (K) and pressure, P_o (psi), ρ_g^o:

$$\rho_g^o = \frac{298(K)}{T_o(K)} * \frac{P_o(psi)}{15(psi)} * \rho_g^{(std)}(kg/m^3) \qquad \text{(C1.11)}$$

At T_o = 1,323 K and P_o = 450 psi: $\rho_{CO}^o = 8.45 kg/m^3$; $\rho_{CO_2}^o = 13.2 kg/m^3$

Average gas density of the mixed gas stream (SR07):

$$\rho_{avg}^o = \frac{12{,}340 kg/hr}{14{,}764 kg/hr} * 8.45 \frac{kg}{m^3} + \frac{2{,}424 kg/hr}{14{,}764 kg/hr} * 13.2 \frac{kg}{m^3} = 9.2 kg/m^3$$

Equation (C1.10) gives:

$$q_g(m^3/s) = \frac{14{,}764 kg/hr}{9.2 kg/m^3} * \frac{1hr}{3600s} = 0.45 \text{ m}^3\text{/s}$$

Filter Size, $A_{Z-101} = \frac{0.45}{0.1}$

Filter Size, A_{Z-101} = **4.5 m^2**

C1.D. <u>Reactor Effluent–Feed Recycle Heat Exchanger (E–102)</u>: (Refer to Table B1.3)

The input–output component structure for the reactor effluent–feed recycle cross heat exchanger (E–102) is shown in Figure C1.5. There are two input streams (SR07 and SR17) and two output streams (SR08 and SR18) into and out of the cross heat exchanger. The mixed gas stream (SR07 and SR08) consists of carbon monoxide and carbon dioxide, whereas the single component gas stream (SR17 and SR18) consist of unconverted CO feed recycle. The inlet component mass flow rates equal the outlet component mass flow rates for both sides.

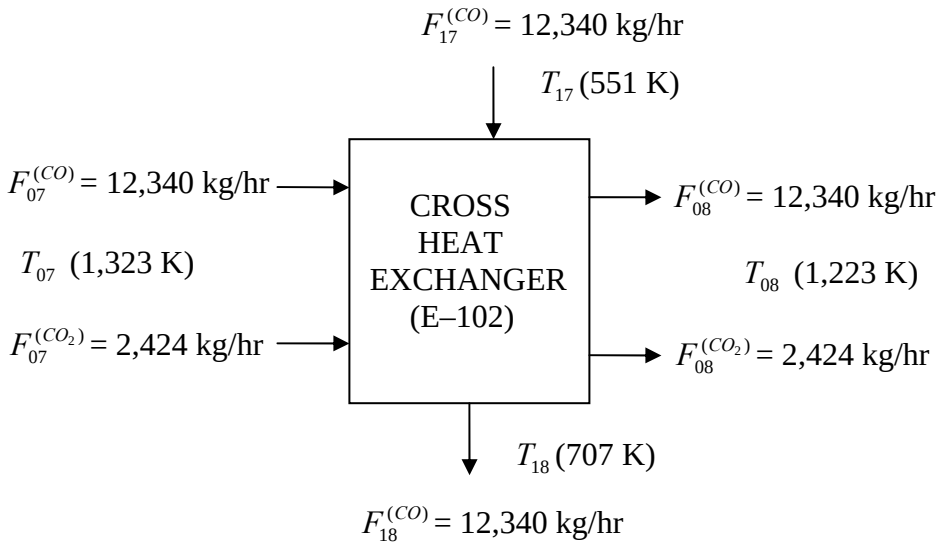

Figure C1.5. Input – Output Component Structure for Cross Heat Exchanger (E–102)

CO: $F_{08}^{(CO)} = F_{07}^{(CO)} =$ **12,340 kg CO/hr**

100% of unconverted CO is recovered and recycled:

$$F_{17}^{(CO)} = F_{18}^{(CO)} = F_{04}^{(CO)}$$

$$F_{17}^{(CO)} = F_{18}^{(CO)} = \textbf{12,340 kg CO/hr}$$

CO_2: $F_{08}^{(CO_2)} = F_{07}^{(CO_2)} =$ **2,424 kg CO_2/hr**

Energy Balance:

Heat exchange occurs in the cross heat exchanger (E–102) between the mixed gas stream and the CO feed recycle stream. The energy liberated by cooling the mixed gas stream from 1,323 K (SR07) to 1,223 K (SR08) is absorbed by the CO feed recycle stream. Consequently, the temperature of the CO feed recycle stream is increased from 551 K (SR17) to 707 K (SR18). The solution to the energy balance equations for the cross heat exchanger (E–102) is given below.

Temperature of CO Recycle (SR17) from Compressor (C–101), T_{17}:

T_{07} = 1,323 K; T_{08} = 1,223 K; T_{16} = 330 K

From Table B1.16:

$$T_{17} = T_{16}\left(\frac{P_{17}}{P_{16}}\right)^{\frac{(k-1)}{k}} \qquad \text{(C1.12)}$$

Suction Pressure, P_{16} = 75 psi; Discharge Pressure, P_{17} = 450 psi

$$k = \left(c_p \big/ c_v\right) = 1.4 \qquad \text{(Perry, et al, 1984)}$$

Equation (C1.12) gives: $T_{17} = 330K * \left(\frac{450 psi}{75 psi}\right)^{\frac{(1.4-1)}{1.4}}$ = **551 K**

Energy Liberated in Heat Exchanger (E–102), Q_{E-102}:

$$Q_{E-102} = \sum_i F_{08}^{(i)} H_{08}^{(i)} - \sum_i F_{07}^{(i)} H_{07}^{(i)} \qquad \text{(C1.13)}$$

The enthalpy data for the mixed gas process streams SR07 (1,323 K) and SR08 (1,223 K) are listed in Table C1.2.

Table C1.2. Enthalpy Data for Cross Heat Exchanger (E–102)

Component	F_{07} kg/hr	$H_{07}(1{,}323K)$ kJ/kg	F_{08} kg/hr	$H_{08}(1{,}223K)$ kJ/kg
CO	12,340	– 5,118	12,340	– 5,278
CO_2	2,424	– 5,327	2,424	– 5,482

Equation (C1.13) gives:

Heat Liberated in E–102, Q_{E-102} = **–2,349,417 kJ/hr**

Temperature of CO Recycle (SR18) exiting E–102, T_{SR18}:

The energy liberated in the cross heat exchanger, Q_{E-102} is absorbed by the CO feed recycle stream. The energy absorbed increases the CO recycle stream temperature from T_{SR17} (551 K) to T_{SR18}.

Energy Liberated = Energy Absorbed

$$Q_{E-102} = \frac{F_{18}^{(CO)}}{MW^{(CO)}} * \int_{T_{17}=551K}^{T_{18}} C_p^{(CO)}(T)dT \qquad \text{(C1.14)}$$

$$\frac{C_p^{(CO)}(T)}{8.314} = 5.7245 - 8.1762*10^{-3}T + 1.4569*10^{-5}T^2 - 1.0877*10^{-8}T^3 + 3.0279*10^{-12}T^4$$

Equation (C1.14) gives:

Temperature of CO Feed Recycle Exiting E–102, T_{18} = **707 K**

Heat Transfer Area of E–102, A_{E-102}

$$Q_{E-102} = U_{E-102}\, A_{E-102}\, \Delta T_{lm}$$

$$\Delta T_{lm} = \frac{(T_{07} - T_{18}) - (T_{08} - T_{17})}{\ln\left((T_{07} - T_{18}) \big/ (T_{08} - T_{17})\right)}$$

ΔT_{lm} = 644 K

U_{E-102} = 204 kJ/ m^2.hr.K (Douglas, 1988)

$$A_{E-102} = \frac{Q_{E-102}}{U_{E-102} * \Delta T_{lm}}$$

$$A_{E-102} = \frac{2{,}349{,}417\ kJ/hr}{204\ kJ/m^2 hrK\ *\ 644\ K}$$

A_{E-102} = **18 m^2**

C1.E. <u>Waste Heat Boiler, E–103</u>: (Refer to Table B1.5)

The input–output component structure for the waste heat boiler (E–103) is shown in Figure C1.6:

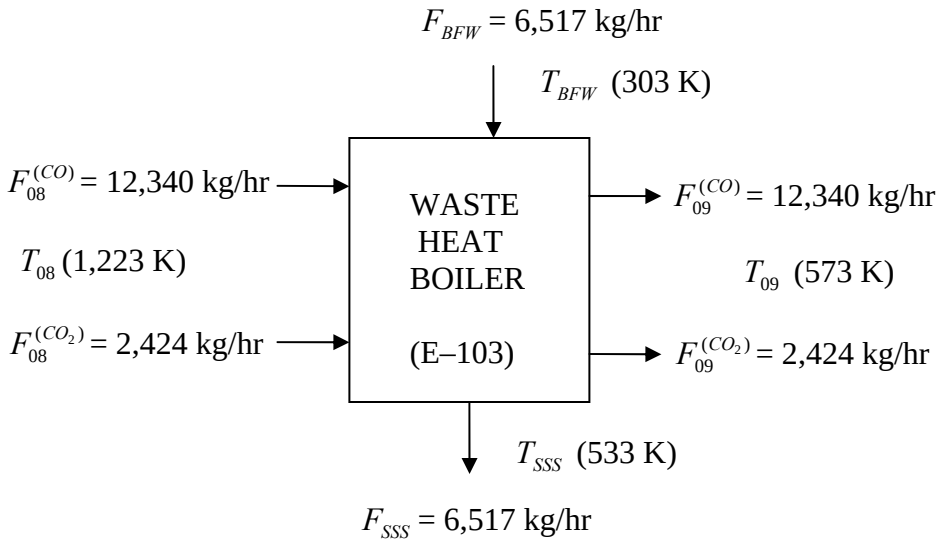

Figure C1.6. Input–Output Component Structure for Waste Heat Boiler (E–103)

There are two input streams (SR08 and BFW) and two output streams (SR09 and SSS) into and out of the waste heat boiler respectively. The mixed gas streams (SR08 and SR09) consists of CO and CO_2, while the boiler feed water (BFW), supplied at 303 K is converted to saturated steam (SSS) at 533 K, in the waste heat boiler.

CO: $F_{09}^{(CO)} = F_{08}^{(CO)} =$ **12,340 kg CO/hr**

CO_2: $F_{09}^{(CO_2)} = F_{08}^{(CO_2)} =$ **2,424 kg/hr**

Energy Liberated in Waste Heat Boiler (E–103), Q_{E-103}:

Energy liberated in the waste heat boiler by the mixed gas stream being cooled from 1,223 K (SR08) to 573 K (SR09) is given by Equation (C1.15):

$$Q_{E-103} = \sum_i F_{08}^{(i)} H_{08}^{(i)} - \sum_i F_{09}^{(i)} H_{09}^{(i)} \qquad \text{(C1.15)}$$

The enthalpy data for the waste heat boiler (E–103) is given in Table C1.3:

Table C1.3. Enthalpy Data for Waste Heat Boiler (E–103)

Component	F_{08} kg/hr	$H_{08}(1{,}223K)$ kJ/kg	F_{09} kg/hr	$H_{09}(573K)$ kJ/kg
CO	12,340	– 5,278	12,340	– 3,099
CO_2	2,424	– 5,481	2,424	– 7,910

Equation (C1.15) gives the energy liberated in E–103, Q_{E-103}:

Q_{E-103} = (–78,416,464 kJ/hr) – (– 57,415,500 kJ/hr) = – **21,000,964 kJ/hr**

Boiler Feed Water Supplied to E–103, F_{BFW}

The mass flow rate of the boiler feed water supplied to the waste heat boiler is calculated from Equation (C1.16), (Luyben, et. al., 1988):

$$Q = F_{BFW} * (C_p \Delta T + \lambda_s) \qquad \text{(C1.16)}$$

Q = Energy Absorbed, kJ/hr = 21,000,964 kJ/hr

F_{BFW} = Mass Flow Rate of Boiler Feed Water, kg/hr

C_p = Specific heat capacity of water = 4.184 kJ/kg K

ΔT = Change in Temperature = (533 – 303) = 230 K

λ_s = Latent Heat of Steam, kJ/kg = 2,260 kJ/kg (Luyben, et al, 1988)

Equation C1.16 gives: $F_{BFW} = \dfrac{21{,}000{,}964 kJ/hr}{(4.184 kJ/kgK * 230K + 2{,}260 kJ/kg)}$ = 6,517 kg/hr

$F_{BFW} = F_{SSS}$ = **6,517 kg/hr**

Heat Transfer Area of E–103, A_{E-103}:

$$A_{E-103} = \frac{Q_{E-103}}{U_{E-103} * \Delta T_{lm}} \qquad \text{(C1.17)}$$

$$\Delta T_{lm} = \frac{(T_{08} - T_{SSS}) - (T_{09} - T_{BFW})}{\ln\left(\frac{(T_{08} - T_{SSS})}{(T_{09} - T_{BFW})}\right)} = 448 \text{ K}$$

$$U_{E-103} = 409\ kJ/m^2\ hr\ K \qquad \text{(Douglas, 1988)}$$

Equation (C1.17) gives:

$$A_{E-103} = \frac{21,000,964\ kJ\ /\ hr}{409\ kJ\ /\ m^2 hrK\ *\ 448\ K} = \mathbf{116\ m^2}$$

C1.F. <u>Heat Exchanger Water Cooler (E–104):</u> (Refer to Table B1.6)

The input–output component structure for the heat exchanger water cooler (E–104) is shown in Figure C1.7. There are two input streams (SR09 and CW1) into the cooler and two

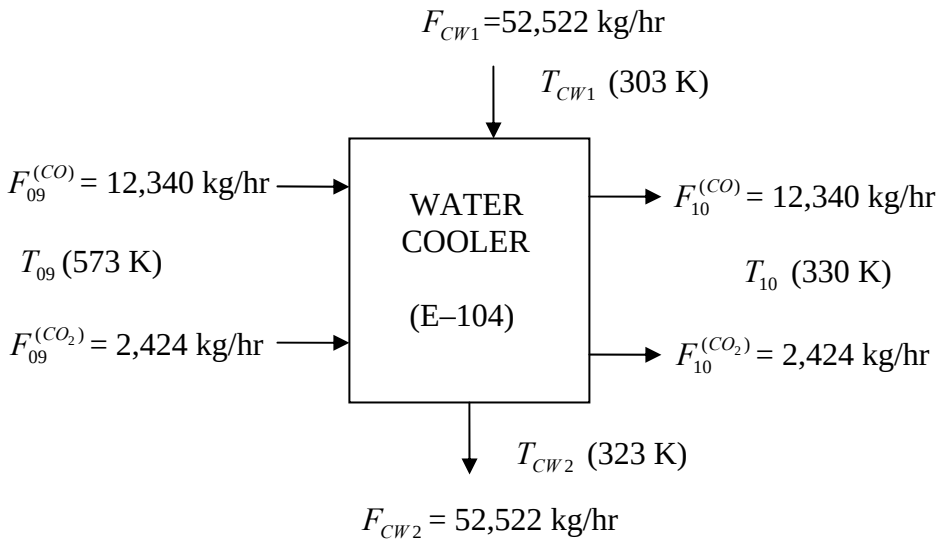

Figure C1.7. Input – Output Component Structure for Water Cooler (E–104)

output streams (SR10 and CW2) out of the water cooler. The mixed gas stream (SR09 and SR10) consists of CO and CO_2. Cooling water is supplied to the water cooler at 303 K (CW1) and exits at 323 K (CW2).

CO: $F_{10}^{(CO)} = F_{09}^{(CO)} =$ **12,340 kg CO/hr**

CO_2: $F_{10}^{(CO_2)} = F_{09}^{(CO_2)} =$ **2,424 kg CO_2/hr**

Temperature of Process Streams

$T_{09} = 573$ K; $T_{10} = 330$ K

$T_{CW1} = 303$ K; $T_{CW2} = 323$ K

Energy Liberated in Cooler (E–104), Q_{E-104} :

Energy is liberated from the mixed gas stream being cooled from 573 K (SR09) to 330 K (SR10). The energy liberated is given by Equation (C1.18):

$$Q_{E-104} = \sum_i F_{10}^{(i)} H_{10}^{(i)} - \sum_i F_{09}^{(i)} H_{09}^{(i)} \qquad \text{(C1.18)}$$

The enthalpy data for the mixed gas streams in the heat exchanger water cooler (E–104) is given in Table C1.4.

Table C1.4. Enthalpy Data for Heat Exchanger Water Cooler 1 (E–104)

Component	F_{09} kg/hr	$H_{09}(573K)$ kJ/kg	F_{10} kg/hr	$H_{10}(330K)$ kJ/kg
CO	12,340	– 3,099	12,340	– 3,398
CO_2	2,424	– 7,910	2,424	– 8,201

Equation (C1.18) gives: Q_{E-104} = (–61,810,544 kJ/hr) – (–57,415,500 kJ/hr)

Heat Liberated in Water Cooler, Q_{E-104} = **– 4,395,044 kJ/hr**

Cooling Water Supplied to E–104, F_{CW} :

$$F_{CW} = \frac{Q_{E-104}}{C_p^{(H_2O)} * \Delta T} \qquad \text{(C1.19)}$$

Q = Energy Absorbed, kJ/hr;

ΔT = Change in temperature, K = 20 K

F_{CW} = Flow rate of Cooling Water, kg/hr;

C_p = 4.184 kJ/kg K

Equation (C1.19) gives: $F_{CW} = \frac{4{,}395{,}044 kJ/hr}{4.184 kJ/kgK * 20K}$

$F_{CW2} = F_{CW1}$ = **52,522 kg Cooling Water/hr**

Heat Transfer Area of E–104, A_{E-104} :

$$A_{E-104} = \frac{Q_{E-104}}{U_{E-104} * \Delta T_{lm}} \qquad \text{(C1.20)}$$

U_{E-104} = 409 $kJ/m^2\ hr\ K$ (Douglas, 1988)

$$\Delta T_{lm} = \frac{(T_{09} - T_{CW2}) - (T_{10} - T_{CW1})}{\ln\left((T_{09} - T_{CW2}) / (T_{10} - T_{CW1})\right)}$$

ΔT_{lm} =100 K

Equation (C1.20) gives:

$$A_{E-104} = \frac{4{,}395{,}044\ kJ/hr}{409\ kJ/m^2 hrK * 100\ K}$$

Heat Exchanger Cooler (E – 104) Size, A_{E-104} = **107 m^2**

C1.G. <u>CO Feed Recycle Gas–Fired Heater (E–101):</u> (Refer to Table B1.4)

The input–output component structure for the CO feed gas–fired heater (E–101) is shown in Figure C1.8. There is one input stream ($F_{18}^{(CO)}$) and one output stream ($F_{04}^{(CO)}$) into and out of the gas–fired heater respectively. Thermal energy is supplied to the CO feed recycle gas–fired heater by natural gas, F_{CH_4} to increase the temperature of the CO feed recycle stream from 707 K (SR18) to 1,323 K (SR04).

CO: $F_{04}^{(CO)} = F_{18}^{(CO)} =$ **12,340 kg CO/hr**

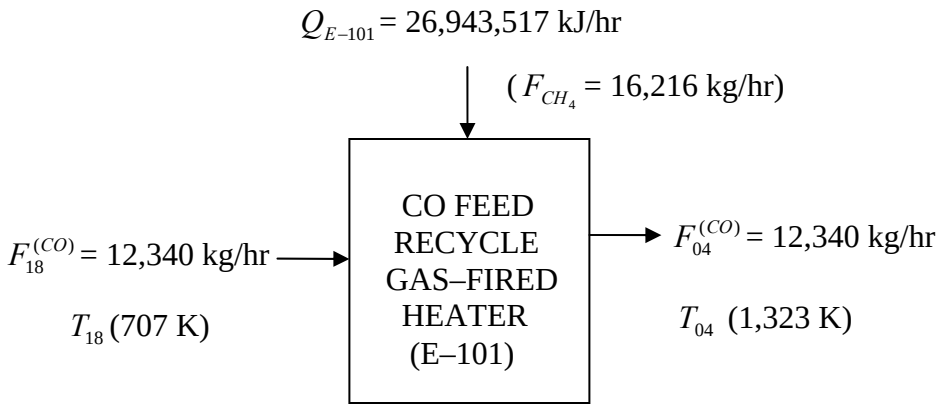

Figure C1.8. Input – Output Component Structure for Gas–Fired Heater (E–101)

Energy Supplied to E–101, Q_{E-101}:

The energy required to heat the CO feed recycle stream from 707 K (SR18) to 1,323 K (SR04) is estimated from Equation (C1.21):

$$Q_{E-101} = F_{04}H_{04} - F_{18}H_{18} \qquad \text{(C1.21)}$$

The enthalpy data for the CO feed recycle gas–fired heater is given in Table C1.5

Heat Supplied to E–101, Q_{E-101} = **26,943,517 kJ/hr**

Table C1.5. Enthalpy Data for CO Recycle Heater (E–101)

Component	F_{18} kg/hr	$H_{18}(707K)$ kJ/kg	F_{04} kg/hr	$H_{04}(1{,}323K)$ kJ/kg
CO	12,340	– 2,935	12,340	– 5,118

Natural Gas Supply to E–101, F_{CH_4}

The energy required to heat the CO feed recycle from 707 K (SR16) to 1,323 K (SR02) is supplied by the heat of combustion, $\Delta H_{comb.ustion}$ of natural gas. Natural gas is supplied at 1,400 K and 450 psia. The enthalpy of combustion natural gas is 55,501.2 kJ/kg (Perry, et al., 1984).

$$\text{Natural Gas required, } F_{CH_4} = \frac{Q_{E-101}(kJ/hr)}{\Delta H_{combustion}(kJ/kg)} \qquad \text{(C1.22)}$$

$$F_{CH_4} = \frac{26{,}943{,}517 kJ/hr}{55{,}501.2 kJ/kg}$$

$$F_{CH_4} = \mathbf{486\ kg/hr}$$

Heat Transfer Area for Gas–Fired Heater (E–101), A_{E-101}

$$A_{E-101} = \frac{Q_{E-101}}{U_{E-101} * \Delta T}$$

U_{E-101} = 204 kJ/m^2 hr K (Douglas, 1988)

Q_{E-101} = 26,943,517 kJ/hr

ΔT = 616 K

$$A_{E-101} = \frac{26{,}943{,}517 kJ/hr}{204 kJ/m^2 hrK * 616K}$$

A_{E-101} = **215 m^2**

C1.H. <u>Gas Compressor (C–101):</u> (Refer to Table B1.16)

The input–output component structure for the gas compressor (C–101) is shown in Figure C1.9. There is one input stream ($F_{16}^{(CO)}$) and one output stream ($F_{17}^{(CO)}$) into and out of the gas compressor. Power is supplied to the gas compressor to increase the pressure of the CO feed recycle from 75 psi (SR16) to 450 psia (SR17). Since the pressure of the CO feed recycle is increased adiabatically, the stream temperature increases from 330 K (SR16) to 551 K (SR17), also.

CO: $F_{17}^{(CO)} = F_{16}^{(CO)} =$ **12,340 kg CO/hr**

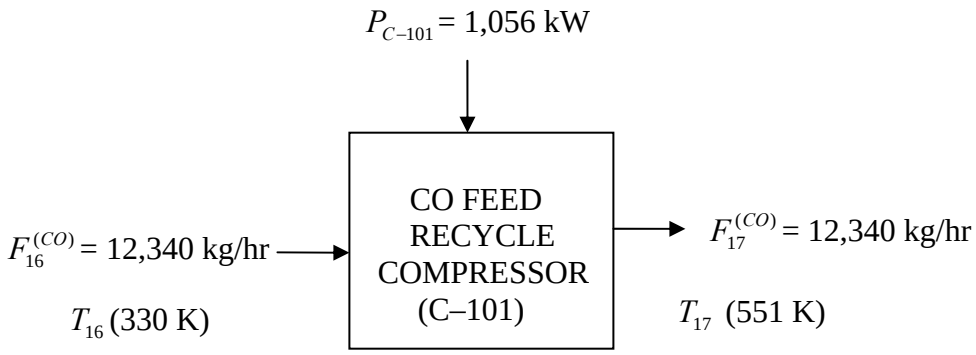

Figure C1.9. Input – Output Component Structure for Gas Compressor (C–101)

Compressor Power, P_{C-101}:

The compressor power is defined as the rate at which the gas compressor delivers work in the process. The gas compressor power is estimated from Equation (C1.23), (Perry et al, 1984):

$$P_{C-101}(kW) = \frac{Flowrate(kg/s) * 9.806 N/kg * Head_{adiabatic}(m)}{1000} \qquad \text{(C1.23)}$$

Adiabatic Head, H (m), (Perry, et al, 1984):

$$H = \frac{k}{k-1} * \frac{RT_{suction}}{9.806} * \left[\left(\frac{P_{discharge}}{P_{suction}} \right)^{(k-1)/k} - 1 \right] \qquad \text{(C1.24)}$$

$$\text{R = Gas constant} = \frac{8314}{MW^{(CO)}} = 296.93 J/kg.K \text{ ;}$$

$T_{suction}$ = 330 K: $P_{suction}$ = 75 *psia*; $P_{discharge}$ = 450 *psia,*

$$k = \frac{C_p}{C_v} = 1.4 \qquad \text{(Perry, et al. 1984)}$$

Equation (C1.24) gives:

$$H = 23{,}567.43 \ m$$

Gas Flow Rate, $F_{16}^{(CO)}$ = 3.43 *kg/s* (12,340 kg/hr);

Compressor Efficiency = 0.75 (Peters, et al., 2003)

Compressor Power, $P_{C-101}(kW)$ at 75% efficiency:

$$P_{C-101}(kW) = \frac{Flowrate(kg/s) * 9.806 N/kg * Head_{adiabatic}(m)}{Efficiency * 1000} \qquad \text{(C1.25)}$$

$$P_{C-101}(kW) = \frac{3.43 kg/s * 9.806 N/kg * 23{,}567.43(m)}{0.75 * 1000} = 1{,}056.20 \ kW$$

P_{C-101} = **1,056 kW**

C1.I <u>Gas Absorption Column (T–101):</u> (Refer to Table B1.12)

The gas absorption column is designed as an isothermal unit with operating temperature of 330 K and operating pressure of 75 psia. The input–output component structure of the gas absorption column is shown in Figure 1.10.

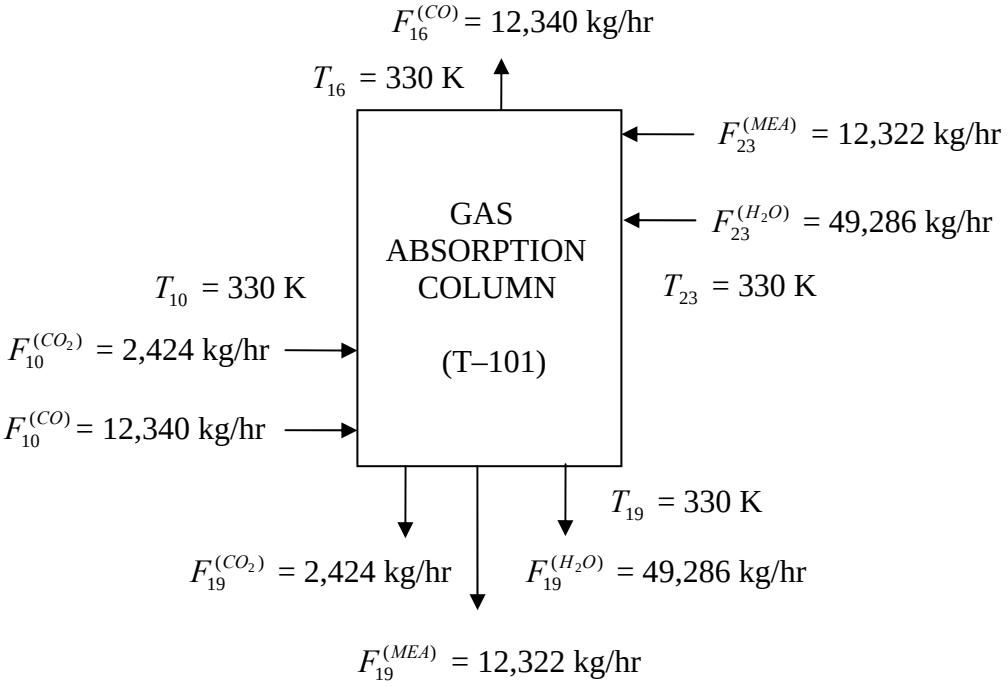

Figure C1.10. Input – Output Component Structure for Absorption Column (T–101)

There are two input streams: the mixed gas stream (SR10) from the water cooler and the lean monoethanol amine solution (SR23) from the cross heat exchanger (E–105). The mixed stream (SR10) consists of CO, $F_{10}^{(CO)}$ and CO_2, $F_{10}^{(CO_2)}$. The liquid MEA absorbent solution consists of 20 weight% monoethanol amine and 80 weight% aqueous (water) fraction (Yeh, et al, 2001).

There are two output streams: the CO feed recycle (SR16) that is recovered from the mixed gas stream in the absorber, and the CO_2–rich monoethanol solution (SR19). The solution to the material balance equations for the gas absorption column (T–101) is given below:

CO: $F_{16}^{(CO)} = F_{10}^{(CO)} =$ **12,340 kg CO/hr**

CO_2: $F_{19}^{(CO_2)} = F_{10}^{(CO_2)}$ = **2,424 kg CO_2/hr**

Liquid Absorbent (MEA Solution) Feed Rate, F_{23}:

The liquid absorbent feed rate, L is estimated based on the rule of thumb for the design of isothermal absorption column, given by Equation (C1.26), (Douglas, 1988):

$$L = 1.4\, mG \qquad \text{(C1.26)}$$

L = Liquid Absorbent Flow Rate = F_{23}

G = Gas Flow Rate = $F_{10}^{(CO)} + F_{10}^{(CO_2)}$ = **14,767 kg/hr**

m = Slope of equilibrium line = $\dfrac{P^o}{P_T}$ (ideal solution)

P^o = Vapor Pressure of CO_2 at 330 K = 223.50 psia (Perry, et al, 1984)

P_T = Operating Pressure = 75 psia

$$m = \frac{P^o}{P_T} = 2.98$$

Equation (C1.26) gives:

L = 1.4*2.98*14,767 kg/hr = 61,608 *kg/hr*

F_{23} = **61,608 kg/hr**

The aqueous fraction in the liquid monoethanol amine absorbent solution feed into the gas absorption column constitutes 80 weight% of the solution (Yeh, et al., 2001). Consequently, the MEA fraction of the liquid absorbent is 20 weight%. The aqueous and MEA fractions are estimated thus:

$F_{23}^{(MEA)}$ = 0.20 x 61,608 kg/hr = **12,322 kg MEA/hr**

$F_{23}^{(H_2O)}$ = 0.80 x 61,608 kg/hr = **49,286 kg H_2O/hr**

Solute Rich Liquid Leaving Gas Absorber (T–101), F_{19}

$$F_{19}^{(CO_2)} = F_{10}^{(CO_2)} \qquad \text{(Perfect Separation)}$$

$$F_{19}^{(CO_2)} = \mathbf{2{,}424\ kg/hr}$$

$$F_{19}^{(MEA)} = F_{23}^{(MEA)} = \mathbf{12{,}322\ kg/hr}$$

$$F_{19}^{(H_2O)} = F_{23}^{(H_2O)} = \mathbf{49{,}286\ kg/hr}$$

$$F_{19} = F_{19}^{(MEA)} + F_{19}^{(CO_2)} + F_{19}^{(H_2O)} = \mathbf{64{,}032\ kg/hr}$$

Number of Theoretical Plates, N:

The number of theoretical trays required in the gas absorption column is estimated from the Kremser Equation (C1.27), (Douglas, 1988):

$$N+1 = \frac{\ln\left[\left(\frac{L}{mG}-1\right)\left(\frac{y_{in}-mx_{in}}{y_{out}-mx_{in}}\right)+1\right]}{\ln\left(\frac{L}{mG}\right)} \qquad \text{(C1.27)}$$

The liquid absorbent feed (SR23) to the absorber is completely free of dissolved CO_2:

CO_2 in MEA Absorbent Liquid (SR23), $x_{in} = 0$ (Pure MEA Solution)

Since all the CO_2 in the mixed gas stream (SR10) is completely absorbed in the counter current flow of the MEA solution (SR23), the gas stream (SR16) exiting the column contains only unconverted CO. Thus, the terms in Equation (C1.27) can be represented by the following approximations:

$$\frac{y_{in}}{y_{out}} \approx 100\% \qquad \text{(Perfect Separation)}$$

Optimal Absorption Factor: $\frac{L}{mG} \approx 1.4$ (Douglas, 1988)

Equation (C1.27) gives:

Theoretical Number of Trays, $N = 10$

Actual Number of Trays, $N_{act.}$:

The number of actual trays required in the gas absorption column is estimated from Equation (C1.28) (Douglas, 1988):

$$N_{act.} = \frac{N}{\varepsilon_o} \qquad \text{(C1.28)}$$

The overall plate efficiency, ε_o, is obtained from a relationship corresponding to O'Connell's correlation (Douglas, 1988):

$$\varepsilon_o = \frac{0.377}{(m * M_L * \mu_L / \rho_L)^{0.209}} = 67.1\%$$

M_L = Molecular weight of liquid = 61 *lb/lbmol*

μ_L = Viscosity of solute = 0.022 *cP* (Peters, et al, 2002)

ρ_L = Density of liquid = 63.052 lb/ft^3 (Prausnitz et al, 1983)

Equation (C1.28) gives:

Actual Number of Trays, $N_{act} = \frac{10}{0.671} =$ **15**

Column Height, H_{T-101} :

The column height with a stage separation distance of 0.61 m is estimated from Equation (C1.29). The column height includes 15% allowance additional space, H_o at the ends of the column for vapor disengagement and liquid sump, (Douglas, 1988):

$$H_{T-101} = \frac{0.61 * N}{\varepsilon_o} + H_o = \frac{0.61 * (1.15) N}{\varepsilon_0} \qquad \text{(C1.29)}$$

Equation (C1.29) gives:

Column Height, H_{T-101} = **11 *m***

Column Diameter, D_{T-101}:

The column diameter is estimated from Equation (C1.30), based on a cylindrical configuration for the column (Ulrich, 1984):

$$D_{T-101} = \left(\frac{4 * G}{\pi * \rho_g * u_{s,g}} \right)^{1/2} \qquad \text{(C1.30)}$$

G = Maximum Vapor Rate, F_{10} = 14,767 kg/hr

ρ_g = Average Gas Density = 5.6 kg/m^3

ρ_l = (0.20 *1,015) + (0.80* 1,000) = 1,003 *kg/m^3*

$$\text{Superficial vapor velocity, } u_{s,g} = K_{SB} * \left(\frac{\rho_l - \rho_g}{\rho_g} \right)^{1/2} \qquad \text{(C1.31)}$$

K_{SB} = Souders–Brown Constant = 216 *m/hr* (Ulrich, 1984)

$u_{s,g}$ = 2.89 x 10^3 *m/hr*

Equation (C1.30) gives:

Column Diameter, D_{T-101} = **1.08 m**

C1.J. <u>Gas Stripping Column (T–102):</u> (Refer to Table B1.13)

The gas stripping column is designed as a non–isothermal unit with stripping temperature of 393 K and operating pressure of 45 psia. The input–output structure of the stripping column is shown in Figure C1.11. There are three input streams, which include, the

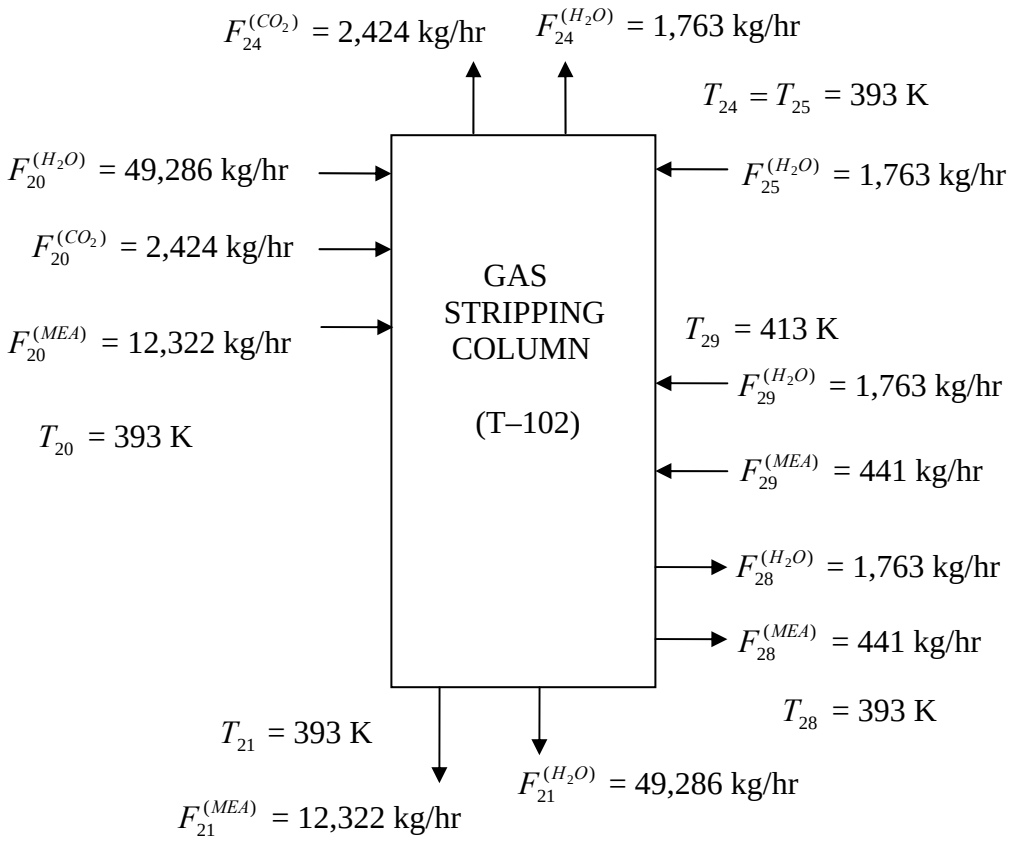

Figure C1.11. Input – Output Component Structure for the Stripping Column (T–102)

carbon dioxide–rich monoethanol amine (MEA) solution (SR20) from the cross heat exchanger (E–105), the liquid condensate (SR25) recovered from the flash drum (V–105), and the partially vaporized MEA solution (SR29) from the reboiler (E–106).

There are three output streams: the lean monoethanol amine (MEA) solution (SR21) recovered in the gas stripping column, the stripped carbon dioxide vapor stream (SR24) leaving the stripping column at the top, and the lean monoethanol amine solution (SR28) sent to the reboiler for partial vaporization. The solution to the material and energy balance equations given in Table B1.13, and included in Figure C1.11, is given below:

CO_2: $F_{20}^{(CO_2)} = F_{19}^{(CO_2)} =$ **2,424 kg CO_2/hr**

$F_{24}^{(CO_2)} = F_{20}^{(CO_2)} =$ 2,424 kgCO_2/hr (Perfect Separation)

MEA: $F_{20}^{(MEA)} = F_{19}^{(MEA)} =$ **12,322 kg MEA/hr**

Water: $F_{20}^{(H_2O)} = F_{19}^{(H_2O)} =$ **49,286 kg/hr**

Liquid Carryover in SR24, $F_{24}^{(H_2O)}$:

Vapor Pressure of Water, $P^o(393K)$

$$\ln P^o(393K) = 18.3036 - \frac{3{,}816.44}{393 - 46.13}$$

$P^o =$ 1,482 mmHg = 28.66 psia

$$y_{SR24}^{(H_2O)} = \frac{P^o}{P_T} = \frac{28.66}{45} = 0.64$$

$$y_{SR24}^{(CO_2)} + y_{SR24}^{(H_2O)} = 1$$

$$y_{SR24}^{(CO_2)} = \frac{2{,}424/44}{(2{,}424/44 + F_{24}^{(H_2O)}/18)} = 0.36$$

$F_{24}^{(H_2O)} =$ **1,763 kg H_2O/hr**

The liquid carryover in the gas stream exiting the absorber (SR24) is equivalent to the aqueous fraction recirculated through the reboiler. Thus, the MEA fraction in the feed to the reboiler is estimated based on the evaporation rate of the aqueous fraction in the reboiler:

$F_{24}^{(H_2O)} = F_{28}^{(H_2O)} = F_{29}^{(H_2O)} =$ 1,763 kg/hr

$F_{24}^{(H_2O)} = 0.80 * F_{28}$

$F_{28} =$ 2,204 kg/hr

$F_{28}^{(MEA)} = F_{29}^{(MEA)} =$ 2,204 – 1,763 kg/hr = **441 kg MEA/hr**

Energy Balance – Gas Stripping Column, (T–102):

The energy balance around the stripping column is given by Equation (C1.32):

$$Q_{T-102} = \sum_i F_{outlet}^{(i)} H_{outlet}^{(i)} - \sum_i F_{inlet}^{(i)} H_{inlet}^{(i)} \qquad \text{(C1.32)}$$

The enthalpy data for the component streams (SR19 and SR20) in and out of the gas stripping column is given in Table C1.6:

Table C1.6. Enthalpy Data for Gas Stripping Column (T–102)

	Inlet Streams,(kJ/kg)			Outlet Streams, (kJ/kg)		
Component	H_{20} (393 K)	H_{25} (393 K)	H_{29} (413 K)	H_{21} (393 K)	H_{24} (393 K)	H_{28} (393 K)
CO_2	– 6,770	–	–	–	– 6,770	–
MEA	1,206	–	1,490	1,206	–	1,206
H_2O	– 15,479	– 15,479	– 6,009	– 15,479	– 6,397	– 15,479

The heat supplied to the gas stripping column, Q_{T-102} is calculated from Equation (C1.32):

$$Q_{T-102} = (-801{,}674{,}396 \text{ kJ/hr}) - (-802{,}483{,}684 \text{ kJ/hr})$$

$$Q_{T-102} = \mathbf{809{,}288 \text{ kJ/hr}}$$

Number of Theoretical Plates, N

The number of theoretical plates in the gas stripping column is estimated from Equation (C1.33), (Perry, et al, 1984):

$$N = \frac{\ln\left[(1-A)(x_2 - x_1^o)/(x_1 - x_1^o) + A\right]}{\ln(S)} \qquad \text{(C1.33)}$$

$$\text{Stripping Factor, } S = \frac{mG}{L} = 1.4 \qquad \text{(Perry, et al, 1984)}$$

Absorption Factor, $A = S^{-1} = \frac{L}{mG}$ = 0.714 (Perry et al, 1984)

Stripping Medium is Pure Steam: x_1^o = 0

$$\frac{x_2}{x_1} \approx 100$$ (Perfect Separation)

Equation (C1.33) using the above approximation gives:

Number of Theoretical Plates, N = 10

Actual Number of Trays, N_{act} :

Plate efficiency, ε_o = 67.1%

$$N_{act} = \frac{N}{\varepsilon_o} = 15$$

Height of Stripping Column, H_{T-102} :

Equation (C1.29) gives:

Height of Column, H_{T-102} = **15 m**

Diameter of Stripping Column, D_{T-102} :

G = Maximum Vapor Rate, F_{24} = 4,187 kg/hr

ρ_g = (0.36*4.09) + (0.64 * 1.67) = 2.54 kg/m^3

ρ_l = (0.20 *1,015) + (0.80* 1,000) = 1,003 *kg/m^3*

Superficial vapor velocity $u_{s,g} = K_{SB} * \left(\frac{\rho_l - \rho_g}{\rho_g} \right)^{1/2}$ = 4.29 x 10^3 m/hr

Equation (C1.30) gives:

Column Diameter, D_{T-102} = **0.70 m**

C1.K. <u>Solute–Rich – Lean MEA Cross Heat Exchanger (E–105)</u>: (Refer to Table B1.7)

The input–output component structure for the solute rich–lean MEA solution cross heat exchanger (E–105) is shown in Figure C1.12. There are two input streams (SR19 and SR21), and two output streams (SR20 and SR23). The lean MEA solution (SR21 and SR23) consists of two components: MEA and H_2O, while the solute rich MEA solution (SR19 and SR20) consists of three components: absorbed CO_2, MEA and H_2O.

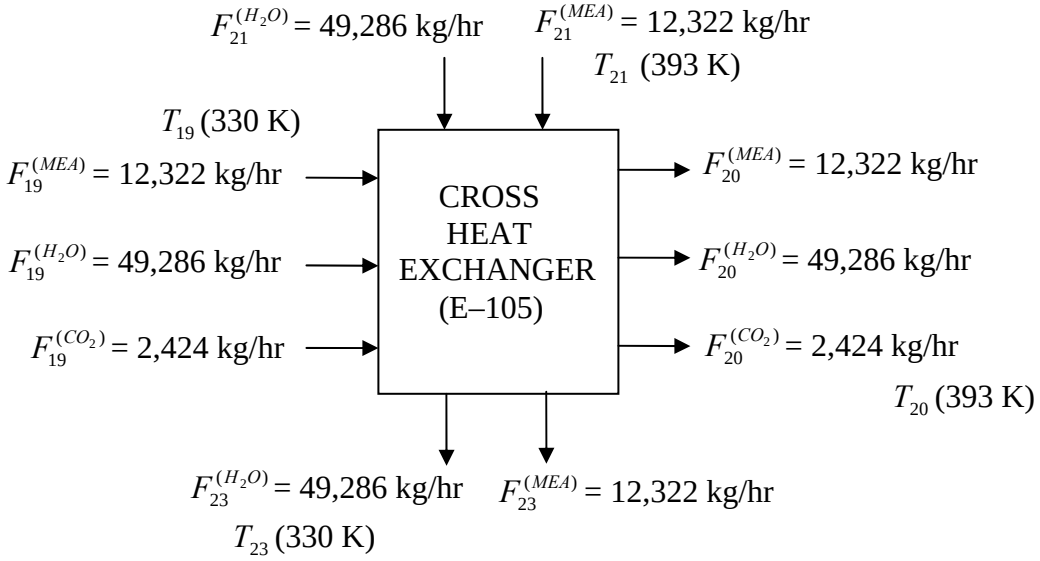

Figure C1.12. Input – Output Component Structure for Cross Heat Exchanger (E–105)

The material balance around the cross heat exchanger (E–105) is given below:

CO_2: $F_{19}^{(CO_2)} = F_{20}^{(CO_2)} = F_{10}^{(CO_2)} =$ **2,424 kg/hr**

MEA: $F_{19}^{(MEA)} = F_{20}^{(MEA)} = F_{23}^{(MEA)} =$ **12,322 kg/hr**

$F_{22}^{(MEA)} = F_{21}^{(MEA)} = F_{20}^{(MEA)} =$ **12,322 kg/hr**

Water: $F_{19}^{(H_2O)} = F_{20}^{(H_2O)} = F_{23}^{(H_2O)} =$ **49,286 kg/hr**

$F_{22}^{(H_2O)} = F_{21}^{(H_2O)} = F_{20}^{(H_2O)} =$ **49,286 kg/hr**

Energy Absorbed in the Cross Heat Exchanger, Q_{E-105}:

$$Q_{E-105} = \sum_i F_{20}^{(i)} H_{20}^{(i)} - \sum_i F_{19}^{(i)} H_{19}^{(i)} \qquad \text{(C1.34)}$$

T_{19} = 330 K; T_{20} = 393 K

The enthalpy data for the component streams (SR19 and SR20) in and out of the cross heat exchanger is given in Table C1.7:

Table C1.7. Enthalpy Data for Cross Heat Exchanger (E–105)

Component	F_{19} kg/hr	$H_{19}(330K)$ kJ/kg	F_{20} kg/hr	$H_{20}(393K)$ kJ/kg
CO_2	2,424	– 6,869	2,424	– 6,771
H_2O	49,286	– 15,745	49,286	– 15,479

The enthalpy change for the MEA component in the cross heat exchanger is calculated from Equation (C1.35):

$$\Delta H^{(MEA)} = \frac{F_{20}^{(MEA)}}{MW^{(MEA)}} * \int_{330K}^{393K} C_p^{(MEA)}(T)dT \qquad \text{(C1.35)}$$

$$\frac{C_p^{(MEA)}(T)}{8.314} = 9.3110 + 3.0010 * 10^{-1} T - 1.8180 * 10^{-4} T^2 - 4.6557 * 10^{-9} T^3$$

Equation C1.35 gives enthalpy change for the MEA component, $\Delta H^{(MEA)}$:

$\Delta H^{(MEA)}$ = 10,210,581 kJ/hr

Equation (C1.34) gives:

Q_{E-105} = (–779,310,898 kJ/hr) – (–792,685,526 kJ/hr) + 10,210,581

Heat Absorbed in Cross Heat Exchanger (E–105), Q_{E-105}

Q_{E-105} = **23,585,209 kJ/hr**

Temperature of Lean MEA Solution (SR23) Exiting E–105, T_{23} :

$$T_{21} = 393 \text{ K}$$

Energy Liberated = Energy Absorbed

$$Q_{E-105} = \frac{F_{21}^{(MEA)}}{MW^{(MEA)}} * \int_{393K}^{T_{23}} C_p^{(MEA)} dT + \frac{F_{21}^{(H_2O)}}{MW^{(H_2O)}} * \int_{393K}^{T_{23}} C_p^{(H_2O)} \qquad \text{(C1.36)}$$

$$\frac{C_p^{(H_2O)}(T)}{8.314} = 92{,}782 - 2.7224 * 10^2 T + 4.4792 * 10^{-1} T^2 - 3.9193 * 10^{-4} T^3 + 1.4257 * 10^{-7} T^4$$

Equation (C1.36) gives:

$$T_{23} = 330 \text{ K}$$

Area of the cross heat exchanger (E–105), A_{E-105}

$$A_{E-105} = \frac{Q_{E-105}}{U_{E-105} * \Delta T_m}$$

$$\Delta T_m = 63 \text{ K}$$

U_{E-105} = 4,104 kJ/ m^2.hr.K (Ulrich, 1984)

$$A_{E-105} = \frac{23{,}585{,}209 kJ/hr}{4{,}104 kJ/m^2 hrK * 63K}$$

$$A_{E-105} = \mathbf{92\ m^2}$$

C1.L. <u>Reboiler (E–106):</u> (Refer to Table B1.14)

The feed stream entering the stripping column, (SR20), is preheated from 330 K to 393 K, which is the stripping temperature in the stripping column. The bottoms stream (SR21 and SR28) exits the column at 393 K also. However the temperature driving force in the reboiler must be constrained to be less than 30 K, to prevent film boiling (Douglas,

1988). Thus, the temperature of the stream (SR29) leaving the reboiler is specified at 413 K.

The input–output component structure for the reboiler (E–105) is shown in Figure C1.13:

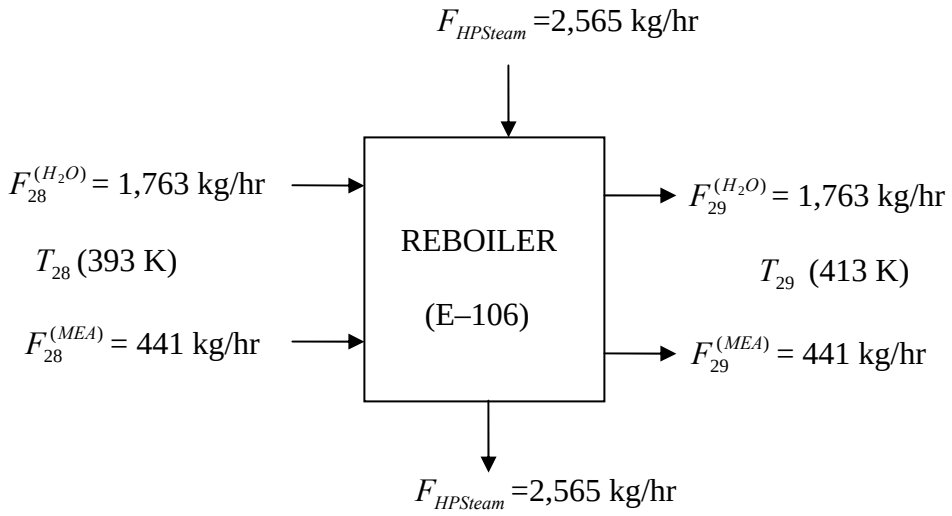

Figure C1.13. Input – Output Component Structure for Reboiler (E–106)

MEA: $F_{28}^{(MEA)} = F_{29}^{(MEA)}$ = **441 kg/hr**

Water: $F_{28}^{(H_2O)} = F_{29}^{(H_2O)} = F_{24}^{(H_2O)}$ = **1,763 kg/hr**

Heat Duty to Reboiler, Q_{E-106} : (Latent heat for steam, $\lambda_s = 2{,}260 kJ/kg$)

$$Q_{E-106} = \frac{F_{28}^{(MEA)}}{MW^{(MEA)}} * \int_{393K}^{413K} C_p^{(MEA)}(T)dT + [F_{28}^{(H_2O)} * (H_{29}^{(H_2O)} - H_{28}^{(H_2O)}) + \lambda_s] \qquad \text{(C1.37)}$$

The enthalpy data for the reboiler is given in Table C1.8

Table C1.8. Enthalpy Data for Reboiler (E–106)

Component	F_{28} kg/hr	$H_{28}(393K)$ kJ/kg	F_{29} kg/hr	$H_{29}(413K)$ kJ/kg
H_2O	1,763	– 15,479	1,763	– 15,393

Equation (C1.37) gives: Q_{E-106} = (125,157 kJ/hr) + (4,135,998 kJ/hr) = **4,261,155 kJ/hr**

HP Steam Supplied to Reboiler, $F_{HPSteam}$

$$F_{HPSteam} = \frac{4{,}261{,}155 kJ/hr}{1{,}661.5 kJ/kg} = \mathbf{2{,}565\ kg/hr}$$

Heat Transfer Area of Reboiler, A_{E-106}:

$$A_{E-106} = \frac{Q_{E-106}}{U_{E-106} * \Delta T_m}$$

U_{E-106} = 5,112 kJ/m^2 hr K (Ulrich, 1984)

ΔT_m = 20 K (to prevent film boiling in the reboiler)

$$A_{E-106} = \frac{4{,}261{,}155\ kJ/hr}{5{,}112\ kJ/m^2 hrK * 20\ K}$$

A_{E-106} = **42 m^2**

C1.N. <u>Flash Drum (V–105):</u> (Refer to Table B1.15)

The flash calculations are based on a perfect split in the CO_2–MEA binary system in an isothermal flash drum. Thus, the vapor stream (SR26) exiting the flash vessel contains the lighter component (CO_2 fraction) in the feed stream (SR24), whereas the liquid stream (SR25) contains the lighter component (H_2O)of the liquid fraction in the feed stream (Douglas, 1988).

CO_2: $F_{26}^{(CO_2)} = F_{24}^{(CO_2)} =$ **2,424 kg/hr**

Water: $F_{25}^{(H_2O)} = F_{24}^{(H_2O)} =$ **1,763 kg/hr**

The input–output component structure for the isothermal flash drum (V–105) is shown in Figure C1.14:

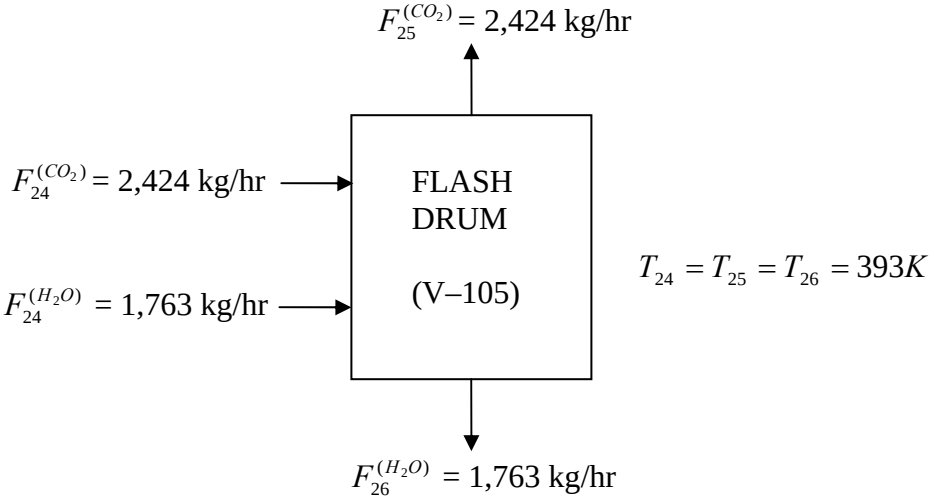

Figure C1.14. Input – Output Component Structure for Flash Drum (V–105)

Drum Diameter, D_{V-104}:

$$\text{Superficial vapor velocity, } u_g = 0.064 m/s * \left(\frac{\rho_l - \rho_g}{\rho_g} \right)^{1/2} \qquad \text{(C1.36)}$$

$$\rho_g = 1.364 \text{ kg/m}^3; \quad \rho_l = 1{,}000 \text{ kg/m}^3$$

Equation C1.36 gives: $u_g = 5.9 \times 10^3$ m/hr

The vessel diameter is estimated from Equation (C1.37), (Ulrich, 1984):

$$D_{V-105} = \left(\frac{4 * V}{\pi * \rho_g * u_g} \right)^{1/2} \qquad \text{(C1.37)}$$

V = Maximum Vapor Rate in Flash Drum, F_{24} = 4,187 kg/hr

Equation (C1.37) gives: Drum Diameter, D_{V-105} = **0.8 m**

Vessel Height, H_{V-105}, (Ulrich, 1984):

$$H_{V-105} = 4 D_{V-105} = \mathbf{3.2\ m}$$

C1.P. <u>Vent Valve (Z–105):</u> (Refer to Table B1.18)

The input–output component structure for the vent valve (Z–104) is shown in Figure C1.15:

CO_2: $F_{27}^{(CO_2)} = F_{26}^{(CO_2)}$ = **2,424 kg/hr**

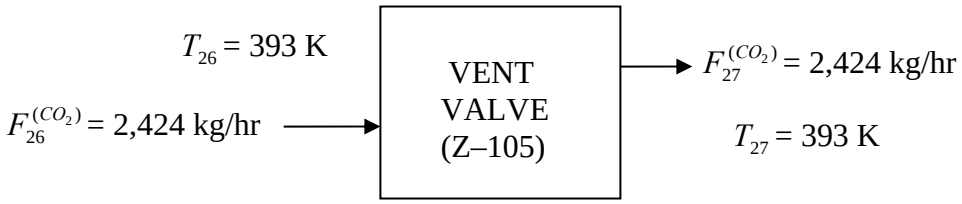

Figure C1.15. Input – Output Component Structure for Vent Valve (Z–105)

C1.Q. <u>Air Oxidizer (V–103):</u> (Refer to Table B1.9)

CNT: $F_{11}^{(CNT)} = F_{06}^{(CNT)}$ = **595 kg CNT/hr**

The oxidizer uses air to selectively oxidize the carbon nanotube product (SR06) from the reactor to remove the amorphous carbon impurities without affecting the structural integrity of the final product. The amorphous carbon ($F_{06}^{(C)}$ = 66 kg C/hr) supplied to the oxidizer is oxidized to carbon dioxide according to Equation (C1.38):

$$C + O_2 \xrightarrow{Ar} CO_2 \qquad \text{(C1.38)}$$

CO_2 from Amorphous Carbon Oxidation, $F_{ARout}^{(CO_2)}$:

Using the stoichiometric coefficients in Equation (C1.38):

$$F_{ARout}^{(CO_2)} = \frac{1 kgmol CO_2}{1 kgmol C} * \frac{44 kg CO_2}{kgmol CO_2} * \frac{1 kgmol C}{12 kg C} * 66 \frac{kg C}{hr}$$

$F_{ARout}^{(CO_2)}$ = **242 kg CO_2/hr**

Oxygen Required for Amorphous Carbon Oxidation, $F_{ARin(Carbon)}^{(O_2)}$

Using stoichiometric ratios in Equation (C1.38):

$$F_{ARin(Carbon)}^{(O_2)} = \frac{1kgmolO_2}{1kgmolC} * \frac{32kgO_2}{1kgmolO_2} * \frac{1kgmolC}{12kgC} * 66\frac{kgC}{hr}$$

$F_{ARin(Carbon)}^{(O_2)}$ = **176 kg O_2/hr**

In addition to amorphous carbon oxidation, the residual iron particles in the carbon nanotube product from the reactor are oxidized to iron oxide according to Equation (C1.39). However, the final product contains 3 mol % of iron particles (Bronikowski, et al., 2001). The oxidation of residual iron particles to iron oxide follows Equation (C1.39):

$$2Fe_{(s)} + O_{2(g)} \longrightarrow 2FeO_{(s)} \qquad \text{(C1.39)}$$

Amount of Iron Oxidized to Iron Oxide, $F_{06}^{(Fe)}$:

Since all the residual iron particles are oxidized to iron oxide, then the amount of iron oxidized to iron oxide equals the amount of iron formed in the flow reactor:

$F_{06}^{(Fe)}$ = **179 kg Fe/hr**

Oxygen Required for Iron Oxidation to Iron Oxide, $F_{ARin(Iron)}^{(O_2)}$

Using stoichiometric ratios in Equation (C1.39):

$$F_{ARin(Iron)}^{(O_2)} = \frac{1kgmolO_2}{2kgmolFe} * \frac{1kgmolFe}{56kgFe} * 179\frac{kgFe}{hr} * 32\frac{kgO_2}{kgmolO_2} = \textbf{51 kg } O_2\textbf{/hr}$$

Amount of Iron Oxide Formed, $F_{11}^{(FeO)}$:

Using stoichiometric ratios in Equation (C1.39):

$$F_{11}^{(FeO)} = \frac{2kgmolFeO}{2kgmolFe} * \frac{1kgmolFe}{56kgFe} * \frac{179kgFe}{hr} * \frac{72kgFeO}{1kgmolFeO} = \textbf{230 kg FeO/hr}$$

Total Oxygen Supplied to Oxidizer, $F_{ARin}^{(O_2)}$:

$F_{ARin}^{(O_2)}$ = O_2 for amorphous carbon oxidation + O_2 for iron oxidation

$F_{ARin}^{(O_2)}$ = (51 + 176) kg/hr = **227 kg O_2/hr**

The input–output component structure for the air oxidizer (V–103) is shown in Figure C1.16.

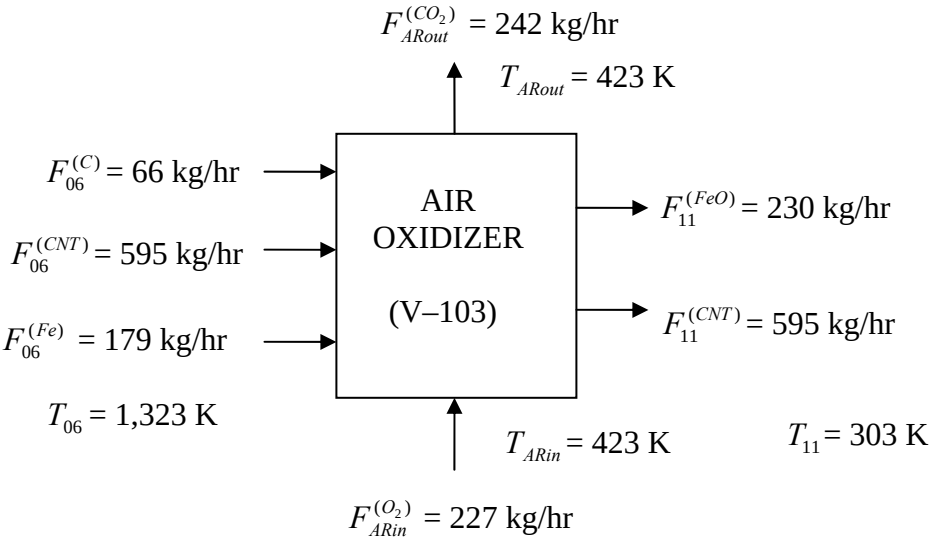

Figure C1.16. Input – Output Component Structure for Air Oxidizer (V–103)

Energy Balance for Air Oxidizer:

The energy balance around the air oxidizer is given by Equation (C1.40):

$$Q_{V-103} = \sum_{OUT} F^{(i)} H^{(i)} - \sum_{IN} F^{(i)} H^{(i)} \qquad \text{(C1.40)}$$

The enthalpy data for the air oxidizer (V–103) is given in Table C1.9.

Equation (C1.40) gives the heat liberated in the air oxidizer, Q_{V-103}

$$Q_{V-103} = \sum_{OUT} F^{(i)} H^{(i)} - \sum_{IN} F^{(i)} H^{(i)}$$

Q_{V-103} = **–3,010,562 kJ/hr**

Table C1.9. Enthalpy Data for Air Oxidizer (V–103)

Components	IN		OUT	
	F (kg/hr)	H (T) (kJ/kg)	F (kg/hr)	H (T) (kJ/kg)
CNT	595	14.93	595	14.37
C	66	1,657	–	–
Fe	179	584	–	–
O_2	227	– 33.10	–	–
CO_2	–	–	242	– 8,092
FeO	–	–	230	– 0.104

Cooling water required to remove heat liberated in Air Oxidizer:

$$F_{CW(V-103)} = \frac{2{,}165{,}006 kJ/hr}{4.184 kJ/kgK * (1{,}323 - 303)K} = \textbf{506 kg CW/hr}$$

Air Oxidizer Size, V_{V-103}

The solid residence time in the air oxidizer is used to estimate the equipment size according Equation (C1.41), (Ulrich 1984):

$$\theta(s) = \frac{V_{V-103} * f_s * \rho_s}{F_{06}^{(CNT)}} \qquad \text{(C1.41)}$$

Average Residence time, $\theta = 3{,}600 s$ (Chiang, et al, 2001)

Raw CNT density, $\rho_s = 1{,}365 kg/m^3$ (Kelley, 2003)

Mass flow rate of solids, $F_{06}^{(CNT)}$ = 0.165 kg/s (595 kg/hr)

Fraction of Contactor occupied by solids, f_s = 0.15 (Ulrich, 1984)

Equation (C1.41) gives the volume of the oxidizer, V_{V-103}

$$V_{V-103} = \frac{0.165 kg/s * 3600 s}{1{,}365 kg/m^3 * 0.15} = \mathbf{2.9\ m^3}$$

Length to Diameter Ratio = 4 (Branan, 2002)

$$V_{V-103} = \frac{\pi D^2}{4} * 4D = \pi D^3 = 2.91\ \text{m}^3$$

Diameter, D_{V-103} = **0.97 m**

Length, $L_{V-103} = 4 * D_{V-103}$ = **3.9 m**

C1.R. <u>Acid Treatment Tank (V–104):</u> (Refer to Table B1.10)

CNT: $F_{12}^{(CNT)} = F_{11}^{(CNT)}$ = **595 kg/hr**

FeO: $F_{11}^{(FeO)}$ = **230 kg/hr**

The iron oxides formed in the air oxidizer is removed by dissolution in 12% hydrochloric acid solution. The amount of hydrochloric acid required to dissolve the iron oxides is estimated from the reaction between iron oxide and HCl according to Equation (C1.42):

$$FeO_{(s)} + 2HCl_{(aq)} \longrightarrow FeCl_{2(aq)} + H_2O_{(l)} \qquad \text{(C1.42)}$$

Acid Supply to Treatment Tank, $F_{15}^{(HCl)}$:

The amount of hydrochloric acid required to dissolve the iron oxide is estimated based on the stoichiometric ratios of iron oxide and HCl reactants in Equation (C1.42):

$$F_{15}^{(HCl)} = \frac{2 kgmolHCl}{1 kgmolFeO} * \frac{230 kgFeO}{hr} * \frac{1 kgmolFeO}{72 kgFeO} * \frac{37 kgHCl}{1 kgmolHCl} = \mathbf{236\ kg\ HCl/hr}$$

The iron oxide (FeO) residue formed in the oxidizer is dissolved in 12% hydrochloric acid solution (Meyyappan, 2005). Consequently, the amount of water in the acid solution used is estimated thus:

$$F_{15}^{(H_2O)} = \frac{0.88 kgH_2O}{0.12 kgHCl} * 236 \frac{kgHCl}{hr} = \textbf{1,731 kg } \mathbf{H_2O/hr}$$

Using the stoichiometric ratios of reactants and products in Equation (C1.42):

Iron Chloride Produced in V–104, $F_{12}^{(FeCl_2)}$:

$$F_{12}^{(FeCl_2)} = \frac{1 kgmolFeCl_2}{1 kgmolFeO} * \frac{230 kgFeO}{hr} * \frac{1 kgmolFeO}{72 kgFeO} * \frac{128 kgFeCl_2}{1 kgmolFeCl_2}$$

Iron Chloride Produced, $F_{12}^{(FeCl_2)}$ = **409 kg $FeCl_2$/hr**

Water Produced in Equation (C1.42):

$$= \frac{1 kgmolH_2O}{1 kgmolFeO} * \frac{230 kgFeO}{hr} * \frac{1 kgmolFeO}{72 kgFeO} * \frac{18 kgH_2O}{1 kgmolH_2O} = \textbf{58 kg } \mathbf{H_2O/hr}$$

Water Leaving Acid Treatment Tank, $F_{12}^{(H_2O)}$

$F_{12}^{(H_2O)}$ = (1,731 + 58) kg/hr = **1,789 kg H_2O/hr**

The input–output component structure for the acid treatment tank (V–103) is shown in Figure C1.17.

Acid Treatment Tank Size, V_{V-104}, (Ulrich, 1984)

$$\theta(s) = \frac{V_{V-104} * f_s * \rho_s}{F_{12}^{(CNT)}} \qquad \text{(C1.43)}$$

Residence time, $\theta = 900s$ (Chiang, et al, 2001)

Raw CNT density, $\rho_s = 1{,}365 kg/m^3$ (Kelley, 2003)

Flow rate of CNT, $F_{12}^{(CNT)}$ = 0.165 kg/s (595 kg/hr)

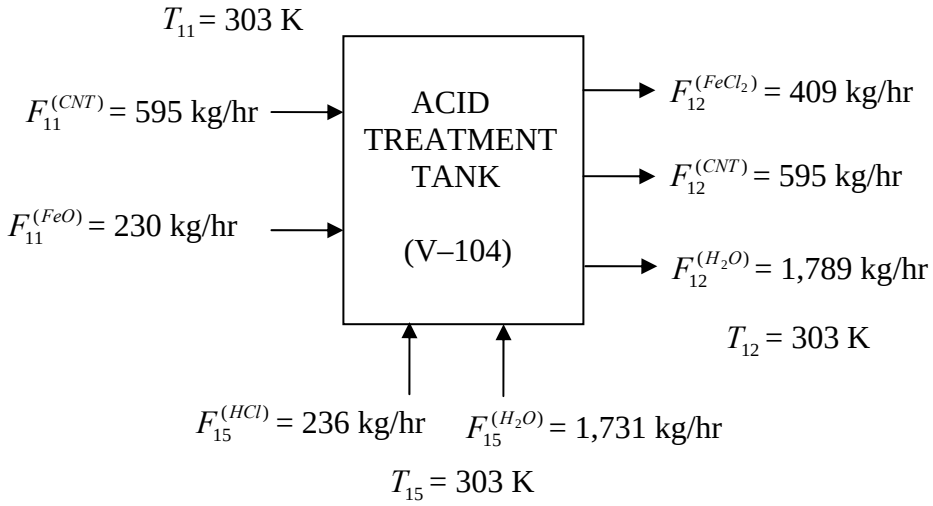

Figure C1.17. Input – Output Component Structure for Acid Treatment Tank (V–104)

Fraction of Contactor occupied by solids, f_s = 0.15 (Ulrich, 1984)

Volume of tank, $V_{V-104} = \dfrac{0.165 kg/s * 900 s}{1{,}365 kg/m^3 * 0.15}$ = **0.73 m^3**

Length to Diameter Ratio = 4 (Branan, 2002)

$V_{V-104} = (\pi D^2/4) * 4D = \pi D^3 = 0.73$ m^3

Diameter, D_{V-104} = **0.90 m**

Length, $L_{V-104} = 4 * D_{V-104}$ = **3.6 m**

C1.S. <u>Liquid–Solid Filter (Z–102):</u> (Refer to Table B1.11)

The amount of iron chloride in the final product, $F_{30}^{(FeCl_3)}$ is equal to the amount of iron chloride in the wet carbon nanotube product from the filter, $F_{13}^{(FeCl_3)}$. Thus, the iron chloride in the liquid stream (SR14) from the filter is calculated as the difference between the iron chloride from the acid treatment tank and the iron chloride in the wet product:

$FeCl_2$: $F_{13}^{(FeCl_2)} = F_{30}^{(FeCl_2)} =$ **0.07 kg/hr**

$F_{14}^{(FeCl_2)} = F_{12}^{(FeCl_2)} - F_{13}^{(FeCl_2)} =$ **408.93 kg/hr**

In addition to iron chloride, the carbon nanotube product from liquid–solid filter contains water. The amount of solution in the wet product (SR13) is estimated from the percentage characteristics of a liquid–solid rotary drum filter. The average cake dryness for a liquid–solid rotary drum filter is 70 weight% solids (Ulrich, 1984):

H_2O: $F_{13}^{(H_2O)} = 595\frac{kgCNT}{hr} * \frac{0.30 kgH_2O}{0.70 kgCNT} =$ **255 kg H_2O/hr**

$F_{14}^{(H_2O)} = F_{12}^{(H_2O)} - F_{13}^{(H_2O)} =$ **1,534 kg H_2O/hr**

CNT: $F_{13}^{(CNT)} = F_{12}^{(CNT)} =$ **595 kg CNT/hr**

The input–output component material structure for the liquid–solid filter (Z–102) is shown in Figure C1.18. The inlet component mass flow rates equal the outlet component mass flow rates into and out of the filter respectively.

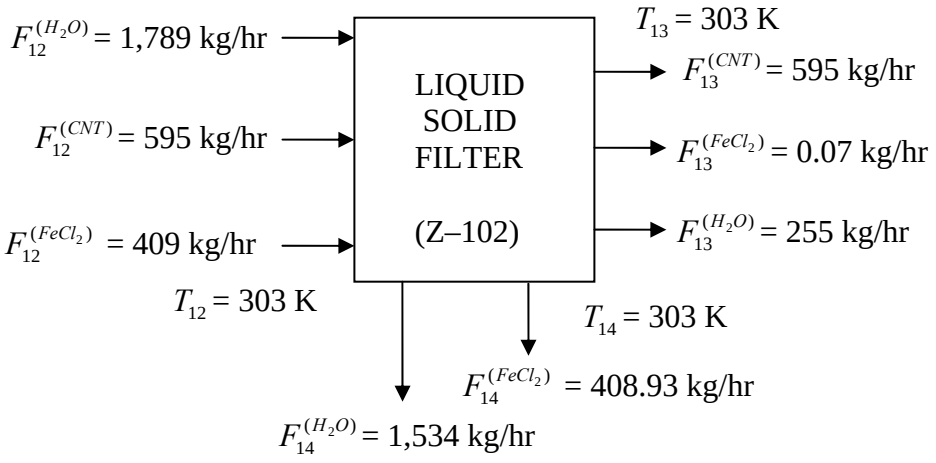

Figure C1.18. Input – Output Component Structure for Liquid–Solid Filter (Z–102).

Liquid–Solid Filter Size, A_{Z-102}

The filter size is estimated from preliminary design criteria relating the solid feed rate through the filter, $F_{12}^{(CNT)}(kg/s)$ to the filter nominal area $A(m^2)$ (Ulrich, 1984):

$$F_{12}^{(CNT)} = 0.02 * A_{Z-102} \qquad \text{(Ulrich, 1984)}$$

$F_{12}^{(CNT)}(kg/s)$ = 595 kg/hr = 0.165 kg/s

$$A_{Z-102} = \frac{0.165 kg/s}{0.02 kg/m^2 s}$$

A_{Z-102} = **9 m^2**

C1.T. <u>Product Drier (Z–103):</u> (Refer to Table B1.18)

Thermal energy is supplied to the product drier in form of HP steam to evaporate the water contained in the wet carbon nanotube product. The input–output component material structure for the product drier (Z–103) is shown in Figure C1.19:

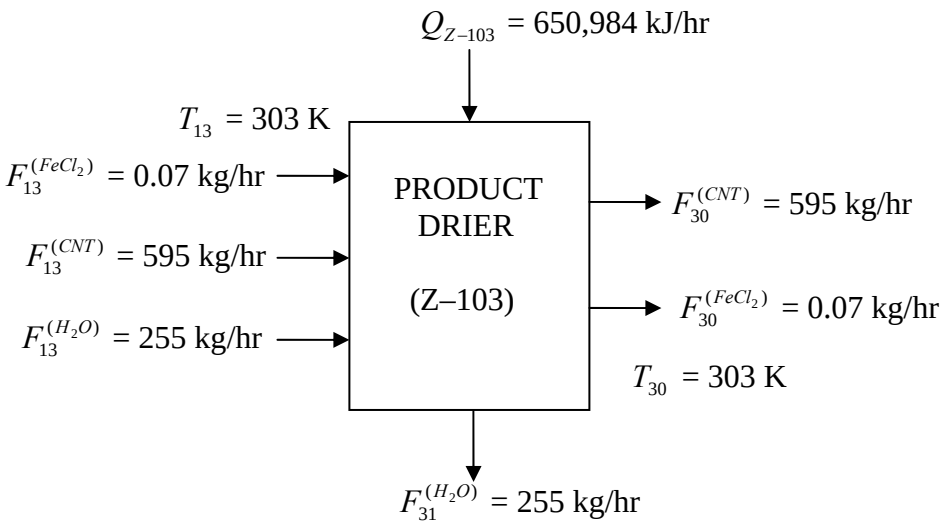

Figure C1.19. Input – Output Component Structure for Product Drier (Z–103)

CNT: $F_{30}^{(CNT)} = F_{13}^{(CNT)}$ = **595 kg/hr**

$FeCl_2$: $F_{30}^{(FeCl_2)} = F_{13}^{(FeCl_2)}$ = **0.07 kg/hr**

Energy Required to Evaporate Water from Drier, Q_{Z-103}

$$Q_{Z-103} = F_{13}^{(H_2O)} * (C_p^{(H_2O)} \Delta T + \lambda_s)$$

$F_{13}^{(H_2O)}$ = 255 kg/hr; $C_p^{(H_2O)}$ = 4.184 kJ/kg K

ΔT = (373 – 303) K = 70 K; λ_s = 2,260 kJ/kg

Q_{Z-103} = **650,984 kJ/hr**

HP Steam Supplying Heat to Drier, $F_{HPSteam}$

$$F_{HPSteam(IN)} = \frac{Q_{Z-103}}{\Delta H_{vap}} = \frac{821{,}692 kJ/hr}{1661.5 kJ/kg} = \textbf{392 kg/hr}$$

Water Evaporated from Product Drier:

$$F_{31}^{(H_2O)} = F_{13}^{(H_2O)} = \textbf{255 kg/hr}$$

Drier Size, V_{Z-103}

The solid residence time in the product drier is used to estimate the equipment size according Equation (C1.43), (Ulrich 1984):

$$\theta(s) = \frac{V_{Z-103} * f_s * \rho_s}{F_{30}^{(CNT)}} \qquad \text{(C1.43)}$$

Average Residence time, $\theta = 3{,}600 s$ (Chiang, et al, 2001)

Raw CNT density, $\rho_s = 1{,}365 kg/m^3$ (Kelley, 2003)

Mass flow rate of solids, $F_{06}^{(CNT)}$ = 0.165 kg/s (595 kg/hr)

Fraction of Contactor occupied by solids, f_s = 0.15 (Ulrich, 1984)

Equation (C1.43) gives the volume of the product drier, V_{Z-103}

$$V_{Z-103} = \frac{0.165 kg/s * 3600 s}{1{,}365 kg/m^3 * 0.15} = \mathbf{2.9\ m^3}$$

Length to Diameter Ratio = 4 (Branan, 2002)

$$V_{Z-103} = \frac{\pi D^2}{4} * 4D = \pi D^3 = 2.91\ \text{m}^3$$

Diameter, D_{Z-103} = **0.97 m**

Length, $L_{Z-103} = 4 * D_{Z-103}$ = **3.9 m**

C1.U. Acid Regeneration Column (Z–104)

In the acid regeneration column, the hydrochloric acid used in the acid dissolution step is regenerated by the reaction given in Equation (C1.44), (www.en.wikipedia.org):

$$4FeCl_{2(aq)} + 4H_2O_{(l)} + O_{2(g)} \longrightarrow 2Fe_2O_{3(s)} + 8HCl_{(aq)} \qquad \text{(C1.44)}$$

Using the stoichiometric ratio of reactants and products in Equation (C1.44):

HCl Regenerated from Acid Regeneration Column, $F_{32}^{(HCl)}$:

$$F_{32}^{(HCl)} = 409 \frac{kgFeCl_2}{hr} * \frac{8 kgmolHCl}{4 kgmolFeCl_2} * \frac{1 kgmolFeCl_2}{128 kgFeCl_2} * \frac{37 kgHCl}{1 kgmolHCl}$$

$$F_{32}^{(HCl)} = \mathbf{236\ kg/hr}$$

Iron Oxide Produced in Regenerator (Z–104), $F_{32}^{(Fe_2O_3)}$

$$F_{32}^{(Fe_2O_3)} = 409 \frac{kgFeCl_2}{hr} * \frac{2 kgmolFe_2O_3}{4 kgmolFeCl_2} * \frac{1 kgmolFeCl_2}{128 kgFeCl_2} * \frac{160 kgFe_2O_3}{1 kgmolFe_2O_3}$$

$$F_{32}^{(Fe_2O_3)} = \mathbf{256\ kg/hr}$$

The iron oxide residue produced leaves the acid regeneration column is saturated with hydrochloric acid. However, the hydrochloric acid is recovered from the saturated iron oxide residue by passing the mixed stream (SR32) from the acid regeneration column through a centrifuge separator (Z–106) (www.acidrecovery.com).

Oxygen Required for Acid Regeneration, $F_{RG1}^{(O_2)}$

$$F_{RG1}^{(O_2)} = 409 \frac{kgFeCl_2}{hr} * \frac{1kgmolO_2}{4kgmolFeCl_2} * \frac{1kgmolFeCl_2}{128kgFeCl_2} * \frac{32kgO_2}{1kgmolO_2}$$

$$F_{RG1}^{(O_2)} = \mathbf{26\ kg/hr}$$

Make–up Water Supplied to Acid Regeneration Column, $F_{RG1}^{(H_2O)}$

$$F_{RG1}^{(H_2O)} = F_{13}^{(H_2O)} = \mathbf{255\ kg/hr}$$

$$F_{32}^{(H_2O)} = F_{14}^{(H_2O)} + F_{RG1}^{(H_2O)} = \mathbf{1{,}731\ kg/hr}$$

The input–output component balance for the acid regeneration column (Z–104) is given in Figure C1.20.

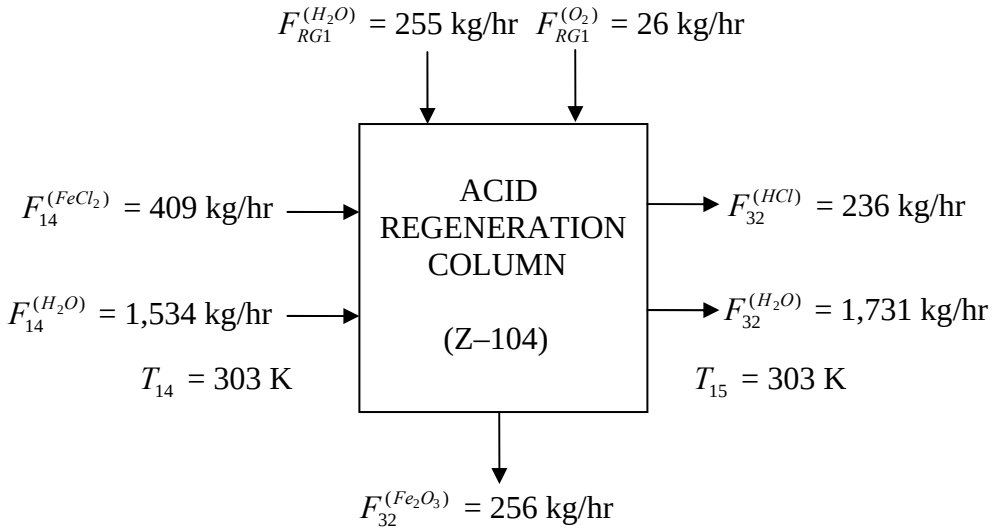

Figure C1.20. Input – Output Component Balance for Acid Regeneration Column (Z–104)

Acid Regeneration Column Size,

The average solid residence time of the iron oxide produced in the regeneration column is used to estimate the equipment size according Equation (C1.45), (Ulrich 1984):

$$\theta(s) = \frac{V_{Z-104} * f_s * \rho_s}{F_{32}^{(Fe_2O_3)}} \qquad \text{(C1.45)}$$

Average Residence time, $\theta = 3{,}600s$ (Ulrich, 1984)

Fe_2O_3 density, $\rho_s = 5{,}180 kg/m^3$ (Chiang, et al, 2003)

Mass flow rate of solids, $F_{32}^{(Fe_2O_3)}$ = 0.071 kg/s (256 kg/hr)

Fraction of Contactor occupied by solids, f_s = 0.15 (Ulrich, 1984)

Equation (C1.45) gives the volume of the acid regenerator, V_{Z-104}

$$V_{Z-104} = \frac{0.071 kg/s * 3600s}{5{,}180 kg/m^3 * 0.15} = \mathbf{0.33\ m^3}$$

Length to Diameter ratio = 4 (Ulrich.1984)

$$V_{Z-104} = \frac{\pi D^2}{4} * 4D = \pi D^3 = 0.33\ \text{m}^3$$

Diameter, D_{Z-104} = **0.5 m**

Length, $L_{Z-104} = 4 * D_{Z-104}$ = **2 m**

C1.V. Centrifuge Separator (Z–106) (Refer to Table B1.20)

The iron oxide residue which leaves the acid regeneration column saturated with hydrochloric acid is sent to the centrifuge separator (Z–106), where the hydrochloric acid is recovered and recycled to the acid treatment tank for another reaction cycle. The input stream (SR32) to the centrifuge from the acid regeneration column consists of three

components, $F_{32}^{(Fe_2O_3)}$, $F_{32}^{(HCl)}$, and $F_{32}^{(H_2O)}$. There are two output streams from the centrifuge: the iron oxide residue (RG2) and the recovered acid solution (SR15).The input–output component material balance for the centrifuge separator (Z–106) is given in Figure C1.21.

$$F_{32}^{(HCl)} = F_{15}^{(HCl)} = 236 \text{ kg/hr}$$

$$F_{32}^{(H_2O)} = F_{15}^{(H_2O)} = 1{,}731 \text{ kg/hr}$$

$$F_{32}^{(Fe_2O_3)} = F_{RG2}^{(Fe_2O_3)} = 256 \text{ kg/hr}$$

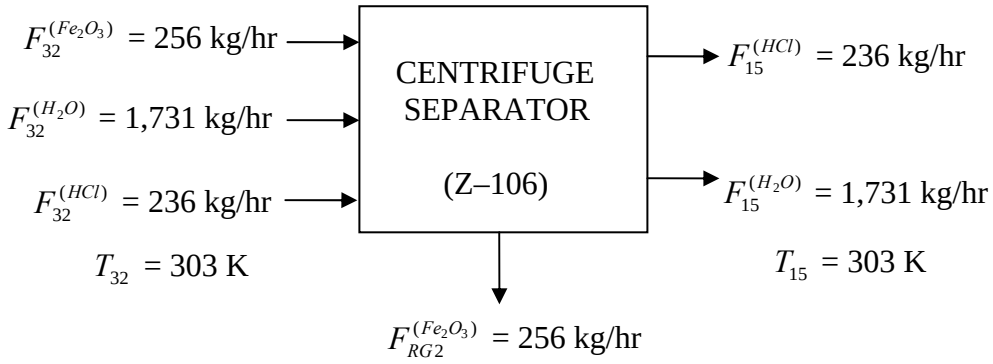

Figure C1.21. Input – Output Component Balance for Centrifuge Separator (Z–106)

This completes the analysis of the material and energy balance equations for all the process equipments in the HiPCO carbon nanotube process model. In addition, the size and other preliminary design criteria and data for the selection of the various process equipments in the process model were specified. In the next section, the analysis of the material and energy balance equations for the process equipments in the CoMoCAT carbon nanotubes process model will be discussed.

C2. CoMoCAT Model

● Production Rate of Carbon Nanotube

Design Carbon Nanotube Production Capacity: 5,000 metric tons/year

Production Basis: 8,410 hrs per year

Stream Factor, SF = 0.96

Production Rate (kg/hr), $F_{33}^{(CNT)}$:

$$F_{33}^{(CNT)} = 5000\frac{tonsCNT}{yr} * 1000\frac{kg}{ton} * \frac{1yr}{365days * 24\frac{hr}{day} * 0.96}$$

$F_{33}^{(CNT)}$ = **595 kg CNT/hr**

The final carbon nanotube product produces by the CoMoCAT process contains 97 mol% carbon nanotubes and 3 mol% of residual cobalt and molybdenum metal particles (Resasco, et al, 2001). The ratio of cobalt to molybdenum in the final carbon nanotube product is 1:1. Hence, the final product contains 1.5 mol% Co and 1.5 mol% Mo respectively.

Residual Cobalt (1.5 mol%) in Final Product, $F_{33}^{(Co)}$:

$$F_{33}^{(Co)} = \frac{595kgCNT}{hr} * \frac{1kgmolCNT}{36{,}000kgCNT} * \frac{0.015kgmolCo}{0.97kgmolCNT} * 59\frac{kgCo}{kgmolCo}$$

$F_{33}^{(Co)}$ = **0.02 kg Co/hr**

Residual Molybdenum in Final Product, $F_{33}^{(Mo)}$:

$$F_{33}^{(Mo)} = \frac{595kgCNT}{hr} * \frac{1kgmolCNT}{36{,}000kgCNT} * \frac{0.015kgmolMo}{0.97kgmolCNT} * 96\frac{kgMo}{kgmolMo}$$

$F_{33}^{(Mo)}$ = **0.03 kg Mo/hr**

The input–output structure for the overall CoMoCAT process flow diagram is shown in Figure C2.1.There are six input streams into the CoMoCAT overall process diagram: the make–up CO feed ($F_{01}^{(CO)}$) to the heater (E–201); the fresh cobalt ($F_{RGS1}^{(Co)}$) and fresh molybdenum ($F_{RGS1}^{(Mo)}$) metals added to the catalyst regeneration bed to make up for the Co and Mo metal losses in the final product/acid treatment step, and the high pressure (HP) steam ($F_{RGS1}^{(H_2O)}$) added to the catalyst regeneration bed for catalyst regeneration. The other input streams in the overall CoMoCAT process include: the oxygen ($F_{RG3}^{(O_2)}$) and the make–up water ($F_{RG3}^{(H_2O)}$) added to the acid regenerator column; sodium hydroxide ($F_{AK1}^{(NaOH)}$) added to the silica leaching tank (V–202); and air (F_{Air}), employed as a separation medium in the froth flotation column.

There are seven output streams from the overall CoMoCAT process diagram: the final product stream, consisting of carbon nanotube ($F_{33}^{(CNT)}$), cobalt chloride ($F_{33}^{(CoCl_2)}$), molybdenum chloride ($F_{33}^{(MoCl_2)}$) from the product drier; water evaporated from the wet carbon nanotube product in the product drier, $F_{34}^{(H_2O)}$; carbon dioxide ($F_{28}^{(CO_2)}$), produced in the fluidized bed reactor, exiting the process from the vent valve (Z–209); cobalt and molybdenum oxide ($F_{RG4}^{(Co_2O_3)}$ and $F_{RG4}^{(MoO_3)}$) residues, produced in the acid regeneration step, leaving the centrifugal separator (Z–203). The other output streams in the overall CoMoCAT process include: carbon dioxide ($F_{RGS2}^{(CO_2)}$) and hydrogen ($F_{RGS2}^{(H_2)}$) produced during the oxidation of amorphous carbon in the catalyst regeneration bed (Z–207); waste stream containing sodium hydroxide ($F_{WS1}^{(NaOH)}$) leaving the liquid–solid filter (Z–204).

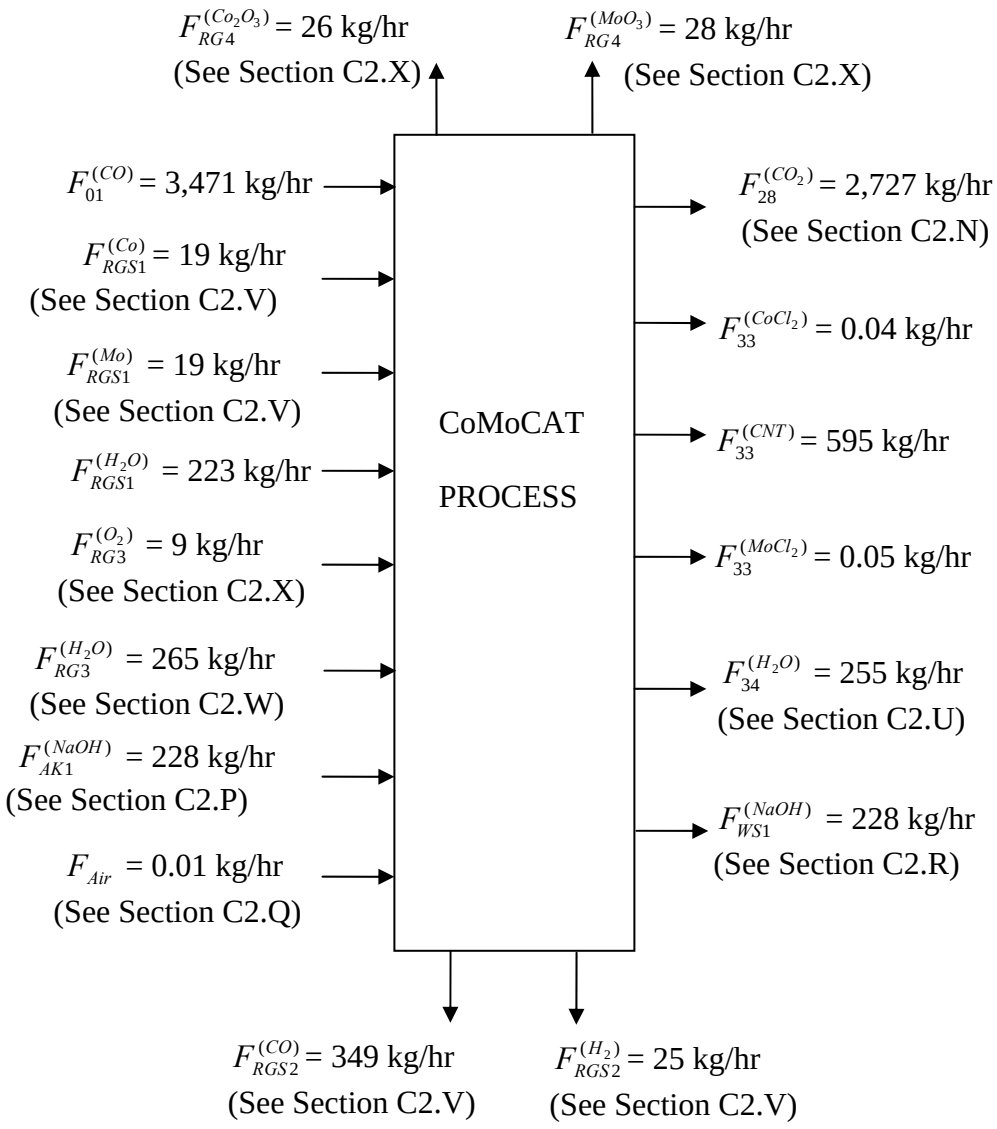

Figure C2.1. Input – Output Component Structure for Overall CoMoCAT Process

Make–Up CO Feed Supplied to CoMoCAT Process, $F_{01}^{(CO)}$:

The CO reactant consumed in the CoMoCAT process is estimated based on the amount of carbon nanotube product formed per reaction cycle using the carbon monoxide

selectivity to form carbon nanotube. The stoichiometrically balanced form of the carbon nanotube reaction is represented by Equation (C2.1):

$$6000CO_{(g)} \xrightarrow{SiO_2/Co/Mo} C_{3000} + 3000CO_{2(g)} \qquad \text{(C2.1)}$$

Moles of CO Converted = Moles of CNT Formed / Selectivity

Selectivity = 80%, i.e., 0.8 kgmol CO reacted to form CNT/kgmol CO Converted

Using the stoichiometric ratios of reactants and products in Equation (C2.1), and based on the production rate of carbon nanotubes by the CoMoCAT process:

$$F_{01}^{(CO)} = \frac{595kgCNT}{hr} * \frac{6{,}000kgmolCO}{1kgmolCNT} * \frac{1kgmolCO}{0.8kgmol} * \frac{1kgmolCNT}{36{,}000kgCNT} * \frac{28kgCO}{1kgmolCO}$$

CO Consumed in Process, $F_{01}^{(CO)}$ = **3, 471 kg CO/hr**

C2.A. <u>Reactor (V–201)</u>: (Refer to Table B2.2)

The input–output structure of the CoMoCAT fluidized bed reactor (V–201) is shown in Figure C2.2. There are two input streams: the CO feed stream (SR02) at 1,223 K and the silica supported bimetallic catalyst (SR11) at 1,223 K. The CO feed stream, $F_{02}^{(CO)}$ consists of the make–up CO and the CO feed recycle streams. The catalyst stream consists of three components: silica, $F_{11}^{(SiO_2)}$, cobalt, $F_{11}^{(Co)}$ and molybdenum, $F_{11}^{(Mo)}$.

The output stream (SR03) consists of seven components: carbon nanotube product, $F_{03}^{(CNT)}$, amorphous carbon, $F_{03}^{(C)}$, silica, $F_{03}^{(SiO_2)}$, cobalt, $F_{03}^{(Co)}$, molybdenum $F_{03}^{(Mo)}$, unconverted carbon monoxide, $F_{03}^{(CO)}$, and carbon dioxide, $F_{03}^{(CO_2)}$. Heat is added to the reactor, Q_{V-201} to maintain the reaction temperature at 1,223 K, while the operating pressure is 150 psia (Resasco, et al, 2001).

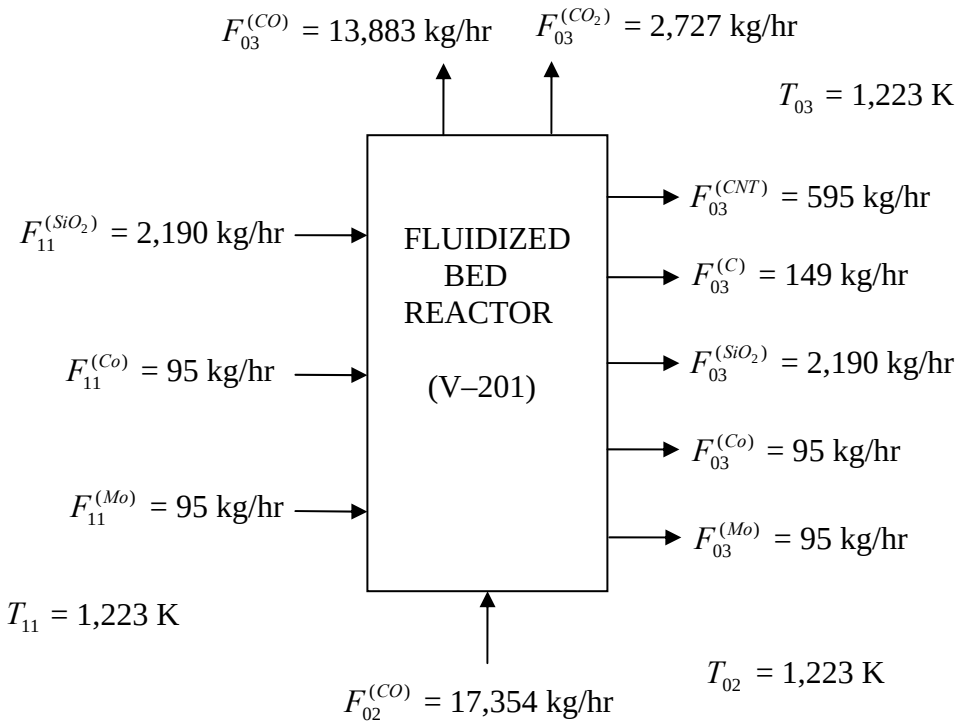

Figure C2.2. Input – Output Component Structure for Fluidized Bed Reactor (V–201)

The solution to the material and energy balance equations for the fluidized bed reactor (V–201), given in Table B2.2, and included in the input–output structure of the CoMoCAT fluidized bed reactor in Figure C2.2, is given below:

Carbon Nanotube Reaction:

$$6000CO_{(g)} \xrightarrow{SiO_2 / Co / Mo} C_{3000} + 3000CO_{2(g)} \qquad \text{(C2.1)}$$

Conversion (*conv2*) = 20 mol%; 0.20 kgmol CO converted to CNT/kgmol CO Fed

Selectivity (*selc2*) = 80%; 0.80 kgmol CO form CNT/kgmol CO Converted

Amorphous Carbon Reaction

$$2CO_{(g)} \rightarrow C + CO_{2(g)} \qquad \text{(C2.2)}$$

Selectivity = 20%, i.e., 0.20 kgmol CO reacted to form carbon per kgmol of CO reacted

Total CO Feed Supplied to Reactor, $F_{02}^{(CO)}$:

The total CO feed fed to the fluidized bed reactor is estimated based on the amount of CO converted to carbon nanotube. The total CO supplied to the reactor consists of the make–up CO feed, $F_{01}^{(CO)}$ and the CO feed recycle $F_{17}^{(CO)}$.

Total Moles of CO Fed = Moles of CO Consumed / Conversion

$$F_{02}^{(CO)} = \frac{3{,}471 kgCO}{hr} * \frac{1 kgmolCO}{28 kgCO} * \frac{1 kgmolCO}{0.20 kgmolCO} * \frac{28 kgCO}{1 kgmolCO}$$

CO Supplied to Reactor, $F_{02}^{(CO)}$ = **17,354 kg CO/hr**

Catalyst Loading Rate to Reactor, $F_{11}^{(Cat.)}$

Resasco, et al, 2002, reported the rate of production of carbon nanotubes per weight of silica–supported Co–Mo bimetallic catalyst to be 0.25 kg carbon nanotube per kg catalyst. Using this basis, the flow rate of the solid catalysts (SR11) into the fluidized bed reactor can be estimated as follows:

$$\text{Catalyst loading rate, } F_{11}^{(Cat.)} = \frac{595 kgCNT / hr}{0.25 kgCNT / kgCat} = \textbf{2,380 kg } \textbf{\textit{Cat}}\textbf{/hr}$$

The catalyst particles contain silica, cobalt and molybdenum. The ratio of cobalt and molybdenum metals in the supported bimetallic catalyst is 1:1 (Resasco, et al, 2001).

Unconverted CO from Reactor, $F_{03}^{(CO)}$:

$$F_{03}^{(CO)} = (1 - conv2) * F_{02}^{(CO)}$$

$$F_{03}^{(CO)} = (1 - \frac{0.20 kgmolCO}{1 kgmolCO}) * 17{,}354 \frac{kgCO}{hr}$$

$$F_{03}^{(CO)} = \textbf{13,883 kg CO/hr}$$

Carbon Nanotube Produced in the Reactor, $F_{03}^{(CNT)}$

The amount of carbon nanotube produced in the reactor is estimated based on the stoichiometric ratios of reactants to products in Equation C2.1:

$$6000CO_{(g)} \xrightarrow{SiO_2/Co/Mo} C_{3000} + 3000CO_{2(g)}$$

$$F_{03}^{(CNT)} = \frac{1kgmolCNT}{6{,}000kgmolCO} * \frac{0.2kgmolCO}{1kgmolCO} * \frac{0.8kgmolCO}{kgmolCO} * \frac{36{,}000\frac{kgCNT}{kgmolCNT}}{28\frac{kgCO}{kgmolCO}} * 17{,}354\frac{kgCO}{hr}$$

$F_{03}^{(CNT)}$ = **595 kg CNT/hr**

Amorphous Carbon from Reactor, $F_{03}^{(C)}$

The amount of amorphous carbon formed is based on the carbon nanotube produced. The stoichiometric ratios of reactant and products are given by Equation C2.2:

$$2CO_{(g)} \longrightarrow C + CO_{2(g)} \qquad \text{(C2.2)}$$

Selectivity = 20%, i.e., 0.2kgmol CO forms amorphous carbon per kgmol CO converted

$$F_{03}^{(C)} = \frac{1kgmolC}{2kgmolCO} * \frac{0.20kgmolCO}{1kgmolCO} * \frac{0.2kgmolCO}{1kgmolCO} * \frac{12\frac{kgC}{kgmolC}}{28\frac{kgCO}{kgmolCO}} * 17{,}354\frac{kgCO}{hr}$$

$F_{03}^{(C)}$ =**149 kg C/hr**

Carbon dioxide Produced in Reactor, $F_{03}^{(CO_2)}$

Carbon dioxide is produced from the carbon nanotube reaction (Equation C2.1) and the amorphous carbon reaction (Equation C2.2). The total mass flow rate of carbon dioxide leaving the reactor is the sum of carbon dioxide

produced from both reactions:

CO_2 from Carbon Nanotube Reaction (Equation C2.1):

$$= 595\frac{kgCNT}{hr} * \frac{1kgmolCNT}{36{,}000kgCNT} * \frac{3{,}000kgmolCO_2}{1kgmolCNT} * \frac{44kgCO_2}{1kgmolCO_2} = \textbf{2,182 kg } \mathbf{CO_2}\textbf{/hr}$$

CO_2 from Amorphous Carbon Reaction (Equation C2.2):

$$= 149\frac{kgC}{hr} * \frac{1kgmolC}{12kgC} * \frac{1kgmolCO_2}{1kgmolC} * \frac{44kgCO_2}{1kgmolCO_2} = \textbf{545 kg } \mathbf{CO_2}\textbf{/hr}$$

Carbon dioxide Produced in Fluidized Bed Reactor, $F_{03}^{(CO_2)}$

$$F_{03}^{(CO_2)} = (2{,}182 + 545) \text{ kg/hr}$$

$$F_{03}^{(CO_2)} = \textbf{2,727 kg } \mathbf{CO_2}\textbf{/hr}$$

The carbon dioxide produced in both the carbon nanotube and amorphous carbon reactions is based on the production rate of carbon nanotube in the fluidized bed reactor.

Catalyst Flow Rate from Reactor, $F_{03}^{(Cat)}$

$$F_{03}^{(Cat.)} = F_{11}^{(Cat.)} = \textbf{2,380 kg/hr}$$

The solid product from the fluidized bed reactor contains carbon nanotubes and amorphous carbon (24 wt.%), silica (70 wt.%), and cobalt (3 wt.%) and molybdenum (3 wt.%) (Pisan, et al., 2004). Consequently, the composition of the supported catalyst can be determined based on the total weight of solid particles leaving the fluidized bed reactor.

Total Solid from Reactor: $F_{03}^{(CNT)} + F_{03}^{(C)} + F_{03}^{(Cat)} = \textbf{3,124 kg solids/hr}$

Silica in Supported Catalyst, $F_{03}^{(SiO_2)}$

$$F_{03}^{(SiO_2)} = \frac{0.70kgSiO_2}{1kgsolid} * 3{,}124\frac{kgsolid}{hr} = \textbf{2,190 kg } \mathbf{SiO_2}\textbf{/hr}$$

$$F_{03}^{(SiO_2)} = F_{11}^{(SiO_2)} = \textbf{2,190 kg } \mathbf{SiO_2}\textbf{/hr}$$

Cobalt in Supported Catalyst, $F_{03}^{(Co)}$

$$F_{03}^{(Co)} = \frac{0.03 kgCo}{1 kgsolid} * 3{,}124 \frac{kgsolid}{hr} = \textbf{95 kg Co/hr}$$

$$F_{03}^{(Co)} = F_{11}^{(Co)} = \textbf{95 kg Co/hr}$$

Molybdenum in Supported Catalysts, $F_{03}^{(Mo)}$

$$F_{03}^{(Mo)} = \frac{0.03 kgMo}{1 kgsolid} * 3{,}124 \frac{kgsolid}{hr} = \textbf{95 kg Mo/hr}$$

$$F_{03}^{(Mo)} = F_{11}^{(Mo)} = \textbf{95 kg Mo/hr}$$

Reactor Heat Effects, Q_{V-201}

The heat added to the reactor, Q_{V-201} is estimated from the reactor energy balance:

$$Q_{V-201} = \sum_i F_{inlet}^{(i)} H_{inlet}^{(i)} - \sum_i F_{outlet}^{(i)} H_{outlet}^{(i)} \qquad \text{(C2.3)}$$

The enthalpy data for the component streams into and out of the CoMoCAT fluidized bed reactor (V–201) is given in Table C2.1. The heats of reaction terms are not included in Equation (C2.3) since the elements are chosen at their reference states: 298 K and 1 bar. The heats of reaction are implicitly included when the heats of formation of the reactants are subtracted from those of the products (Felder, et al, 2000). The enthalpy for the catalyst particles is estimated as the enthalpy of the silica supports.

Equation (C2.3) gives the energy added to fluidized bed reactor, Q_{V-201}

$$Q_{V-201} = (-85{,}114{,}550 \text{ kJ/hr}) - (-88{,}716{,}992 \text{ kJ/hr})$$

$$Q_{V-201} = \textbf{3,602,442 kJ/hr}$$

Table C2.1. Enthalpy Data for CoMoCAT Fluidized Bed Reactor (V–201)

	SR02		SR11		SR03	
Species	*F* (kg/hr)	*H*(1,223K) kJ/kg	*F* (kg/hr)	*H* (1,223 K) (kJ/kg)	*F* (kg/hr)	*H* (1,223 K) (kJ/kg)
CO	17,354	– 5,278	–	–	13,883	– 5,278
SiO_2	–	–	2,380	1,209	2,380	1,209
CNT	–	–	–	–	595	14.9
CO_2	–	–	–	–	2,727	– 5,482
C	–	–	–	–	149	1,497

HP Steam Required to Supply Heat to Reactor:

$$F_{HPSteam(V-201)} = \frac{Q_{V-201}}{\Delta H_{vap}} = \frac{3{,}602{,}442 kJ/hr}{1661.5 kJ/kg} = \textbf{2,168 kg HP Steam/hr}$$

Fluidized Bed Reactor Size, V_{V-201}:

The size of the fluidized bed reactor (V–201) is estimated based on the solid residence time given by Equation (C2.4), (Ulrich, 1984):

$$\theta = \frac{V_{V-201} * f_s * \rho_{cat}}{F_{11}^{(Cat)}} \qquad \text{(C2.4)}$$

θ = Residence time = 2 hr (Resasco, et. al., 2002)

f_s = Fraction of Reactor Occupied by Solids = 70% (Ulrich, 1984)

ρ_{cat} = Catalyst Density = 2,320 kg/m^3 (Perry, 1984)

$F_{11}^{(Cat)}$ = Catalyst Flow Rate = 2,380 kg/hr

Reactor Volume, $V_{V-201} = \frac{2{,}380 kg/hr * 2hr}{2{,}320 kg/m^3 * 0.70}$ = **2.9 m^3**

Bed Diameter, D_{V-201}

The ratio of the bed height to diameter in a well mixed fluidized bed reactor is typically on the order of 0.5 to 2 (Ulrich, 1984). In this design, the upper limit of the bed height to diameter ratio of 2 is used in estimating the fluidized bed dimensions:

Bed Height, $H_{V-201} = 2\,D_{V-201}$ (Ulrich, 1984)

$$V_{V-201} = \pi * \frac{D_{V-201}^2}{4} * H_{V-201}$$

$$V_{V-201} = \pi * \frac{D^2}{4} * 2D = 2.93 m^3$$

Bed Diameter, D_{V-201} = **1.2 m**

Bed Height, H_{V-201} = **2.5 m**

C2.B. <u>CO Feed Gas–Fired Heater (E–201):</u> (Refer to Table B2.1)

The input–output component structure for the CO feed gas–fired heater is shown in Figure C2.3. There are two input streams: the make–up CO stream (SR01) at 303 K and the CO feed recycle (SR17) at 402 K. The output stream (SR02) supplies CO to the fluidized bed reactor at 1,223 K.

Make–up CO, $F_{01}^{(CO)}$: $F_{01}^{(CO)}$ = **3,471 kg CO/hr**

CO Feed Recycle, $F_{17}^{(CO)}$: $F_{17}^{(CO)} = F_{03}^{(CO)}$ = **13,883 kg/hr**

Total CO feed to Reactor, $F_{02}^{(CO)}$

$$F_{02}^{(CO)} = F_{01}^{(CO)} + F_{17}^{(CO)}$$

$F_{02}^{(CO)}$ = **17,354 kg/hr**

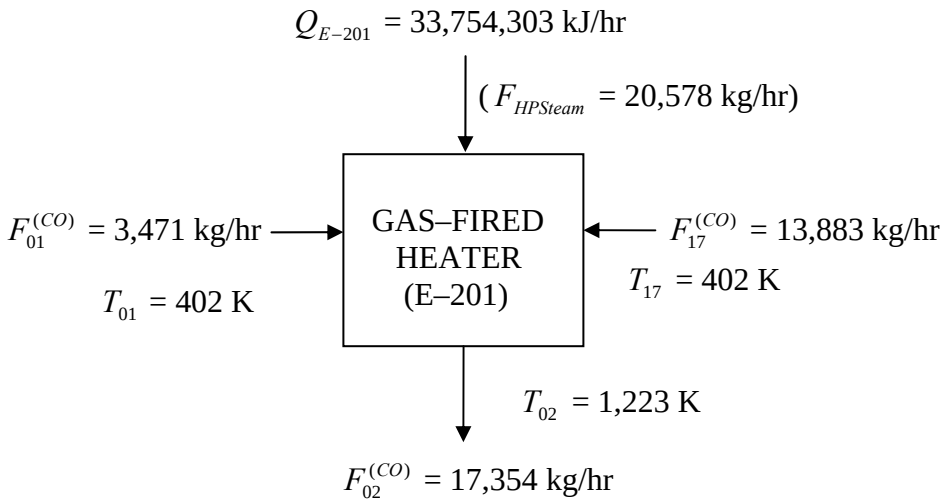

Figure C2.3. Input – Output Component Structure for CO Feed Heater (E–201)

Temperature of CO Feed Recycle (SR17), T_{17}: (Refer to Table B2.18)

$$T_{17} = T_{16}\left(\frac{P_{17}}{P_{16}}\right)^{\frac{(k-1)}{k}} \qquad \text{(C2.5)}$$

T_{16} = 330 K; P_{17} = 150 psi; P_{16} = 75 psi; k =1.4

Equation (C2.5) gives: T_{17} = **402 K**

Energy Supplied to Heater (E–201), Q_{E-201}:

$$Q_{E-201} = (F_{01}H_{01} + F_{17}H_{17}) - F_{02}H_{02} \qquad \text{(C2.6)}$$

The enthalpy data for the component streams in and out of the gas–fired heater (E–201) is given in Table C2.2

Table C2.2. Enthalpy Table for CO Feed Gas–Fired Heater (E–201)

Component	Inlet Stream				Outlet Stream	
	F_{01} kg/hr	$H_{01}(402K)$ kJ/kg	F_{17} kg/hr	$H_{17}(402K)$ kJ/kg	F_{02} kg/hr	$H_{02}(1223K)$ kJ/kg
CO	3,470	– 3,308	13,883	– 3,308	17,354	– 5,278

Equation (C2.6) gives:

Energy Supplied to E–201, Q_{E-201} = **34,190,688 kJ/hr**

The enthalpy of combustion, $\Delta H_{comb.}$ of natural gas is 55,501.2 kJ/kg (Perry, et al., 1984). The amount of natural gas required to supply the thermal energy is calculated from Equation (C2.7):

$$\text{Natural Gas required, } F_{CH_4} = \frac{Q_{E-201}(kJ/hr)}{\Delta H_{comb.}(kJ/kg)} \qquad \text{(C2.7)}$$

$$F_{CH_4} = \textbf{616 kg/hr}$$

Heat Transfer Area for Gas–Fired Heater (E–201), A_{E-201}

$$A_{E-201} = \frac{Q_{E-201}}{U_{E-201} * \Delta T} \qquad \text{(C2.8)}$$

U_{E-201} = 204 kJ/m^2 hr K (Douglas, 1988)

$$A_{E-201} = \frac{34{,}190{,}688 kJ/hr}{204 kJ/m^2 hrK * 821K}$$

A_{E-201} = **205 m^2**

C2.C. <u>Cyclone Separator (Z–201):</u> (Refer to Table B2.3)

The input–output component structure for the cyclone separator (Z–201) is shown in Figure C2.4. The output stream (SR03) from the fluidized bed reactor acts as the input stream to the cyclone separator. The cyclone separates the solid reaction product from the mixed gas stream. However, since the efficiency of the cyclone separator is less than 100%, some solid particles are carried over in the mixed gas stream (SR04) leaving the cyclone:

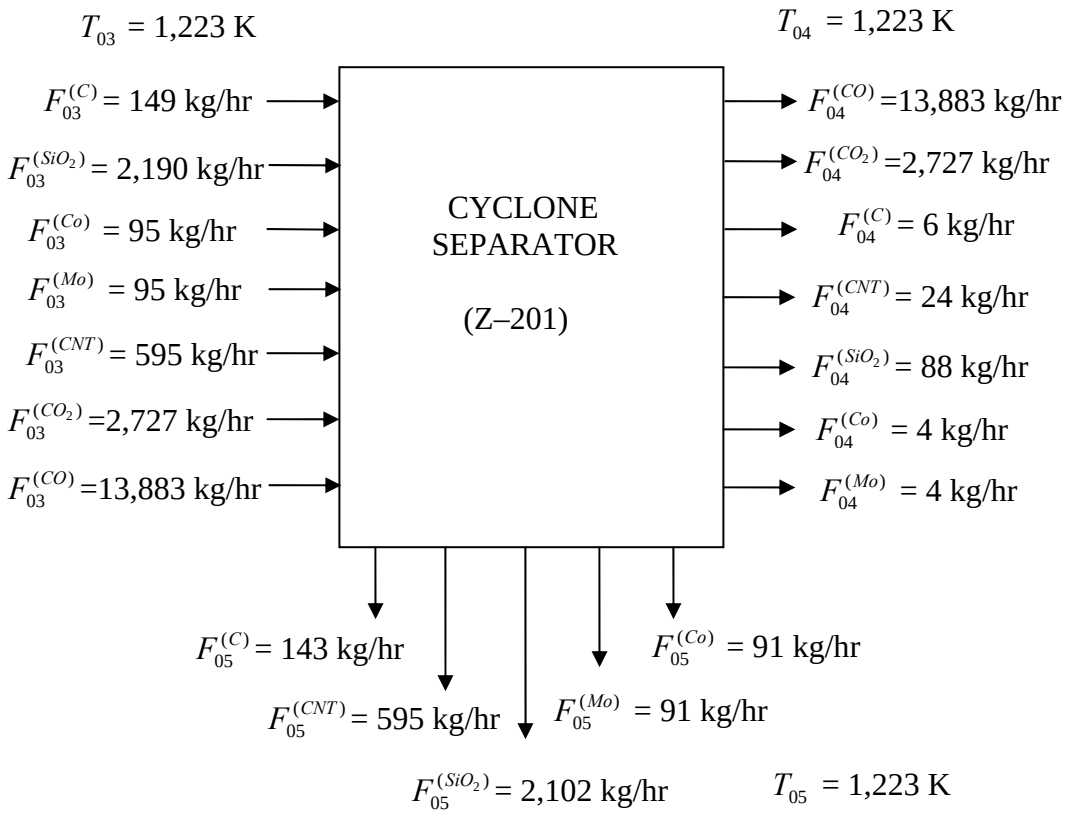

Figure C2.4. Input – Output Component Structure for Cyclone Separator (Z–201)

Cyclone Collection Efficiency, η_{Z-201} = 96 % (Wark, et al, 1998)

CO: $F_{04}^{(CO)} = F_{03}^{(CO)} =$ **13,883 kg CO/hr**

CO_2: $F_{04}^{(CO_2)} = F_{03}^{(CO_2)} =$ **2,727 kg CO_2/hr**

CNT: $F_{03}^{(CNT)} =$ **595 kg CNT/hr**

$F_{05}^{(CNT)} = \eta_{Z-201} * F_{03}^{(CNT)} =$ **571 kg CNT/hr**

$F_{04}^{(CNT)} = (1-\eta_{Z-201}) * F_{03}^{(CNT)} =$ **24 kg CNT/hr**

C: $F_{03}^{(C)} =$ **149 kg/hr**

$F_{05}^{(C)} = \eta_{Z-201} * F_{03}^{(C)} =$ **143 kg/hr**

$$F_{04}^{(C)} = (1-\eta_{Z-201}) * F_{03}^{(C)} = \textbf{6 kg/hr}$$

Silica: $F_{03}^{(SiO_2)} = \textbf{2,190 kg/hr}$

$$F_{05}^{(SiO_2)} = \eta_{Z-201} * F_{03}^{(SiO_2)} = \textbf{2,102 kg/hr}$$

$$F_{04}^{(SiO_2)} = (1-\eta_{Z-201}) * F_{03}^{(SiO_2)} = \textbf{88 kg/hr}$$

Cobalt: $F_{03}^{(Co)} = \textbf{95 kg/hr}$

$$F_{05}^{(Co)} = \eta_{Z-201} * F_{03}^{(Co)} = \textbf{91 kg/hr}$$

$$F_{04}^{(Co)} = (1-\eta_{Z-201}) * F_{03}^{(Co)} = \textbf{4 kg/hr}$$

Molybdenum: $F_{03}^{(Mo)} = 95$ kg/hr

$$F_{05}^{(Mo)} = \eta_{Z-201} * F_{03}^{(Mo)} = \textbf{91 kg/hr;}$$

$$F_{04}^{(Mo)} = (1-\eta_{Z-201}) * F_{03}^{(Mo)} = \textbf{4 kg/hr}$$

C2.D. <u>Gas–Solid Filter (Z–202):</u> (Refer to Table B2.7)

The input–output component structure for the gas–solid filter (Z–202) is shown in Figure C2.5:

CO: $F_{13}^{(CO)} = F_{04}^{(CO)} = \textbf{13,883 kg/hr}$

CO_2: $F_{13}^{(CO_2)} = F_{04}^{(CO_2)} = \textbf{2,727 kg/hr}$

CNT: $F_{12}^{(CNT)} = F_{04}^{(CNT)} = \textbf{24 kg/hr}$

C: $F_{12}^{(C)} = F_{04}^{(C)} = \textbf{6 kg/hr}$

SiO_2: $F_{12}^{(SiO_2)} = F_{04}^{(SiO_2)} = \textbf{88 kg/hr}$

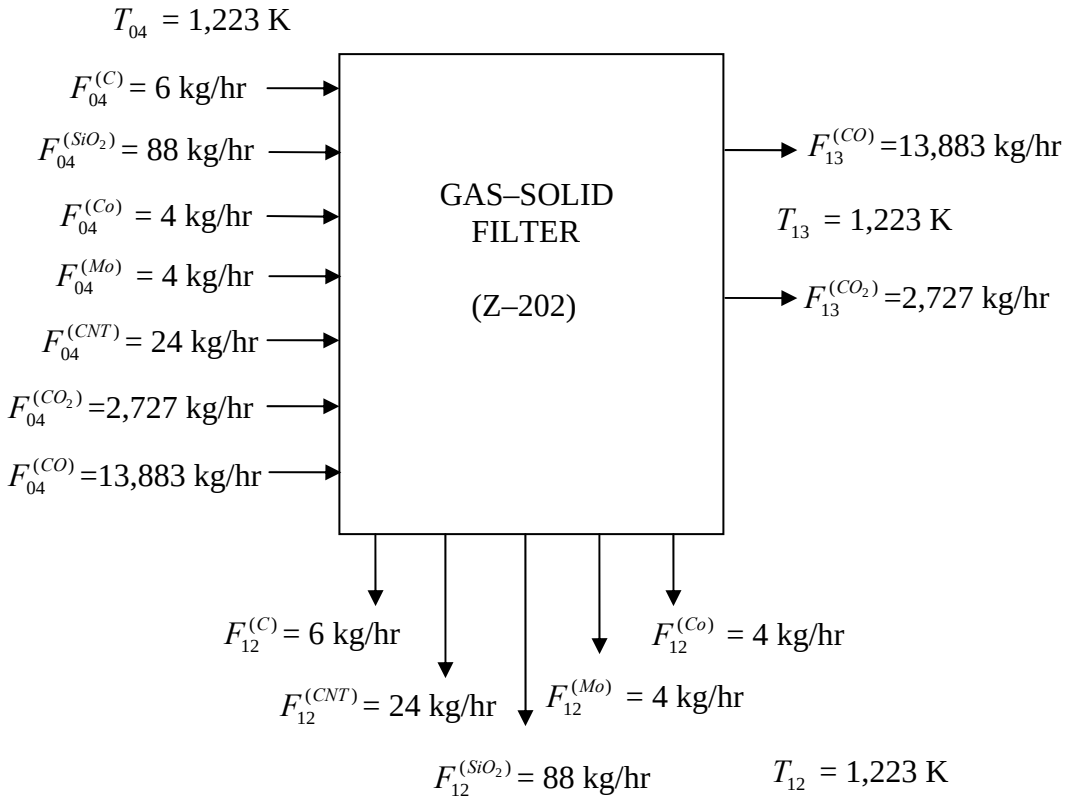

Figure C2.5. Input – Output Component Structure for Gas–Solid Filter (Z–202)

Co: $F_{12}^{(Co)} = F_{04}^{(Co)}$ = **4 kg Co/hr**

Mo: $F_{12}^{(Mo)} = F_{04}^{(Mo)}$ = **4 kg Mo/hr**

Gas–Solid Filter Size, A_{Z-202}, (Ulrich,1984):

$$q_{gas} = 0.1 * A_{Z-202}$$

Total Gas Flow Rate, $F_{13} = F_{13}^{(CO)} + F_{13}^{(CO_2)}$ = 16,610 kg/hr

The average gas density, ρ_g is calculated from the ideal gas law requirement:

Gas density at standard conditions (298 K, 15 psia): $\rho_g^{std} = MW^{(g)} * \frac{1 kgmol}{22.4 m^3}$

ρ_{CO}^{std} = 1.25 kg/m^3; $\rho_{CO_2}^{std}$ = 1.96 kg/m^3

Gas density at temperature, T_o (K) and pressure, P_o (psi), ρ_g^o:

$$\rho_g^o = \frac{298(K)}{T_o(K)} * \frac{P_o(psia)}{15(psia)} * \rho_g^{(std)}(kg/m^3)$$

At T_o = 1,223 K and P_o = 150 psia:

$$\rho_{CO}^o = 3.01 kg/m^3; \quad \rho_{CO_2}^o = 4.78 kg/m^3$$

Average gas density of the mixed gas stream (SR13):

$$\rho_{avg}^o = \frac{13{,}883 kg/hr}{16{,}610 kg/hr} * 3.01 \frac{kg}{m^3} + \frac{2{,}727 kg/hr}{16{,}610 kg/hr} * 4.78 \frac{kg}{m^3}$$

$$\rho_{avg}^o = 3.3 kg/m^3$$

Volumetric Flow rate, q_g

$$q_g(m^3/s) = \frac{16{,}610 kg/hr}{3.3 kg/m^3} * \frac{1 hr}{3600 s} = 1.4 \text{ m}^3/\text{s}$$

Filter Size, A_{Z-202}

$$A_{Z-202} = \frac{q_g(m^3/s)}{0.1} = \frac{1.4}{0.1} = \mathbf{14\ m^2}$$

C2.E. <u>Waste Heat Boiler (E–202):</u> (Refer to Table B2.4)

The input–output component structure for the waste heat boiler (E–202) is shown in Figure 2.6. There are two input streams (SR13 and BFW), and two output streams (SR14 and SST). The inlet component mass flow rates are equal to the outlet component mass flow rates streams on either sides.

CO: $F_{14}^{(CO)} = F_{13}^{(CO)} =$ **13,883 kg/hr**

CO_2: $F_{14}^{(CO_2)} = F_{13}^{(CO_2)} =$ **2,727 kg/hr**

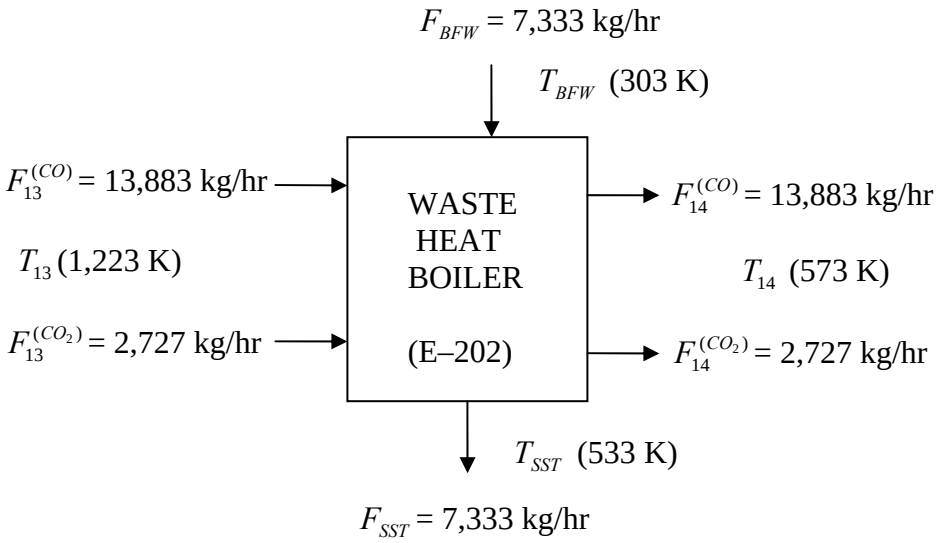

Figure C2.6. Input – Output Component Structure of Waste Heat Boiler (E–202)

Energy Liberated in Waste Heat Boiler (E–202), Q_{E-202}:

$$Q_{E-202} = \sum_i F_{14}^{(i)} H_{14}^{(i)} - \sum_i F_{13}^{(i)} H_{13}^{(i)} \qquad \text{(C2.9)}$$

The enthalpy data for the mixed CO and CO_2 stream into and out of the waste heat boiler (E–202) is given in Table C2.3:

Table C2.3. Enthalpy Data for Waste Heat Boiler (E–202)

Component	F_{13} kg/hr	$H_{13}(1223K)$ kJ/kg	F_{14} kg/hr	$H_{14}(573K)$ kJ/kg
CO	13,883	– 5,278	13,883	– 3,099
CO_2	2,727	– 5,482	2,727	– 7,910

Equation (C2.9) gives the heat liberated in E–202, Q_{E-202}

Q_{E-202} = (– 88,223,888 kJ/hr) – (– 64,593,987) kJ/hr = – **23,629,901 kJ/hr**

Boiler Feed Water Supplied to E–202, F_{BFW}

$$F_{BFW} = \frac{Q_{E-202}}{(C_p^{(H_2O)} * \Delta T + \lambda_s)} \qquad \text{(C2.10)}$$

T_{BFW} = 303 K, T_{SST} = 533 K, ΔT = 230 K

$$F_{BFW} = \frac{23{,}629{,}901 kJ/hr}{(4.184 kJ/kgK * 230K + 2{,}260 kJ/kg)} = \textbf{7,333 kg/hr}$$

Area of Waste Heat Boiler (E–202) , A_{E-202} :

$$A_{E-202} = \frac{Q_{E-202}}{U_{E-202} * \Delta T_{lm}} \qquad \text{(C2.11)}$$

$T_{SR\,13}$ = 1,223 K, $T_{SR\,14}$ = 573 K,

$$\Delta T_{lm} = \frac{(T_{13} - T_{BFW}) - (T_{14} - T_{SST})}{\ln\left((T_{13} - T_{BFW}) / (T_{14} - T_{SST})\right)} = 448 \text{ K}$$

U_{E-202} = 468 $kJ/m^2\ hr\ K$ (Peters, et al., 2002)

Equation (C2.11) gives:

A_{E-202} = **113 m^2**

C2.F. <u>Heat Exchanger Water Cooler (E–203):</u> (Refer to Table B2.5)

CO: $F_{15}^{(CO)} = F_{14}^{(CO)}$ = **13,883 kg CO/hr**

CO_2: $F_{15}^{(CO_2)} = F_{14}^{(CO_2)}$ = **2,727 kg CO_2/hr**

The input–output component structure of the heat exchanger water cooler (E–203) is shown in Figure C2.7:

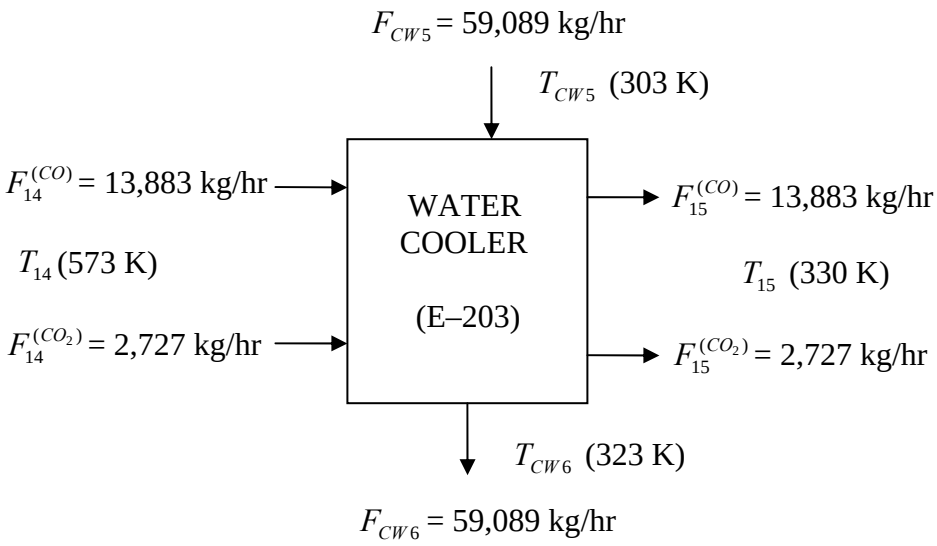

Figure C2.7. Input – Output Component Structure for Water Cooler (E–203)

Energy Liberated in Water Cooler, Q_{E-203}:

$$Q_{E-203} = \sum_i F_{14}^{(i)} H_{14}^{(i)} - \sum_i F_{15}^{(i)} H_{15}^{(i)} \qquad \text{(C2.12)}$$

The enthalpy data for components into and out of the heat exchanger water cooler (E–203) is given in Table C2.4:

Table C2.4. Enthalpy Data for Heat Exchanger Product Cooler (E–203)

Component	F_{14} kgmol/hr	$H_{14}(573K)$ kJ/kgmol	F_{15} kgmol/hr	$H_{15}(330K)$ kJ/kgmol
CO	13,883	– 3,099	13,883	– 3,398
CO_2	2,727	– 7,910	2,727	– 8,201

Equation (C2.12) gives:

$$Q_{E-203} = (-\ 69{,}538{,}561 \text{ kJ/hr}) - (-\ 64{,}593{,}987 \text{ kJ/hr})$$

Energy Liberated in Cooler, Q_{E-203} = **– 4,944,574 kJ/hr**

Cooling Water Supplied to Cooler (E–203), F_{CW} :

$$F_{CW} = \frac{Q_{E-203}}{C_p^{(H_2O)} * \Delta T} \qquad \text{(C2.13)}$$

T_{CW3} = 303 K; T_{CW4} = 323 K; ΔT = 20 K

$$F_{CW} = \frac{4{,}944{,}577 kJ/hr}{4.184 kJ/kgK * 20K}$$

$F_{CW5} = F_{CW6}$ = **59,089 kg/hr**

Area of Water Cooler 1 (E–203) A_{E-203} :

$$A_{E-203} = \frac{Q_{E-203}}{U_{E-203} * \Delta T_{lm}} \qquad \text{(C2.14)}$$

U_{E-203} = 468 $kJ/m^2\ hr\ K$ (Peters, et al., 2002)

$$\Delta T_{lm} = \frac{(T_{14} - T_{CW4}) - (T_{15} - T_{CW3})}{\ln\left((T_{14} - T_{CW4}) / (T_{15} - T_{CW3})\right)} = 100 \text{ K}$$

Equation (C2.14) gives:

A_{E-203} = **106 m^2**

C2.G. <u>Gas Compressor (C–201):</u> (Refer to Table B2.18)

The input–output component structure for the gas compressor (C–201) is shown in Figure C2.8. The gas compressor increases adiabatically the pressure of the CO feed recycle stream from 75 psia (SR16) to 150 psia (SR17). Consequently, the temperature of the CO recycle stream also increases from 330 K to 402 K.

CO: $F_{17}^{(CO)} = F_{16}^{(CO)} = F_{15}^{(CO)}$ = **13,883 kg/hr**

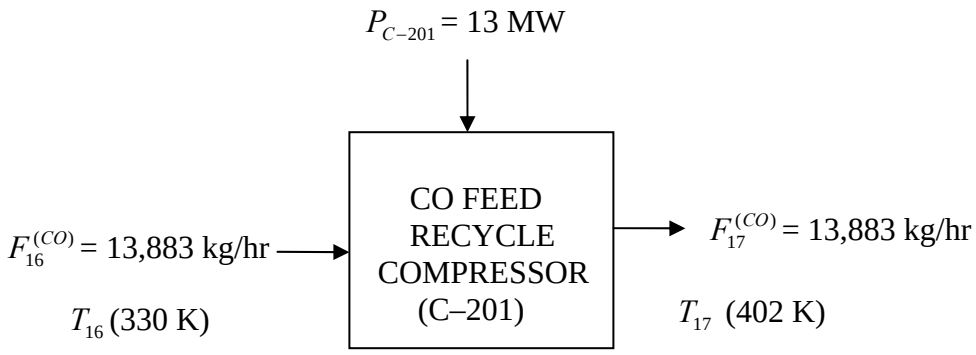

Figure C2.8. Input–Output Component Structure for CO Recycle Gas Compressor (C–201)

Compressor Power, P_{C-201}

$$P_{C-201}(kW) = \frac{Flowrate(kg/s) * 9.806 N/kg * Head_{adiabatic}(m)}{1000}$$

Adiabatic Head, H (m), (Perry, et al, 1984):

$$H = \frac{k}{k-1} * \frac{RT_{suction}}{9.806} * \left[\left(\frac{P_{discharge}}{P_{suction}} \right)^{(k-1)/k} - 1 \right]$$

$$\text{R = Gas constant} = \frac{8314}{MW^{(CO)}} = 296.93 J/kg.K ;$$

$T_{suction}$ = 330 K: $P_{suction}$ = 75 *psia*; $P_{discharge}$ = 150 *psia,*

$$k = \frac{C_p}{C_v} = 1.4 \qquad \text{(Perry, et al. 1984)}$$

Adiabatic Head, $H = \frac{1.4}{(1.4-1)} * \frac{296.93 J/kg.K * 330 K}{9.806 N/kg} * \left[\left(\frac{150 psia}{75 psia} \right)^{0.286} - 1 \right]$

H = 7,668.21 *m*

Gas Flow Rate, $F_{16}^{(CO)}$ = 3.86 *kg/s* (13,883 kg/hr);

Compressor Efficiency = 0.75 (Peters, et al., 2003)

Compressor Power, $P_{C-201}(kW)$ at 75% efficiency:

$$P_{C-201}(kW) = \frac{Flowrate(kg/s) * 9.806 N/kg * Head_{adiabatic}(m)}{Efficiency * 1000} \qquad \text{(C1.25)}$$

$$P_{C-201}(kW) = \frac{3.86 kg/s * 9.806 N/kg * 7{,}668.21(m)}{0.75 * 1000} = 386.6\ kW$$

$$P_{C-201} = \mathbf{387\ kW}$$

C2.H. <u>Gas Absorption Column (T–201):</u> (Refer to Table B2.14)

Temperature, T = 330 K; Pressure, P_T = 75 psia

CO: $F_{16}^{(CO)} = F_{15}^{(CO)} =$ **13,883 kg/hr**

CO_2: $F_{18}^{(CO_2)} = F_{15}^{(CO_2)} =$ **2,727 kg/hr**

Liquid Absorbent (MEA Solution) Feed Rate, F_{23}:

The liquid absorbent feed rate, L is estimated based on the rule of thumb for the design of isothermal absorption column, given by Equation (C2.15), (Douglas, 1988):

$$L = 1.4\ mG \qquad \text{(C2.15)}$$

L = Liquid Absorbent Flow Rate = F_{22}

G = Gas Flow Rate = $F_{15}^{(CO)} + F_{15}^{(CO_2)}$ = **16,610 kg/hr**

m = Slope of equilibrium line = $\frac{P^o}{P_T}$ = 2.98 (Ideal solution)

P^o = Vapor Pressure of CO_2 at 330 K = 223.50 psia (Perry, et al, 1984)

Equation (C2.15) gives:

L = 1.4*2.98*16,610 kg/hr = 69,297 *kg/hr*

Liquid Absorbent Feed Rate to Absorption Column, F_{22}

$$F_{22} = \mathbf{69{,}297\ kg/hr}$$

The aqueous fraction of the liquid absorbent feed into the absorption column constitutes 80 wt.% of the solution (Yeh, et al., 2001). Consequently, the MEA fraction of the liquid absorbent is 20 wt.%.

$$F_{22}^{(MEA)} = 0.20 \text{ x } 69{,}297 \text{ kg/hr}$$

$$F_{22}^{(MEA)} = \mathbf{13{,}859\ kg\ MEA/hr}$$

$$F_{23}^{(H_2O)} = 0.80 \text{ x } 69{,}297 \text{ kg/hr}$$

$$F_{23}^{(H_2O)} = \mathbf{55{,}438\ kg\ H_2O/hr}$$

Solute Rich Liquid Leaving Gas Absorber (T–201), F_{18}

$$F_{18}^{(CO_2)} = F_{15}^{(CO_2)} \qquad \text{(Perfect Separation)}$$

$$F_{18}^{(CO_2)} = \mathbf{2{,}727\ kg/hr}$$

$$F_{18}^{(MEA)} = F_{22}^{(MEA)} = \mathbf{13{,}859\ kg/hr}$$

$$F_{18}^{(H_2O)} = F_{22}^{(H_2O)} = \mathbf{55{,}438\ kg/hr}$$

$$F_{18} = F_{18}^{(MEA)} + F_{18}^{(CO_2)} + F_{18}^{(H_2O)}$$

$$F_{18} = (13{,}859 + 2{,}727 + 55{,}438) \text{ kg/hr}$$

$$F_{18} = \mathbf{72{,}024\ kg/hr}$$

The input–output component structure for the gas absorption column (T–201) is shown in Figure C2.9. The operating pressure and temperature in the gas absorption column is 75 psia and 330 K respectively.

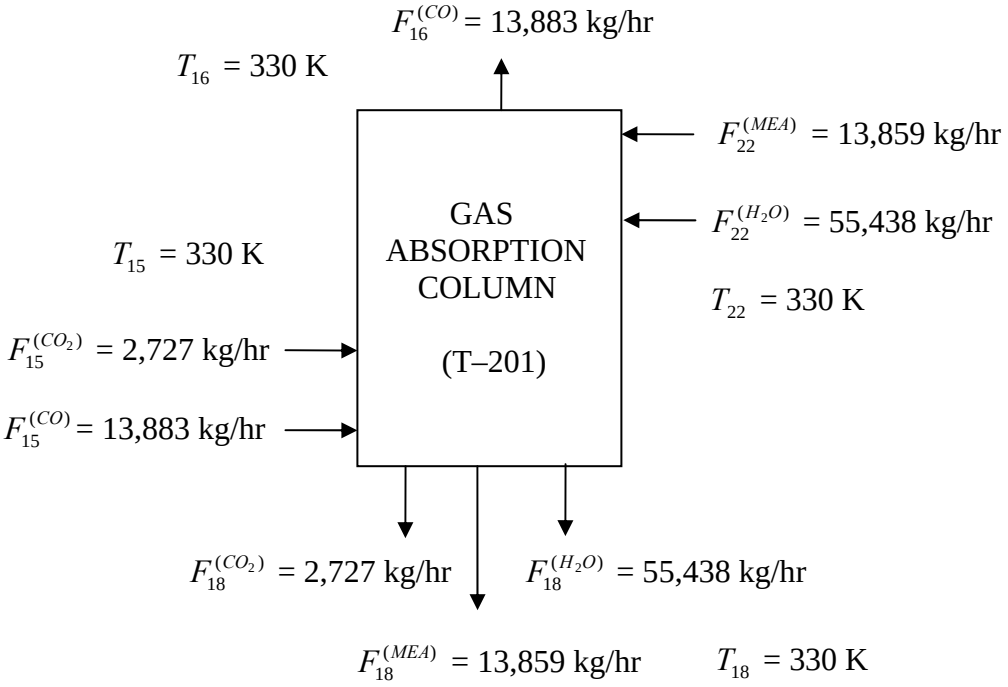

Figure C2.9. Input – Output Component Structure for Gas Absorption Column (T–201)

Number of Theoretical Plates, N:

$$N = 10$$

Actual Number of Trays:

$$N_{act.} = \frac{N}{\varepsilon_o} = \frac{10}{0.67} = 15$$

Column Height, H_{T-201}:

Stage Separation Distance = 0.61 m,

H_o = 15 % allowance (for vapor disengagement and liquid sump)

$$H_{T-201} = \frac{0.61 * N}{\varepsilon_o} + H_o = \frac{0.61 * (1.15)N}{\varepsilon_0}$$

$$H_{T-201} = \mathbf{11\ m}$$

Column Diameter, D_{T-201}, (Ulrich, 1984):

$$D_{T-201} = \left(\frac{4 * G}{\pi * \rho_g * u_{s,g}} \right)^{1/2} \qquad \text{(C2.16)}$$

G = Maximum Vapor Rate, F_{15} = 16,610 kg/hr

ρ_g = Average Gas Density = 5.56 kg/m^3

ρ_l = 1,003 *kg/m^3*

Superficial vapor flow velocity $u_{s,g} = K_{SB} * \left(\frac{\rho_l - \rho_g}{\rho_g} \right)^{1/2}$ = 2.89 x 10^3 *m/hr*

K_{SB} = Souders–Brown Constant = 216 *m/hr* (Ulrich, 1984)

Equation (C2.16) gives:

Tower Diameter, D_{T-201} = **1.2 m**

C2.I. <u>Gas Stripping Column (T–202):</u> (Refer to Table B2.15)

Stripping Temperature = 393 K

Stripping Pressure = 45 psia

CO_2: $F_{19}^{(CO_2)} = F_{18}^{(CO_2)}$ = **2,727 kg CO_2/hr**

$F_{25}^{(CO_2)} = F_{19}^{(CO_2)}$ (Perfect Separation)

$F_{25}^{(CO_2)}$ = **2,727 kg CO_2/hr**

MEA: $F_{19}^{(MEA)} = F_{18}^{(MEA)}$ = **13,859 kg MEA/hr**

Water: $F_{19}^{(H_2O)} = F_{18}^{(H_2O)}$ = **55,438 kg/hr**

Liquid Carryover in SR25, $F_{25}^{(H_2O)}$:

Vapor Pressure of Water, $P^o(393K)$

$$\ln P^o(393K) = 18.3036 - \frac{3{,}816.44}{393 - 46.13}$$

$$P^o = 1{,}482 \text{ mmHg} = 28.66 \text{ psia}$$

$$y_{SR24}^{(H_2O)} = \frac{P^o}{P_T} = \frac{28.66}{45} = 0.64$$

$$y_{SR24}^{(CO_2)} + y_{SR24}^{(H_2O)} = 1$$

$$y_{SR24}^{(CO_2)} = \frac{2{,}727/44}{(2{,}727/44 + F_{25}^{(H_2O)}/18)} = 0.36$$

$$F_{24}^{(H_2O)} = \textbf{1,983 kg } \mathbf{H_2O/hr}$$

The liquid carryover in the gas stream exiting the gas stripping column (SR25) is equivalent to the aqueous fraction recirculated through the reboiler. Thus, the MEA fraction in the feed to the reboiler is estimated based on the evaporation rate of the water in the reboiler:

$$F_{25}^{(H_2O)} = F_{23}^{(H_2O)} = F_{24}^{(H_2O)} = \textbf{1,983 kg/hr};$$

$$F_{25}^{(H_2O)} = 0.80 * F_{23}$$

$$F_{23} = 2{,}479 \text{ kg/hr}$$

$$F_{23}^{(MEA)} = (2{,}479 - 1{,}983) \text{ kg/hr} = \textbf{496 kg MEA/hr}$$

$$F_{24}^{(MEA)} = \textbf{496 kg MEA/hr}$$

The input–output component structure for the gas stripping column (T–202) is shown in Figure C2.10:

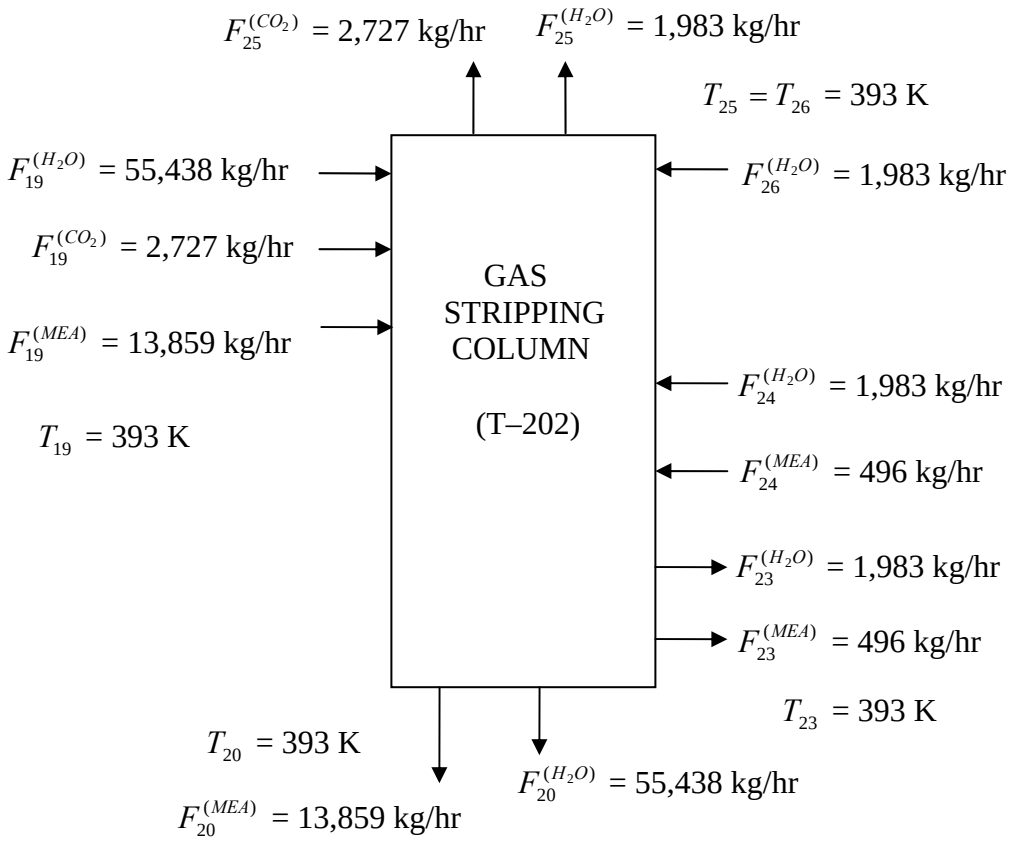

Figure C2.10. Input – Output Component Structure for the Gas Stripping Column (T–202)

Energy Balance – Gas Stripping Column, (T–202):

The energy balance around the stripping column is given by Equation (C2.17):

$$Q_{T-202} = \sum_i F_{outlet}^{(i)} H_{outlet}^{(i)} - \sum_i F_{inlet}^{(i)} H_{inlet}^{(i)} \qquad \text{(C2.17)}$$

The enthalpy data for the component streams in and out of the gas stripping column is given in Table C2.5. The heat supplied to the gas stripping column, Q_{T-202} is calculated from Equation (C2.17):

$$Q_{T-202} = (-901{,}744{,}302 \text{ kJ/hr}) - (-902{,}654{,}570 \text{ kJ/hr})$$

$$Q_{T-202} = \mathbf{910{,}268 \text{ kJ/hr}}$$

Table C2.5. Enthalpy Data for Gas Stripping Column (T–202)

Component	Inlet Streams,(kJ/kg)			Outlet Streams, (kJ/kg)		
	H_{19} (393 K)	H_{26} (393 K)	H_{24} (413 K)	H_{20} (393 K)	H_{25} (393 K)	H_{23} (393 K)
CO_2	– 6,770	–	–	–	– 6,770	–
MEA	1,206	–	1,490	1,206	–	1,206
H_2O	– 15,479	– 15,479	– 6,009	– 15,479	– 6,397	– 15,479

Number of Theoretical Plates, N, (Perry, 1984):

Equation (C1.32) gives: $N = 10$

Actual Number of Trays, N_{act} :

Plate efficiency, ε_o = 67.1%

$$N_{act} = \frac{N}{\varepsilon_o} = \mathbf{15}$$

Column Height, H_{T-202} :

$$H_{T-202} = \frac{0.61 * N}{\varepsilon_o} + H_o = \frac{0.61 * (1.15)N}{\varepsilon_0}$$

$$H_{T-202} = \mathbf{11\ m}$$

Column Diameter, D_{T-202} :

Equation C2.16 gives:

$$D_{T-202} = \left(\frac{4 * 4{,}710 kg/hr}{\pi * 2.54 kg/m^3 * 4.29 * 10^3 m/hr} \right)^{1/2}$$

$$D_{T-202} = \mathbf{0.75\ m}$$

C2.J. <u>Solute Rich–Lean MEA Cross Heat Exchanger (E–204)</u>: (Refer to Table B2.6)

The input–output component structure for the cross heat exchanger (E–204) is shown in Figure C2.11:

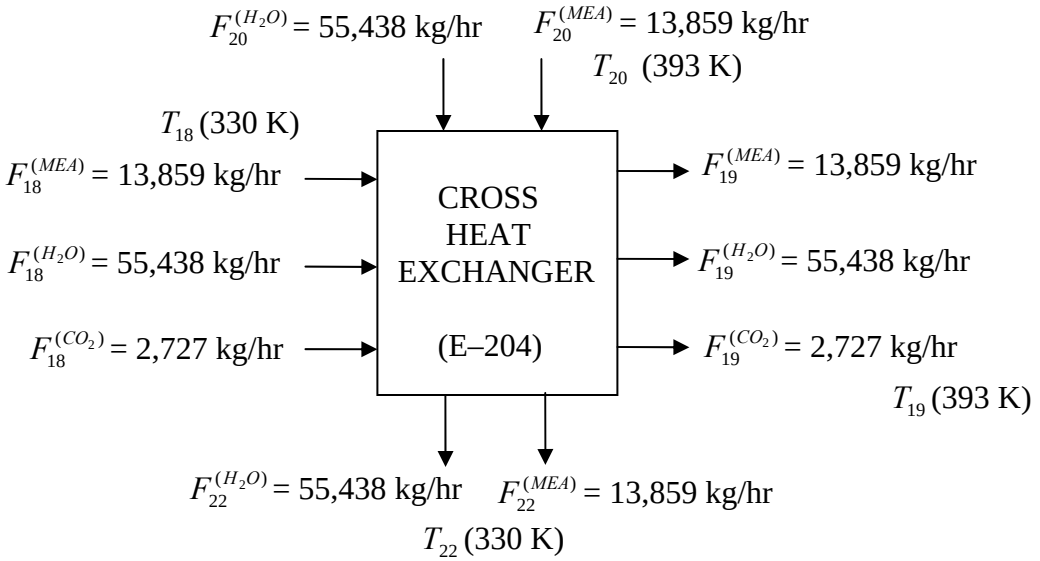

Figure C2.11. Input – Output Component Structure for Cross Heat Exchanger (E–204)

CO_2: $F_{19}^{(CO_2)} = F_{18}^{(CO_2)} = F_{15}^{(CO_2)} =$ **2,727 kg/hr**

MEA: $F_{19}^{(MEA)} = F_{18}^{(MEA)} = F_{22}^{(MEA)} =$ **13,859 kg/hr**

$F_{22}^{(MEA)} = F_{20}^{(MEA)} = F_{19}^{(MEA)} =$ **13,859 kg/hr**

Water: $F_{19}^{(H_2O)} = F_{18}^{(H_2O)} = F_{22}^{(H_2O)} =$ **55,438 kg/hr**

$F_{22}^{(H_2O)} = F_{20}^{(H_2O)} = F_{19}^{(H_2O)} =$ **55,438 kg/hr**

Energy Absorbed in the Cross Heat Exchanger (E–204), Q_{E-204}:

$$Q_{E-204} = \sum_i F_{19}^{(i)} H_{19}^{(i)} - \sum_i F_{18}^{(i)} H_{18}^{(i)} \qquad \text{(C2.18)}$$

T_{SR18} = 330 K; T_{SR19} = 393 K

The enthalpy data for the component streams in and out of the cross heat exchanger (E–204) is given in Table C2.6:

Table C2.6. Enthalpy Data for Cross Heat Exchanger (E–204)

Component	F_{18} kg/hr	$H_{18}(330K)$ kJ/kg	F_{19} kg/hr	$H_{19}(393K)$ kJ/kg
CO_2	2,727	– 6,869	2,727	– 6,771
H_2O	55,438	– 15,745	55,438	– 15,479

The enthalpy change for the MEA component in the cross heat exchanger is calculated from Equation (C2.19):

$$\Delta H^{(MEA)} = \frac{F_{19}^{(MEA)}}{MW^{(MEA)}} * \int_{330K}^{393K} C_p^{(MEA)}(T)dT \qquad \text{(C2.19)}$$

$\Delta H^{(MEA)}$ = 11,484,211 kJ/hr

Equation (C2.18) gives the energy exchanged in the cross exchanger (E–204):

Q_{E-204} = (– 876,589,319 kJ/hr) – (– 891,603,073 kJ/hr) + 11,484,211 kJ/hr

Q_{E-204} = **26,497,965 kJ/hr**

Temperature of Lean Solution (SR22) Exiting E–204, T_{SR22}:

T_{SR20} = 393 K

Energy Liberated = Energy Absorbed

$$Q_{E-204} = \frac{F_{22}^{(MEA)}}{MW^{(MEA)}} * \int_{393K}^{T_{SR22}} C_p^{(MEA)}dT + \frac{F_{22}^{(H_2O)}}{MW^{(H_2O)}} * \int_{393K}^{T_{SR22}} C_p^{(H_2O)}(T)dT \qquad \text{(C2.20)}$$

Equation (C2.20) gives:

T_{SR22} = 330 K

Area of the Cross Heat Exchanger, A_{E-204}

$$A_{E-204} = \frac{Q_{E-204}}{U_{E-204} * \Delta T_m}$$

ΔT_m = 63 K

U_{E-204} = 4,104 kJ/ m^2.hr.K (Ulrich, 1984)

$$A_{E-204} = \frac{26{,}497{,}965 kJ/hr}{4{,}104 kJ/m^2 hrK * 63K}$$

A_{E-204} = **103 m^2**

C2.K. <u>Reboiler (E–205):</u> (Refer to Table B2.16)

The input–output component structure for the kettle reboiler (E–205) is shown in Figure C2.12:

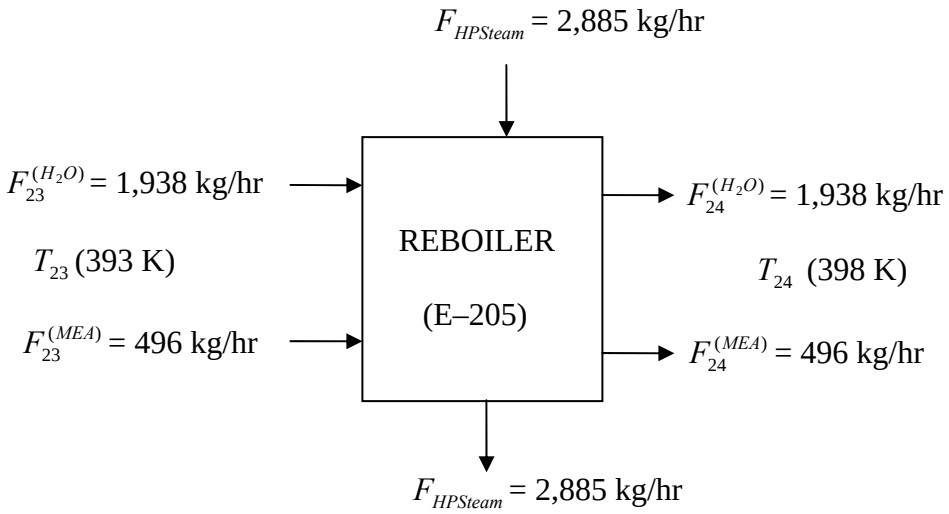

Figure C2.12. Input – Output Component Structure for Reboiler (E–205)

MEA: $F_{23}^{(MEA)} = F_{24}^{(MEA)}$ = **496 kg/hr**

Water: $F_{23}^{(H_2O)} = F_{24}^{(H_2O)} = F_{25}^{(H_2O)}$ = **1,983 kg/hr**

Heat Duty to Reboiler, Q_{E-205}:

$$Q_{E-205} = \frac{F_{23}^{(MEA)}}{MW^{(MEA)}} * \int_{393K}^{413K} C_p^{(MEA)}(T)dT + [F_{23}^{(H_2O)} * (H_{24}^{(H_2O)} - H_{23}^{(H_2O)}) + \lambda_s] \qquad \text{(C2.21)}$$

Latent Heat, $\lambda_s = 2{,}260 kJ/kg$; $T_{SR20} = T_{SR28} = 393$ K (Stripping Temperature)

$T_{SR29} = 413$ K (Temperature Driving Force Constraint: $T_{SR29} - T_{SR28} < 30$ K)

The enthalpy data for the reboiler is given in Table C2.7

Table C2.7. Enthalpy Data for Reboiler (E–205)

Component	F_{23} kg/hr	$H_{23}(393K)$ kJ/kg	F_{24} kg/hr	$H_{24}(413K)$ kJ/kg
H_2O	1,983	– 15,479	1,983	– 15,393

Equation (C2.21) gives: Q_{E-205} = (140,766 kJ/hr) + (4,652,118 kJ/hr)

Heat Duty to Reboiler, Q_{E-205} = **4,792,884 kJ/hr**

HP Steam Supplied to Reboiler, $F_{HPSteam}$

$$F_{HPSteam} = \frac{4{,}792{,}884 kJ/hr}{1{,}661.5 kJ/kg} = \textbf{2,885 kg HP Steam/hr}$$

Heat Transfer Area of Reboiler, A_{E-205}:

$$A_{E-205} = \frac{Q_{E-205}}{U_{E-205} * \Delta T_m}$$

U_{E-205} = 5,112 kJ/m^2 hr K (Ulrich, 1984)

ΔT_m = 20 K (to prevent film boiling in the reboiler)

$$A_{E-205} = \frac{4{,}792{,}3884 \ kJ/hr}{5{,}112 \ kJ/m^2 hrK * 20 \ K} = \textbf{47 m}^2$$

C2.M. <u>Flash Drum (V–204):</u> (Refer to Table B2.17)

The input–output component material structure for the flash drum (V–204) is shown in Figure C2.13.

CO_2: $F_{27}^{(CO_2)} = F_{25}^{(CO_2)} =$ **2,727 kg/hr**

Water: $F_{26}^{(H_2O)} = F_{25}^{(H_2O)} =$ **1,983 kg/hr**

Drum Diameter, D_{V-204}:

The vapor superficial velocity, u_g in the flash drum is determined according to the Souders–Brown Equation (C2.22), (Ulrich, 1984):

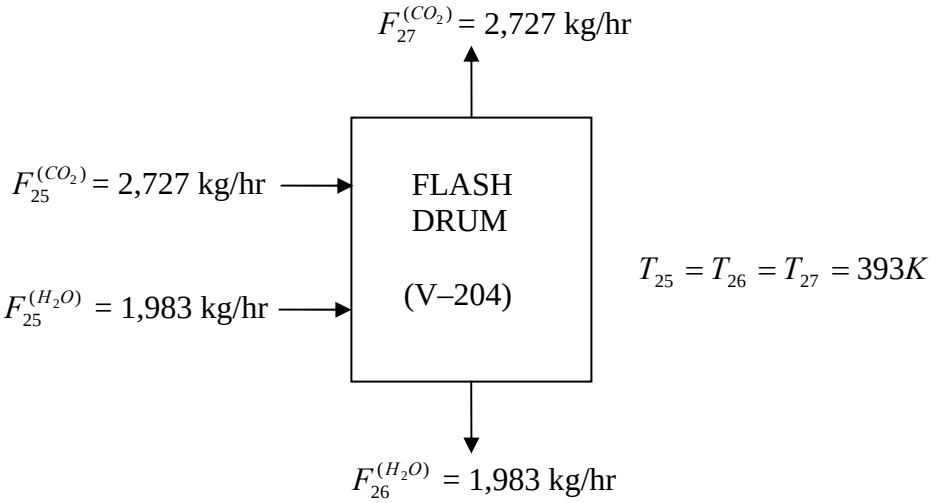

Figure C2.13. Input – Output Component Structure of Flash Drum (V–204)

$$u_g = 0.064 m/s * \left(\frac{\rho_l - \rho_g}{\rho_g} \right)^{1/2} \qquad \text{(C2.22)}$$

ρ_g = 2.49 kg/m^3; ρ_l = 1,000 kg/m^3

Equation (C2.21) gives: u_g = 4.32 x 10^3 m/hr

The diameter of the flash drum is estimated from Equation C2.16:

$$D_{V-204} = \left(\frac{4 * V}{\pi * \rho_g * u_g} \right)^{1/2}$$

V = Maximum Vapor Rate in Flash Drum, F_{25} = 4,710 kg/hr

Drum Diameter, D_{V-204} = **0.75 m**

Drum Height, H_{V-204}, (Ulrich, 1984):

$$H_{V-204} = 4\, D_{V-204} = \textbf{3 m}$$

C2.N. <u>Discharge Valve (Z–209):</u> (Refer to Table B2.19)

The input–output component structure for the vent valve (Z–209) is shown in Figure C2.14:

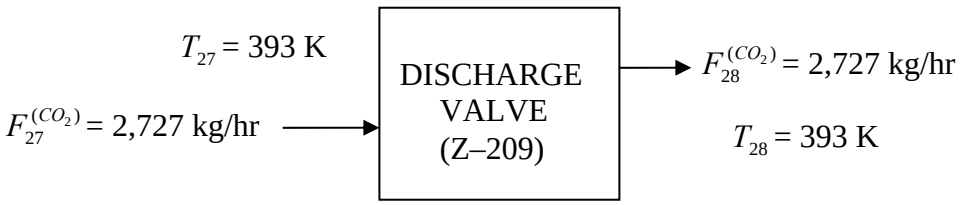

Figure C2.14. Input – Output Component Structure for Discharge Valve (Z–209)

CO_2:

$$F_{28}^{(CO_2)} = F_{27}^{(CO_2)} = F_{25}^{(CO_2)}$$

$$F_{28}^{(CO_2)} = F_{27}^{(CO_2)} = \textbf{2,727 kg/hr}$$

C2.P. <u>Silica Leaching Tank (V–202):</u> (Refer to Table B2.8)

The input–output component structure for the silica leaching tank (V–202) is shown in Figure C2.15:

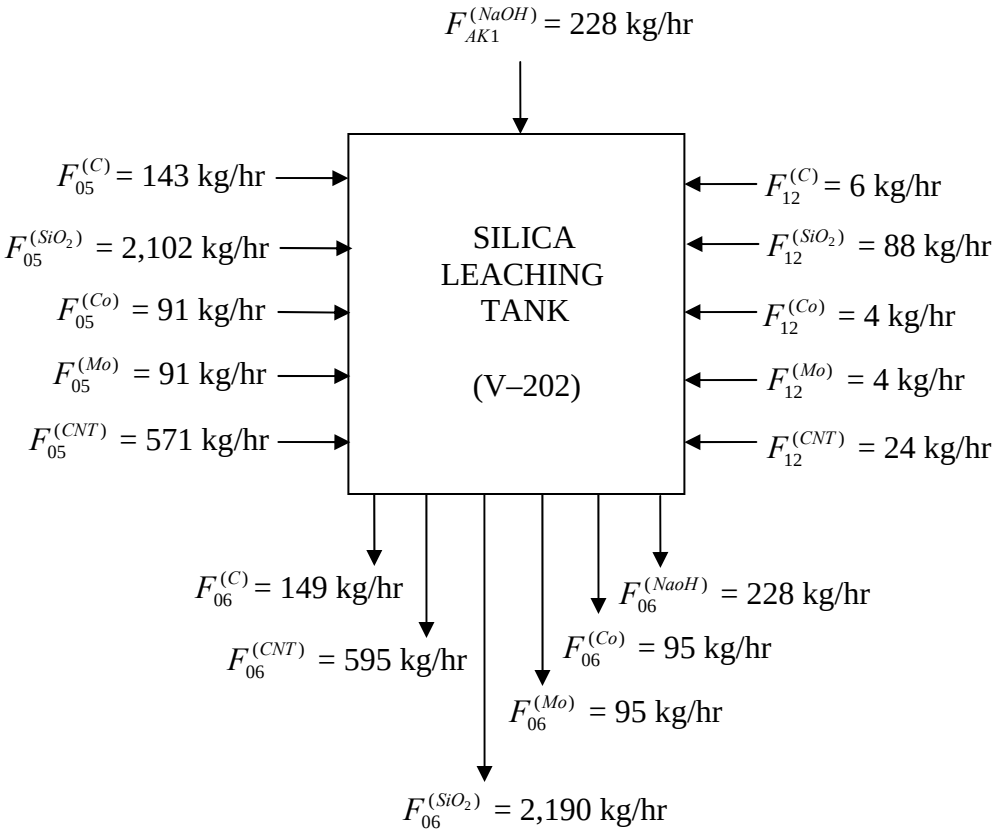

Figure C2.15. Input – Output Component Structure for Silica Leaching Tank (V–202)

CNT: $F_{05}^{(CNT)} = 571$ kg/hr; $F_{12}^{(CNT)} = 24$ kg/hr

$$F_{06}^{(CNT)} = F_{05}^{(CNT)} + F_{12}^{(CNT)} = \mathbf{595\ kg/hr}$$

C: $F_{05}^{(C)} = 143$ kg/hr; $F_{12}^{(C)} = 6$ kg/hr

$$F_{06}^{(C)} = F_{05}^{(C)} + F_{12}^{(C)} = \mathbf{149\ kg/hr}$$

SiO_2: $F_{05}^{(SiO_2)}$ = 2,102 kg/hr; $F_{12}^{(SiO_2)}$ = 88 kg/hr;

$$F_{06}^{(SiO_2)} = F_{05}^{(SiO_2)} + F_{12}^{(SiO_2)} = \mathbf{2{,}190\ kg/hr}$$

Co: $F_{05}^{(Co)}$ = 91 kg/hr; $F_{12}^{(Co)}$ = 4 kg/hr;

$$F_{06}^{(Co)} = F_{05}^{(Co)} + F_{12}^{(Co)} = \mathbf{95\ kg/hr}$$

Mo: $F_{05}^{(Mo)}$ = 91 kg/hr; $F_{12}^{(Mo)}$ = 4 kg/hr;

$$F_{06}^{(Mo)} = F_{05}^{(Mo)} + F_{12}^{(Mo)} = \mathbf{95\ kg/hr}$$

Alkali Supply to Leaching Tank, $F_{AK1}^{(NaOH)}$

Volume of Contactor filled with solution = 0.75 * V_{V-202} = 2.85 m^3 (Ulrich, 1984)

2M NaOH (Resasco, et al, 2001)

$$F_{AK1}^{(NaOH)} = \frac{2kgmolNaOH}{1m^3} * \frac{40kgNaOH}{1kgmolNaOH} * \frac{2.85m^3}{hr} = \mathbf{228\ kg/hr}$$

Leaching Tank Size, V_{V-202} (Ulrich, 1984)

$$\text{Residence Time, } \theta(s) = \frac{V_{Z-202} * f_s * \rho_s}{F_{05}^{(SiO_2)}}$$

Residence time, $\theta = 3{,}600s$ (Resasco, et al, 2001)

Density, $\rho_s = 2{,}260kg/m^3$ (Perry, et al, 1984)

$F_{05}^{(SiO_2)}$ = 0.608 kg/s (2,190 kg/hr)

Fraction of Contactor occupied by solids, f_s = 0.25 (Ulrich, 1984)

Volume of the silica leaching tank, V_{V-202}

$$V_{V-202} = \frac{0.608kg/s * 3{,}600s}{2{,}260kg/m^3 * 0.80} = \mathbf{3.8\ m^3}$$

Length to Diameter Ratio = 4 (Branan, 2002)

$$V_{V-202} = \frac{\pi D^2}{4} * 4D = \pi D^3 = 3.8 \text{ m}^3$$

Diameter, D_{V-202} = **1.2 m**

Length, $L_{V-202} = 4 * D_{V-202}$ = **4.8 m**

C2.Q.Froth Flotation Column (T–203) (Refer to Table B2.9)

The carbon nanotube product is separated from the silica–supported bimetallic catalysts in the froth flotation column. However, only about 80% carbon nanotube purity is obtained from the froth flotation purification process, and the carbon nanotube product from the flotation column still contains significant amount of residual metal particles. The residual cobalt and molybdenum particles are subsequently removed in the acid dissolution step. The input–output component structure for the froth flotation column (T–203) is shown in Figure C2.16:

CNT: $F_{08}^{(CNT)} = F_{06}^{(CNT)}$ = **595 kg/hr**

C: $F_{07}^{(C)} = F_{06}^{(C)}$ = **149 kg/hr**

SiO_2: $F_{07}^{(SiO_2)} = F_{06}^{(SiO_2)}$ = **2,190 kg/hr**

Co: $F_{07}^{(Co)} = 0.80 * F_{06}^{(Co)}$ = **76 kg/hr**

$F_{08}^{(Co)} = (1 - 0.80) * F_{06}^{(Co)}$ = **19 kg/hr**

Mo: $F_{07}^{(Mo)} = 0.80 * F_{06}^{(Mo)}$ = **76 kg/hr**

$F_{08}^{(Mo)} = (1 - 0.80) * F_{06}^{(Mo)}$ = **19 kg/hr**

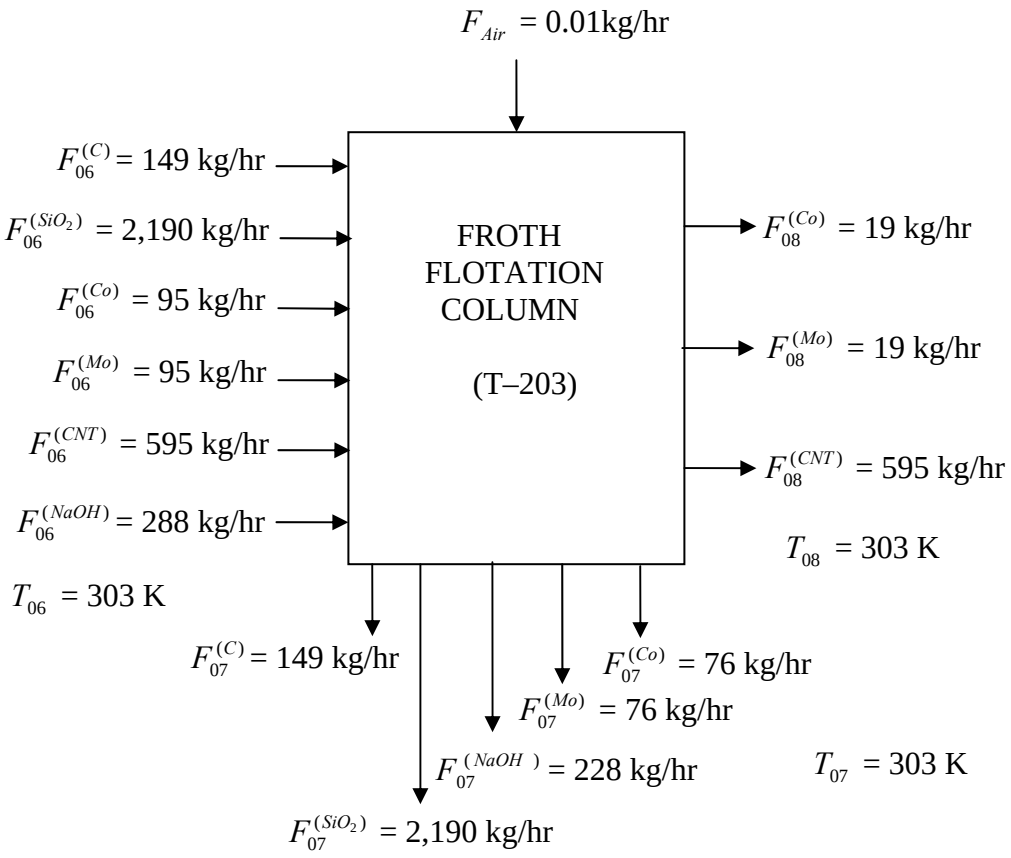

Figure 2.16. Input – Output Component Structure for Flotation Column (T–203)

Air Supply to Flotation Column, F_{Air}

The air supply rate to the froth flotation column (T–203) is calculated by the geometrical scale up of the laboratory–scale froth flotation model (Pisan, et al, 2004):

Laboratory Model: Aeration rate = 0.24 liter/hr; H_{Lab} = 0.20 m, (Pisan, et al, 2004)

Density, ρ_{Air} = 0.0013 kg/liter (Luyben, et al, 1988)

H_{T-203} = 5.9 m

$$F_{Air} = \frac{0.24 liter}{hr} * \frac{5.9 m}{0.20 m} * \frac{0.0013 kg Air}{1 liter} = \mathbf{0.01\ kg\ Air/hr}$$

Flotation Column Size, A_{T-203}

The expression relating the mass flow rate of the silica particles in the carbon nanotube slurry from the leaching tank to the nominal area of the flotation column is given by Equation (C2.23), (Ulrich, 1984):

$$F_{06}^{(SiO_2)}(kg/s) = 0.2 * A_{T-203} \qquad \text{(C2.23)}$$

$$F_{06}^{(SiO_2)}(kg/s) = 2{,}190\frac{kg}{hr} * \frac{1hr}{3600s} = 0.608 \text{ kg/s}$$

$$A_{T-203} = \frac{0.608 kg/s}{0.2 kg/m^2 s} = \mathbf{3.04\ m^2}$$

Column Diameter, D_{T-203}

$$A_{T-203} = \pi\frac{D^2}{4} = 3.04 \text{ m}^2$$

$$D_{T-203} = \mathbf{1.97\ m}$$

Column Height, $H_{T-203} = 3\,D_{T-203} = \mathbf{5.9\ m}$ (Branan, 2005)

C2.R. Liquid–Solid Filter 1 (Z–204): (Refer to Table B2.10)

The input–output component structure for the liquid–solid filter 1 (Z–204) is shown in Figure C2.17. The mass flow rate of solid particles through the filter is given below and included in Figure C2.17.

Silica: $F_{10}^{(SiO_2)} = F_{07}^{(SiO_2)} = \mathbf{2{,}190\ kg/hr}$

C: $F_{10}^{(C)} = F_{07}^{(C)} = \mathbf{149\ kg/hr}$

Co: $F_{10}^{(Co)} = F_{07}^{(Co)} = \mathbf{76\ kg/hr}$

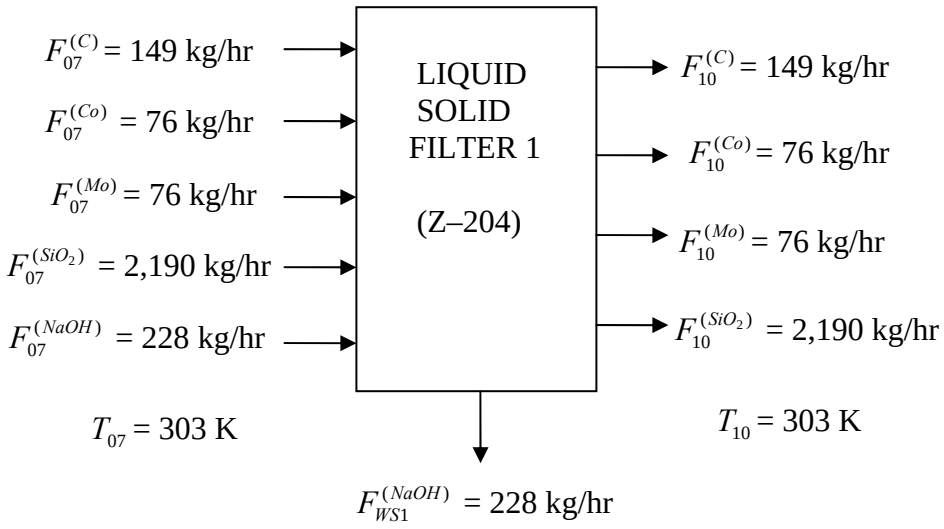

Figure 2.17. Input – Output Component Structure for Liquid Filter 1 (Z–204)

Mo: $F_{10}^{(Mo)} = F_{07}^{(Mo)}$ = **76 kg/hr**

NaOH: $F_{WS1}^{(NaOH)} = F_{07}^{(NaOH)}$ = **228 kg/hr**

Liquid–Solid Filter Size, A_{Z-204} (Ulrich, 1984):

$$A_{Z-204} = \frac{F_{10}(kg/s)}{0.02 kg/m^2 s} \qquad \text{(C2.24)}$$

F_{10} = 2,456 kg/hr = 0.682 kg/s

$$A_{Z-204} = \frac{0.682 kg/s}{0.02 kg/m^2 s} = \mathbf{35\ m^2}$$

C2.S. Acid Dissolution Tank (V–203): (Refer to Table B2.12)

The residual cobalt and molybdenum metal particles in the carbon nanotube product (SR09) from the flotation column are removed by dissolution in 12% hydrochloric acid solution (Meyyappan, 2005). The ratio of the amount of HCl used to the amount of

metals removed is based on the reaction between hydrochloric acid and the residual cobalt/molybdenum metal catalyst particles. However, the final nanotube product (SR33) contains 97 mol% carbon nanotubes, 1.5 mol% cobalt and 1.5 mol% molybdenum metal particles (Resasco, et al, 2001).

The amount of hydrochloric acid required to extract the residual cobalt and molybdenum metals in the acid dissolution tank is estimated from the stoichiometric ratios of the reactants in the reaction between: HCl and cobalt (Equation C2.25); HCl and molybdenum (Equation C2.26):

$$Co_{(s)} + 2HCl_{(aq)} \rightarrow CoCl_{2(aq)} + H_{2(g)} \qquad \text{(C2.25)}$$

$$Mo_{(s)} + 2HCl_{(aq)} \rightarrow MoCl_{2(aq)} + H_{2(g)} \qquad \text{(C2.26)}$$

Residual Metal Particles removed by HCl:

$$F_{31}^{(Co)} = F_{09}^{(Co)} - F_{33}^{(Co)} = \textbf{18.98 kg Co/hr}$$

$$F_{31}^{(Mo)} = F_{09}^{(Mo)} - F_{33}^{(Mo)} = \textbf{18.97 kg Mo/hr}$$

Hydrochloric Acid Supplied to Acid Dissolution Tank, $F_{32}^{(HCl)}$:

$$F_{32}^{(HCl)} = [(\frac{2kgmolHCl}{1kgmolCo} * \frac{19\frac{kgCo}{hr}}{59\frac{kgCo}{kgmolCo}}) + (\frac{2kgmolHCl}{1kgmolMo} * \frac{19\frac{kgMo}{hr}}{96\frac{kgMo}{kgmolMo}})] * \frac{37kgHCl}{1kgmolHCl}$$

$$F_{32}^{(HCl)} = \textbf{39 kg HCl/hr}$$

Water Supplied to Acid Dissolution Tank, $F_{32}^{(H_2O)}$

$$F_{32}^{(H_2O)} = \frac{0.88kgH_2O}{0.12kgHCl} * 39\frac{kgHCl}{hr} = \textbf{286 kg H₂O/hr}$$

$$F_{32}^{(H_2O)} = F_{29}^{(H_2O)} = \textbf{286 kg/hr}$$

Cobalt Chloride Produced in Acid Dissolution Tank, $F_{29}^{(CoCl_2)}$

$$F_{29}^{(CoCl_2)} = \frac{1kgmolCoCl_2}{1kgmolCo} * \frac{19kgCo}{hr} * \frac{1kgmolCo}{59kgCo} * \frac{128kgCoCl_2}{1kgmolCoCl_2}$$

$$F_{29}^{(CoCl_2)} = \mathbf{41\ kg/hr}$$

Molybdenum Chloride Produced in Acid Dissolution Tank, $F_{29}^{(MoCl_2)}$

$$F_{29}^{(MoCl_2)} = \frac{1kgmolMoCl_2}{1kgmolMo} * \frac{19kgMo}{hr} * \frac{1kgmolMo}{96kgMo} * \frac{168kgMoCl_2}{1kgmolMoCl_2}$$

$$F_{29}^{(MoCl_2)} = \mathbf{33\ kg/hr}$$

CNT: $F_{29}^{(CNT)} = F_{09}^{(CNT)} = \mathbf{595\ kg/hr}$

The input–output component structure for the acid dissolution tank (V–203) is shown in Figure C2.18.

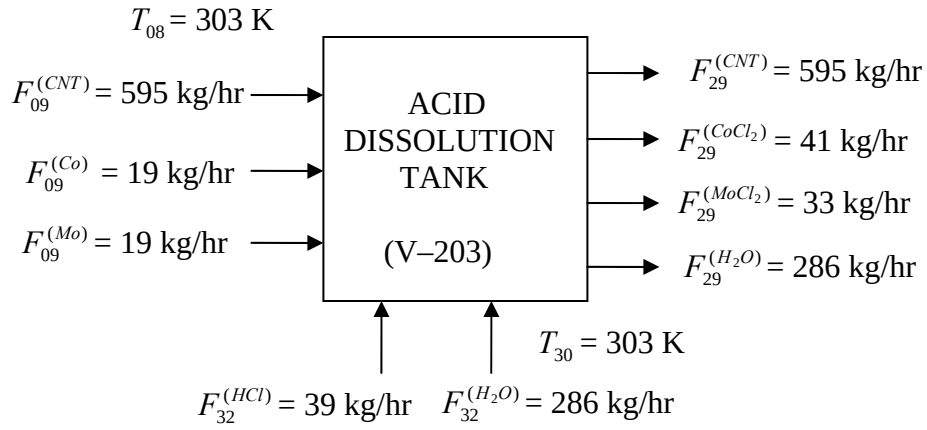

Figure C2.18. Input – Output Component Structure for Acid Dissolution Tank (V–203)

Acid Dissolution Tank Size, V_{V-203} (Ulrich, 1984)

$$\text{Residence Time, } \theta(s) = \frac{V_{Z-203} * f_s * \rho_s}{F_{29}^{(CNT)}}$$

Residence time, $\theta = 900s$ (Chiang, et al, 2001)

Carbon Nanotube density, $\rho_s = 1{,}365 kg/m^3$ (Kelley, 2003)

Flow rate of CNT, $F_{29}^{(CNT)}$ = 0.165 kg/s (595 kg/hr)

Fraction of Contactor occupied by solids, f_s = 0.15 (Ulrich, 1984)

Volume of the acid dissolution tank, V_{V-203}

$$V_{V-203} = \frac{0.165 kg/s * 900s}{1{,}365 kg/m^3 * 0.15} = \mathbf{0.73\ m^3}$$

Length to Diameter Ratio = 4 (Branan, 2002)

$$V_{V-203} = \frac{\pi D^2}{4} * 4D = \pi D^3 = 0.73\ \text{m}^3$$

Diameter, D_{V-203} = **0.90 m**

Length, $L_{V-203} = 4 * D_{V-203}$ = **3.6 m**

C2.T. Liquid–Solid Filter 2 (Z–205): (Refer to Table B2.13)

CNT: $F_{30}^{(CNT)} = F_{29}^{(CNT)}$ = **595 kg/hr**

$CoCl_2$: $F_{30}^{(CoCl_2)} = F_{33}^{(CoCl_2)}$ = **0.04 kg/hr**

$F_{29}^{(CoCl_2)}$ = 41 kg/hr

$F_{31}^{(CoCl_2)} = F_{29}^{(CoCl_2)} - F_{30}^{(CoCl_2)}$ = **40.96 kg/hr**

$MoCl_2$: $F_{30}^{(MoCl_2)} = F_{33}^{(MoCl_2)}$ = **0.05 kg/hr**

$F_{29}^{(CoCl_2)}$ = 33 kg/hr

$F_{31}^{(CoCl_2)} = F_{29}^{(CoCl_2)} - F_{30}^{(CoCl_2)}$ = **32.95 kg/hr**

In addition to the metal chlorides, the wet carbon nanotube product from filter contains water. The amount of solution in the wet product (SR13) is estimated from the percentage characteristics of the rotary drum liquid–solid filter, (Ulrich, 1984). The average cake dryness from a rotary liquid–solid filter is 70 weight% solids (Ulrich, 1984):

H_2O: $$F_{30}^{(H_2O)} = 595\frac{kgCNT}{hr} * \frac{0.30 kgH_2O}{0.70 kgCNT} = \mathbf{255\ kg\ H_2O/hr}$$

$$F_{31}^{(H_2O)} = F_{29}^{(H_2O)} - F_{30}^{(H_2O)} = \mathbf{31\ kg\ H_2O/hr}$$

The input–output component structure for the liquid–solid filter (Z–205) is shown in Figure C2.19:

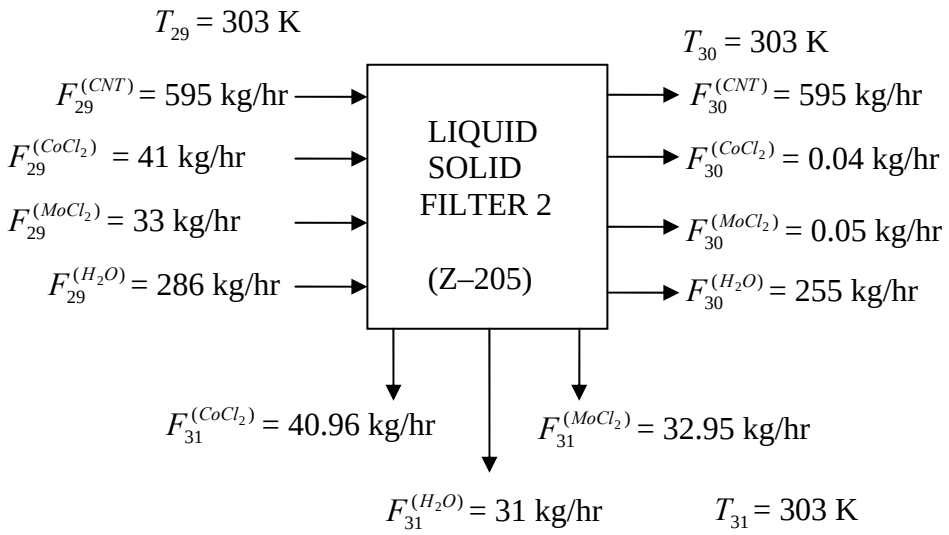

Figure C2.19. Input – Output Component Structure for Liquid–Solid Filter (Z–205)

Filter Size, A_{Z-205} (Ulrich, 1984):

$$F_{30}^{(CNT)}(kg/s) = \frac{595 kg/hr}{3600 s/hr} = 0.165 \text{ kg/s}$$

$$A_{Z-205} = \frac{F_{30}(kg/s)}{0.02} = \frac{0.165(kg/s)}{0.02} = \mathbf{8.3\ m^2}$$

C2.U. Product Drier (Z–206): (Refer to Table B2.20)

CNT: $F_{33}^{(CNT)} = F_{30}^{(CNT)} =$ **595 kg/hr**

$CoCl_2$: $F_{33}^{(CoCl_2)} = F_{30}^{(CoCl_2)} =$ **0.04 kg/hr**

$MoCl_2$: $F_{33}^{(MoCl_2)} = F_{30}^{(MoCl_2)} =$ **0.05 kg/hr**

Water Evaporated from Drier:

$$F_{34}^{(H_2O)} = F_{32}^{(H_2O)} = \textbf{255 kg/hr}$$

The input–output component structure for the product drier (Z–206) is shown in Figure C2.20:

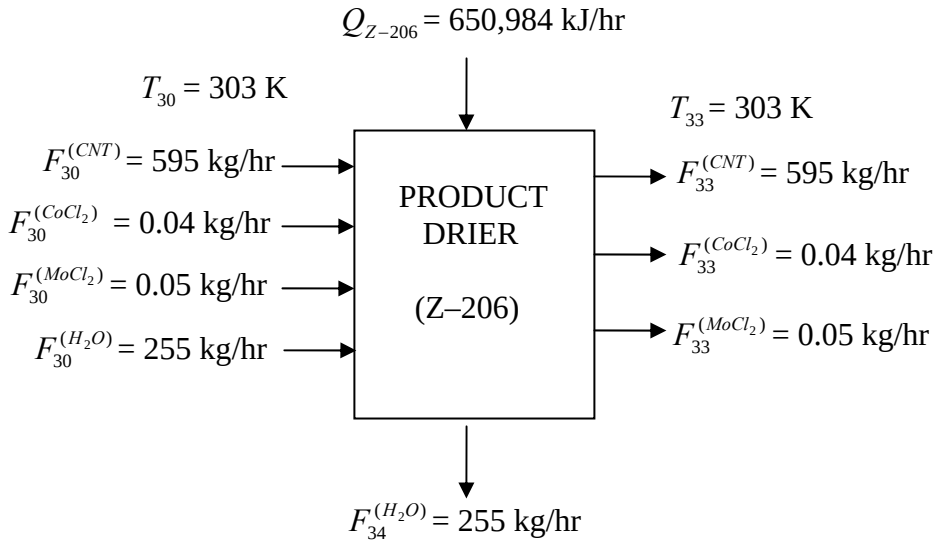

Figure C2.20. Input – Output Material Structure for the Product Drier (Z–206)

Cobalt and Molybdenum Chloride in Final Product, $F_{33}^{(CoCl_2)}$,:

$$F_{33}^{(CoCl_2)} = F_{30}^{(CoCl_2)} = \textbf{0.04 kg/hr}$$

Molybdenum Chloride in Final Product:

$$F_{33}^{(MoCl_2)} = F_{30}^{(MoCl_2)} = \textbf{0.05 kg/hr}$$

Energy Required to Evaporate Water from Wet Product in Drier, Q_{Z-206}

$$Q_{Z-206} = F_{34}^{(H_2O)} * (C_p^{(H_2O)} \Delta T + \lambda_s)$$

$F_{34}^{(H_2O)}$ = 255 kg/hr

$C_p^{(H_2O)}$ = 4.184 kJ/kg K

ΔT = (373 – 303) K = 70 K; λ_s = 2,260 kJ/kg

$$Q_{Z-206} = 255\frac{kg}{hr} * (4.184\frac{kJ}{kgK} * 70K + 2{,}260\frac{kJ}{kg})$$

Q_{Z-206} = **650,984 kJ/hr**

HP Steam Supplying Heat to Drier, $F_{HPSteam}$

$$F_{HPSteam(In)} = \frac{Q_{Z-206}}{\Delta H_{vap}} = \frac{650{,}984 kJ/hr}{1661.5 kJ/kg} = \textbf{392 kg/hr}$$

Drier Size, V_{Z-206}

The residence time of the solid product in the product drier (Z–206) is used to estimate the equipment size according Equation (C1.43), (Ulrich 1984):

$$\theta(s) = \frac{V_{Z-206} * f_s * \rho_s}{F_{33}^{(CNT)}}$$

Average Residence time, $\theta = 3{,}600 s$ (Chiang, et al, 2001)

Raw CNT density, $\rho_s = 1{,}365 kg/m^3$ (Kelley, 2003)

Mass flow rate of solids, $F_{33}^{(CNT)}$ = 0.165 kg/s (595 kg/hr)

Fraction of Contactor occupied by solids, f_s = 0.15 (Ulrich, 1984)

$$V_{Z-206} = \frac{0.165 kg/s * 3600 s}{1{,}365 kg/m^3 * 0.15} = \textbf{2.9 m}^{\textbf{3}}$$

$$V_{Z-206} = \frac{\pi D^2}{4} * 4D = \pi D^3 = 2.91 \text{ m}^3$$

Diameter, D_{Z-206} = **0.97 m**

Length, $L_{Z-206} = 4 * D_{Z-206}$ = **3.9 m**

C2.V. Catalyst Regeneration Bed (Z–207) (Refer to Table B2.22)

In the catalyst regeneration bed, the spent silica–supported Co–Mo bimetallic catalysts are regenerated before being recycled back to the fluidized bed for another reaction cycle. In the regeneration bed, make–up cobalt and molybdenum metal particles are added to the silica supported bimetallic catalyst to compensate for the cobalt and molybdenum catalysts losses in the final product and in the acid regeneration column. In addition, high pressure steam is used to oxidize amorphous carbon in the spent silica supported catalyst stream to carbon monoxide and hydrogen according to Equation (2.27):

$$C_{(s)} + H_2O_{(g)} \rightarrow CO_{(g)} + H_{2(g)} \qquad (2.27)$$

Using the stoichiometric ratio in Equation (2.27):

HP Steam Supply to Catalyst Regeneration Bed, $F_{RGS1}^{(H_2O)}$

$$F_{RGS1}^{(H_2O)} = \frac{1 kgmol H_2O}{1 kgmol C} * \frac{18 kg H_2O}{1 kgmol H_2O} * \frac{1 kgmol C}{12 kg C} * 149 \frac{kgC}{hr} = \textbf{223 kg/hr}$$

CO Produced from Oxidation of Amorphous Carbon, $F_{RGS2}^{(CO)}$

$$F_{RGS2}^{(CO)} = \frac{1 kgmol CO}{1 kgmol C} * \frac{28 kg CO}{1 kgmol CO} * \frac{1 kgmol C}{12 kg C} * 149 \frac{kgC}{hr} = \textbf{349 kg/hr}$$

H_2 Produced from Oxidation of Amorphous Carbon, $F_{RGS2}^{(H_2)}$

$$F_{RGS2}^{(H_2)} = \frac{1kgmolH_2}{1kgmolC} * \frac{2kgH_2}{1kgmolH_2} * \frac{1kgmolC}{12kgC} * 149\frac{kgC}{hr} = \mathbf{25\ kg/hr}$$

SiO_2: $F_{11}^{(SiO_2)} = F_{10}^{(SiO_2)} = \mathbf{2{,}190\ kg/hr}$

The input–output component balance for the catalyst regeneration bed (Z–207) is shown in Figure C2.21:

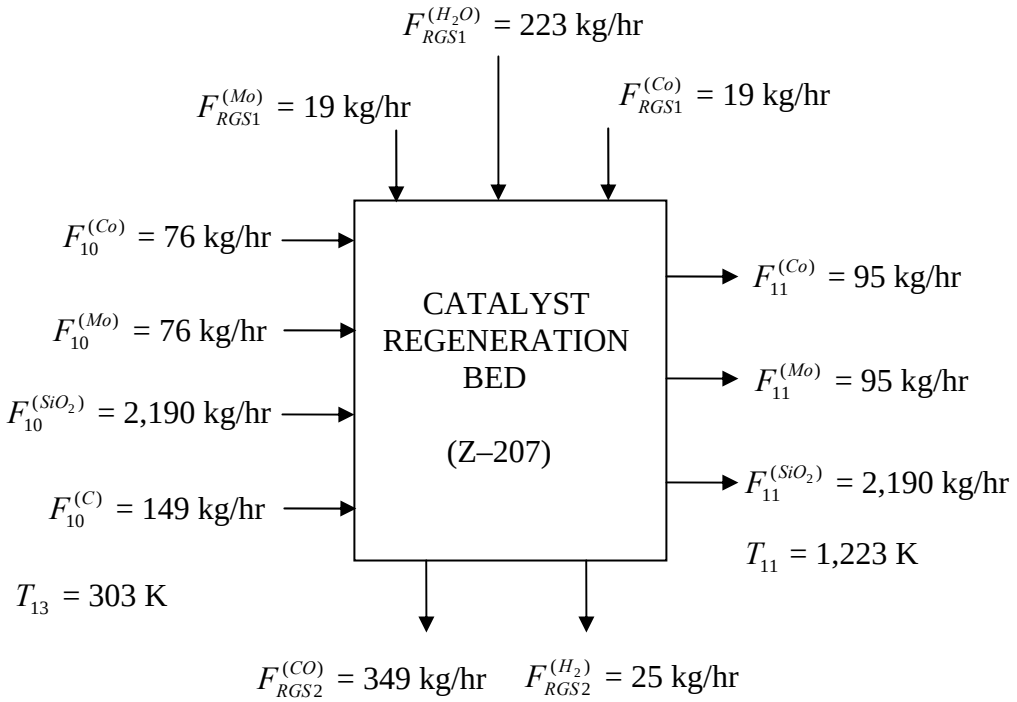

Figure C2.21. Input – Output Component Balance for Catalyst Regeneration Bed (Z–207)

Co: $F_{11}^{(Co)} = F_{10}^{(Co)} + F_{RGS1}^{(Co)} = \mathbf{95\ kg/hr}$

$F_{10}^{(Co)} = 76$ kg/hr; $F_{RGS1}^{(Co)} = 19$ kg/hr

Mo: $F_{11}^{(Mo)} = F_{10}^{(Mo)} + F_{RGS1}^{(Mo)} = \mathbf{95\ kg/hr}$

$F_{10}^{(Mo)} = 76$ kg/hr; $F_{RGS1}^{(Mo)} = 19$ kg/hr

Regeneration Bed Size, V_{Z-207}

The average residence time of the supported silica particles in the catalyst regeneration bed (Z–207) is used to estimate the size of the catalyst regeneration column, according to Equation (C2.28), (Ulrich 1984):

$$\theta(s) = \frac{V_{Z-207} * f_s * \rho_s}{F_{10}^{(SiO_2)}} \qquad \text{(C2.28)}$$

Average Residence time, $\theta = 3{,}600s$ (Ulrich, 1984)

Silica density, $\rho_s = 2{,}250 kg/m^3$ (Felder, et al, 2000)

Mass flow rate of silica, $F_{10}^{(SiO_2)}$ = 0.608 kg/s (2,190 kg/hr)

Fraction of Contactor occupied by solids, f_s = 0.15 (Ulrich, 1984)

Equation (C2.28) gives:

$$V_{Z-207} = \frac{0.608 kg/s * 3600s}{2{,}250 kg/m^3 * 0.15} = \mathbf{6.5\ m^3}$$

$$V_{Z-207} = \frac{\pi D^2}{4} * 4D = \pi D^3 = 6.5\ \text{m}^3$$

Diameter, D_{Z-207} = **1.3 m**

Length, $L_{Z-207} = 4 * D_{Z-207}$ = **5.2 m**

C2.W. Acid Regeneration Column (Z–208) (Refer to Table B2.21)

In the acid regeneration column, the hydrochloric acid used in the acid dissolution step is regenerated by the reactions given in Equations (C2.29 and C2.30), (www.en.wikipedia.org):

$$4CoCl_{2(aq)} + 4H_2O_{(l)} + O_{2(g)} \longrightarrow 2Co_2O_{3(s)} + 8HCl_{(aq)} \qquad \text{(C2.29)}$$

$$MoCl_{2(aq)} + H_2O_{(l)} + O_{2(g)} \longrightarrow MoO_{3(s)} + 2HCl_{(aq)} \qquad \text{(C2.30)}$$

Using the stoichiometric ratio of reactants and products in Equation (C2.29 and C2.30):

HCl Regenerated from Acid Regeneration Column, $F_{09}^{(HCl)}$:

$$F_{09}^{(HCl)} = 41\frac{kgCoCl_2}{hr} * \frac{8kgmolHCl}{4kgmolCoCl_2} * \frac{1kgmolCoCl_2}{131kgCoCl_2} * \frac{37kgHCl}{1kgmolHCl}$$

$$+ 33\frac{kgMoCl_2}{hr} * \frac{2kgmolHCl}{1kgmolMoCl_2} * \frac{1kgmolMoCl_2}{168kgMoCl_2} * \frac{37kgHCl}{1kgmolHCl} = \mathbf{39\ kg/hr}$$

Cobalt Oxide Produced in Regenerator (Z–208), $F_{RG4}^{(Co_2O_3)}$

$$F_{RG4}^{(Co_2O_3)} = 41\frac{kgCoCl_2}{hr} * \frac{2kgmolCo_2O_3}{4kgmolCoCl_2} * \frac{1kgmolCoCl_2}{131kgCoCl_2} * \frac{166kgCo_2O_3}{1kgmolCo_2O_3} = \mathbf{26\ kg/hr}$$

Molybdenum Oxide Produced in Regenerator (Z–208), $F_{RG4}^{(Co_2O_3)}$

$$F_{RG4}^{(MoO_3)} = 33\frac{kgMoCl_2}{hr} * \frac{1kgmolMoO_3}{1kgmolMoCl_2} * \frac{1kgmolMoCl_2}{168kgMoCl_2} * \frac{144kgMoO_3}{1kgmolMoO_3} = \mathbf{28\ kg/hr}$$

The metal oxide (cobalt oxide and molybdenum oxide) residues produced in the acid regeneration column is saturated with hydrochloric acid. However, the hydrochloric acid is recovered from the saturated metal oxide residues in the centrifugal separator (Z–203) and recycled for another reaction cycle (www.acidrecovery.com).

Oxygen Required for Acid Regeneration, $F_{RG1}^{(O_2)}$

$$F_{RG3}^{(O_2)} = (41\frac{kgCoCl_2}{hr} * \frac{1kgmolO_2}{4kgmolCoCl_2} * \frac{1kgmolCoCl_2}{131kgFeCl_2} * \frac{32kgO_2}{1kgmolO_2})$$

$$+ (33\frac{kgMoCl_2}{hr} * \frac{1kgmolO_2}{1kgmolMoCl_2} * \frac{1kgmolMoCl_2}{168kgMoCl_2} * \frac{32kgO_2}{1kgmolO_2}) = \mathbf{9\ kg/hr}$$

Make–up Water Supplied to Acid Regeneration Column, $F_{RG3}^{(H_2O)}$

$$F_{RG3}^{(H_2O)} = \mathbf{265\ kg/hr}$$

The input–output component balance for the acid regeneration column (Z–208) is given in Figure C2.22.

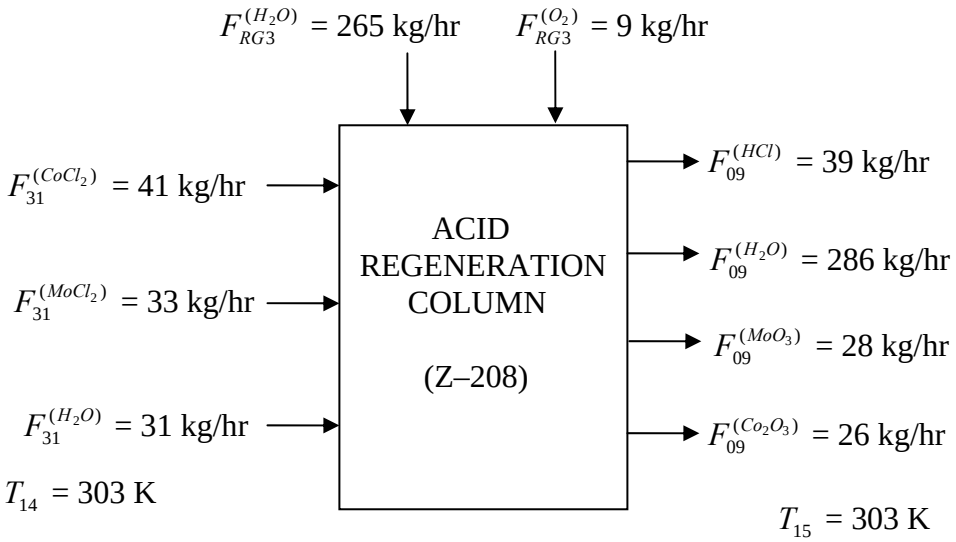

Figure C2.22. Input – Output Component Balance for Acid Regeneration Column (Z–208)

Acid Regeneration Column Size,

The average solid residence time of the iron oxide produced in the regeneration column is used to estimate the equipment size according Equation (C2.31), (Ulrich 1984):

$$\theta(s) = \frac{V_{Z-208} * f_s * \rho_s}{F_{RG4}^{(Co_2O_3)} + F_{RG4}^{(MoO_3)}} \qquad \text{(C2.31)}$$

Average Residence time, $\theta = 3{,}600s$ (Ulrich, 1984)

Density: $\rho^{(Co_2O_3)} = 5{,}180 kg/m^3$ (Perry, et al, 1984)

$\rho^{(MoO_3)} = 4{,}500 kg/m^3$ (Perry, et al, 1984)

Average density, $\rho_s = (\frac{26}{54} * 5{,}180 kg/m^3 + \frac{28}{54} * 4{,}500 kg/m^3) = 4{,}827$ kg/m^3

Mass flow rate of solids, $F_{RG4} = 0.015$ kg/s (54 kg/hr)

Fraction of Contactor occupied by solids, $f_s = 0.15$ (Ulrich, 1984)

Equation (C2.31) gives the volume of the product drier, V_{Z-208}

$$V_{Z-208} = \frac{0.015 kg/s * 3600 s}{4{,}827 kg/m^3 * 0.15}$$

$V_{Z-208} =$ **0.75 m^3**

Length to Diameter ratio = 4 (Ulrich.1984)

$$V_{Z-208} = \frac{\pi D^2}{4} * 4D = \pi D^3 = 0.75 \text{ m}^3$$

Diameter, D_{Z-208} = **0.9 m**

Length, $L_{Z-208} = 4 * D_{Z-208} =$ **3.6 m**

C2.X. **Centrifuge Separator (Z–203):** (Refer to Table B2.11)

The saturated cobalt oxide and molybdenum oxide residues are removed from the hydrochloric acid solution in the centrifuge separator. The input–output component material structure for the centrifuge separator (Z–203) is shown in Figure C2.23:

$$F_{32}^{(HCl)} = F_{09}^{(HCl)} = 39 \text{ kg/hr}$$

$$F_{32}^{(H_2O)} = F_{09}^{(H_2O)} = 286 \text{ kg/hr}$$

$$F_{RG4}^{(Co_2O_3)} = F_{09}^{(Co_2O_3)} = 26 \text{ kg/hr}$$

$$F_{RG4}^{(MoO_3)} = F_{09}^{(MoO_3)} = 28 \text{ kg/hr}$$

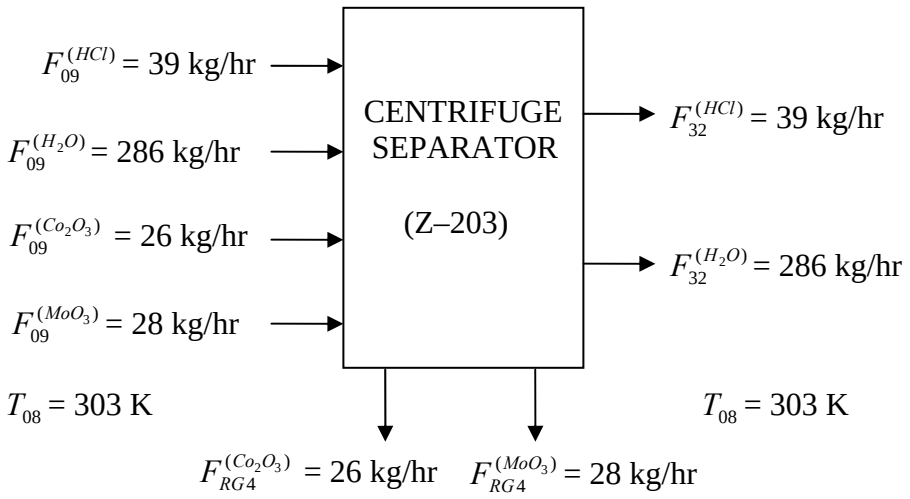

Figure 2.23. Input – Output Material Structure for Centrifuge Separator (Z–203)

This concludes the analysis of the material and energy balance equations for the process equipment in the CoMoCAT process model. In this section, the mass flow rates of component species into and out of individual process equipment were determined. Furthermore, the sizes of the major process equipment were determined, and preliminary design criteria and data for the selection of major process equipment specified.

APPENDIX D: SAMPLE CALCULATION COST ESTIMATES

The procedure for calculating the annual costs of the cost elements in the total product estimates is discussed below. The total product estimates include raw materials costs, utilities costs and operating labor costs. In order to determine the annual estimate of these cost elements, the fraction of time that the plant is operating in year must be specified. This fraction is known as the stream factor (SF). Assuming the plant is shut down for 15 days in a year for mandatory maintenance:

$$\text{SF = Number of days plant operate in a year/365= } \frac{350}{365} = 0.96$$

D.1 Raw Materials Costs:

Yearly Cost = (Yearly Flow Rate) x (Cost per unit mass)

a) HiPCO Process:

The rate of consumption of CO reactant, iron pentacarbonyl catalyst precursor and oxygen in the HiPCO production process is given by the mass flow rates of CO in SR01, $Fe(CO)_5$ in SR02 and oxygen (AR_{in}) supplied to the air oxidizer.

Carbon monoxide:

$$\text{Yearly Cost = } 2{,}637\frac{kgCO}{hr} * 24\frac{hr}{day} * 365\frac{day}{yr} * 0.96 * \frac{\$0.031}{kgCO} = \textbf{\$688,000/yr}$$

Iron Pentacarbonyl:

$$\text{Cost = } 627\frac{kgFe(CO)_5}{hr} * 24\frac{hr}{day} * 365\frac{day}{yr} * 0.96 * \frac{\$26.40}{kgFe(CO)_5} = \textbf{\$139,000,000/yr}$$

Oxygen:

$$\text{Yearly Cost = } 227\frac{kgO_2}{hr} * 24\frac{hr}{day} * 365\frac{day}{yr} * 0.96 * \frac{\$0.06}{kgO_2} = \textbf{\$115,000/yr}$$

b) CoMoCAT Process:

The rate of consumption of CO reactant and silica supported bimetallic catalyst in the CoMoCAT process is given by the mass flow rates of CO in SR01 and supported catalyst in SR11 respectively. The CoMoCAT design is based on a 8 hour catalyst loading–regeneration cycle, and consequently fresh supported catalyst loading takes place three times in a 24 hour production cycle. The total costs of supported catalyst consumed in the process include the cost of fresh catalyst and catalyst regeneration costs.

Carbon monoxide:

$$\text{Yearly Cost} = 3{,}471\frac{kgCO}{hr} * 24\frac{hr}{day} * 365\frac{day}{yr} * 0.96 * \frac{\$0.031}{kgCO} = \textbf{\$905,000/yr}$$

Fresh Silica Supported Co–Mo Catalyst:

$$\text{Yearly Cost} = 2{,}380\frac{kgCatalyst}{loading} * 3\frac{loading}{day} * 365\frac{day}{yr} * 0.96 * \frac{\$26.00}{kgCatalyst}$$

Yearly Cost = **$65,000,000/yr**

Catalyst Regeneration Costs:

$$\text{Yearly Cost} = 2{,}380\frac{kgCatalyst}{hr} * 24\frac{hr}{day} * 365\frac{day}{yr} * 0.96 * \frac{\$0.90}{kgCatalyst}$$

Annual Regeneration Costs = **$18,000,000/yr**

D.2 Utilities Costs

a) HiPCO Process:

Boiler Feed Water (BFW) Costs:

$$\text{Yearly Cost} = 6{,}517\frac{kgBFW}{hr} * 24\frac{hr}{day} * 365\frac{day}{yr} * 0.96 * \frac{\$2.5 * 10^{-3}}{kgBFW} = \textbf{\$137,000/yr}$$

Cooling Water Costs:

$$\text{Yearly Cost} = 53{,}228\frac{kgCW}{hr} * 24\frac{hr}{day} * 365\frac{day}{yr} * 0.96 * \frac{\$6.7 * 10^{-5}}{kgCW} = \textbf{\$30,000/yr}$$

HP Steam Costs:

The high pressure (HP) steam consumed in the HiPCO process is the difference between the HP steam consumed in the process and the HP steam produced in the process. HP steam is consumed by these process units: the flow reactor (V–101), and the kettle reboiler (E–105), while the HP steam is produced in the waste heat boiler (E–102). The net HP steam consumed in the HiPCO process is estimated below:

$$F_{HPSteam}(kg/hr) = \frac{Q(kJ/hr)}{\Delta H_{vap}(kJ/kg)}$$

$$\Delta H_{vap} = 1{,}661.5 \text{ kJ/kg} \qquad \text{(Smith, et al, 1996)}$$

Reactor (V–102): $F_{HPSteam}(kg/hr) = 2{,}000$ kg/hr

Reboiler (E–106): $F_{HPSteam} = 3{,}000$ kg/hr

Waste Heat Boiler (E–103): $F_{HPSteam} = 7{,}000$ kg/hr

HP Steam Requirement = (2,000 +3,000 + 7,000) kg/hr

$$F_{HPSteam} = \textbf{12,000 kg HP Steam/hr}$$

$$\text{Yearly Cost} = 12{,}000\frac{kgSteam}{hr} * 24\frac{hr}{day} * 365\frac{day}{yr} * 0.96 * \frac{\$0.00865}{kgSteam} = \textbf{\$1,000,000/yr}$$

b) <u>CoMoCAT Process:</u>

Boiler Feed Water (BFW) Costs:

$$\text{Yearly Cost} = 7{,}333\frac{kgBFW}{hr} * 24\frac{hr}{day} * 365\frac{day}{yr} * 0.96 * \frac{\$2.5 * 10^{-3}}{kgBFW} = \textbf{\$154,000/yr}$$

Cooling Water Costs:

$$\text{Yearly Cost} = 59{,}089\frac{kgCW}{hr} * 24\frac{hr}{day} * 365\frac{day}{yr} * 0.96 * \frac{\$6.7 * 10^{-5}}{kgCW} = \textbf{\$33,000/yr}$$

HP Steam Costs:

$$F_{HPSteam}(kg/hr) = \frac{Q(kJ/hr)}{\Delta H_{vap}(kJ/kg)}$$

$$\Delta H_{vap} = 1{,}661.5 \text{ kJ/kg} \qquad \text{(Smith, et al, 1996)}$$

Reactor (V–201): $F_{HPSteam}(kg/hr) = 3{,}000$ kg/hr

Reboiler (E–105): $F_{HPSteam} = 3{,}000$ kg/hr

Waste Heat Boiler (E–202): $F_{HPSteam} = 8{,}000$ kg/hr

$F_{HPSteam} = (3{,}000 + 3{,}000 + 8{,}000)$ kg/hr = 14,000 kg/hr

$$\text{Yearly Cost} = 14{,}000\frac{kgSteam}{hr} * 24\frac{hr}{day} * 365\frac{day}{yr} * 0.96 * \frac{\$0.00865}{kgSteam} = \textbf{\$1,100,000/yr}$$

D.3 Labor Costs

The operating labor requirement for chemical processing plant can be estimated from Equation (D.1) (Turton, et al., 2003):

$$N_{OL} = (6.29 + 31.7P^2 + 0.23N_{np})^{0.5} \qquad \text{(D.1)}$$

$$N_{np} = \sum Equipment$$

N_{OL} = Number of operators required to run the process unit per shift

N_{np} = Number of non–particulate processing steps

P = Number of processing steps involving particulate solids handling

The operator works five 8–hour shifts a week for 49 weeks. This translates to 245 shifts per operator per year, and requires 1,095 operating shifts per year. The number of operators required to provide this number of shift is about 5 operators:

a) HiPCO Process:

P = 7,

$$N_{np} = 13$$

$$N_{OL} = (6.29 + 31.7P^2 + 0.23N_{np})^{0.5} = 39.54$$

Number of operators required per shift = 39.54

Operating Labor = (4.5) (39.54) = **178**

b) CoMoCAT Process:

P = 9,

$$N_{np} = 12$$

$$N_{OL} = (6.29 + 31.7P^2 + 0.23N_{np})^{0.5} = 50.76$$

Operating Labor = (4.5) (50.76) = **229**

D.4 Rate of Return (ROR):

$$NPV = -TCI + I_{xt} * \left(\frac{1-(1+i)^{-n}}{i} \right) = 0$$

n = 10

Solution obtained by MathCAD

a) HiPCO Process:

$$F(i) := -4{,}600{,}000 + 171{,}880{,}000 * \left(\frac{1-(1+i)^{-10}}{i} \right)$$

$$i := 0.20$$

$$so\ln := root(F(i), i)$$

$$so\ln = 37.4$$

b) CoMoCAT Process:

$$F(i) := -4{,}400{,}000 + 212{,}000{,}000 * \left(\frac{1-(1+i)^{-10}}{i} \right)$$

$$i := 0.20$$

$$so\ln := root(F(i), i)$$

$$so\ln = 48.2$$

VITA

Adedeji Agboola was born on September 10, 1974, in Ibadan, Nigeria. He completed his secondary school education from Loyola College, Ibadan, Nigeria, in December, 1991. He obtained the degree of Bachelor of Science in Chemical Engineering from Obafemi Awolowo University, Ile–Ife, Nigeria, in December, 1999. He worked with Shell Petroleum Development Company (SPDC), Nigeria, as company site representative in the installation of oil production facilities, from August, 2001 to July, 2003. Later in August, 2003, he was enrolled in the Department of Chemical Engineering at Louisiana State University, Baton Rouge, Louisiana, to attend graduate school. He is presently a candidate for the degree of Master of Science in Chemical Engineering.